

Wave Phenomena in Phononic Crystals

by

Alexey Sukhovich

A Thesis

submitted to the Faculty of Graduate Studies of
the University of Manitoba

in partial fulfillment of the requirements of the degree of

Doctor of Philosophy

DEPARTMENT OF PHYSICS AND ASTRONOMY

UNIVERSITY OF MANITOBA

WINNIPEG, MANITOBA

CANADA

Copyright © June, 2007 by Alexey Sukhovich

In the memory of my father

Abstract

Novel wave phenomena in two- and three-dimensional (2D and 3D) phononic crystals were investigated experimentally using ultrasonic techniques. These ultrasonic techniques allow the full wave field to be imaged directly, which is a considerable advantage in fundamental studies of wave propagation in periodic media.

Resonant tunnelling of ultrasonic waves was successfully observed for the first time by measuring the transmission of ultrasound pulses through a double barrier consisting of two 3D phononic crystals separated by a cavity. This effect is the classical analogue of resonant tunnelling of a quantum mechanical particle through a double potential barrier, in which transmission reaches unity at resonant frequencies. For phononic crystals, the tunnelling peak was found to be less than unity, an effect that was explained by absorption. Absorption introduces a small propagating component inside the crystals in addition to the dominant evanescent mode at band gap frequencies, and causes leakage of the pulse from the cavity. The dynamics of resonant tunnelling was explored by measuring the group velocities of the ultrasonic pulses. Very slow and very fast velocities were found at frequencies close to and at the resonance, respectively. These extreme values are less than the speed of sound in air and greater than the speed of sound in any of the crystal's constituent materials.

Negative refraction and focusing effects in 2D phononic crystals were also observed. Negative refraction of ultrasound was demonstrated unambiguously in a prism-shaped 2D crystal at frequencies in the 2nd pass band, where the equifrequency contours are circular so that the wave vector and group velocity are antiparallel. The Multiple Scattering Theory and Snell's law allowed theoretical predictions of the refraction angles.

Excellent agreement was found between theory and experiment. The negative refraction experiments revealed a mechanism that can be used to focus ultrasound using a flat phononic crystal, and experiments to demonstrate the focusing of ultrasound emitted by several point sources were successfully carried out. The importance of using phononic crystals with circular equifrequency contours, as well as matching the size of the contours inside and outside the crystal, was established. Both conditions were satisfied by a flat phononic crystal of steel rods, in which the liquid inside the crystal (methanol) was different from the outside medium (water). The possibility of achieving *subwavelength* resolution using this phononic crystal was investigated with a subwavelength line source (a miniature strip-shaped transducer, approximately $\lambda/5$ wide). A resolution of 0.55λ was found, which is just above the diffraction limit $\lambda/2$.

Acknowledgements

Here I would like to thank everyone, whose help and participation made this thesis possible. First of all, I wish to express the deepest gratitude and respect to my thesis supervisor Dr. John H. Page for all the support and guidance that he gave me during my Ph.D. research. I benefited a lot from the knowledge and experience that he shared with me and it was a great honour for me to be his student.

I would like to thank all members of the Ultrasonic Research Laboratory, both past and present, for creating a friendly and enjoyable atmosphere. My special thanks are addressed to: Dr. Anatoliy Strybulevych, with whom I happened to work side-by-side for six years and who was always there to give me a hand when I needed it; Matthew Hasselfield, for creating numerous and enormously useful MATLAB codes and interfaces, which greatly facilitated data acquisition in all the experiments; Dr. Tomohisa Norisue who introduced me to and gave me an initial tutoring in IGOR – a software package that proved to be invaluable in the process of data analysis at the latest stage of my studies; Dr. Susan Yang, for helpful discussions.

I also wish to thank our collaborator Dr. Zhengyou Liu for providing the FORTRAN code, based on the MST, which allowed theoretical calculations of phononic crystal properties.

It is impossible to overlook Gilles Roy, a wise man, who knows everything about the life and how tough *she* is in particular, and who was always helpful whenever I asked him for assistance. I also would like to thank our technical staff, machinist Grant Mollard for creating templates for all my samples with precision and accuracy, and electronics technician Richard Hamel for his help with electronic equipment.

Financial support from the University of Manitoba in the form of a University of Manitoba Graduate Fellowship is gratefully acknowledged.

My special thanks are addressed to my family, my mother and my brother, for their endless love. They are always in my thoughts, just as I am in theirs.

Finally, I would like to thank my wife Sofiya; her contribution in the completion of this thesis cannot be overestimated, for it is her understanding, constant encouragement and love that gave me strength to go through the most difficult moments of my studies.

Table of contents

Abstract	i
Acknowledgements	iii
List of Figures	vii
List of Tables	xiv
1. Introduction	1
1.1 Phononic crystals: past and modern research directions.....	2
1.2 Thesis structure	22
2. Theory	23
2.1 Phononic crystals	24
2.1.1 Periodic structures and their properties.....	24
2.1.2 Two- and three-dimensional phononic crystals	30
2.1.3 Multiple Scattering Theory	37
2.2 Band structure effects in 2D phononic crystals	47
2.2.1 Negative refraction in phononic crystals	47
2.2.2 Focusing properties of 2D phononic crystals.....	58
3. Experiment	63
3.1 Sample preparation	64
3.1.1 2D phononic crystals.....	64
3.1.2 3D phononic crystals.....	68
3.2 Mechanical apparatus.....	73
3.2.1 Apparatus for the experiments with 3D phononic crystals.....	73
3.2.2 Apparatus for the experiments with 2D phononic crystals.....	75
3.3 Electronics.....	76
3.3.1 Generating electronics	76
3.3.2 Receiving electronics.....	79
3.4 Ultrasound generators and detectors	81
3.4.1 Plane wave immersion transducers.....	81
3.4.2 Hydrophone.....	86
3.4.3 Pinducer	87

3.4.5 Line source transducer	87
3.5 Measurements	91
3.5.1 Transmission experiments	91
3.5.2 Field mapping experiments.....	97
4. Experiments with 3D phononic crystals	102
4.1 Properties of single 3D phononic crystals	103
4.1.1 Transmission spectra of single 3D phononic crystals.....	103
4.1.2 Tunnelling of ultrasound pulses through single 3D phononic crystals.....	105
4.2 Resonant tunnelling of ultrasound pulses	110
4.2.1 Resonant tunnelling through a double potential barrier.....	110
4.2.2 Resonant tunnelling of ultrasonic waves: Transmission.....	115
4.2.3 Resonant tunnelling of ultrasonic waves: Group time.....	125
5. Experiments with 2D phononic crystals	141
5.1 Negative refraction of ultrasound	142
5.1.1 Transmission coefficient and band structure	142
5.1.2 Negative refraction experiments with the 2D prism-shaped crystal.....	150
5.2 Near-field imaging with flat 2D phononic crystals.....	183
5.2.1 Imaging experiments with 2D flat crystal filled with water	183
5.2.2 Imaging experiments with 2D flat crystal filled with methanol	199
6. Conclusions	212
Appendices.....	216
Appendix A. Determination of the effective diameter of the pinducer	216
Appendix B. Transfer matrix through a single potential barrier.....	220
Appendix C. Subsidiary peaks observed in transmission spectra of the resonant tunnelling experiments.....	223
Appendix D. The investigation of the effect of a plastic film used to separate methanol and water in 2D phononic crystal	232
References.....	234

List of Figures

2.1.1	A 2D triangular Bravais lattice.	24
2.1.2	Simple-cubic direct lattice and its reciprocal lattice.	27
2.1.3	The first three Brillouin zones of a reciprocal lattice of the 2D square Bravais lattice.	28
2.1.4	The direct and reciprocal lattices of the 2D phononic crystals.	32
2.1.5	The direct and reciprocal crystal lattices of the 3D phononic crystals.	33
2.1.6	Schematic diagram explaining the formation of a 3D crystal in a ABCABC... sequence.	34
2.1.7	The first Brillouin zone of the FCC lattice and its high symmetry points.	35
2.1.8	Geometry of the layer MST.	42
2.1.9	Explanation of the physical significance of the matrices $\mathbf{M}_{kk'}^{ss'}$.	45
2.2.1	Reflection and refraction of a plane wave incident obliquely on the liquid/solid interface from the liquid.	48
2.2.2	Equipfrequency surface of an isotropic medium.	49
2.2.3	Refraction of a plane wave is illustrated with the help of the equipfrequency contours.	51
2.2.4	Equipfrequency contours predicted by MST for the several frequencies in the 2 nd band of the 2D phononic crystal.	52
2.2.5	Refraction of a plane wave at the water/crystal interface.	53
2.2.6	Negative refraction of a plane wave incident obliquely on the water/crystal interface.	54
2.2.7	Propagation of the sound wave through a flat crystal with parallel surfaces.	56
2.2.8	Negative refraction experiment with the prism-shaped phononic crystal.	57
2.2.9	Focusing of the point source radiation by a slab of LH material.	59
2.2.10	Focusing by a slab of LH in case of $n_1 \neq n_2 $.	60

2.2.11	The condition $k_{wat} = k_{cr}$ for matching equipfrequency contours.	62
3.1.1	Unit cell of a 2D phononic crystal.	64
3.1.2	Geometry of the 2D crystals.	65
3.1.3	Pictures of the 2D crystals filled with and immersed in water.	66
3.1.4	Methanol filled 2D crystal cell design.	67
3.1.5	Template for 3D phononic crystal with side views of walls A and B.	69
3.1.6	3D single phononic crystal.	71
3.1.7	Close-up view of the surface of the crystal.	72
3.2.1	Experimental set-up for resonant tunneling experiments.	74
3.2.2	Geometry of the small water tank.	75
3.3.1	Three configurations of generating electronics set-ups.	78
3.3.2	Receiving electronics set-up.	80
3.4.1	Diagram explaining plane wave transducer design.	82
3.4.2	Geometry used for calculation of the field produced by a circular piston.	83
3.4.3	Thin disk radiator pressure along the z -axis.	84
3.4.4	Directivity factor $J_1(x)/x$.	85
3.4.5	Transducer beam pattern.	86
3.4.6	PVDF transducer.	89
3.4.7	PVDF transducer holder with the transducer in place.	90
3.5.1	Input and transmitted pulses through a 3D double phononic crystal.	93
3.5.2	Fourier Transform magnitudes of the input and transmitted pulses.	94
3.5.3	Transmission coefficient through 3D double phononic crystal.	95
3.5.4	Group velocity calculation from the time delay measured between filtered input and transmitted pulses.	97
3.5.5	Sample image plot of the outgoing pulse in the negative refraction experiment with the prism-shaped 2D crystal.	100
3.5.6	Sample image plot showing field amplitude distribution produced in the focusing experiment with the rectangular-shaped 2D crystal.	101
4.1.1	Band structure of the 3D phononic crystal.	104

4.1.2	Transmission coefficient through 2-, 3- and 4-layer single 3D phononic crystals	105
4.1.3	Group velocity of ultrasonic pulses propagating through 2-, 3- and 4-layer single 3D phononic crystals.	106
4.1.4	Group velocity as a function of crystal thickness at 0.95 MHz.	107
4.1.5	Transmitted amplitude as a function of the crystal thickness along with the least-square fits.	108
4.2.1	Double potential barrier of Quantum Mechanics.	110
4.2.2	Transmission coefficient of a particle through double potential barrier.	113
4.2.3	Schematic representation of the transmission experiments with 3D double phononic crystals.	116
4.2.4	Input and transmitted pulses through a 3D double phononic crystal.	117
4.2.5	Transmission spectra through the double crystals.	118
4.2.6	Comparison between transmission experiment through the double crystal and MST calculations.	121
4.2.7	Frequency dependence of the group time and group velocity of the pulses transmitted through different double crystals.	126
4.2.8	Comparison of the measured group velocity and time for 4-layer double crystal with the predictions of the MST.	128
4.2.9	Schematic diagram of the transmission experiment with 3D double phononic crystals.	129
4.2.10	The main pulses transmitted through 3- and 4-layer double crystals along with the overlapping echoes.	130
4.2.11	The evolution of the group time at resonance as a function of the pulse truncation time for 3- and 4-layer double crystals.	132
4.2.12	The evolution of the group time at resonance as a function of the individual crystal thickness in case of no absorption.	133
4.2.13	The comparison of the measured group times at resonance with those predicted by the MST in case of the absorption present in the system.	134

4.2.14	Representative data illustrating the problem of subsidiary peaks in transmission coefficient and group time.	136
4.2.15	Measured transmission coefficient and group time for the new 3-layer double crystal.	138
4.2.16	Comparison of the measured transmission and group time through the new 3-layer double crystal with the calculations by the MST.	139
5.1.1	12-layer rectangular-shaped 2D phononic crystal.	143
5.1.2	Band structure of the 2D phononic crystal.	144
5.1.3	Experimental and theoretical transmitted amplitudes for a 6-layer 2D phononic crystal along the ΓM direction.	145
5.1.4	Comparison of the experimental and theoretical band structure curves for a 6-layer 2D phononic crystal along the ΓM direction.	146
5.1.5	Experimental and theoretical transmission curves for a 12-layer 2D phononic crystal along the ΓK direction.	147
5.1.6	Experimental and theoretical band structure curves for a 12-layer 2D phononic crystal along the ΓK direction.	148
5.1.7	Negative refraction experiment geometry.	151
5.1.8	Outgoing pulses in the negative refraction experiment at 0.85 MHz and 0.75 MHz.	152
5.1.9	Experimentally measured band structure displayed in the reduced-zone and extended-zone schemes.	154
5.1.10	Negative and positive refraction at the crystal/water interface.	155
5.1.11	The scan of the opposite side of the prism-shaped crystal.	158
5.1.12	Ray diagram of the experiment considered in Figure 5.1.11.	159
5.1.13	Images of the emerging field at 0.85 MHz and 0.95 MHz frequency.	160
5.1.14	Positively refracted beam at the crystal/water interface.	161
5.1.15	Negatively and positively refracted beams at the crystal/water interface perpendicular to the ΓK direction.	163
5.1.16	1 st band of the 2D phononic crystal.	164
5.1.17	Snapshot of the outgoing pulse in the experiment probing the behaviour at frequencies lying in the 1 st band.	165

5.1.18	Geometry of the inverse experiment.	166
5.1.19	1 st Brillouin zone, water and crystal equifrequency contours.	168
5.1.20	Ray diagram of the inverse experiment.	168
5.1.21	Snapshot of the outgoing pulse in the inverse experiment at 0.85 MHz frequency.	170
5.1.22	Snapshot of the outgoing pulse in the inverse experiment at 0.75 MHz frequency.	170
5.1.23	Geometry of the experiment with the input pulse incident along the ΓK direction.	171
5.1.24	Snapshot of the output field when the input pulse is incident along the ΓK direction.	172
5.1.25	The possible field distributions inside the crystal corresponding to coupling band and non-coupling band.	174
5.1.26	Field calculated using the MST for the case of a plane wave incident along the ΓK direction.	175
5.1.27	The image plot in Figure 5.1.26 displayed on a smaller colour scale.	176
5.1.28	Left portion of the field pattern inside the crystal displayed in Figure 5.1.27.	177
5.1.29	The outgoing part of the field displayed in Figure 5.1.26.	178
5.1.30	Snapshot of the field emerging from the output side with the input pulse incident along the ΓK direction.	179
5.1.31	Comparison of the input beam profile used in the calculations with the one produced experiment along the ΓK direction.	180
5.2.1	Geometry of the near-field imaging experiment with the rectangular-shaped phononic crystal.	184
5.2.2	2D image plot of wave amplitude at 0.75 MHz.	185
5.2.3	Wave field amplitude as a function of a position obtained from Figure 5.2.2.	186
5.2.4	Focal spot amplitude at 0.75 MHz and fit of the absolute value of the sinc function.	188
5.2.5	Explanation of the origin of the cut-off angle.	189

5.2.6	Percentage deviation of the wavevector along the ΓK direction with respect to the wavevector along the ΓM direction.	190
5.2.7	2D image plot of wave amplitude at 0.69 MHz.	191
5.2.8	Wave field amplitude as a function of a position obtained from Figure 5.2.7.	192
5.2.9	2D image plot of wave amplitude at 0.67 MHz.	193
5.2.10	Wave field amplitude as a function of a position obtained from Figure 5.2.9.	194
5.2.11	Distance L_2 as a function of the angle of incidence.	196
5.2.12	Measured focal profiles along the perpendicular direction for three different frequencies.	197
5.2.13	Comparison between calculated by the MST and experimentally measured band structures crystal filled with methanol.	200
5.2.14	Image plot at 0.55 MHz in the experiment on imaging pinducer field with the methanol matrix crystal.	201
5.2.15	Wave field amplitude at 0.55 MHz read from the image plot shown in Figure 5.2.14.	202
5.2.16	Amplitude peak at 0.55 MHz along with fitted sinc function.	203
5.2.17	Image plot at 0.55 MHz in the experiment on imaging the line source transducer with the methanol matrix crystal.	205
5.2.18	Wave field amplitude at 0.55 MHz read from the image plot shown in Figure 5.2.17.	206
5.2.19	Amplitude peak at 0.55 MHz along with fitted sinc function.	207
A.1	Top view of the pinducer.	216
A.2	Initial field distribution amplitude used in calculations of the pinducer field.	217
A.3	2D image plot obtained by scanning pinducer field.	218
A.4	Comparison of calculated and measured pinducer field profiles.	219
B.1	A single rectangular potential barrier.	220
C.1	Transmission spectrum through one of the 3-layer double crystals.	223

C.2	The transmitted pulse, from which the transmission coefficient in Figure C.1 was found.	224
C.3	The envelope of the pulse shown in Figure C.2.	225
C.4	Comparison of the resonant tunnelling peaks for three generating transducers of different diameters.	226
C.5	The waveforms transmitted through the 3-layer double crystal in case of three different generating transducers.	227
C.6	Comparison of the two resonant tunnelling peaks, measured under different conditions through the same 3-layer double crystal.	229
D.1	Comparison of the transmission spectra through the crystal immersed with and without plastic film wrapped around the crystal.	233

List of Tables

3.1.1	Properties of the constituent materials used for 2D phononic crystals.	68
4.2.1	Values of the absorption coefficients found from the best MST fits to the measured transmission and group times.	123
4.2.2	Comparison of group times measured at the largest truncation time and determined from the extrapolation procedure.	131
5.1.1	The predicted magnitudes of \vec{k}_{red} and \vec{k}_{ext} for some frequencies.	156
5.1.2	Comparison between experimentally measured and theoretically calculated angles of refraction.	157

1. Introduction

In this chapter I will provide an overview of the research activities, both past and recent, in the field of phononic crystals. Nonwithstanding of my best effort, by no means should this account be considered as full and complete. I hope, however, that it will still serve a useful purpose of introducing the subject and setting up a framework within which the importance of my own findings, and how they fit in the general picture of the field, can be perceived.

1.1 Phononic crystals: past and modern research directions

Phononic crystals, which are acoustic or elastic composite structures made of periodically arranged inclusions surrounded by a host background material, have attracted a lot of attention within the past 15 years from both theoretical and experimental communities. According to the generally accepted convention, one speaks about an elastic or acoustic phononic crystal depending on whether the host material can (gas or liquid) or cannot (solid) support transversely polarized waves. The interest in phononic crystals is based on the fundamental physics involved in the process of propagation of acoustic or elastic waves through the periodic media as well as their potential applications, which will be discussed later in this section.

Although most of the research effort in the field of phononic crystals has been concentrated within relatively short period of time (since about 1993), the issue of periodic elastic structures was also addressed before this period. For example, in 1979 Narayanamurti *et al.* investigated the propagation of high-frequency phonons through a GaAs/AlGaAs superlattice, which can be regarded as a one-dimensional phononic crystal [1]. They observed filtering action (selective transmission) by the superlattice when the phonons' wavelength satisfied the Bragg condition, i.e. it was equal to twice the superlattice period. In close analogy with optical dielectric filters, the authors called their structure a "dielectric" phonon filter. In 1987, Achenbach *et al.* published a theoretical work in which they calculated a low-frequency part of a dispersion curve of an infinite three-dimensional structure made by stacking parallel planes of solids with a rectangular array of spherical voids in each layer [2]. They predicted the existence of a stop band (the absence of propagating modes) for a longitudinal plane wave incident normally on the

structure. It was not, however, until the beginning of the 90's that phononic crystals began receiving considerable interest, which has been steadily increasing ever since. One should mention that this interest was partially fuelled by the successes of the rapidly growing field of *photonic* crystals, which are periodic composites of different *dielectric* materials. They were introduced initially by Yablonovitch in 1987 [3], who suggested that three-dimensional (3D) dielectric structures might possess complete band gaps in which no optical modes will exist. The existence of such forbidden frequency regions in photonic crystals immediately attracted a wide interest from many researchers in the field of photonics, by offering many new exciting possibilities. With the help of photonic crystals one can imagine, for example, constructing perfect dielectric mirrors working at the gap frequencies, trapping and guiding light by introducing defects into crystals, or even improving the efficiency of a semiconductor laser by inhibiting the spontaneous electron-hole recombination in the case when the photonic band gap overlaps with the electronic band edge. Although they are not the main subject of this thesis, some of the key developments in the field of photonic crystals will also be mentioned in this overview, as many of the ideas proposed initially for photons have made their way into the area of phonons.

Just as in case of photonic crystals, the idea of creating materials with complete acoustic or elastic band gaps, i.e., frequency regions in which wave propagation is blocked for any direction inside the material, sparked a new interest in periodic elastic materials. The phononic crystals with complete band gaps can be potentially used as sound filters and noise-proof devices to provide a vibrationless environment for high-precision mechanical systems. From the point of view of the fundamental physics involved, phononic crystals are even more challenging than photonic crystals to model theoretically

due to a number of additional parameters entering the problem such as density and Lamé coefficients as well as an extra polarization of the wave field inside the crystal. The strong coupling between longitudinal and transverse waves is another complicating factor, which must also be taken into account. At the same time, these new parameters can be advantageous since they allow greater control of the crystal properties and thus provide an easier way to create periodic structures with large full band gaps. The search for periodic composite materials possessing complete elastic and acoustic band gaps was initiated in 1993 by Kushwaha *et al.* [4]. The major effort in the field was initially concentrated on elucidating the conditions that favor the formation of full band gaps in different types of phononic crystals (2D and 3D, solid/solid, liquid/liquid and mixed). The existence of full band gaps was demonstrated both theoretically and experimentally for 2D and 3D phononic crystals [5-12]. The formation and width of complete band gaps was found to depend on the density contrast as well as differences of the sound velocities and elastic constants in the constituent materials, with the density contrast playing the most important role [8]. The investigations have also shown that another factor influencing the opening of a complete band gap is the geometry of the crystal structure. For example, Sainidou *et al.* investigated theoretically 3D phononic crystals with different crystal structures made of steel spheres in polyester matrix and found that width of a band gap increased with the filling ratio of a corresponding crystal lattice [10]. The above authors also pointed out the important role played by resonant elastic modes of the individual spheres in the formation of large elastic band gaps. They have shown that in the 3D samples, which they investigated, large complete band gaps open as a result of hybridization between narrow bands due to weak coupling between rigid-body resonance modes of single spheres and the continuum bands corresponding to propagation in an effective homogeneous medium.

The importance of the single sphere scattering resonances in band gap formation was also addressed in a review paper by Sigalas *et al.* [11]. It was shown experimentally by Page *et al.* that the width of the band gap increases significantly as one moves from a mixed phononic crystal (solid scatterers in a liquid matrix, which does not support transverse waves) to the identical crystal structure with a solid matrix [12]. Page *et al.*' findings provided experimental confirmation of the hybridization mechanism for band formation proposed by Sainidou *et al.* [10].

Another way to increase width of the band gap was reported by Caballero *et al.*, who found that the full sonic band gap of a 2D periodic structure of rigid rods in air can be increased by reducing the symmetry of the structure [13]. Goffaux *et al.* suggested a phononic crystal with a *tunable* band gap, which was realized with an array of rods of square cross-section allowed to rotate around their axis. The gap width was found to change with the change in angle through which all rods were rotated [14]. The ability of phononic crystals to block sound waves in the frequency ranges corresponding to the band gaps suggests one of their potential applications as noise-proof devices. The idea of creating sonic shields that would provide noise control at audible frequencies has attracted attention of several groups [15-17]. The sound attenuation by a periodic structure was first demonstrated by Martinez-Sala in the experiments with a sculpture by Spanish artist Eusebio Sempere, which consisted of hollow steel cylinders of 29 mm in diameter arranged in square lattice with a lattice constant of 100 mm [15]. The researchers found a significant sound attenuation around 1.67 kHz frequency. Vasseur *et al.* investigated sound propagation through a square array (with lattice constant of 30 mm) of hollow copper tubes (13 mm in diameter, 450 mm long) in air along the [10] direction and found a band gap between 4.0 and 8.8 kHz [16]. Kushwaha *et al.* proposed a tandem structure

made of several phononic crystals (each being a 3-layer array of circular metallic rods) stacked in series. The stacked crystals differed from each other by rod diameter and lattice constant, which ranged from 2.0 to 7.6 cm. They showed that by varying the filling ratio of the crystals (i.e. rod diameters and lattice constants) the widths of the band gaps of each crystal can be adjusted so that together they would form one ultra-wide stop band spanning the frequency range between 2 and 11 kHz [17].

The governing mechanism opening full band gaps in phononic crystals described in the preceding paragraph is the one due to Bragg reflections ensuing from the crystals' periodicity. Their potential widespread use as acoustic shields working at audible frequencies is, however, severely limited by the large sizes that follow from the requirement that the lattice constant and unit scatterer dimensions must be comparable to the sound wavelength. Alternative composite structures, in which full band gaps open due to *local resonances* associated with individual scatterers, were proposed theoretically and demonstrated experimentally by Liu *et al.* [18]. They considered structures in which each scattering unit consisted of a high density solid core (1.0 cm-diameter lead balls) coated with an elastically soft material (silicon rubber) that was embedded in a matrix made of another rigid material (epoxy). Due to presence of the soft material in between two highly rigid materials, low-frequency resonances associated with a single scattering unit arise, which are manifested as the motion of its hard core with respect to the surrounding matrix. The group investigated sound propagation at audible frequencies (0.2-1.4 kHz) through a 3D simple cubic sonic crystal (8×8×8 layers with lattice constant of 15.5 mm) made of the locally resonant scattering units described above and residing in the epoxy matrix. They found the existence of two wide attenuation bands at around 0.4 and 1.3 kHz [18]. This is

a remarkable result considering that sound wavelength in epoxy at 0.4 kHz is about 6.4 m, which is about 400 times larger than the crystal's lattice constant. By rigorous calculations Liu *et al.* have also shown that, at the frequencies above the resonance frequency, real part of the *effective* mass density becomes negative, which physically means that the core spheres oscillate in phase opposition to the applied wave field. As a result, waves propagating through the structure become exponentially attenuated [19]. This situation is analogous to absorption of the electromagnetic waves by an atom when frequency of the incident radiation is around the resonant frequency of the atom. The positions of calculated resonances agreed very well with the observed dips of the transmission. It is also worth noting that the existence of sonic gaps in locally resonant materials does not rely on the geometry, in which scattering units are arranged, and requires only the density of the scatterers to exceed certain threshold. Liu *et al.* verified this prediction experimentally by measuring the transmission coefficient through a *monolayer* of the locally resonant scatterers arranged randomly. Transmission minima were observed at about the same positions as in case of a 3D crystal, thus emphasizing the crucial role of local resonances played in the formation of sonic gaps in this type of materials [18]. The ability of locally resonant materials to effectively attenuate acoustic waves of audible frequencies combined with their compact size makes them promising candidates in all sorts of practical problems where the necessity of reducing level of audible noise exists.

One can also envision a potential application of phononic crystals as frequency filters. Such a filter ideally should possess a very broad full band gap with a narrow pass band in its centre. There should also exist a convenient and quick way of tuning the frequency of a pass band. The easiest way of creating a pass band at the band gap

frequencies is to introduce a defect (or defects) into otherwise perfect phononic crystal (recall the existence of the defect states created and occupied by impurity electrons and holes in the band gap of doped semiconductors). James *et al.* performed studies of the sound transmission through a composite structure of alternating layers of water and perspex, which can be viewed as a one-dimensional (1D) phononic crystal, and observed existence of several band gaps at frequencies between 0.1 and 0.5 MHz. The transmission spectrum of a crystal with a defect (introduced by removing central perspex plate) exhibited narrow transmission peaks due to formation of pass bands in the middle of each band gap [20]. Defect states leading to the narrow transmission bands within the band gap of a periodic waveguide made of alternating segments of cylindrical pipes of two different diameters (1D phononic crystal) were investigated by Munday *et al.* [21]. Psarobas *et al.* studied theoretically the transmission spectra through 3D phononic crystals made of spherical scatterers (lead spheres in an epoxy matrix) with the impurity plane, i.e. a planar defect introduced by changing the diameter of the spheres, which constituted a particular plane (or layer) of the crystal. They found the existence of the vibrational mode of the elastic field, which is localized on the impurity plane and extends to infinity parallel to the plane while rapidly decaying in the direction normal to the plane. This mode showed up as a narrow transmission peak at a frequency within the complete band gap. Interestingly, the magnitude of the transmission peak was unity, when the impurity plane was located at the *centre* of the crystal, and rapidly decreased and disappeared altogether when the impurity plane was moved progressively to the surface of the crystal. This behavior was considered to be a signature of the resonant tunneling in analogy to the quantum mechanical effect of resonant tunneling of an electron through the double potential barrier [22].

Khelif *et al.* showed experimentally the possibility of introducing a defect state in a 2D phononic crystal (steel rods in water arranged in a square lattice) by removing single rod from the crystal. The measured transmission spectrum exhibited a transmission peak located at frequencies within the complete band gap [23]. In their theoretical paper, by employing the Finite Difference Time Domain (FDTD) method, Khelif *et al.* found that a narrow pass band (i.e. the transmission peak) appears at a frequency inside the full band gap of a 2D phononic crystal similar to the one considered above, when solid cylinders are substituted with *hollow* (but filled with water) cylinders of the same outer radius [24]. The frequency of the pass band could be tuned as it depended on the inner radius of the cylinders. In the same paper, the authors also suggested a design of a *waveguide* formed by a row of hollow cylinders (inside a crystal with otherwise solid cylinders) and directed along the [10] direction. By calculating the transmission at the exit of the waveguide, they showed that an input pulse incident along the [10] direction would propagate through the waveguide within the narrow pass band located inside the band gap of the ideal crystal at the frequency controlled by the inner diameter of the waveguide rods [24]. Finally, Khelif *et al.* investigated experimentally the transmission through a straight waveguide formed in the 2D crystal considered in [23] by removing one row of cylinders along the [10] direction [25]. For the input pulse incident along the direction of the waveguide, they found a pass band inside the band gap of the corresponding perfect crystal. The observed pass band, however, was very broad (extending from 260 kHz to 315 kHz and covering almost entire range of the full band gap) and thus not very useful in possible applications, where filtering and waveguiding properties need to be combined. The authors also successfully demonstrated the bending of the acoustic waves by a one-period wide

waveguide with two sharp 90° bends (again formed by removing rods from a perfect crystal). A similar broad pass band was observed.

Pennec *et al.* [26] continued the theoretical study of the waveguides considered by Khelif *et al.* (hollow cylinders filled with water). By using simulations based on the FDTD approach, they showed that the frequency of the narrow pass bands of the waveguides can be tuned by filling hollow rods with a liquid different from the matrix liquid (water) rather than by changing the inner diameters of the cylinders, which allows the tuning procedure to be speeded up. The above authors also found that a straight waveguide made of alternating hollow cylinders with two different inner radii can guide simultaneously waves of two different frequencies, each corresponding to a waveguide made of hollow cylinders of only one radius. Alternatively, the same result can be achieved by using hollow cylinders of the same inner radii but filled with different liquids in an alternating pattern. This allowed them to speculate on a possible sound filtering device in which the pass frequency through the waveguide can be quickly changed by flushing the appropriate hollow cylinders and filling them with a different liquid that shifts the pass band to a different frequency. Such a waveguide can also be readily blocked from transmitting signals by changing the pattern, in which hollow cylinders are filled with two different liquids, from an alternating one to the one with two continuous segments of cylinders, each segment filled with the liquid of single type only. Finally, Pennec *et al.* investigated the possibilities of multiplexing and demultiplexing of acoustic waves by considering a *Y*-shaped waveguide capable of transmitting two different frequencies. Such a waveguide consists of an initial single segment with alternating hollow cylinders of two types (differing by either inner radii or the filling liquid), which

splits at the end into two branches, each supporting the transmission of only one of the frequencies, i.e. each branch is made of the hollow cylinders with the same inner radius or the same filling liquid. By performing the FDTD simulations and calculating the transmission spectrum at the exit of each branch, they showed that the initial input signal containing both frequencies is split and channeled into the corresponding branch [26]. In the case when the situation is reversed and the input pulse is incident on the crystal from the opposite side, each branch of the Y-shaped waveguide selects its own frequency and two signals appear superimposed at the single exit of the waveguide.

In 1994, Spielmann *et al.* demonstrated the tunneling of electromagnetic wave packets by investigating propagation of optical pulses through the band gap of a one-dimensional *photonic* crystal [27]. They found that the measured transit time of the pulses was independent of the thickness of the photonic crystal, which is analogous to the tunneling of an electron through an opaque barrier as predicted by Hartman [28]. For the phononic crystals the fundamental physical question of how acoustic/elastic waves travel through the band gaps in the absence of any propagating modes was answered in 2002 by Yang *et al.*, who performed experiments with 3D phononic crystals made of tungsten carbide spheres assembled in an fcc crystal structure in water [29]. By investigating the dynamics of the propagation of ultrasound pulses through 3D phononic crystals with different thicknesses, they conclusively demonstrated that at the band gap frequencies ultrasound pulses travel via tunneling. The propagation of acoustic waves through phononic crystals at the gap frequencies is therefore a classical analogue of quantum mechanical tunneling of a particle through a potential barrier. As one of the directions of my Ph.D. research I investigated a classical analogue of another quantum mechanical effect, namely resonant tunneling of a particle through a double potential barrier [30].

This was achieved by using two 3D phononic crystals (tungsten carbide spheres in water) separated by a uniform medium. Similar experiments in 1D case of a periodic waveguide with a pass band introduced by a defect inside the full band gap were performed by Robertson *et al.* for acoustic pulses at audible frequencies [31].

In order to introduce another direction of modern research in the field of phononic crystals—a direction in which I was involved myself during my Ph.D. studies—a digression into the area of photonics is required. As early as 1964, Victor Veselago studied theoretically the properties of hypothetical materials with both electric permittivity ϵ and magnetic permeability μ simultaneously negative, which he called Left-Handed (LH) materials as opposed to regular Right-Handed (RH) materials with both ϵ and μ positive [32]. The main consequence, which follows from the simultaneous flip of signs in ϵ and μ , is that for a plane electromagnetic wave propagating inside the LH material, the wavevector \vec{k} (indicating direction of the propagation of planes of constant phase) and the Poynting vector \vec{S} (indicating direction of the energy transport by a plane electromagnetic wave) are antiparallel to each other. This property of LH materials leads to a number of unusual properties predicted by Veselago, one of them being *negative* refraction, which occurs when a light ray is refracted on the negative side of the normal to the interface between LH and RH materials. As no LH materials occur naturally, the issue, however, remained in the theoretical domain for more than 30 years. A whole new chapter in the field of photonics was opened by Sir John Pendry and his co-authors, who pointed out a practical way of realizing LH materials. This work was published in two theoretical papers published in 1996 and 1999 [33, 34]. In short, the LH materials proposed by Pendry *et al.* (also known as *metamaterials*) are *artificial* structures made of split-ring

resonators and metallic wires. Pendry *et al.* showed that a periodic array of thin metallic wires mimics the response of electronic plasma in metals and therefore has negative ε in a certain frequency range [33]. On the other hand, the response of a periodic structure made of split-ring resonators exhibits resonances such that effective μ of the structure is negative for a certain range of frequencies around the resonance [34]. It is important to emphasize that effective ε and μ can be ascribed to both structures only when the wavelength of external radiation is much longer than the size of the elementary building unit, in which case they behave as homogeneous materials. When the frequency ranges of negative ε and μ overlap, the combined structure becomes a LH material. Such metamaterials were quickly constructed and negative refraction of electromagnetic waves at microwave frequencies was successfully observed in experiment [35]. For extra details on metamaterials, the reader is referred to a review paper by Pendry [36].

Even greater interest in the photonics community towards LH materials was induced by Pendry in 2000, when he published another theoretical work [37], which showed that a slab of a LH material must be able to focus radiation of a point source with resolution better than the diffraction limit, thus acting effectively as a “superlens”. It is well-known that the diffraction limit is always imposed on conventional lens imaging systems, because an evanescent component of the field initially emitted by the object to be imaged is not used in the image restoration, due to exponential decay of the evanescent waves. The origin of the unprecedented resolution of a slab of LH materials according to Pendry is its ability to *amplify* evanescent waves via their coupling to surface plasmon resonances, so that *both* evanescent and propagating parts are used in the image restoration. In the same paper he also suggested a practical realization of such a lens with

the help of a silver layer. For more details on the physics of the amplification mechanism, the reader is referred to an excellent review paper by Ramakrishna [38]. Although initially the idea of super-resolution (better than the diffraction limit) sparked many debates [39, 40], Pendry's predictions are now accepted as correct, and were verified experimentally in 2005 by Fang *et al.*, who observed super-resolution of one-sixth of the illumination wavelength (365 nm) using a silver layer as a natural superlens [41]. Amplification of evanescent waves and super-resolution was also observed by Grbic *et al.* [42] with the help of a planar lens made of metallic strips loaded with series capacitors and shunt inductors, which is another way of synthesizing a LH metamaterial [43].

The idea of negative refraction and the possibility of imaging with resolution not limited by the diffraction limit captured the minds of many researchers. In 2000 Notomi published a theoretical work in which he suggested that the effect of negative refraction of electromagnetic waves can also be achieved with the help of *photonic* crystals [44]. Negative refraction suggested by Notomi is essentially a *band structure* effect, which employs the shape of equifrequency surfaces (in 3D) or contours (in 2D) of the photonic crystals to achieve antiparallelism of vectors \vec{S} and \vec{k} . It is fundamentally different from negative refraction exhibited by LH materials, since photonic crystals are made of conventional materials and thus both ϵ and μ are locally positive anywhere inside the crystal. He also suggested the possibility of using photonic crystals in imaging applications. Notomi's ideas were further developed by Luo *et al.*, who studied theoretically the possibility of achieving negative refraction with the help of a 2D photonic crystal with square lattice [45]. The mechanism invoked by Luo *et al.* employed convex equifrequency contours located at the corners of the first Brillouin zone (i.e. along

the ΓM or the $[11]$ directions) in the first (valence) band. They also introduced the concept of All-Angle Negative Refraction (AANR), meaning that a single negatively refracted beam is obtained inside the photonic crystal for all incident angles. With the help of the FDTD simulations, Luo *et al.* showed the possibility of achieving high resolution images when working in the regime of AANR. Experimentally, negative refraction of microwaves in 2D photonic crystals made of metallic rods in air was demonstrated by Cubukcu *et al.* [46] and Parimi *et al.* [47]. In the first case, equifrequency contours in the first band of a slab-shaped photonic crystal (square lattice) were used and negative refraction was verified by monitoring the displacement of a beam transmitted through the crystal (and negatively refracted twice) with respect to the input reference beam. By contrast, Parimi *et al.* employed equifrequency contours in the second band of a prism-shaped photonic crystal with triangular lattice. The possibility of achieving resolution better than diffraction limit while imaging with photonic crystals was investigated in another theoretical paper by Luo *et al.* [48], in which they studied imaging properties of 2D slab-shaped photonic crystals. The authors showed that evanescent components of the incident field can be amplified via their resonant coupling to bound photon states (guided either by the air/crystal interface or by the crystal as a whole) characterized by flat dispersion curves. Luo *et al.* also derived upper and lower limits on the best achievable resolution and showed that both limits are set by the *surface* period a_s of the crystal. More details on this subject will be provided in Chapter 5, when focusing experiments with 2D flat photonic crystals will be described. Cubukcu *et al.* observed the superlensing effect experimentally with a 2D flat photonic crystal made of a square array of dielectric rods in air by imaging a monopole antenna used as a point source [49]. The

negative refraction was achieved with the help of convex equifrequency contours in the first band, just as was proposed by Luo *et al.* in [45]. The full width at half maxima of the observed intensity peak was measured to be 0.21λ (where λ is the incident radiation wavelength) and its full width falls within the resolution limits predicted by Luo *et al.* in the previously discussed paper. Cubukcu *et al.* were also able to resolve two incoherent point sources separated by a distance equal to $\lambda/3$. It should be noted that the idea of super-resolution applies only to *near-field* imaging, i.e. the source must be positioned within a wavelength from the superlens. This restriction comes from the fact that the evanescent component of the field emitted by the source decays exponentially to irrecoverably small magnitudes when the superlens is positioned in the far-field of the source. In the imaging experiments by Cubukcu *et al.* [49], their sources were placed 0.7 mm or 0.03λ away from the crystal's surface. They also observed a decrease of the superlensing effect when the distance between the source and the crystal was increased. Unfortunately, no quantitative description of this effect was provided by the authors.

Just as in case of the photonics community, researchers working in the field of phononic crystals were fascinated by the idea of observation negative refraction of sound waves and possibly superlensing effect with the help of phononic crystals. The first experimental observation of focusing of ultrasound by a 3D phononic crystal (tungsten carbide spheres in water assembled in an fcc structure) by negative refraction was done by Yang *et al.* [50]. In their experiments the authors employed certain features of the shape of the equifrequency contours in the narrow frequency range of the 3rd band to negatively refract sound waves incident obliquely with respect to the [111] direction. They clearly observed a field pattern with a tight (about five wavelength) focal spot, which disappeared

with the slight shift of the frequency due to rapid variation of the shape of the equifrequency contours. Zhang *et al.* [51] demonstrated theoretically the existence of negative refraction of acoustic waves in 2D phononic crystals with square lattices by employing equifrequency contours of the 1st band along the ΓM direction in a manner similar to Luo *et al.* in [45]. They also performed a numerical simulation with the help of Multiple Scattering Theory (which is described in some detail in Chapter 2) of the near-field imaging of a point source by a 2D flat phononic crystal (water cylinders in mercury host matrix). The authors found the existence of an image on the output side of the crystal with the full width at half maximum of 0.14λ , which is better than diffraction limit and significantly smaller than the lower limit predicted by Luo *et al.* in [48]. This intriguing disagreement indicates the importance of further investigation of focusing by phononic crystals. Qiu *et al.* performed a theoretical study of the far-field imaging of point sources by a 2D flat sonic crystal (steel cylinders in air with the source-to-crystal distance of 3.9λ) by employing equifrequency contours in the 2nd band and found the formation of high quality images [52]. Using the Multiple Scattering Theory (MST), Li *et al.* investigated the focusing properties of a 2D three-component phononic crystal made of rubber-coated tungsten cylinders immersed in water and assembled in a square lattice [53]. The focusing was achieved in a similar way by employing equifrequency contours at the corner of the first Brillouin zone at the frequencies in the 1st band. The three-component crystal was used instead of two-component one (uncoated rods) because local resonances, associated with each scattering unit, allowed to achieve *circular* shape of the equifrequency contours used in imaging. Good quality images of a point source positioned 1.3λ away from the crystal surface were observed, however the size of the

focal spot was found to be just above the diffraction limit meaning that super-resolution was not achieved.

To the best of my knowledge, at the moment of writing of this thesis, there exists only one paper by Ke *et al.* (Prof. Zhengyou Liu's group from Wuhan University, China) that reports experimental observation of focusing and negative refraction in a 2D phononic crystal made of stainless steel rods arranged in a triangular lattice and immersed in water [54]. In this work the authors employed circular equifrequency contours in the 2nd band, with all experiments conducted at the frequency range just below 1 MHz. Negative refraction of ultrasound waves was demonstrated by measuring the displacement of the outgoing beam transmitted through the slab-shaped crystal with respect to the input beam (in analogy to the microwave experiments by Cubukcu *et al.* [46]). The same flat crystal was employed to image the focal spot of a commercial focusing transducer, which was positioned about 3.4λ from the crystal surface. By measuring field distribution the focal pattern on the output side of the crystal was conclusively observed. Part of my Ph.D. research also concentrated on the experimental observation of negative refraction and focusing in 2D phononic crystals, which were very similar to those employed by Ke *et al.* in [54]. In contrast to Ke *et al.*' work, I used a prism-shaped phononic crystal, which, due to its shape, offered a more direct way of verification of negative refraction of sound waves, as will be explained in the first part of Chapter 5. In my focusing experiments, the line source was positioned about half a wavelength away from the crystal surface, meaning that evanescent components of the field emitted by the source did not decay beyond the recovery limit. On the contrary, experiments by Ke *et al.* had no chance to verify superlensing properties of their 2D crystal, as the source was positioned too far from the crystal surface. Recall also that their "point" source was the focal spot produced

by a focusing transducer, which is inevitably diffraction limited since the focal length was much larger than the wavelength. Even bringing the focal spot to the very surface of the crystal would not help since the focal spot of a focusing transducer occurs at distances far greater than a sound wavelength in water at the experiment frequency range. Therefore, my focusing experiments were different in principle to those by Ke *et al.* by allowing the possibility of observation of superlensing effect should my 2D phononic crystals be capable of amplifying evanescent waves. The results of these experiments are reported in the second part of Chapter 5.

An absolutely different type of a 2D acoustic lens capable of focusing the sound radiation of an incident *plane* wave (as opposed to focusing of the fields emitted by point sources considered in previous examples) into a focal spot about a wavelength wide was demonstrated by Hakansson *et al.* [55]. The acoustic lens was designed, which consisted of rigid cylinders in air with their *positions* and *diameters* optimized by a design tool (combining the MST and a genetic algorithm), so as to produce sound amplification via constructive interference of multiply scattered waves at the focus of the lens. The position of the lens focus was chosen arbitrarily by the investigators. During the optimization procedure, positions of the rods were restricted to the lattice points of a triangular lattice and rods were allowed to either occupy a lattice point or leave it empty. It should be emphasized that such a lens operates solely due to multiple scattering of the waves inside the lens and does *not* require negative refraction. The actual lens was constructed from aluminum rods according to the theoretical design and its focusing ability was confirmed experimentally with a good agreement found between numerical simulations and the experiment. In addition to focusing, the lens was designed to *amplify* the sound field and

this property was also verified experimentally by observing amplification of 6 dB at the focal spot.

As was mentioned previously, antiparallelism of vectors \vec{S} and \vec{k} in metamaterials arises due to built-in resonances of two types, which provide negative response of both ϵ and μ to an external electromagnetic radiation. At the end of this chapter it is worthwhile discussing the possibility of realizing *acoustic* analogues of metamaterials, i.e. composite structures in which acoustic waves will propagate with vectors \vec{S} and \vec{k} antiparallel. The question was considered in a theoretical paper by Li and Chan [56]. According to these authors, the opposite directions of \vec{S} and \vec{k} in a composite material require negative values of *effective* density and bulk modulus. Physically this means that the composite medium will display an anomalous response at some frequencies, such as expanding under compression (because of negative bulk modulus) and moving to the left when being pushed to the right (because of negative density). This might sound fantastic, but Li and Chan predicted that this behavior of effective density and bulk modulus can exist at a certain frequency range in a system of soft rubber spheres suspended in water. The negative values of both quantities are achieved via low-frequency resonances exhibited by spheres. In the doubly negative frequency regime, the two lowest resonances overlap in frequency so that the volume dilation of a single sphere will be out of phase with the hydrostatic pressure field, and motion of the centre of mass of a sphere will be out of phase with the incident direction of the oscillating pressure field. These resonances are analogues of the resonances created by wires and split-ring resonators in electromagnetic metamaterials. The double-negativity in this acoustic case originates from the resonances of the same structure, while

in electromagnetic case negative values of ε and μ are provided by two different resonant mechanisms. Li and Chan conclude their paper by noting that the double-negative acoustic composite must exhibit all the intriguing properties of LH materials such as negative refraction and subwavelength focusing. Their theoretical predictions still await experimental verification.

1.2 Thesis structure

The purpose of this section is to provide a concise description of the contents of this thesis. Chapter 2 presents the theory relevant to the experiments reported in the subsequent sections. Section 2.1 starts by briefly reviewing some major concepts from solid state physics that are used to describe periodic systems such as atomic crystals. These concepts are then applied to the phononic crystals investigated in this thesis. The section finishes with a description of the Multiple Scattering Theory (MST), which is the main theory used extensively throughout this thesis to interpret the experimental results. In Section 2.2, the role of the phononic crystal band structure in the negative refraction and focusing experiments is discussed.

Chapter 3 presents the details of the experimental apparatus used to collect the data and describes the samples (2D and 3D phononic crystals), including the particulars of their construction. The details of the data analysis are also presented in this chapter.

Chapter 4 describes the experiments on resonant tunnelling of ultrasonic pulses through two 3D phononic crystals separated by a cavity. The experimental findings are interpreted using the MST.

Chapter 5 is split into two sections. The first section deals with the experiments on negative refraction of ultrasound in a 2D prism-shaped phononic crystal, while the second section provides a description of the ultrasound focusing experiments with flat 2D phononic crystals.

The conclusions are presented in Chapter 6, while some extra details are given by the appendices collected at the end of the thesis.

2. Theory

The purpose of this chapter is to introduce the major theoretical concepts and models which lay the foundation for the interpretation of the experimental work I have done during the course of my Ph.D. studies. This chapter is split into two sections. The first section recalls some fundamental notions from the theory of crystalline solids (such as reciprocal vectors and lattices, Brillouin zones, etc.) and continues by applying those concepts to my phononic crystals. It also contains a brief discussion of the most important points of the Multiple Scattering Theory (MST), whose predictions were extensively used throughout my entire thesis. The second section uses the theoretical results obtained using the MST to explain the underlying physics behind such effects as negative refraction and focusing of acoustic (ultrasonic in my case) waves propagating through the 2D phononic crystals, which I investigated experimentally.

2.1 Phononic crystals

2.1.1 Periodic structures and their properties

Solids possessing crystalline structure are periodic arrays of atoms. The starting point in the description of the symmetry of any periodic arrangement is the concept of a *Bravais* lattice. A Bravais lattice is defined as an infinite array of discrete points with such an arrangement and orientation that it appears exactly the same from whichever of its points the array is viewed [57]. Mathematically, a Bravais lattice in three dimensions is defined as a collection of points with position vectors \vec{R} of the form:

$$\vec{R} = n\vec{a}_1 + m\vec{a}_2 + k\vec{a}_3 \quad (2.1)$$

where $\vec{a}_1, \vec{a}_2, \vec{a}_3$ are any three vectors not all in the same plane and n, m, k are any three integer numbers. Vectors $\vec{a}_1, \vec{a}_2, \vec{a}_3$ are called *primitive* vectors of a given Bravais lattice. When any of the primitive vectors are zero, the equation (2.1) also defines a two-dimensional Bravais lattice, one example of which is shown in Figure 2.1.1.

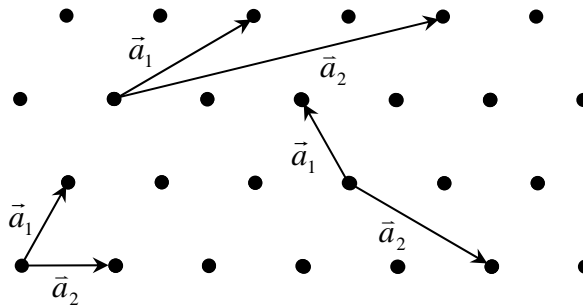


Figure 2.1.1: A 2D triangular Bravais lattice. Several possible choices of the primitive vectors \vec{a}_1 and \vec{a}_2 are indicated.

It is also worth mentioning that for any given Bravais lattice the set of primitive vectors is not unique, and there are very many different choices, as shown in Figure 2.1.1.

In three dimensions there exist a total of fourteen different Bravais lattices. The symmetry of any physical crystal is described by one of the Bravais lattices plus a *basis*. The basis consists of identical units (usually made by group of atoms), which are attached to every point of the underlying Bravais lattice. A crystal, whose basis consists of a single atom or ion, is said to have a monatomic Bravais lattice.

Another important concept widely used in the study of crystals is that of a *primitive cell*. The primitive cell is a volume of space that contains precisely one lattice point and can be translated through all the vectors of a Bravais lattice to fill all the space without overlapping itself or leaving voids. Just as in the case of primitive vectors, there is no unique way of choosing a primitive cell. The most common choice, however, is the *Wigner-Seitz* cell, which has the full symmetry of the underlying Bravais lattice. The Wigner-Seitz cell about a lattice point also has a property of being closer to that point than to any other lattice point. It can be constructed by drawing lines connecting a given point to nearby lying points, bisecting each line with a plane and taking the smallest polyhedron bounded by these planes.

The Bravais lattice, which is defined in *real* space, is sometimes referred to as a *direct* lattice. At the same time, there exist the concepts of a *reciprocal* space and a *reciprocal* lattice, which play an extremely important role in virtually any study of wave propagation, diffraction and other wave phenomena in crystals. For any Bravais lattice, given by a set of vectors \vec{R} (see (2.1)), and a plane wave $\exp(i\vec{k} \cdot \vec{r})$, the reciprocal lattice is defined as a set of all wavevectors \vec{G} that yield plane waves with the periodicity of a

given Bravais lattice [57]. Mathematically, a wavevector \vec{G} belongs to the reciprocal lattice of a Bravais lattice with vectors \vec{R} , if the equation:

$$\exp(i\vec{G} \cdot (\vec{r} + \vec{R})) = \exp(i\vec{G} \cdot \vec{r}) \quad (2.2)$$

is true for any \vec{r} and \vec{R} of the given Bravais lattice. It follows from equation (2.2) that a reciprocal lattice can also be viewed as a set of points, whose positions are given by a set of wavevectors \vec{G} satisfying the condition:

$$\exp(\vec{G} \cdot \vec{R}) = 1 \quad (2.3)$$

for all \vec{R} in the Bravais lattice. The reciprocal lattice itself is a Bravais lattice. The primitive vectors $\vec{b}_1, \vec{b}_2, \vec{b}_3$ of the reciprocal lattice are constructed from the primitive vectors $\vec{a}_1, \vec{a}_2, \vec{a}_3$ of the direct lattice and given in three dimensions by the following expressions:

$$\begin{aligned} \vec{b}_1 &= 2\pi \frac{\vec{a}_2 \times \vec{a}_3}{\vec{a}_1 \cdot (\vec{a}_2 \times \vec{a}_3)} \\ \vec{b}_2 &= 2\pi \frac{\vec{a}_3 \times \vec{a}_1}{\vec{a}_2 \cdot (\vec{a}_3 \times \vec{a}_1)} \\ \vec{b}_3 &= 2\pi \frac{\vec{a}_1 \times \vec{a}_2}{\vec{a}_3 \cdot (\vec{a}_1 \times \vec{a}_2)} \end{aligned} \quad (2.4)$$

As an example, Figure 2.1.2 shows a simple-cubic Bravais lattice with a lattice constant a as well as its reciprocal lattice, which is also a simple-cubic one with a lattice constant $2\pi/a$ (as follows from relations (2.4)).

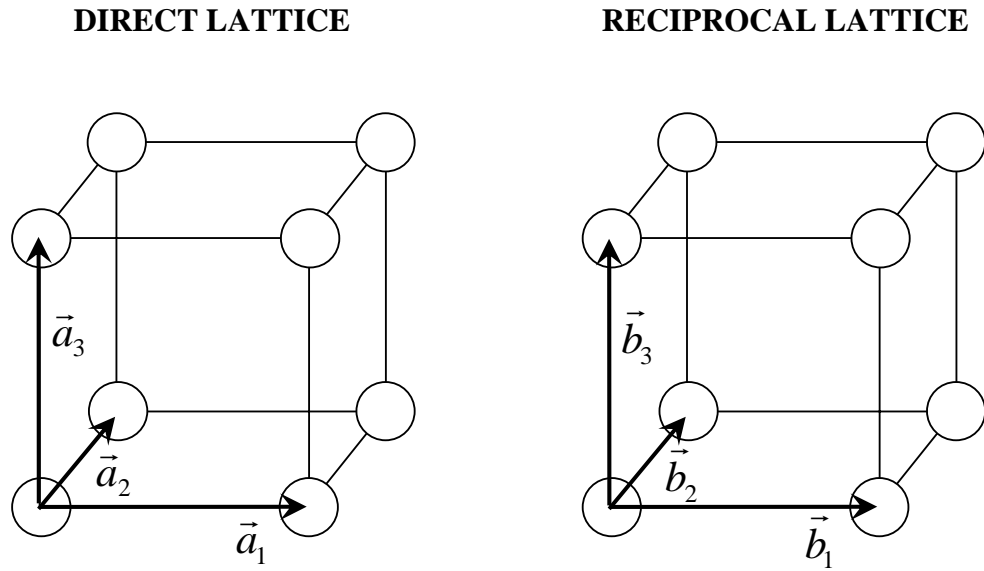


Figure 2.1.2: Simple-cubic direct lattice and its reciprocal lattice. The primitive vectors of both lattices are also indicated.

Since the reciprocal lattice is a Bravais lattice, one can also find its Wigner-Seitz cell. The Wigner-Seitz cell of a reciprocal lattice is conventionally called a *first Brillouin zone*. Planes in k -space, which bisect the lines joining a particular point of a reciprocal lattice with all other points, are known as *Bragg planes*. Therefore, the first Brillouin zone can also be defined as the set of all points in k -space that can be reached from the origin without crossing *any* Bragg plane. The Brillouin zones of higher orders also exist, with the n th Brillouin zone defined as the set of points that can be reached from the origin by crossing $(n-1)$ Bragg planes [57]. The first Brillouin zone is of great importance in the

theory of solids with periodic structures, since the periodicity of the structure allows the description of the properties of the solids within the first Brillouin zone. Figure 2.1.3 shows the first three Brillouin zones of the 2D square Bravais lattice.

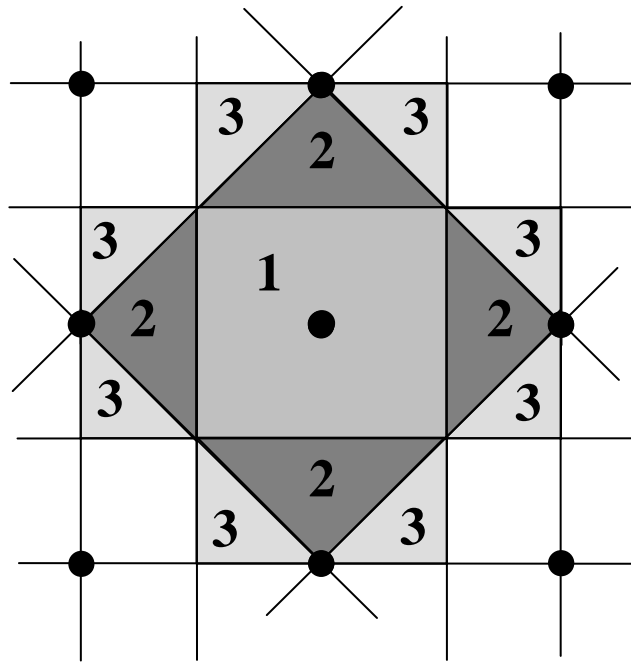


Figure 2.1.3: The first three Brillouin zones of a reciprocal lattice of the 2D square Bravais lattice. The dots indicate reciprocal lattice points, the solid lines indicate Bragg planes and digits indicate the order of the corresponding Brillouin zone.

It is well known from Quantum Mechanics that the energy of an electron in an atom assumes discrete values. However, when the atomic orbitals overlap as the atoms come close together in a solid, the energy levels of the electrons broaden and form continuous regions, also known as energy *bands*. At the same time, because of the periodicity of the crystal structure, the electronic wave functions undergo strong Bragg reflections at the boundaries of the Brillouin zones. The destructive interference of the

Bragg-scattered wave functions gives rise to the existence of the energy regions, in which no electronic energy levels exist. Since these regions are not accessible by the electrons, they are also known as *forbidden* bands. If the forbidden band occurs along the particular direction inside the crystal, it is conventionally called a *stop* band. If it happens to span *all* the directions inside the crystal, the term “complete *band gap*”, or simply *band gap*, is used instead. The electronic properties of crystalline solids are conveniently described with the help of the *band structure* plots, which represent energy levels of the electrons of the solid as a function of the direction inside the solid.

The concepts of the direct and reciprocal lattices, Brillouin zones and energy bands discussed in this section are of general nature and can be applied to *any* periodic system without being limited to atomic crystals. These concepts will be illustrated in the next section with regard to two- and three-dimensional phononic crystals, which I studied experimentally during my Ph.D. work.

2.1.2 Two- and three-dimensional phononic crystals

In general, a phononic crystal is a collection of sound scatterers (solid or liquid), which are arranged in a regular pattern and surrounded by a solid or liquid matrix. In by far most of the cases, the regular pattern is chosen to be one of the Bravais lattices and each scattering unit is located in one of the points of the lattice. Therefore, we can say that phononic crystals are macroscopic analogues of the natural crystals (with monatomic Bravais lattices) with respect to the *sound* waves. They can also be regarded as acoustic analogues of the *photonic* crystals (made of periodically arranged units with the dielectric constant different from that of the host matrix), which are designed to interact with *electromagnetic* waves.

One can distinguish between one-, two- and three-dimensional (1D, 2D and 3D) phononic crystals. The simplest type is a 1D crystal, which is simply a periodic array of different alternating layers. The difference between 2D and 3D phononic crystals lies in the dimensionality of their corresponding Bravais lattices. Most frequently, 2D crystals employ rods (chiefly of circular cross-section) as scattering units, while 3D crystals are regularly realized as arrangements of spheres. It is very common in theoretical studies of the phononic crystals to investigate crystals with scattering units that are simply air voids (e.g. empty cylinders) in a matrix. Although there are many different ways of realizing the phononic crystal theoretically and experimentally (by varying material of the scattering units and the host matrix), one thing still remains in common: the characteristic size of the scattering unit (rod or sphere) and lattice constant should be on the order of the wavelength of the incident radiation to ensure that the peculiar crystal features arising from its regularity affect the wave propagating through the crystal. In other words, the frequency range of the crystal operation is set by the characteristic dimensions of the

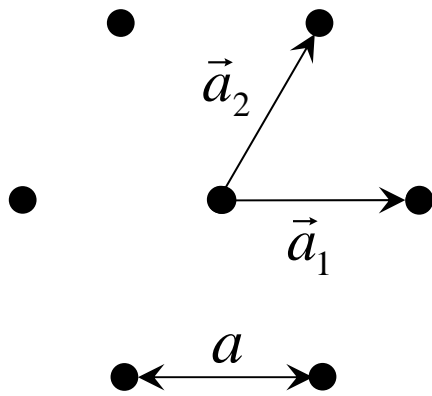
crystal (i.e. the size of its unit scatterer and its lattice constant). The exception from this rule, however, is resonant sonic materials, which exhibit a profound effect on the propagating radiation, whose wavelength can be as much as two orders of magnitude larger than the characteristic size of the structure, as was shown by Liu *et al.* [18].

Just as in the case of the atomic crystals and electrons, which were described in the previous section, the regularity of the arrangement of scattering units of the phononic crystal gives rise to the Bragg reflections of the sound waves multiply scattered inside the crystal. Their constructive or destructive interference creates ranges of frequencies at which waves are either allowed to propagate through (pass bands) or effectively blocked (stop bands and complete band gaps) by the crystal. The width of the band gap obviously depends on the crystal structure and increases with the increase of density contrast between the material of the scattering unit and that of a host matrix. Switching from the liquid matrix to the solid one, e.g. from water to epoxy, which can support both longitudinal and transverse polarizations, results in even larger band gaps, as was shown by Page *et al.* [12].

My 2D phononic crystals were made out of stainless steel rods, immersed in water and assembled in a *triangular* Bravais lattice, in which points are located at the vertices of the equilateral triangles (the detailed description of the practical realization of the crystals is provided in Section 3.1.1). Both the lattice constant a and the rod diameter d were chosen to be comparable to the wavelength of sound in water at frequencies around 1 MHz. Figure 2.1.4 presents the diagram of the direct and reciprocal lattices with corresponding primitive vectors \vec{a}_1, \vec{a}_2 and \vec{b}_1, \vec{b}_2 . Since $|\vec{a}_1| = |\vec{a}_2| = a$, where a is a lattice constant, it follows from (2.4) that $|\vec{b}_1| = |\vec{b}_2| = 4\pi/\sqrt{3}a$ (one should formally set $\vec{a}_3 = \hat{z}$).

By working out components of \vec{b}_1 and \vec{b}_2 , one can be convinced that the reciprocal lattice of a triangular lattice is also a triangular lattice but rotated through 30° with respect to a direct lattice. Both direct and reciprocal lattices possess six-fold symmetry. The first Brillouin zone has a shape of a hexagon with two high symmetry directions, which are commonly referred to as ΓM and ΓK [Figure 2.1.4].

DIRECT LATTICE



RECIPROCAL LATTICE

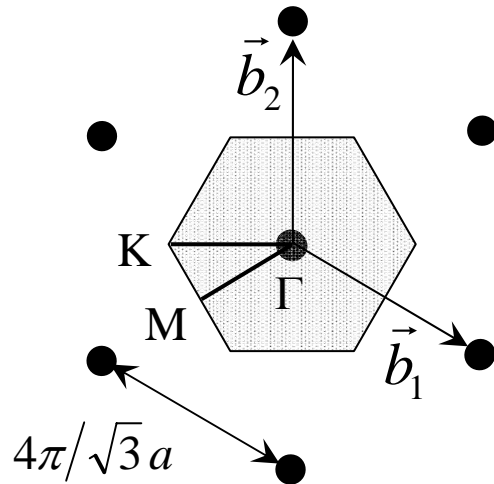


Figure 2.1.4: The direct and reciprocal lattices of the 2D phononic crystals, which were investigated experimentally. The shaded hexagon indicates the first Brillouin zone. In the actual phononic crystal the rods were positioned at the points of the direct lattice (perpendicular to the plane of the figure).

The 3D crystals were composed of the tungsten carbide spherical beads immersed in water. This choice of the material provided huge density contrast between the scatterers and the host matrix, which in its turn ensured that most of the energy of the sound wave traveling through the crystal was mostly concentrated in the water and not in the beads.

The beads were assembled in a face-centered cubic (FCC) structure, which is obtained from the simple-cubic lattice by adding one bead to the centre of every face of the cubic unit cell. Figure 2.1.5 presents schematically a direct lattice of an FCC structure along with the corresponding reciprocal lattice, which turns out to be a body-centered cubic (BCC) crystal structure (obtained from the simple-cubic structure by adding one atom in the centre of its unit cell). Also displayed are the sets of primitive vectors $\vec{a}_1, \vec{a}_2, \vec{a}_3$ and $\vec{b}_1, \vec{b}_2, \vec{b}_3$ of both lattices. It can be easily seen from Figure 2.1.5 that with this particular choice of the primitive vectors of the direct lattice we have $|\vec{a}_1| = |\vec{a}_2| = |\vec{a}_3| = a/\sqrt{2}$, and then after some calculations it also follows from (2.4) that $|\vec{b}_1| = |\vec{b}_2| = |\vec{b}_3| = 2\sqrt{3}\pi/a$, where a is a lattice constant of the direct lattice.

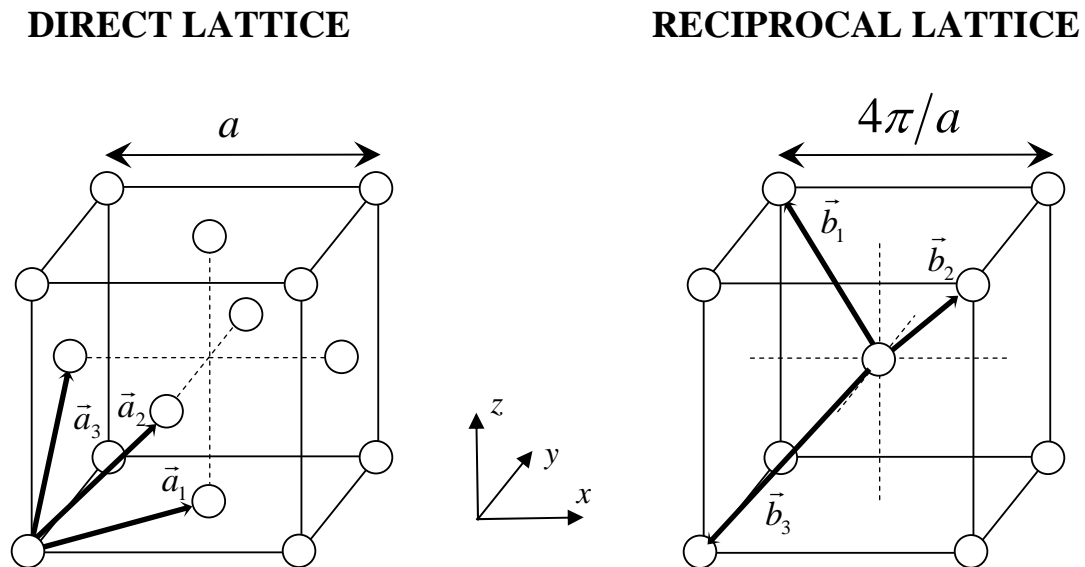


Figure 2.1.5: The direct (FCC) and reciprocal (BCC) crystal lattices of the 3D phononic crystals.

The crystal layers were stacked along the direction of the body diagonal of the unit conventional FCC unit cell, which is indicated as the $[111]$ direction. The spheres were close packed in an ABCABC... sequence, which is shown in Figure 2.1.6. The spheres belonging to the first layer are denoted by the letter A. The next layer is formed by placing the spheres in the interstitials indicated by the letter B, and the third layer is formed by placing spheres in the interstitials of the second layer, which are denoted by the letter C. The sequence is then repeated again with the fourth layer beads to occupy interstitials in the third layer, which are positioned directly above beads denoted by the letter A. This packing results in the highest filling ratio of 74%.

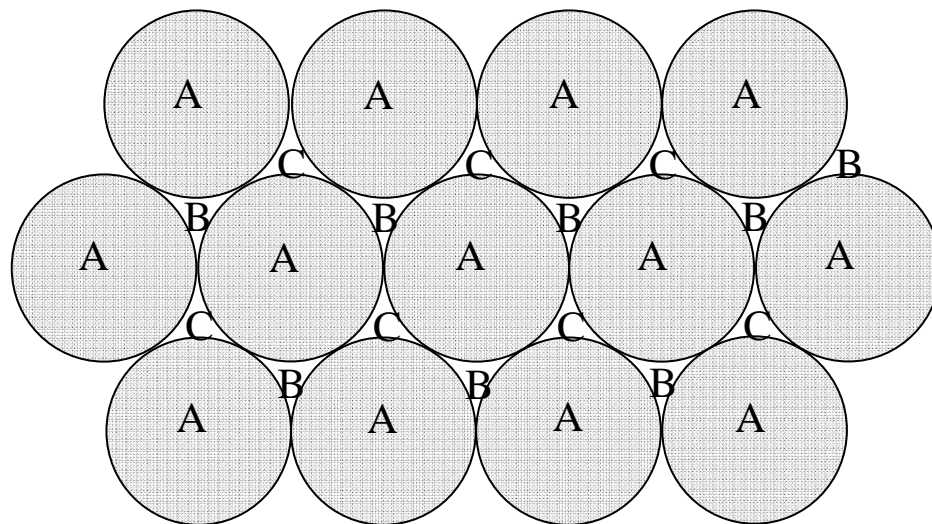


Figure 2.1.6: Schematic diagram explaining the formation of a 3D crystal in a ABCABC... sequence.

The first Brillouin zone of the FCC lattice is called a “truncated octahedron” and coincides with Wigner-Seitz cell of the BCC lattice. It is presented in Figure 2.1.7 along with its high symmetry directions. The investigation of the figure reveals that the $[111]$

direction is also a high symmetry direction ΓL . With respect to the coordinate system in Figure 2.1.7, the coordinates of the high symmetry points (in units of $2\pi/a$) are: Γ [000], X [100], L [$\frac{1}{2}$; $\frac{1}{2}$; $\frac{1}{2}$], W [$\frac{1}{2}$; 1; 0], and K [$\frac{3}{4}$; $\frac{3}{4}$; 0].

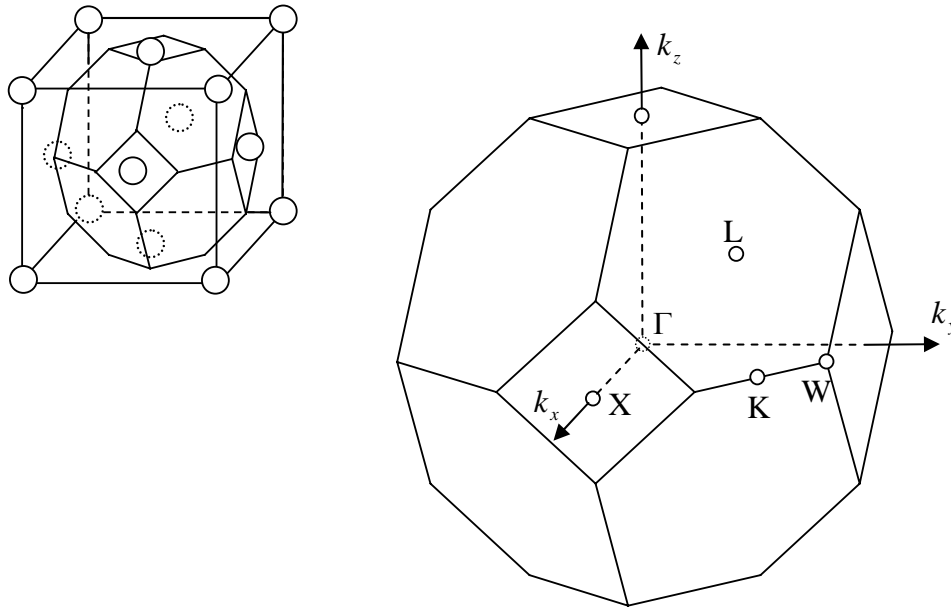


Figure 2.1.7: The first Brillouin zone of the FCC lattice and its high symmetry points.

One can expect that, because of the periodic arrangement of the crystal scatterers, the propagation of the sound radiation through the phononic crystal should be very different from the case of the uniform medium and depend strongly on the *direction* of propagation (much in the same way as the electrons moving inside the solids are affected by the periodicity of their crystal structures). In particular, one can also expect the existence of the frequency regions for which sound propagation will be forbidden in one (stop band) or in all (complete band gap) directions inside the crystal. Just like crystalline

solids, the phononic crystal properties are most conveniently described with the help of the band structure plots, except that in case of phononic crystals the band structure plot displays the wavevector dependence of the *frequency* of the propagating modes inside the crystal as a function of the direction of propagation. In other words, the band structure of a phononic crystal is a dispersion relation, which differs from a uniform medium by having direction and frequency dependence. The band structures of my 3D and 2D crystals will be presented in Chapters 4 and 5 correspondingly. For now, it suffices to note that, for any progress to be achieved in the studies of the phononic crystals of any kind, one needs a reliable theory to allow the calculation of the crystal's band structure. For comparison with experiment, the theory should also be able to calculate some other properties of the phononic crystals, such as transmission or reflection coefficients, which are measured directly in the experiment. If one follows the chronological order in which different theoretical approaches were employed for the calculation of the phononic crystals' band structures, the plane-wave (PW) method is the first one to be mentioned. The PW method is a fast and easy-to-apply method that is based on the expansion of the periodic coefficients (e.g. density, velocity) in the wave equation and the periodic wave amplitude in Fourier series. By approximating these infinite series with the finite sums, the solution of the wave equation is reduced to the solution of a finite matrix eigenvalue equation. With the help of this method, extensive band structure calculations were performed [4, 5, 7, 8, 58] for acoustic or elastic waves propagating in 2D and 3D phononic crystals, where *both* scatterers and matrix were either fluids or solids. However, the PW method is known to have convergence problems when dealing with *mixed* crystals, such as solid scatterers in a liquid matrix, due the existence of the *transverse* modes inside the scatterers. These modes, although of non-propagating character, are strongly coupled to

the longitudinal modes both *inside* and *outside* the scatterers. The PW method also fails when treating systems of either very high or very low filling ratios. Another drawback of the PW method is that it calculates the band structure of infinitely long periodic systems and therefore its results can only be *indirectly* compared with the transmission measurements in a finite system.

The other two theoretical methods used in studies of phononic crystals are the Multiple Scattering Theory (MST) and the Finite-Difference Time-Domain (FDTD) method. With the help of the FDTD method, in which the elastic wave equations are discretized in both the spatial and the time domains with proper boundary conditions, one is able to calculate *both* the band structure and the transmission coefficients through the phononic crystal. This method was applied to a mixed phononic crystal [59] and showed no convergence problems that limited the usefulness of the PW method. FDTD also allows monitoring of the time evolution of the elastic field as it propagates through the crystal. However, the FDTD method is rather time consuming, especially for accurate calculations in 3D systems since it requires a fine grid of points.

The last approach, which was employed for the interpretation of all my experimental results, is the MST. The next section outlines the basic ideas of the MST, with the goal of conveying the essential physics of the theory without obscuring it with the mathematical details, which can be found in the papers by Liu *et al.* [61], Kafesaki *et al.* [60] and Psarobas *et al.* [62].

2.1.3 Multiple Scattering Theory

The Multiple Scattering Theory was introduced for 3D phononic crystals by three different groups at about the same time [60-62] and its 2D version was developed three years later by Prof. Liu's group in the theoretical work by Mei *et al.* [63]. The MST is

essentially an extension of the Korringa-Kohn-Rostocker (KKR) theory (which is a well-known method used by the solid-state community for electronic band structure calculations) to the case of elastic/acoustic waves. The MST is ideally suited for my phononic crystals (both 2D and 3D) since it is designed for problems in which scattering units have simple symmetries, such as spheres or cylinders. It is also a quickly converging method that takes into account the full vector character of the elastic field and is able to deal with the phononic crystals of any type (e.g. liquid/solid crystals, for which the PW method fails). Since it was introduced, theoretical predictions of the MST have been used in the interpretation of the results of many experiments [29, 30, 50, 54, 67], including the experiments reported in this thesis. In all cases an excellent agreement between the theory and experiments was observed, allowing the MST to be experimentally validated for these types of phononic crystals. Below I will briefly summarize the main points of the MST in case of the 3D phononic crystals by following the steps along which it was developed by Liu *et al.* in [61].

In a homogeneous medium, the elastic wave equation may be written as

$$(\lambda + 2\mu)\vec{\nabla}(\vec{\nabla} \cdot \vec{u}) - \mu\vec{\nabla} \times \vec{\nabla} \times \vec{u} + \rho\omega^2\vec{u} = 0 \quad (2.5)$$

where ρ is the density of the medium and λ , μ are its Lamé constants and \vec{u} is the displacement field. Because of the spherical symmetry of the scatterers, it is natural to work with the general solution of (2.5) expressed in the spherical coordinates:

$$\vec{u}(\vec{r}) = \sum_{lm\sigma} [a_{lm\sigma} \vec{J}_{lm\sigma}(\vec{r}) + b_{lm\sigma} \vec{H}_{lm\sigma}(\vec{r})] \quad (2.6)$$

where $\vec{J}_{lm\sigma}(\vec{r}), \vec{H}_{lm\sigma}(\vec{r})$ are defined as:

$$\begin{aligned}
\vec{J}_{lm1}(\vec{r}) &= \frac{1}{\alpha} \vec{\nabla}[j_l(\alpha r)Y_{lm}(\hat{r})] \\
\vec{J}_{lm2}(\vec{r}) &= \frac{1}{\sqrt{l(l+1)}} \vec{\nabla} \times [\vec{r}j_l(\beta r)Y_{lm}(\hat{r})] \\
\vec{J}_{lm3}(\vec{r}) &= \frac{1}{\beta\sqrt{l(l+1)}} \vec{\nabla} \times \vec{\nabla} \times [\vec{r}j_l(\beta r)Y_{lm}(\hat{r})]
\end{aligned} \tag{2.7}$$

and

$$\begin{aligned}
\vec{H}_{lm1}(\vec{r}) &= \frac{1}{\alpha} \vec{\nabla}[h_l(\alpha r)Y_{lm}(\hat{r})] \\
\vec{H}_{lm2}(\vec{r}) &= \frac{1}{\sqrt{l(l+1)}} \vec{\nabla} \times [\vec{r}h_l(\beta r)Y_{lm}(\hat{r})] \\
\vec{H}_{lm3}(\vec{r}) &= \frac{1}{\beta\sqrt{l(l+1)}} \vec{\nabla} \times \vec{\nabla} \times [\vec{r}h_l(\beta r)Y_{lm}(\hat{r})]
\end{aligned} \tag{2.8}$$

where $\alpha = \omega\sqrt{\rho/(\lambda + 2\mu)}$, $\beta = \omega\sqrt{\rho/\mu}$, $j_l(x)$ is the spherical Bessel function, $h_l(x)$ is the spherical Hankel function of the 1st kind and $Y_{lm}(\hat{r})$ is the usual spherical harmonic with \hat{r} denoting angular coordinates (θ, ϕ) of \vec{r} in spherical coordinate system. In equation (2.6) index σ assumes values from 1 to 3, where $\sigma = 1$ indicates the longitudinal wave and $\sigma = 2, 3$ indicates two transverse waves of different polarizations. In the case when the coefficients $b_{lm\sigma}$ in (2.6) are equal zero, $\vec{u}(\vec{r})$ represents an *incident* wave, and in the case of $a_{lm\sigma} = 0$, $\vec{u}(\vec{r})$ represents a *scattered* wave. Therefore, the wave incident on an i th scatterer is expressed as

$$\vec{u}_i^{in}(\vec{r}_i) = \sum_{lm\sigma} a_{lm\sigma}^i \vec{J}_{lm\sigma}^i(\vec{r}_i) \tag{2.9}$$

where \vec{r}_i indicates some point in space as measured from the center of the i th scatterer.

The wave scattered by scatterer i can be expressed as

$$\vec{u}_i^{sc}(\vec{r}_i) = \sum_{lm\sigma} b_{lm\sigma}^i \vec{H}_{lm\sigma}^i(\vec{r}_i) \tag{2.10}$$

The first key point of MST is the idea that the wave (2.9) incident on a given scatterer i can be viewed as a sum of the externally incident wave $\vec{u}_i^{(0)}(\vec{r}_i)$ expressed as

$$\vec{u}_i^{(0)}(\vec{r}_i) = \sum_{lm\sigma} a_{lm\sigma}^{i(0)} \vec{J}_{lm\sigma}^i(\vec{r}_i) \quad (2.11)$$

and *all* other scattered waves *except* the one scattered by the i th scatterer, which can be expressed as

$$\sum_{j \neq i} \vec{u}_j^{sc}(\vec{r}_j) = \sum_{j \neq i} \sum_{lm\sigma} b_{lm\sigma}^j \vec{H}_{lm\sigma}^j(\vec{r}_j) \quad (2.12)$$

so that (2.9) can also be written as

$$\vec{u}_i^{in}(\vec{r}_i) = \vec{u}_i^{(0)}(\vec{r}_i) + \sum_{j \neq i} \vec{u}_j^{sc}(\vec{r}_j) \quad (2.13)$$

Here \vec{r}_i and \vec{r}_j refer to the position of the same point in space and are measured from the centers of scatterers i and j respectively.

Another crucial point of MST is that for a given scatterer, the scattered field is *completely* determined from the incident field with the help of the scattering matrix T . In other words, the expansion coefficients $A = \{a_{lm\sigma}^j\}$ and $B = \{b_{lm\sigma}^j\}$ are related through $T = \{t_{lm\sigma'l'm'\sigma'}\}$ as follows

$$B = TA$$

or more explicitly

$$b_{lm\sigma}^j = \sum_{l'm'\sigma'} t_{lm\sigma'l'm'\sigma'} a_{l'm'\sigma'}^j \quad (2.14)$$

For objects of simple geometry, such as spheres or cylinders, the calculation of the scattering matrix T is an *exactly* solvable boundary-value problem and this is the origin of MST's reliability and precision when handling arrangements of scatterers of spherical symmetry. In short, the coefficients $t_{lm\sigma'l'm'\sigma'}$ are found by applying the boundary

conditions that require the continuity of the normal components of both the displacement and the stress vectors at the scatterer/matrix interface. The explicit expressions of the T matrix coefficients for an elastic sphere can be found in [60] (liquid matrix) and in [62] (elastic matrix), and in [63] for an elastic cylinder in an elastic matrix.

The final MST equation is obtained by substituting (2.9), (2.11), (2.12) and (2.14) into (2.13) and reads

$$\sum_{j'l'm'\sigma'} \left(\delta_{ij} \delta_{ll'} \delta_{mm'} \delta_{\sigma\sigma'} - \sum_{l''m''\sigma''} t_{l''m''\sigma''l'm'\sigma'}^j G_{l''m''\sigma''l'm\sigma}^{ij} \right) a_{l'm'\sigma'}^j = a_{l'm\sigma}^{i(0)} \quad (2.15)$$

where $G_{l'm\sigma'l'm'\sigma'}$ is the so-called vector structure constant, which relates $\vec{H}_{l'm\sigma}^j(\vec{r}_j)$ in (2.12) and $\vec{J}_{l'm\sigma}^i(\vec{r}_i)$ through the relation:

$$\vec{H}_{l'm\sigma}^j(\vec{r}_j) = \sum_{l'm'\sigma'} G_{l'm\sigma'l'm'\sigma'}^{ij} \vec{J}_{l'm'\sigma'}^i(\vec{r}_i)$$

(more details can be found in [61]). The normal modes of the system may be obtained by solving the secular equation that follows from (2.15) in the absence of an external incident wave (i.e., when all $a_{l'm\sigma}^{i(0)}$ are zero):

$$\det \left| \delta_{ij} \delta_{ll'} \delta_{mm'} \delta_{\sigma\sigma'} - \sum_{l''m''\sigma''} t_{l''m''\sigma''l'm'\sigma'}^j G_{l''m''\sigma''l'm\sigma}^{ij} \right| = 0 \quad (2.16)$$

In case of the periodic system, $G_{l'm\sigma'l'm'\sigma'}$ is modified to take into account the symmetry of the structure. The solutions of (2.16) give the band structure of an elastic periodic system. The band structures calculated with the MST for my 2D and 3D phononic crystals are presented in Chapters 4 and 5 respectively.

To facilitate the *direct* comparison with the real samples, a successful theory must also be able to calculate the quantities that one measures in a typical experiment, e.g.

transmission and reflection coefficients. This is accomplished in the framework of the *layer* MST, which allows one to calculate the transmission of an elastic wave through a *finite* slab (with an arbitrary number of layers) of periodically arranged scatterers. The approach starts by calculating the field of the elastic wave scattered (or transmitted) by a *single* layer of scatterers. Let us assume that the layer of scatterers (elastic spheres) lies completely in the x - y plane and that positions of the scatterers are given by vectors $\{\vec{R}_n\}$ of a 2D Bravais lattice, which is generated by two primitive vectors \vec{a}_1, \vec{a}_2 , i.e.

$$\vec{R}_n = n_1 \vec{a}_1 + n_2 \vec{a}_2 \quad (2.17)$$

where n_1, n_2 are integers. The positive direction of the z -axis is chosen to be to the left of the layer as explained by Figure 2.1.8.

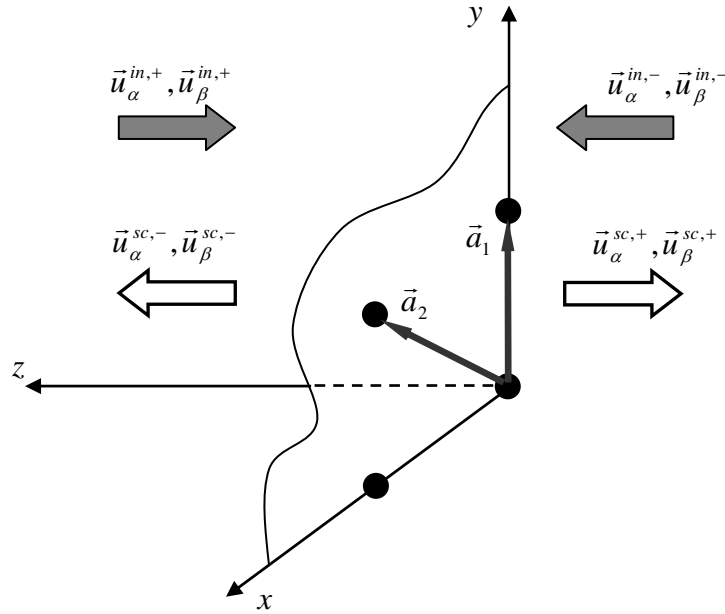


Figure 2.1.8: Geometry of the layer MST. Vectors \vec{a}_1, \vec{a}_2 are the primitive vectors of the corresponding 2D Bravais lattice.

A plane elastic wave $\vec{u}^{in}(\vec{r})$ incident on the layer can be expressed in general as

$$\vec{u}^{in}(\vec{r}) = \sum_s \vec{u}_\alpha^{in,s}(\vec{r}) + \sum_s \vec{u}_\beta^{in,s}(\vec{r}) \quad (2.18)$$

where $s = +/ -$ indicates waves incident from the left (positive z) and from the right (negative z) respectively, while $\alpha = 1$ and $\beta = 2,3$ are identical to index σ in (2.6) and distinguish between the longitudinal and the transverse (with two polarizations) waves [Figure 2.1.7]. Each term in (2.18) can be expressed in terms of the primitive vectors \vec{b}_1, \vec{b}_2 of the 2D reciprocal lattice as follows

$$\vec{u}_\alpha^{in,\pm}(\vec{r}) = \sum_{\vec{g}} \vec{u}_{\alpha g}^{in,\pm}(\vec{r}) = \sum_{\vec{g}} \vec{U}_{\alpha g}^{in,\pm} \exp(i\vec{k}_{\alpha g}^\pm \cdot \vec{r}) \quad (2.19a)$$

$$\vec{u}_\beta^{in,\pm}(\vec{r}) = \sum_{\vec{g}} \vec{u}_{\beta g}^{in,\pm}(\vec{r}) = \sum_{\vec{g}} \vec{U}_{\beta g}^{in,\pm} \exp(i\vec{k}_{\beta g}^\pm \cdot \vec{r}) \quad (2.19b)$$

where wavevectors $\vec{k}_{\alpha g}^\pm$ and $\vec{k}_{\beta g}^\pm$ are given by the expressions

$$\vec{k}_{\alpha g}^\pm = (\vec{k}_\parallel + \vec{g}, \pm \sqrt{\alpha^2 - |\vec{k}_\parallel + \vec{g}|^2}) \quad (2.20a)$$

$$\vec{k}_{\beta g}^\pm = (\vec{k}_\parallel + \vec{g}, \pm \sqrt{\beta^2 - |\vec{k}_\parallel + \vec{g}|^2}) \quad (2.20b)$$

Here \vec{g} is the 2D reciprocal lattice vector ($\vec{g} = m_1 \vec{b}_1 + m_2 \vec{b}_2$, where m_1, m_2 are integers), and \vec{k}_\parallel is a reduced wavevector in the first Brillouin zone of the reciprocal lattice. In equations (2.20a) and (2.20b) $(\vec{k}_\parallel + \vec{g})$ simply represents components of wavevectors $\vec{k}_{\alpha g}^\pm$ and $\vec{k}_{\beta g}^\pm$ that are parallel to the layer of scatterers. These expressions are chosen to simplify subsequent calculations. The constants α and β are defined in (2.7) and (2.8).

Much in the same way, the wave $\vec{u}^{sc}(\vec{r})$ scattered by the layer can be expressed as follows

$$\vec{u}^{sc}(\vec{r}) = \sum_s \vec{u}_\alpha^{sc,s}(\vec{r}) + \sum_s \vec{u}_\beta^{sc,s}(\vec{r}) = \sum_{s,\vec{g}} \vec{U}_{\alpha\vec{g}}^{sc,s} \exp(i\vec{k}_{\alpha\vec{g}}^s \cdot \vec{r}) + \sum_{s,\vec{g}} \vec{U}_{\beta\vec{g}}^{sc,s} \exp(i\vec{k}_{\beta\vec{g}}^s \cdot \vec{r}) \quad (2.21)$$

Indices α and β have the same meaning as in case of incident wave (2.18). The index $s = +/-$, however, reverses its meaning and now indicates the scattered waves propagating away from the layer on its right (negative z) and on its left (positive z) correspondingly (see Figure 2.1.8).

After lengthy and complicated calculations, one can show (see Liu *et al.* [61]) that amplitudes $\vec{U}_{\alpha\vec{g}}^{sc,\pm}$ and $\vec{U}_{\beta\vec{g}}^{sc,\pm}$ of the scattered wave are related to the amplitudes $\vec{U}_{\alpha\vec{g}}^{in,\pm}$ and $\vec{U}_{\beta\vec{g}}^{in,\pm}$ of the incident wave with the help of matrices $\mathbf{M}_{\kappa\kappa'}^{ss'}$ ($s, s' = +/-$ and $\kappa, \kappa' = \alpha, \beta$) as follows

$$\begin{aligned} \begin{bmatrix} \mathbf{U}_\alpha^{sc,+} \\ \mathbf{U}_\beta^{sc,+} \end{bmatrix} &= \begin{bmatrix} \mathbf{M}_{\alpha\alpha}^{++} & \mathbf{M}_{\alpha\beta}^{++} \\ \mathbf{M}_{\beta\alpha}^{++} & \mathbf{M}_{\beta\beta}^{++} \end{bmatrix} \begin{bmatrix} \mathbf{U}_\alpha^{in,+} \\ \mathbf{U}_\beta^{in,+} \end{bmatrix} + \begin{bmatrix} \mathbf{M}_{\alpha\alpha}^{+-} & \mathbf{M}_{\alpha\beta}^{+-} \\ \mathbf{M}_{\beta\alpha}^{+-} & \mathbf{M}_{\beta\beta}^{+-} \end{bmatrix} \begin{bmatrix} \mathbf{U}_\alpha^{in,-} \\ \mathbf{U}_\beta^{in,-} \end{bmatrix} \\ \begin{bmatrix} \mathbf{U}_\alpha^{sc,-} \\ \mathbf{U}_\beta^{sc,-} \end{bmatrix} &= \begin{bmatrix} \mathbf{M}_{\alpha\alpha}^{-+} & \mathbf{M}_{\alpha\beta}^{-+} \\ \mathbf{M}_{\beta\alpha}^{-+} & \mathbf{M}_{\beta\beta}^{-+} \end{bmatrix} \begin{bmatrix} \mathbf{U}_\alpha^{in,+} \\ \mathbf{U}_\beta^{in,+} \end{bmatrix} + \begin{bmatrix} \mathbf{M}_{\alpha\alpha}^{--} & \mathbf{M}_{\alpha\beta}^{--} \\ \mathbf{M}_{\beta\alpha}^{--} & \mathbf{M}_{\beta\beta}^{--} \end{bmatrix} \begin{bmatrix} \mathbf{U}_\alpha^{in,-} \\ \mathbf{U}_\beta^{in,-} \end{bmatrix} \end{aligned} \quad (2.22)$$

In the above equations $\mathbf{U}_\kappa^{sc,\pm}$ and $\mathbf{U}_\kappa^{in,\pm}$ are column vectors defined as

$$\mathbf{U}_\kappa^{sc,\pm} = [\mathbf{U}_{\kappa\vec{g}_1}^{sc,\pm} \quad \mathbf{U}_{\kappa\vec{g}_2}^{sc,\pm} \quad \dots \quad \mathbf{U}_{\kappa\vec{g}_{N-1}}^{sc,\pm} \quad \mathbf{U}_{\kappa\vec{g}_N}^{sc,\pm}]^{Tr} \quad (2.23a)$$

$$\mathbf{U}_\kappa^{in,\pm} = [\mathbf{U}_{\kappa\vec{g}_1}^{in,\pm} \quad \mathbf{U}_{\kappa\vec{g}_2}^{in,\pm} \quad \dots \quad \mathbf{U}_{\kappa\vec{g}_{N-1}}^{in,\pm} \quad \mathbf{U}_{\kappa\vec{g}_N}^{in,\pm}]^{Tr} \quad (2.23b)$$

where the *Tr* superscript denotes the operation of transposing. The explicit expressions for the elements of the matrices $\mathbf{M}_{\kappa\kappa'}^{ss'}$ are given by Liu *et al.* [61]. Being very complicated mathematical objects, matrices $\mathbf{M}_{\kappa\kappa'}^{ss'}$ nevertheless have simple physical meaning. They are transmission and reflection matrices for incident waves $\mathbf{U}_\alpha^{in,\pm}$ and $\mathbf{U}_\beta^{in,\pm}$. For example, by expanding first line in the first matrix equation in (2.22) one obtains:

$$\mathbf{U}_\alpha^{sc,+} = \mathbf{M}_{\alpha\alpha}^{++} \mathbf{U}_\alpha^{in,+} + \mathbf{M}_{\alpha\beta}^{++} \mathbf{U}_\beta^{in,+} + \mathbf{M}_{\alpha\alpha}^{+-} \mathbf{U}_\alpha^{in,-} + \mathbf{M}_{\alpha\beta}^{+-} \mathbf{U}_\beta^{in,-}$$

Figure 2.1.9 shows a schematic diagram explaining the physical meaning of matrices

$\mathbf{M}_{\kappa\kappa'}^{ss'}$ contained in the above equation.

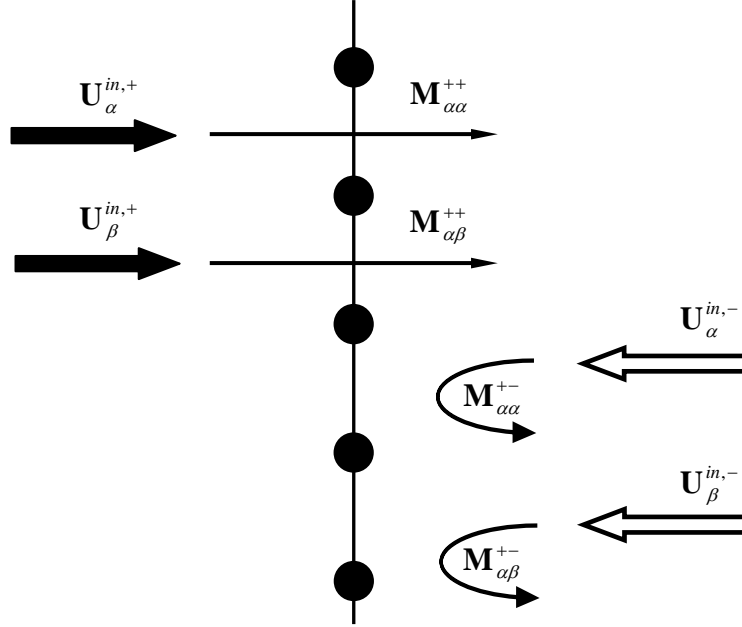


Figure 2.1.9: Schematic illustration of the physical significance of the matrices $\mathbf{M}_{\kappa\kappa'}^{ss'}$.

Having found transmission and reflection matrices through the *single* layer, one needs to find a way to calculate similar matrices for a phononic crystal with an *arbitrary* number of layers. This is accomplished by calculating matrices $\mathbf{Q}_{\kappa\kappa'}^{ss'}$ for each of two single layers that are displaced with respect to the x - y plane by vectors $\vec{a}_3/2$ and $-\vec{a}_3/2$, where \vec{a}_3 is a third primitive vector of the Bravais lattice of the phononic crystal. In other words \vec{a}_3 is a vector by which a single 2D layer of scatterers should be repeated to form

the 3D phononic crystal. Matrices $\mathbf{Q}_{\kappa\kappa'}^{ss'}$ have the same physical meaning as $\mathbf{M}_{\kappa\kappa'}^{ss'}$ and are connected with matrices $\mathbf{M}_{\kappa\kappa'}^{ss'}$ by another translation matrix ϕ_{κ}^s , whose elements are explicitly expressed in [61]. The transmission and reflection matrices for the pair of two successive layers (denoted by N and $N+1$) are obtained by combining corresponding matrices $\mathbf{Q}_{\kappa\kappa'}^{ss'}(N)$ and $\mathbf{Q}_{\kappa\kappa'}^{ss'}(N+1)$. The essential physics here is that two sets of matrices are combined by taking into account all *multiple* reflections that the incident wave undergoes between two layers as it propagates through the two-layer system [62]. By repeating this procedure the transmission and reflection matrices through the slab consisting of 2^n layers can be found. The corresponding matrices for the crystal with an arbitrary number of layers can be obtained by combining matrices for the slab with even number of layers and one extra layer.

It also should be noted that in addition to the band structure, which displays normal modes of the system along high symmetry directions, the MST also allows calculation of the modes along *any* direction inside the crystal. The geometrical set of all points belonging to a particular mode (which is characterized by a certain frequency) is referred to as an Equifrequency Surface or Equifrequency Contour (EQC) for 3D or 2D structures correspondingly. The information on the equifrequency contours for my 2D crystals obtained with the MST plays a very important role in the interpretation of the results of the experiments on negative refraction and focusing of ultrasound as will be seen in the next section.

2.2 Band structure effects in 2D phononic crystals

This section lays the theoretical basis for the experiments conducted on 2D phononic crystals that are described in Chapter 5. It starts by explaining the major ideas behind the negative refraction effect observed with my prism-shaped 2D crystal and continues by discussing the sound focusing properties of the flat rectangular-shaped crystal. It will be shown that both phenomena are essentially *band structure* effects.

2.2.1 Negative refraction in phononic crystals

It is well known that reflection and refraction of waves of any nature (acoustic, elastic or electromagnetic) occurring at the interface between two different media are governed by *Snell's law*. According to Snell's law, the wavevector's component tangential to the interface must be *conserved* as the wave propagates from one medium to another. Let us consider, for example, the simple case of a plane wave obliquely incident from a liquid with Lamé coefficients λ_1 and $\mu_1 = 0$ on an isotropic solid characterized by Lamé coefficients λ_2 and μ_2 [Figure 2.2.1]. As a result of the wave interaction with the boundary, part of the energy of the incident wave is reflected back into the liquid in the form of a reflected wave, which propagates with the phase velocity $c_1 = \sqrt{\lambda_1/\rho}$. The rest of the incident wave is transmitted into the solid and generates two outgoing waves, longitudinal and transverse, which propagate with phase velocities $c_2 = \sqrt{(\lambda_2 + 2\mu_2)/\rho}$ and $b_2 = \sqrt{\mu_2/\rho}$ respectively. Snell's law requires that parallel (to the interface) components of the wavevectors of the incident wave, $k_1 = \omega/c_1$, and of both refracted waves, $k_2 = \omega/c_2$ and $k_{2t} = \omega/b_2$ be equal (note that k_1 lies in the x - z plane and so do k_2 and k_{2t}). Mathematically, this means that the following conditions must be satisfied:

$$k_1 \sin \theta_1 = k_2 \sin \theta_2 = k_{2t} \sin \gamma_2 \quad (2.24)$$

where angles θ_1, θ_2 and γ_2 are indicated in Figure 2.2.1. By introducing the notion of the index of refraction n and n' , where $n = k_2/k_1$ and $n' = k_{2t}/k_1$, Snell's law is frequently written in the following form:

$$\sin \theta_1 = n \sin \theta_2 \quad (2.25)$$

$$\sin \theta_1 = n' \sin \gamma_2$$

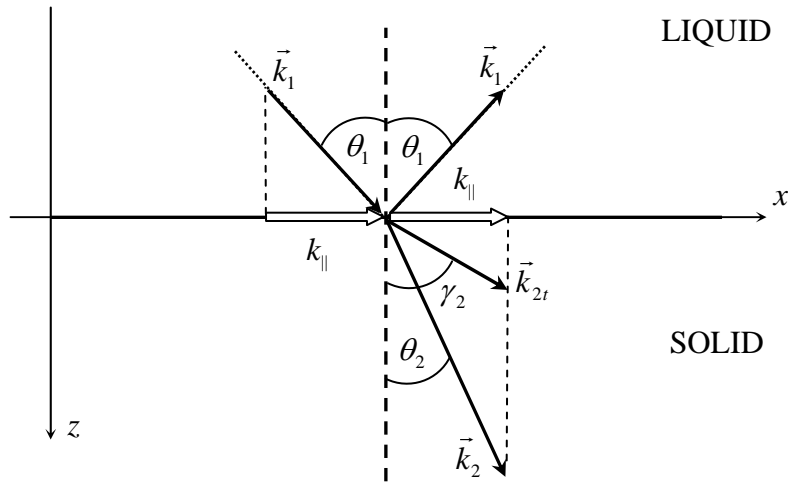


Figure 2.2.1: Reflection and refraction of a plane wave incident obliquely on the liquid/solid interface from the liquid. Note the conservation of the wavevector component k_{\parallel} .

With the help of Snell's law (2.24), one can easily calculate the refraction angles θ_2 and γ_2 when the parameters of the two media and the angle of incidence θ_1 are known (it is clear from Snell's law that the angle of reflection must be equal to the angle of incidence). There is no point in deriving equations (2.24) in this thesis, as the derivation of Snell's law is done for different kinds of waves in numerous textbooks on optics and acoustics (see, for example, [64] and [65] for the case of elastic waves). Physically,

Snell's law implies that refraction and reflection occur in the same way at any point of the interface between two media (i.e. independent of the x coordinate in Figure 2.2.1).

The refraction of the wave from one medium to another can be conveniently visualized with the help of the *equipfrequency* surfaces (or contours in case of 2D systems). Equipfrequency surfaces are formed in k -space by all points whose wavevectors correspond to plane waves of the same frequency ω . Physically, they display the magnitude of the wavevector \vec{k} of a plane wave propagating in the given medium as a function of the *direction* of propagation. For any isotropic medium the equipfrequency surfaces are perfect spheres (circles in 2D), since the magnitude of the wavevector is independent of the direction of propagation, as illustrated in Figure 2.2.2.

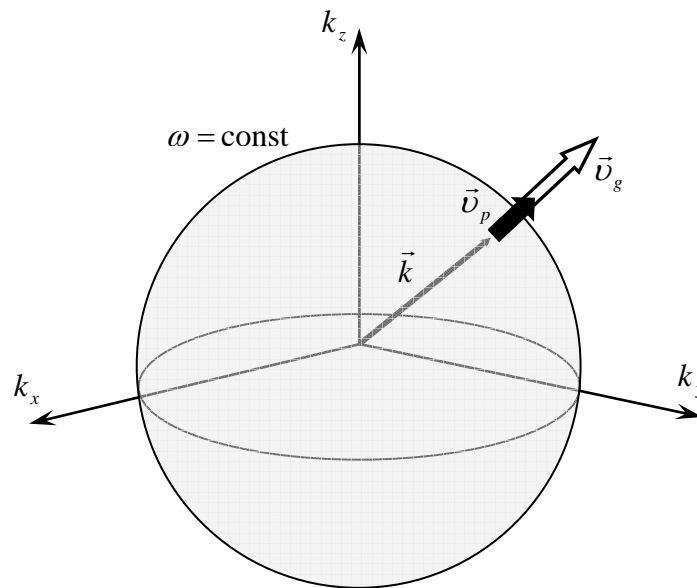


Figure 2.2.2: Equipfrequency surface of an isotropic medium.

Another extremely important property of equipfrequency surfaces is that at its every point the direction of the group velocity \vec{v}_g (or equivalently the direction of the energy transport) in the medium at a given frequency coincides with the direction of the normal to the equipfrequency surface (pointing towards the increase of ω). In other words, \vec{v}_g is given by the gradient of ω as a function of the wavevector \vec{k} :

$$\vec{v}_g = \vec{\nabla}_{\vec{k}} \omega(\vec{k}) \quad (2.26)$$

On the other hand, the direction of the phase velocity \vec{v}_p (or the direction of the propagation of constant phase) is set by the direction of the wavevector \vec{k} . As shown in Figure 2.2.2, in an isotropic medium both phase and group velocities point in the same direction. This is however not the case in an *anisotropic* medium (e.g. GaAs or CdS), in which magnitude of the wavevector is direction dependent and thus equipfrequency surfaces will not be perfect spheres anymore. Another example of anisotropic systems are phononic crystals since the magnitude of the wavevector is strongly modulated by their periodicity.

Having introduced the notion of the equipfrequency surfaces/contours, let us use them to illustrate the refraction of a plane wave in Figure 2.2.1. This is accomplished by drawing the equipfrequency contours (since all wavevectors lie in the x - z plane) for each medium on the scale that would correctly represent the relative magnitudes of the wavevectors of the incident and refracted waves. By projecting the parallel component of the incident wavevector \vec{k}_1 (which must be conserved according to Snell's law) on the contours of the solid, one is able to find the direction of propagation (i.e. refraction angles) of both waves in the solid [Figure 2.2.3]. As was explained in the preceding paragraph,

group velocities \vec{v}_g and wavevectors \vec{k} are *parallel* to each other (because of the spherical shape of the equifrequency contours) and also point in the *same* direction, since ω increases as the magnitude of the wavevector increases, meaning that $\vec{\nabla}_{\vec{k}}\omega(\vec{k})$ points along the *outward* normal to the equifrequency contour. The significance of the last observation will become apparent when the refraction in 2D phononic crystals will be discussed.

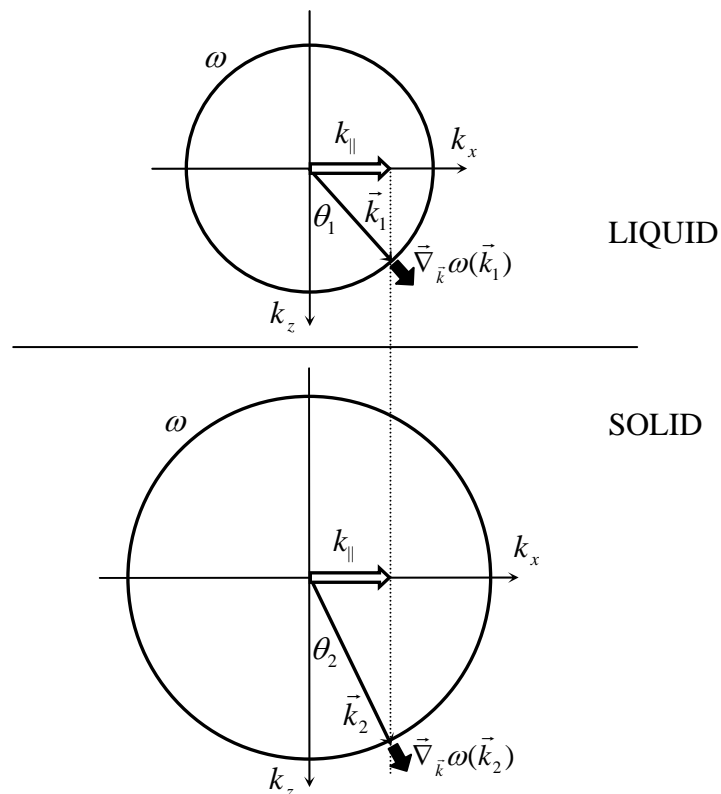


Figure 2.2.3: Refraction of a plane wave in Figure 2.2.1 is illustrated with the help of the equifrequency contours (the same diagram holds for the transverse wave, which is omitted for simplicity).

The periodicity of the phononic crystal makes it an anisotropic medium, in which the magnitude of the wavevector depends on the direction inside the crystal and equipfrequency contours are, in general, not circular. However, the frequency ranges still might exist where the equipfrequency are indeed perfect circles. In the case of my 2D crystals (stainless steel rods in water), the MST predicts the existence of circular equipfrequency contours in the 2nd band for the frequencies that are far enough from the Brillouin zone edges (ranging from 0.75 MHz to 1.04 MHz, which is the top frequency of the 2nd band). The equipfrequency contours for the several frequencies are presented in Figure 2.2.4.

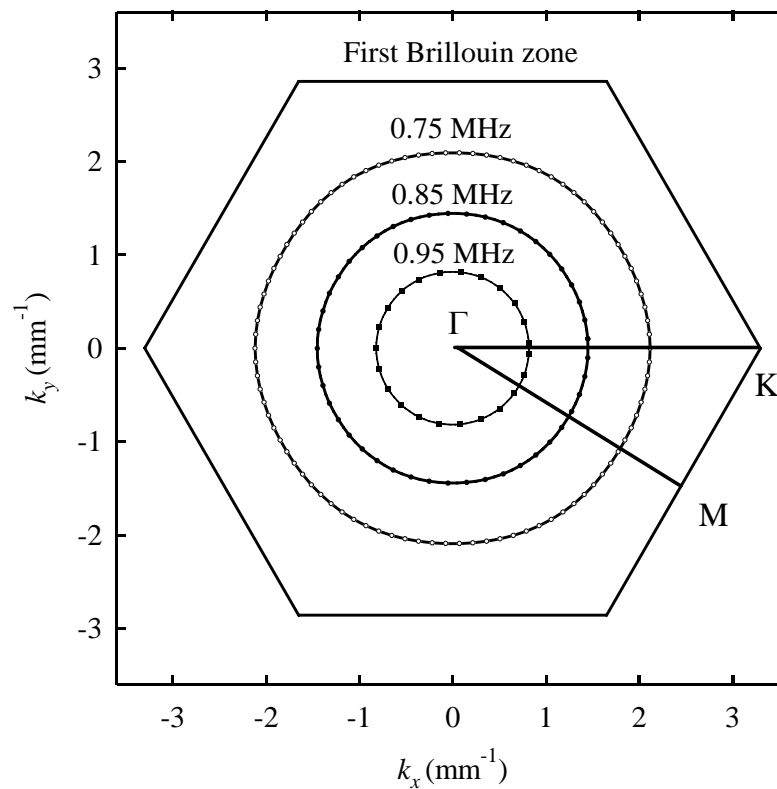


Figure 2.2.4: Equipfrequency contours predicted by MST for the several frequencies in the 2nd band of the 2D phononic crystal made stainless steel rods in water (Calculations courtesy of Dr. Zhengyou Liu).

Note that in this frequency range the wavevector \vec{k}_{cr} and the group velocity \vec{v}_g (which defines the direction of the energy transport inside the crystal) are *antiparallel* to each other, i.e. they point in *opposite* directions. This is the consequence of the fact that ω increases with the *decreasing* magnitude of the wavevector, meaning that $\vec{\nabla}_{\vec{k}}\omega(\vec{k})$ points along the *inward* normal to the equifrequency contour, as explained in Figure 2.2.5. It is also obvious that, because of the circular shape of the equifrequency contours in the 2nd band, \vec{k}_{cr} and \vec{v}_g are antiparallel *irrespective* of the direction inside the crystal.

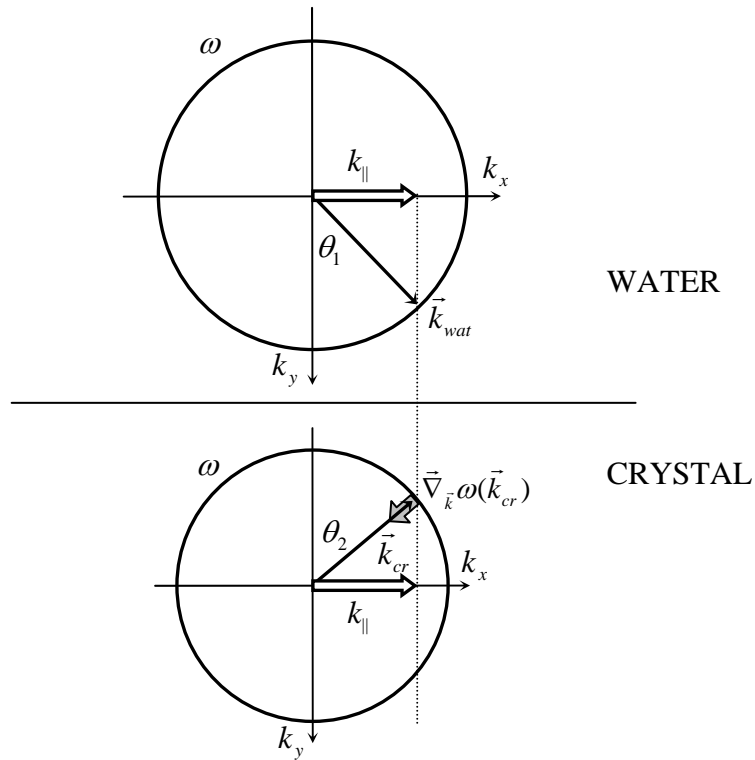


Figure 2.2.5: Refraction of a plane wave at the water/crystal interface. The choice of the upward direction of the wavevector \vec{k}_{cr} provides a wave propagating inside the crystal.

Let us investigate the consequence of this fact by considering the refraction into the 2D phononic crystal of a plane wave at some frequency in the 2nd band of the crystal, when the wave is incident on the liquid/crystal interface from the liquid (water) [Figure 2.2.6]. Of course, the parallel component of the wavevector in both media must be conserved just as it was in the case displayed in Figure 2.2.3. What is different however is that the wavevector inside the crystal and the direction of the wave propagation inside the crystal are now *opposite* to each other. As a result, both incident and refracted rays stay on the *same* side of the normal to the water/crystal interface as shown in Figure 2.2.6 (compare with Figure 2.2.3 in which incident wave crosses the plane though the normal as it refracts into the lower medium).

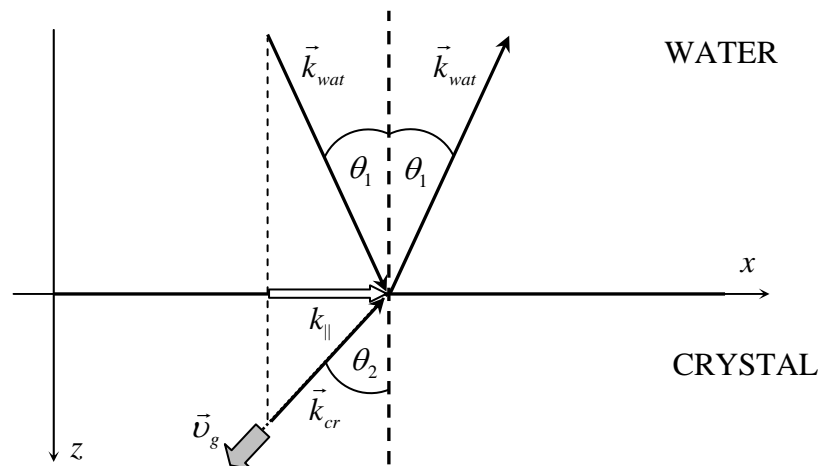


Figure 2.2.6: Negative refraction of a plane wave incident obliquely on the water/crystal interface. Note the conservation of the wavevector component k_{\parallel} .

Since the refracted wave happens to be on the negative side of the normal, this unusual refraction can also be described by assigning an effective *negative* index of refraction to the crystal. In this case we say that the incident wave is *negatively* refracted into the crystal and use the term “*negative* refraction” to indicate this phenomenon. Before we proceed further with discussion of the sound waves refraction in the phononic crystals, it is definitely worth recalling the origin of this term. The term “negative refraction” was first introduced for electromagnetic waves by Viktor G. Veselago in 1964 [32], who investigated theoretically the properties of materials with negative values of both electric permittivity ε and magnetic permeability μ . It follows from Maxwell’s equations that vectors \vec{E}, \vec{H} and \vec{k} of electromagnetic wave propagating in such materials will form a left-handed set. These materials were named left-handed (LH) as opposed to the regular right-handed (RH) materials, in which vectors \vec{E}, \vec{H} and \vec{k} form a right-handed set. As a result, the direction of the wavevector \vec{k} of the electromagnetic wave propagating in a LH material is reversed with respect to the wave in a RH material. However, the direction of the Poynting vector \vec{S} , which gives the direction of the energy transport in an electromagnetic wave, is unchanged in materials of both kinds, meaning that in LH materials vectors \vec{S} and \vec{k} are antiparallel to each other. This fact leads to a number of unusual properties exhibited by LH materials (e.g. reversed Doppler and Vavilov-Cherenkov effects) and one of them is negative refraction, which happens when an electromagnetic wave propagates through the boundary between RH and LH materials and refracts on the negative side of the normal to the boundary in the same way as shown in Figure 2.2.6 for the sound wave. Although both phenomena look similar, there is a major difference between negative refraction in LH materials and phononic crystals. The

first one is brought about by the negative values of the *local* parameters of the medium (ϵ and μ) whereas it is a *band structure* effect in case of phononic crystals.

Let us now move to the question of the *experimental* observation of negative refraction of sound waves. First, it should be mentioned, that the same effect must occur when the direction of the wave in Figure 2.2.6 is reversed, i.e. when the wave is incident on the crystal/water interface from the crystal. One might contemplate an experiment in which a plane wave would be incident obliquely on a *flat* phononic crystal with *parallel* sides. According to the previous discussion, it should be refracted negatively twice before it finally appears on the output side of the crystal, as shown in Figure 2.2.7.

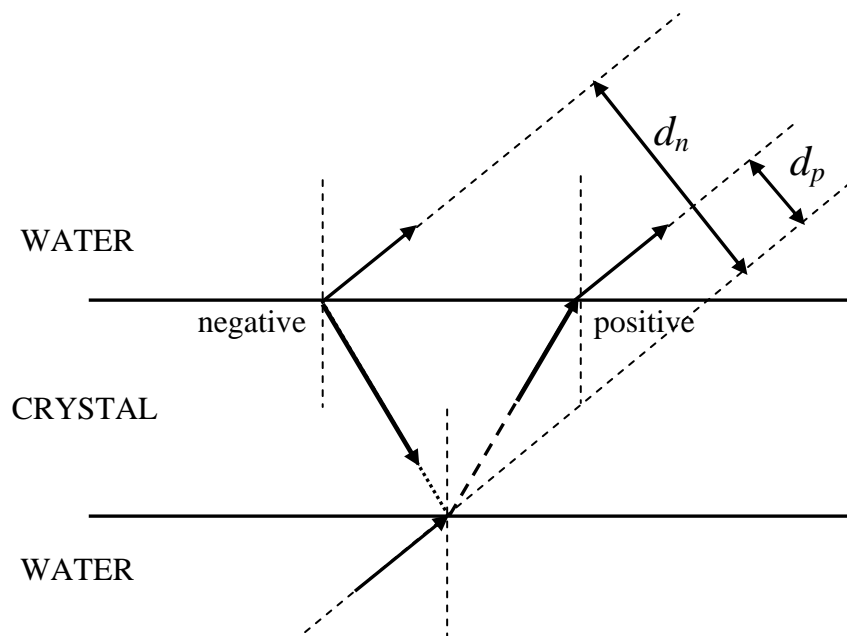


Figure 2.2.7: Propagation of the sound wave through a flat crystal with parallel surfaces. Both negatively and positively refracted waves leave the crystal's surface in the same direction. Also indicated are distances d_p and d_n by which positively and negatively refracted beams are displaced with respect to the input beam.

This type of experiment, however, is not able to provide conclusive evidence of the negative refraction, as the direction of the propagation of the output wave will be the same whether it refracts negatively inside the phononic crystal or positively in a slab of a regular isotropic material [Figure 2.2.7]. Of course, in case of an input beam of finite width, one can try to obtain evidence of either negative or positive refraction inside the slab by measuring the position of the output beam with respect to the input beam and comparing it to the predicted value. Another type of experiment, which is able to provide the *direct* verification of whether positive or negative refraction takes place, employs the *prism-shaped* phononic crystal [Figure 2.2.8].

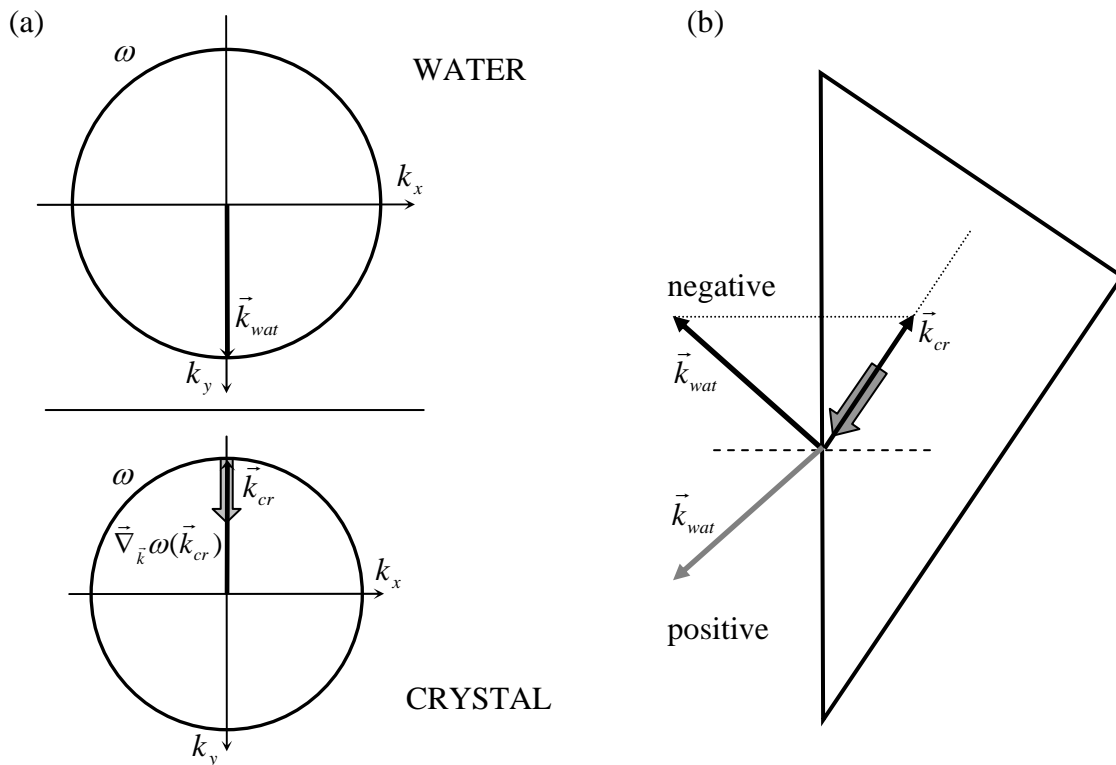


Figure 2.2.8: Negative refraction experiment with the prism-shaped phononic crystal. (a) Equifrequency contours in water and in the crystal. In (b), the directions of positive and negative refraction at the output face of the prism crystal are shown. The thick arrow indicates the direction of wave propagation inside the crystal.

For the prism-shaped crystal the input plane wave is incident normally on the shortest side of the crystal and propagates into the crystal *without* any change in its original direction, just as it would do in the case of a prism made out of a regular material (see Figure 2.2.8(a)). Recall that the ensuing wave inside the crystal will have its wavevector \vec{k} opposite to the direction of its propagation. This wave, however, will be incident *obliquely* on the output side of the crystal and must undergo negative refraction upon crossing the crystal/water interface [Figure 2.2.8(b)], whereas in the case of a prism of a regular material the output wave will be positively refracted. Therefore, by recording on which side of the normal the outgoing wave appears as it leaves the crystal, one is able to directly observe negative refraction of the sound waves. From the predictions of the MST, one would expect the outgoing wave to emerge on the negative side of the normal. This prediction was tested in the experimental configuration considered in Figure 2.2.8 and results of these experiments are reported in the first section of Chapter 5.

2.2.2 Focusing properties of 2D phononic crystals

Veselago also pointed out that a slab of LH material must have the ability to *focus* electromagnetic radiation of a point source [32], which comes as a direct consequence of each incident ray being negatively refracted twice as it propagates through the slab [Figure 2.2.9]. In other words, a flat slab of LH material would act like a lens and is frequently referred to as “Veselago lens” in the literature. The optical system based on such negatively refracting lens would have certain advantages over the conventional optical systems. First, it will be much easier to manufacture, since it takes much less effort to produce a slab with parallel sides than the curved surface of a conventional lens. Second,

a Veselago lens is void of the optical axis, meaning that the displacement of the source along the slab surface would be followed by the same displacement of an image.

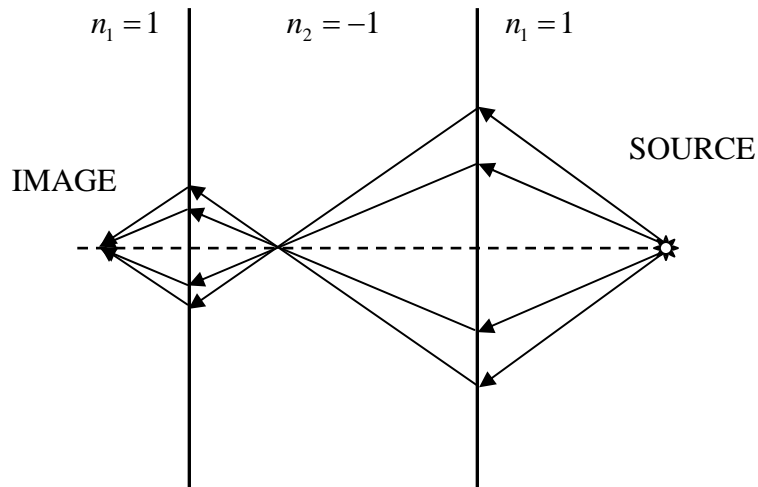


Figure 2.2.9: Focusing of the point source radiation by a slab of LH material. Note that rays incident at different angles to the surface of the slab are brought to the same focal spot.

Much in the same way, the similar focusing property can be expected to be exhibited by my 2D flat phononic crystals for the *sound* field emitted by a point source in the frequency range corresponding to the 2nd band. The experimental demonstration of this effect might open the future possibilities of constructing sound imaging systems based on flat phononic crystals, which would have the same advantages over conventional sound focusing systems (e.g. ultrasound focusing transducers) as those discussed above for a Veselago lens. Before embarking on the experimental work however, it is also useful to analyze theoretically the possible outcomes of the experiment, e.g. under which conditions such an imaging system might exhibit the best focusing.

In his paper Veselago contemplated focusing of electromagnetic radiation of a point source incident from vacuum ($n_1 = 1$) by a slab of LH material with the refraction index $n_2 = -1$ [Figure 2.2.9]. Such system is able to provide a *perfect* focus for the point source in the sense that each pair of rays emitted by a source will be brought to the *same* spatial point on the output side of the slab. This will also be true for any LH material whose refraction index has the same absolute value (but opposite sign) as the one of the surrounding medium. In the general case when $n_1 \neq |n_2|$, it is clear from the ray diagram (see Figure 2.2.10) that the source/slab and slab/image distances L_1 and L_2 are related to the thickness of the slab d by the following equation:

$$L_1 + L_2 = d \frac{\tan(\theta_r)}{\tan(\theta_{in})} \quad (2.27)$$

where θ_{in} and θ_r are the corresponding angles of incidence and refraction.

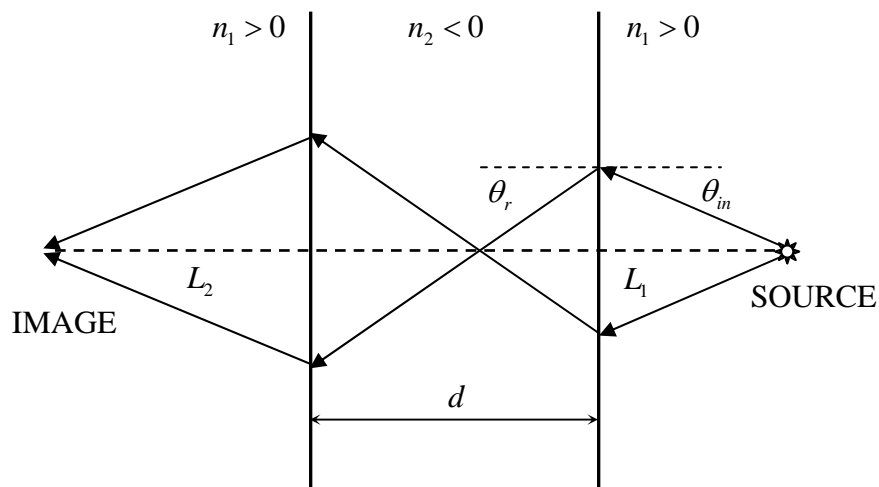


Figure 2.2.10: Focusing by a slab of LH in case of $n_1 \neq |n_2|$.

With the help of Snell's law, the factor multiplying the thickness of the slab d can be expressed as

$$\frac{\tan(\theta_r)}{\tan(\theta_{in})} = \frac{n_1}{|n_2|} \left(\frac{1 - \sin^2(\theta_{in})}{1 - (n_1/n_2)^2 \sin^2(\theta_{in})} \right)^{\frac{1}{2}} \quad (2.28)$$

implying that position of the focal point L_2 depends on the angle of incidence θ_{in} (n_1 and n_2 are refraction indices of the surrounding medium and LH slab respectively). In this case the focal spot is expected to be elongated along the axis connecting the source and the image. Only when the condition $n_1 = |n_2|$ is satisfied, all the rays are brought to the same focal spot independent of θ_{in} ($L_2 = \text{const}$). For phononic crystals, the condition for a perfect focus

$$\frac{\tan(\theta_r)}{\tan(\theta_{in})} = 1 \quad (2.29)$$

implies that equifrequency contours of the surrounding medium (water) and those of the crystal must match (i.e. have the same radius), as shown in Figure 2.2.11. The results of the experiments aimed at observing the focusing of ultrasound waves by flat 2D phononic crystals are presented in the second part of Chapter 5.

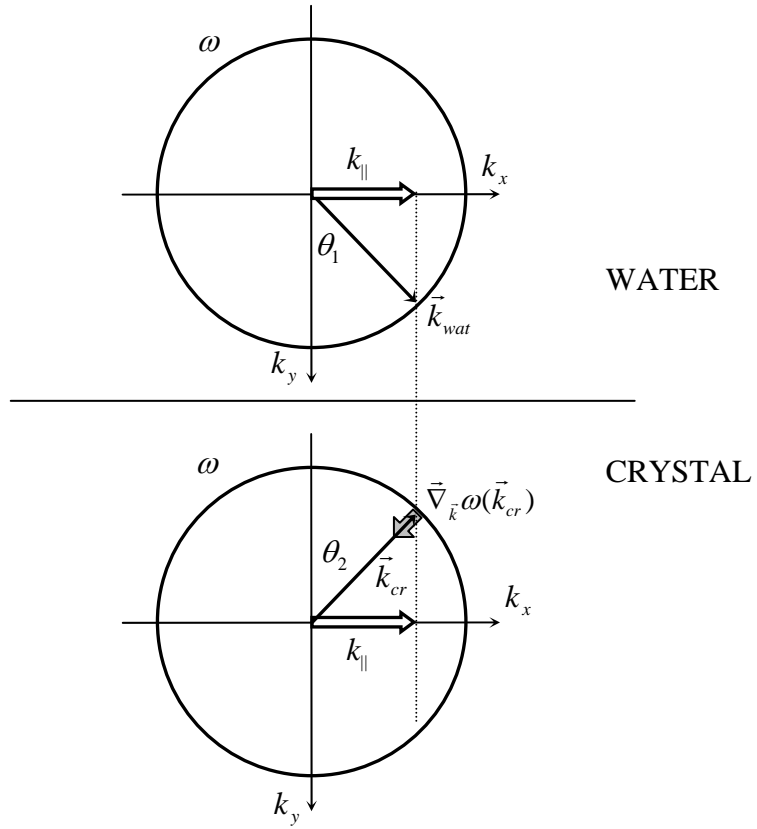


Figure 2.2.11: The condition $k_{wat} = k_{cr}$ for matching of equifrequency contours implies the condition $\theta_1 = \theta_2$.

3. Experiment

The following chapter describes the apparatus, the samples and the experiments presented in this thesis. In the first section, the samples (2D and 3D phononic crystals) are described in detail along with information on how they were assembled. The second section gives a brief overview of the mechanical part of the experimental set-up. The third and fourth sections deal with the electronics and ultrasound transducers, which were employed to generate, detect, process and record ultrasonic signals. The final two sections provide a description of the different types of experiments performed and explain in detail the data analysis procedure for each experiment.

3.1 Sample preparation

3.1.1 2D phononic crystals

For the experiments on the negative refraction of ultrasound waves and sound focusing, two types of 2D phononic crystals, differing in their shape, were constructed. A prism-shaped 2D crystal was used in negative refraction experiments whereas a rectangular shaped crystal was used to investigate the focusing of ultrasound. Both crystals were made out of stainless steel rods 1.02 mm in diameter and assembled in a triangular (also known as hexagonal) 2D crystal lattice with a lattice constant of 1.27 mm [Figure 3.1.1].

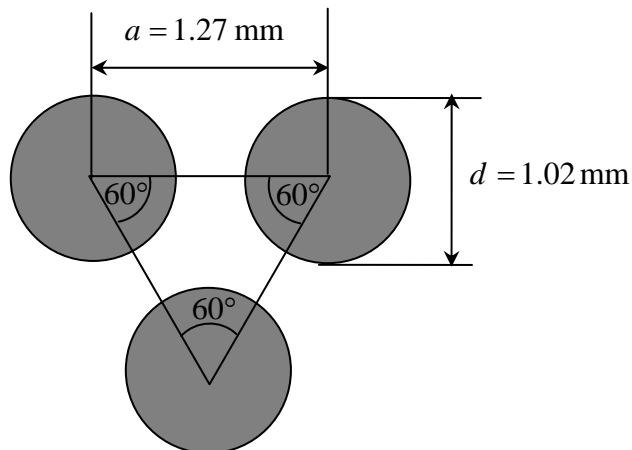


Figure 3.1.1: Unit cell of a 2D phononic crystal.

The rectangular-shaped crystal had 6 layers each consisting of 60 rods and stacked along the ΓM direction [Figure 3.1.2(a)]. The prism-shaped crystal had 58 layers, with its sides forming angles of 30° , 60° and 90° and being perpendicular to the ΓM (shortest and longest sides) and the ΓK directions [Figure 3.1.2(b)].

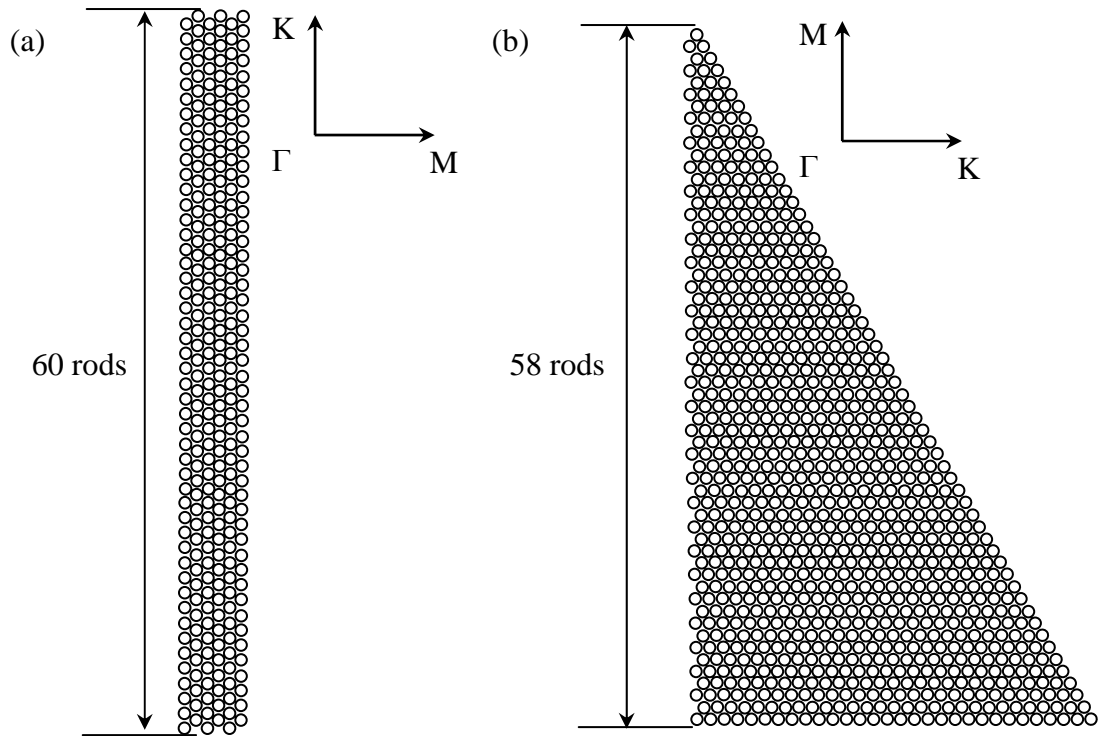
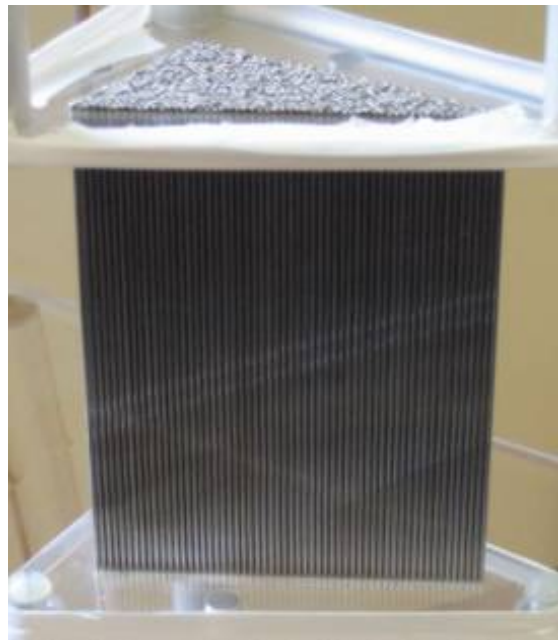


Figure 3.1.2: Geometry of the 2D crystals. (a) Rectangular crystal.
(b) Prism-shaped crystal

The filling ratio for the 2D crystals was 58.4%. The particular details of crystal design depended on the type of liquid, which filled the space between the rods. For the crystals immersed in and filled with water, the rods were kept in place by two parallel polycarbonate plates in which a number of holes were drilled, forming a triangular crystal lattice in the shape of the crystal in question. The diameter of the holes was carefully chosen to allow a snug fit once each rod was slid into the corresponding top and bottom holes [Figure 3.1.3(a)-(b)]. The rectangular crystal was 14 cm high while the prism-shaped crystal height was 9 cm. The water used in all the experiments was purified by a reverse osmosis procedure.



(a)



(b)

Figure 3.1.3: Pictures of the 2D crystals, which were filled with and immersed in water during the experiments: (a) rectangular crystal, (b) prism-shaped crystal.

A second rectangular-shaped crystal (with all the parameters identical to those of the first crystal) was constructed to enable the liquid surrounding the rods to be different to the medium outside the crystal. The design was much more complicated since it was important to prevent mixing of the liquid inside (methanol) and the liquid outside (water). First of all, this time PVC plastic was used because of its excellent resistance to the alcohols and to methanol in particular. To separate methanol from water, the crystal was wrapped in a very thin (0.01 mm) plastic film produced commercially and conventionally available as a food wrap. Finally, the cell was specifically designed both to keep the rods in a triangular crystal lattice and to seal the inside of the crystal from surrounding water by utilizing two rubber O-rings. Two holes drilled in the cell allowed the cell to be conveniently filled and drained before and after experiments [Figure 3.1.4].

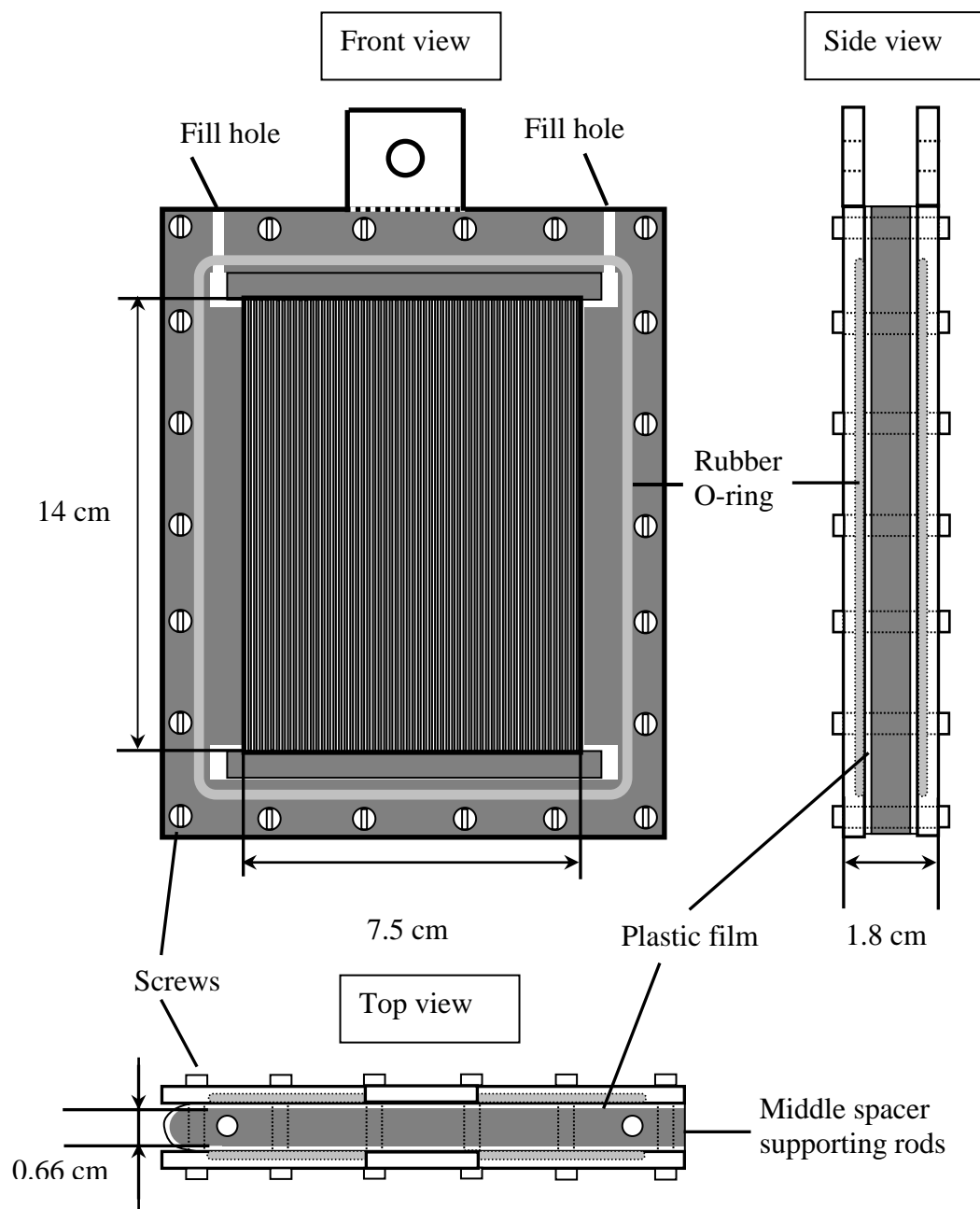


Figure 3.1.4: Methanol-filled 2D crystal cell design.

Finally, it is worth mentioning that the choice of materials for the scatterers (rods) and matrix (water or methanol) provided high density and velocity contrast, thus ensuring that most of the sound energy was scattered by scatterers and concentrated in the host matrix. Table 3.1.1 provides values of the densities and sound velocities for the constituent materials of the 2D crystals.

Material	Density (g/cm ³)	Longitudinal velocity (mm/μs)	Shear velocity (mm/μs)
Stainless steel	7.89	5.80	3.10
Water	1.00	1.49	-
Methanol	0.79	1.10	-

Table 3.1.1: Comparison of the properties of the constituent materials used for 2D phononic crystals [83].

3.1.2 3D phononic crystals

In the experiments on the tunneling of ultrasound pulses, the samples consisted of two 3D phononic crystals with the same number of layers separated by an aluminum plate. For brevity, these samples will be referred to as *double* 3D crystals. Phononic crystals were made out of very monodisperse tungsten carbide beads, 0.800 mm in diameter, that were surrounded by reverse osmosis water. The beads were manually assembled in a face centered cubic (FCC) structure, with triangular layers stacked along the cube body diagonal (also known as the [111] direction) in an ABCABC... sequence. To ensure the absence of air bubbles trapped between the beads, the whole process of assembling crystals was conducted in water. To support the beads in the required structure, acrylic

templates were used. The template consisted of a thick substrate with plastic walls attached to it [Figure 3.1.5].

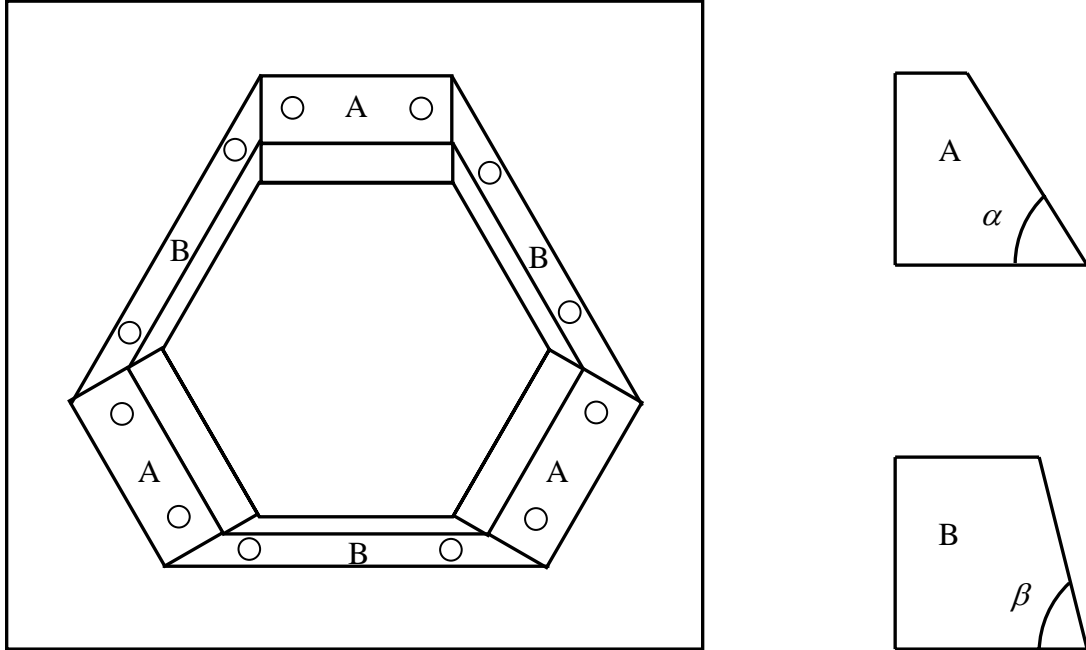


Figure 3.1.5: Template for 3D phonic crystal (top view) with side views of walls A and B. Note that $\tan \alpha = \sqrt{2}$ and $\tan \beta = 2\sqrt{2}$.

One can show that in order to keep beads in an FCC crystal lattice two kinds of walls should be used with sides inclined at angles $\alpha \approx 54.74^\circ$ and $\beta \approx 70.33^\circ$ above the horizontal, and with inner side lengths L_A and L_B . The values of L_A and L_B depend on the number of beads n along each side of the first crystal layer and the bead diameter d . They can be shown to be given by the following expressions:

$$\begin{aligned}
 L_A &= (n-1 + \tan \frac{\alpha}{2})d \\
 L_B &= (n-1 + \tan \frac{\beta}{2} \cot 75^\circ)d
 \end{aligned}
 \tag{3.1}$$

With 49 beads on each side of the bottom layer, (3.1) gives $L_A = 38.814$ mm and $L_B = 38.552$ mm.

As was already mentioned, the crystals were assembled manually with the beads being immersed in water all the time. After the lower crystal was assembled an aluminum spacer was carefully placed onto it without disturbing beads of the crystal. The upper crystal was then assembled on top of the spacer. Spacer edges were machined at angles matching the angles of the walls of the template. Also, the thickness of the spacer was calculated such that it replaced precisely an integer number of layers of the single crystal. This ensured that the beads resting on the spacer filled the entire available surface without leaving any gaps, forming a high quality first layer, on which the quality of the whole upper crystal critically depended. In most of the experiments, the thickness of the spacer was chosen to be 7.05 ± 0.01 mm.

The base of the template was made fairly thick (84.45 mm) to allow temporal separation between the ultrasonic pulse that was directly transmitted through the crystal, and all of its subsequent multiple reflections inside the substrate. At the initial stage of experiments, the substrate was made of acrylic. Later on, acrylic was replaced by polyethylene. The main reason for the change was the higher sound attenuation properties of polyethylene, which helped prevent multiple reflections inside the substrate from overlapping with the directly transmitted pulse. The overlap was not an issue in the transmission experiments with single 3D crystals, but became important in the resonant tunneling experiments with double crystals, since in this case the transmitted pulses extended for times much longer than the round-trip time of multiply reflected echoes inside the substrate. An additional advantage of using polyethylene over acrylic was a

reduction of the reflection coefficient at the water/substrate interface, since the acoustic impedance of polyethylene is closer to that of water (speed of sound in polyethylene is lower than that in acrylic). The density and velocity mismatch in the case of 3D crystals was even larger than for 2D crystals, as tungsten carbide has density of 13.8 g/cm^3 , longitudinal velocity of $6.6 \text{ mm}/\mu\text{s}$ and shear velocity of $3.2 \text{ mm}/\mu\text{s}$. The actual sample (single 3D crystal) is shown in Figure 3.1.6, while the close-up of its surface is presented in Figure 3.1.7.

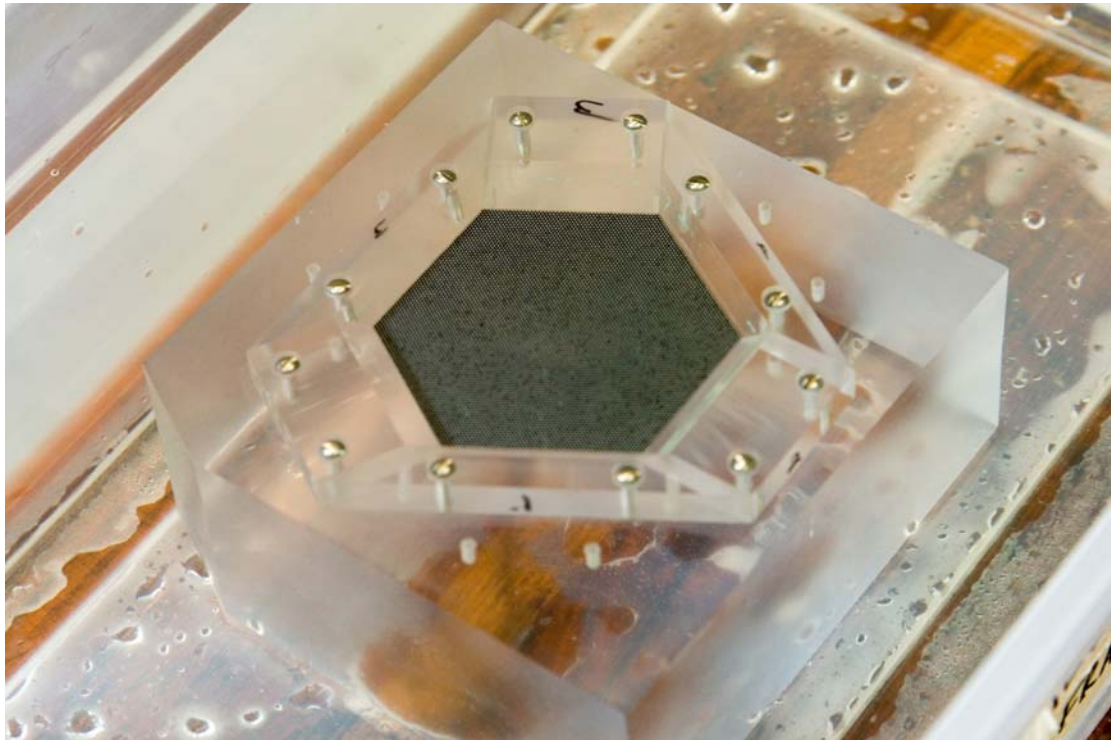


Figure 3.1.6: 3D single phononic crystal.

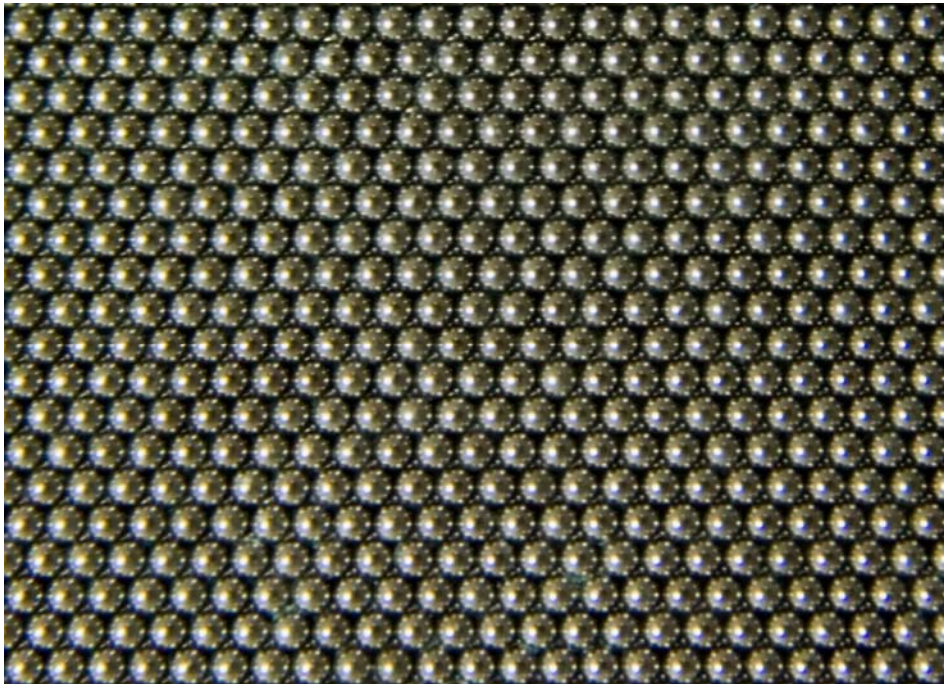


Figure 3.1.7: Close-up view of the surface of the crystal, which is shown in Figure 3.1.6.

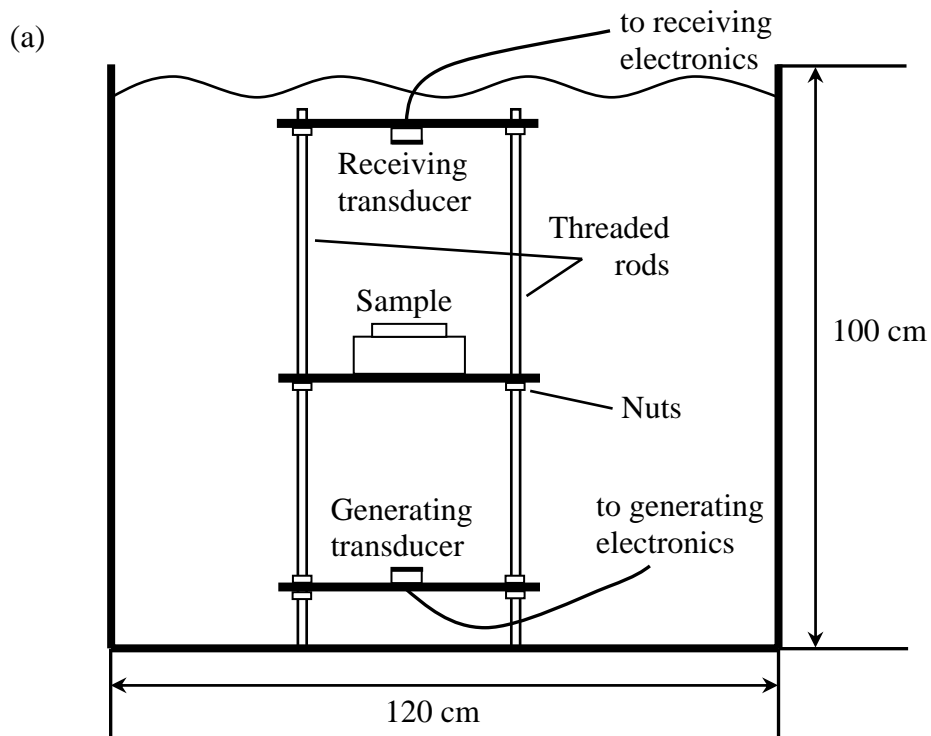
3.2 Mechanical apparatus

3.2.1 Apparatus for the experiments with 3D phononic crystals

All of the experiments described in this thesis were conducted with samples and ultrasonic transducers immersed in a tank filled with reverse osmosis water. Water was a natural choice of surrounding medium for our samples since most of my phononic crystals had solid scatterers in a water matrix and also because water is a convenient (readily available, low attenuation) media for sound propagation at the frequencies used in the experiments.

Two water tanks of different dimensions were used in the course of the experiments. The ultrasound resonant tunneling experiments were performed in a larger tank made of reinforced fiberglass measuring 120 x 120 cm in its base and 100 cm deep, since this tank allowed achieving a larger separation between the sample and the generating and receiving transducers. The significance of this will be explained in the Section 4.2.3. For these experiments a special support stage was designed, which consisted of a stainless steel plate with four threaded rods screwed to it and two plastic plates that were allowed to slide along rods and were secured in a given position by nuts. The generating transducer was mounted on the metal base, the middle plate supported the sample whereas the upper plate had a receiving transducer attached to it. This configuration allowed the distances between the sample and transducers to be quickly changed and greatly facilitated the parallel alignment of the transducers and sample. To eliminate any stray signals, all three plates were wrapped in Teflon tape, which has been shown by previous experiments in our laboratory to be an excellent sound absorber.

Figure 3.2.1 gives a schematic diagram of the experimental set-up along with a picture of the stage sitting in the tank with the sample in place.



(b)



Figure 3.2.1: Experimental set-up for resonant tunneling experiments: (a) Large tank and supporting stage geometry, (b) Picture of the stage with mounted transducers and sample in place (Teflon tape was added later on).

3.2.2 Apparatus for the experiments with 2D phononic crystals

For the negative refraction and focusing experiments a glass aquarium was used with base dimensions of 122×60 cm and a depth of 62 cm. Walls of the tank were lined with Styrofoam to absorb incident sound waves. To break up remaining reflections into many directions vertical Styrofoam strips were glued around the tank at about 10-15 cm intervals. A metal frame was built around the tank to mount the sample as well as the generating and receiving transducers [Figure 3.2.2]. Many of the experiments with 2D phononic crystals involved scanning of the output field with the hydrophone in a controlled grid. This was achieved with the help of the 3D motorized stage, which also was mounted on the metal frame. The motorized stage was controlled directly from the computer using custom written MATLAB codes (courtesy of Matthew Hasselfield).

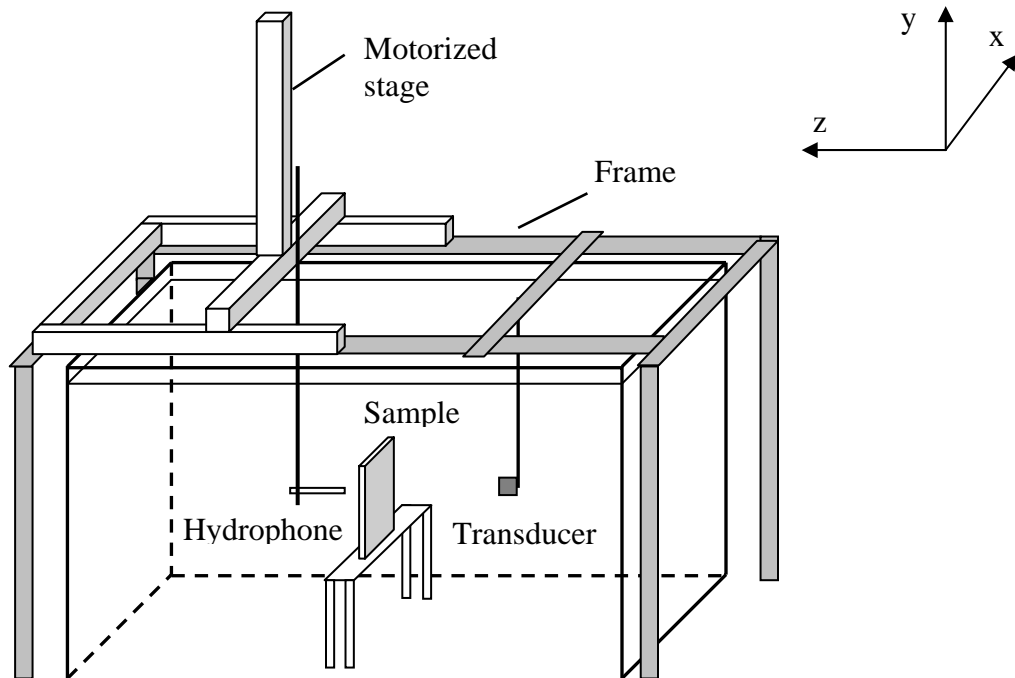


Figure 3.2.2: Geometry of the experiments conducted in the small water tank.

3.3 Electronics

3.3.1 Generating electronics

In all our experiments radio frequency (RF) pulses were used to drive generating and receiving transducers. To produce RF pulses, three different setups were employed.

In the first setup, the tone-bursts were generated with the help of a MATEC pulse modulator & receiver model 6600 with an R.F. plug-in model 755, which covered a frequency range of 1 MHz to 20 MHz. The width of the tone-bursts was controlled by an external custom-built pulse generator. The output of the MATEC generator was connected to two fixed value attenuators totalling 13 dB to reduce the magnitude of the output pulse to the level of the transducer's optimal response. The attenuated pulse was then sent to the generating transducer.

The second set-up used a Fluke digital RF synthesizer model 6060B as a generator. This system is characterized by an outstanding stability due to its internal 10 MHz crystal oscillator, which is kept in a temperature-controlled oven. The device can generate continuous waves in a wide frequency range from 0.01 MHz to 1050MHz, and in an amplitude range from -127 dBm to +13 dBm. To produce square pulses, a Stanford digital delay generator DG535 was used. The generator had four adjustable output channels, A to D. With individual channels set appropriately, the XOR output signal of a square shape could be produced. The Stanford generator used the output CW wave from the Fluke as an external trigger, which ensured no phase drift between the CW signal and the envelope. To produce this trigger signal for the Stanford generator, the output CW wave was split by a power splitter (Merrimac PDM-20-250, with 50 Ω input and output impedances). One part of the split signal was used as a trigger signal for the Stanford

generator, which then produced a square envelope. The output signal from the Stanford generator along with the second part of the split CW signal were sent into mixers, which performed the actual shaping of the CW wave into a square pulse. Three Mini-Circuits ZAY-3 mixers, connected in series to minimize leakage of the CW signal, were used. To fully excite the generating transducer, the square pulse was amplified by the Amplifier Research model 250L power amplifier. In continuous mode its power output was 250 watts over a wide frequency range from 0.01 to 220 MHz.

The last generating set-up used an Agilent 33220A arbitrary waveform generator (AWG) to produce input pulses. This generator was capable of generating pulses of different shapes (e.g. sine, square, triangle, etc.) in different modes (continuous, burst) over a wide span of frequencies from 1 μ Hz to 20 MHz, with peak-to-peak magnitude ranging from 10 mV to 10 V. The AWG also had a GPIB remote interface, which allowed programming the generator to produce pulses of any desired shape in addition to the above mentioned built-in pulse shapes. In my experiments, the AWG was programmed to produce a narrow (in the time domain) Gaussian pulse with a specified carrier frequency. The pulse was then amplified by the Amplifier Research amplifier and sent to the generating transducer. Schematic diagrams of all three generating electronics set-ups are shown in Figure 3.3.1.

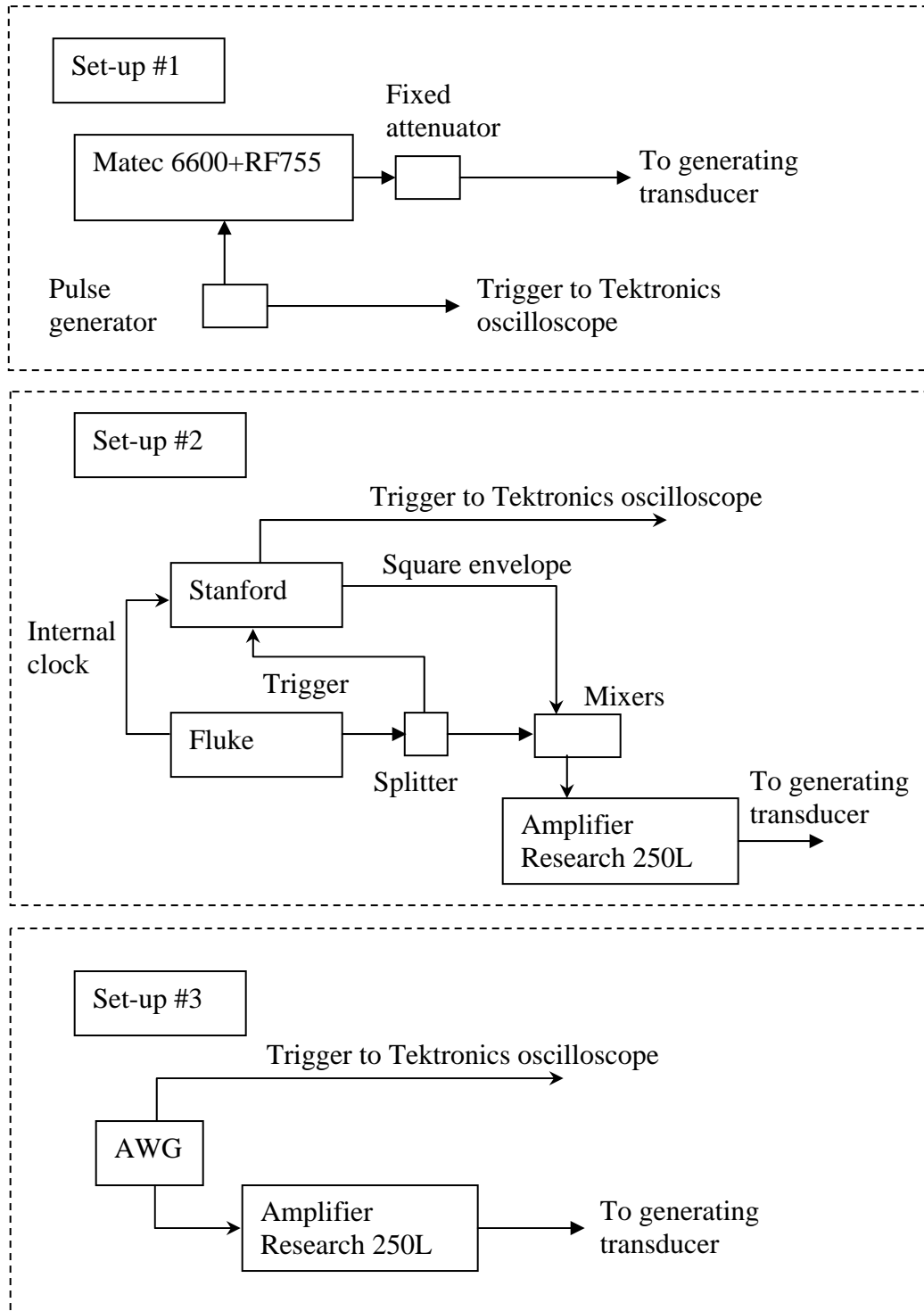


Figure 3.3.1: Three configurations of generating electronics set-ups.

3.3.2 Receiving electronics

The main goal of the receiving setup is to detect, process if necessary, and record output signals. The transmitted signals were detected by ultrasound transducers or a hydrophone, depending on the experiment. These devices will be described in detail in the next section. Processing of the signal chiefly required its amplification and sometimes filtering. Recording the signal ensured that the waveform was saved in a form usable for future analysis.

Before the signal detected by the receiving transducer could be amplified, the signal's magnitude had to be adjusted to avoid saturating the amplifier. This was achieved by inserting a low power, precision Telonic attenuator model 8143S between the transducer and the amplifier, which could be adjusted from 0 to 110 dB in steps of 1dB.

The amplification of the adjusted signals was carried out by three-stage Matec Receiver amplifier model 605, usable in the frequency range from 100 kHz to 25 MHz. At the first stage, a 20 dB broadband (100 kHz – 30 MHz) preamplifier model 253 was used. The second stage adjustable gain (10 to 60 dB) amplifier was not used in the experiments. The final amplification stage provided fixed gain of 24 dB magnitude and was preferred over the adjustable amplifier because of its better noise characteristics.

When needed, high- and/or low-pass Butterworth LC filters were used. For example, a 1.5 MHz low-pass filter was used repeatedly in experiments involving the hydrophone (described in Section 3.4.2) as a detector to remove the high-frequency noise.

After amplification and filtering, the signal was sent to the Tektronics digital oscilloscope model 544A, which is an 8 bit, 1 Giga-sample per second digitizing oscilloscope. The maximum record length is 50,000 points. The scope also has an averaging mode enabling averaging of up to 10,000 consecutive acquired signals. The

GPIB interface of the Tektronics oscilloscope allowed a computer to control the oscilloscope and download waveforms from it. The programs to perform these operations were written in Visual C++ and in MATLAB. Figure 3.3.2 presents a schematic diagram of the receiving electronics configuration.

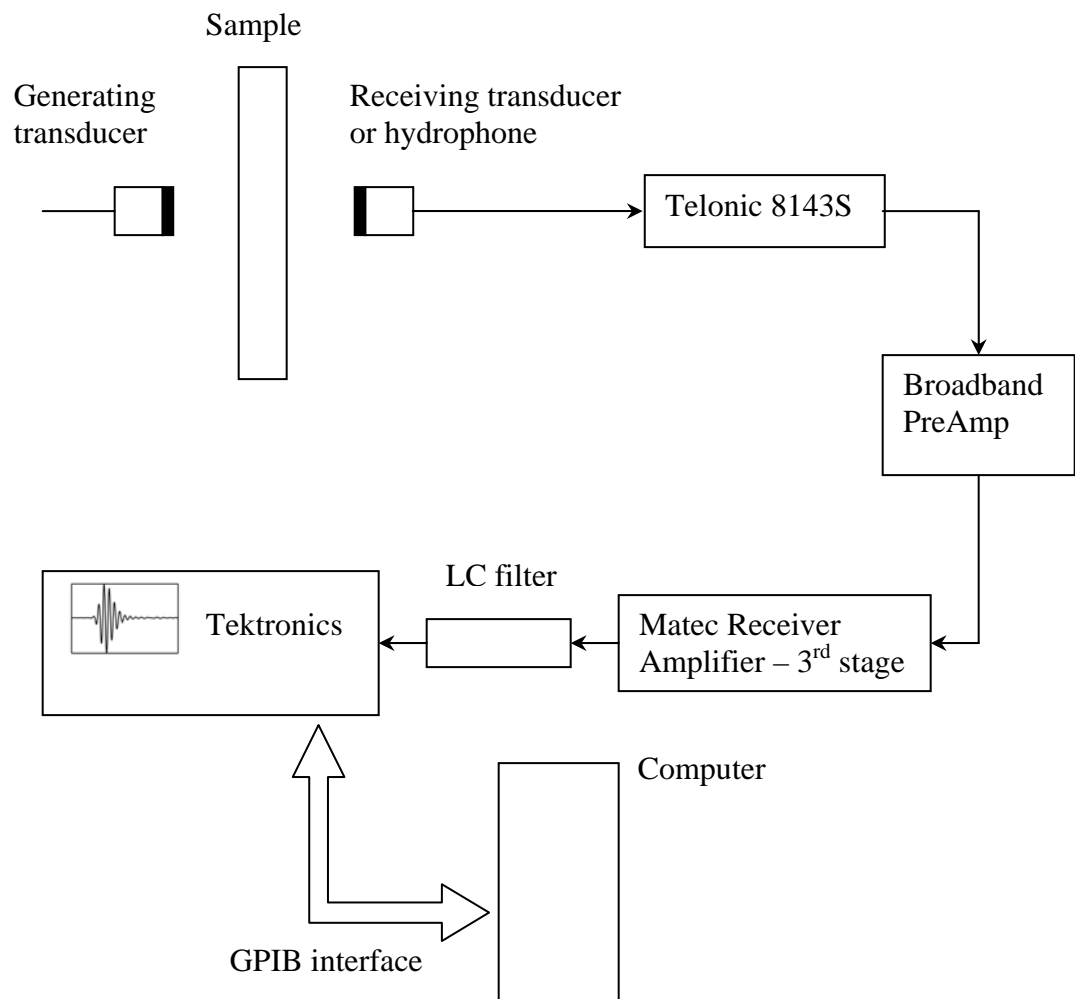


Figure 3.3.2: Receiving electronics set-up.

3.4 Ultrasound generators and detectors

3.4.1 Plane wave immersion transducers

The operation of all ultrasound transducers used in my experiments is based on the well-known piezoelectric effect exhibited by the material from which the transducer is made. When a sound wave is incident on such a material, its crystal lattice is deformed by the oscillatory pressure fluctuations, producing a periodic electric field inside the material, which is proportional to the average pressure field across the face of the piezoelectric crystal. The reverse also holds true, i.e. the crystal lattice is deformed when an electric field is applied to a piezoelectric material. Thus, transducers can be used both to detect and generate acoustic waves.

In most of the experiments, incident plane ultrasound waves were created by flat circular immersion transducers produced by Panametrics INC, which had PZT (lead zirconium titanate) as the piezoelectric material. The basic design of such a transducer is explained in Figure 3.4.1. The main part of the transducer is a thin disk of PZT, which is responsible for generation and detection of ultrasound waves. Upon application of the electrical field, PZT generates ultrasound vibrations that propagate in all directions away from the disk. The thickness of the disk is chosen to be half the wavelength of ultrasound at the central operating frequency of the transducer, since this condition ensures constructive interference of multiple echoes inside the PZT. However, due to high impedance mismatch between the piezoelectric material and the surrounding medium, one cannot use it effectively by simply immersing it into water, as strong reflections of generated ultrasound would occur at the PZT-water interfaces. Also, since PZT is not a highly attenuating material, multiple reflections inside the disk will significantly increase

the length of the pulse in time. This effect is known as ringing of the transducer. To remove this problem a highly attenuative material with impedance comparable to the piezoelectric material is glued on the rear side of the active layer. This backing material absorbs the ultrasound waves transmitted through its interface with the PZT disk, thus significantly reducing its ringing. The problem of strong reflection due to impedance mismatch at the front face of the PZT layer is solved by introducing a matching layer. Its impedance is between that of the active element and water and its thickness is chosen to be a quarter of a wavelength. Because there is a π phase shift acquired upon reflection at the interface with the active layer, and no phase shift at the interface with water, multiple reflections inside the matching layer interfere constructively and enhance the coupling between the transducer and the water.

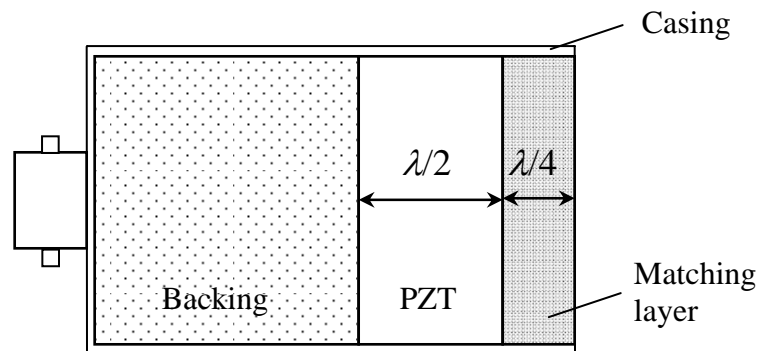


Figure 3.4.1: Diagram showing plane wave transducer design.

The spatial pattern of the transducer field can be calculated with the well-known Rayleigh integral [78]. For the purposes of the calculation, the transducer is approximated as a thin disk radiator of radius a , immersed in liquid (water in our case) and oscillating

uniformly with the speed $U_0 \exp(i\omega t)$ directed along the normal to the surface of the disk.

Figure 3.4.2 shows the geometry used in the calculations.

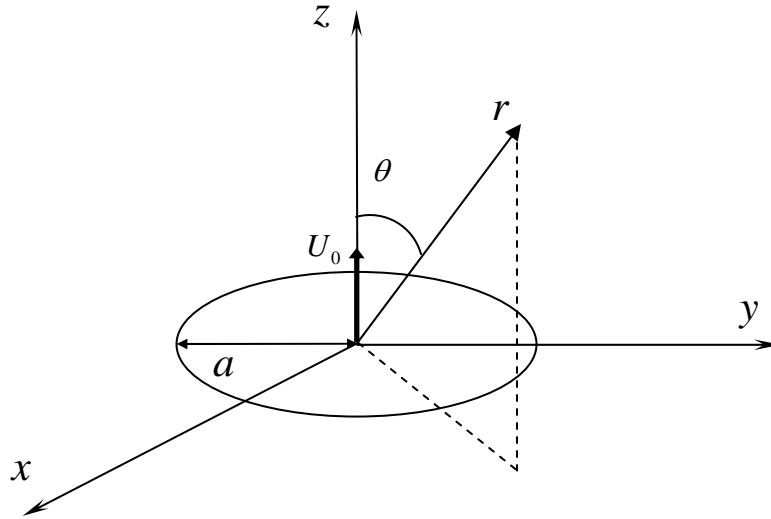


Figure 3.4.2: Geometry used for calculation of the field produced by a circular piston oscillating uniformly in the x - y plane.

The magnitude of the pressure on the axis of the disk (i.e. along the z -axis) is given by the following expression [80]:

$$P(z) = 2\rho_0 c U_0 \left| \sin \left\{ \frac{k}{2} \left[\sqrt{a^2 + z^2} - z \right] \right\} \right| \quad (3.1)$$

where ρ_0 is the density, c is the phase velocity of sound and k is the wavevector in water.

The ratio $|P/(2\rho_0 c U_0)|$ is plotted in Figure 3.4.3 for a half-inch diameter transducer at 1 MHz.

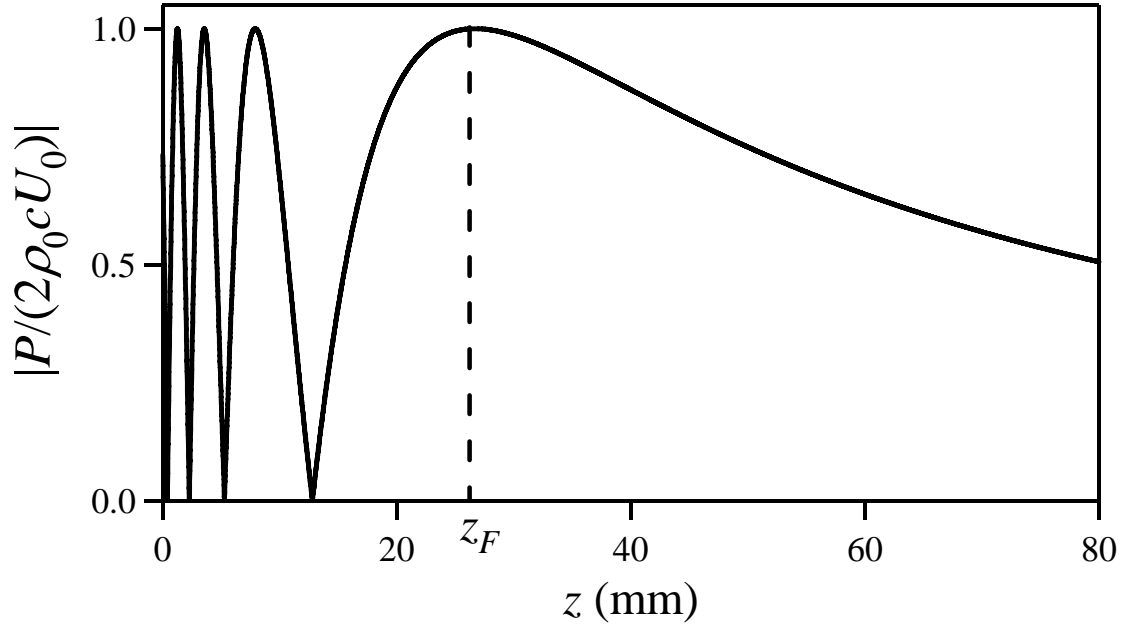


Figure 3.4.3: Thin disk radiator pressure along the z -direction.

In the near-field (Fresnel zone) the pressure is rapidly oscillating due to strong interference of the waves emitted from different points on the disk. In the far-field (Fraunhofer zone) the behaviour changes to a smooth curve slowly decreasing with the distance. The near-field distance z_F is defined as the position of the last maximum in the pressure and is given by the expression:

$$z_F = \frac{a^2 - \frac{\lambda^2}{4}}{\lambda} \quad (3.2)$$

which reduces to:

$$z_F = \frac{a^2}{\lambda} \quad (3.3)$$

when $a \gg \lambda$. Because of these rapid field fluctuations, samples were always positioned in the far-field of the transducers.

In the far-field ($z > z_F$) the off-axis intensity of the transducer field is represented by a spherical wave modulated by a directivity factor, which is represented by the ratio of the Bessel function of order one $J_1(x)$ to its argument [80]:

$$I \propto \frac{1}{r^2} \left[\frac{2J_1\left(\frac{2\pi}{\lambda} a \sin \theta\right)}{\frac{2\pi}{\lambda} a \sin \theta} \right]^2 \quad (3.4)$$

The shape of the directivity factor in (3.4) closely resembles the one of the sinc function [Figure 3.4.4], which is appropriate for a line source.

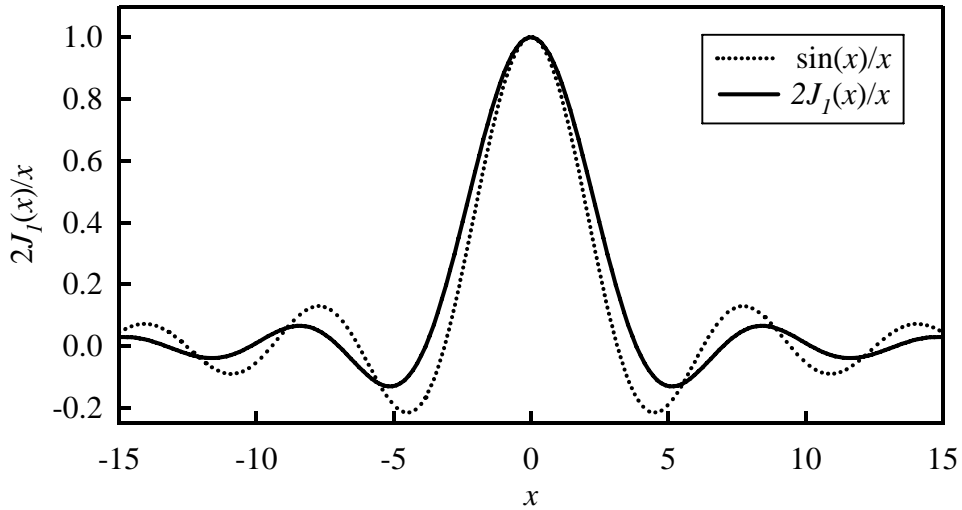


Figure 3.4.4: Directivity factor $J_1(x)/x$. Plot of the sinc function $\sin(x)/x$ is also shown for comparison.

With the help of (3.4), a -6 dB beam divergence angle θ_D (corresponding to the angle at which the intensity drops to half its maximum value at $\theta = 0$) can be defined:

$$\sin \theta_D = \frac{0.257\lambda}{a} \quad (3.5)$$

as explained in Figure 3.4.5.

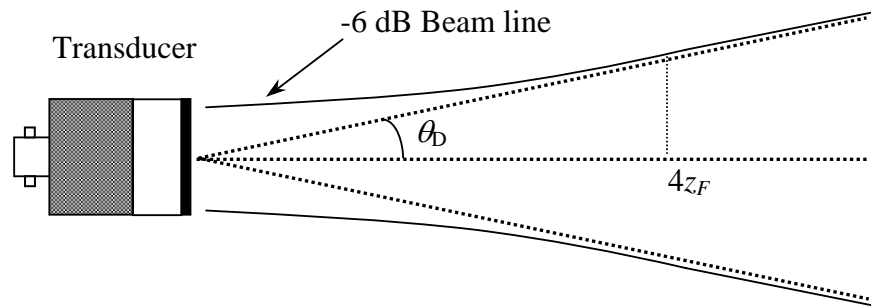


Figure 3.4.5: Transducer beam pattern.

3.4.2 Hydrophone

In some of the measurements a hydrophone produced by Specialty Engineering was used to detect the ultrasound waves instead of Panametrics transducers. The hydrophone is essentially a miniature transducer with the PZT element diameter of 400 μm , which is comparable to the wavelength of the sound wave in water for a frequency of about 4 MHz. Because the active element was so small, the magnitude of the signal produced by the hydrophone is also very small so it was never used for generation of ultrasound. However, for the same reason of small size, the hydrophone was the best candidate to detect ultrasound waves in negative refraction and focussing experiments, which involved mapping of the sound field emerging from the phononic crystals in a rectangular grid pattern. These experiments were conducted in the frequency range from 0.50 to 1.0 MHz with the wavelength in water ranging from 3 to 1.5 mm. At such frequencies the size of the hydrophone's detecting element (0.4 mm) allowed imaging of the individual ripples in the outgoing pulses. This would be impossible to achieve with

regular plane wave Panametrics transducers, the smallest active element of which was 12.7 mm (half an inch) in diameter in this frequency range. Phase and amplitude cancellations of the average field measured by the large diameter transducer would lead to the loss of the fine details of the sound field. Since the PZT element of the hydrophone was very thin, the resonant frequency of the hydrophone was much higher than the frequency of interest in my experiments resulting in a weak but very broad band response to the incident waves. To amplify the detected signal amplitude a 15 dB preamplifier was always used with the hydrophone.

3.4.3 Pinducer

A pinducer is a circular transducer with its active element's diameter larger than the one of the hydrophone but significantly smaller than any of the Panametrics transducers. The pinducer used in my experiments was made by Valpey Fisher. The PZT element of the pinducer was secured inside metal tubing, which had an outer diameter of 2.4 mm. The precise diameter of the pinducer's active element was not known, but from the analysis of the field produced by the pinducer its effective diameter was estimated to be about 2.2 mm. The details of this analysis are presented in Appendix A. As the effective size of the pinducer was found to be about equal to or even smaller than the wavelength of sound in water at frequencies up to 1 MHz, it served as a good approximation to the point source and was used in some of the experiments on imaging by the rectangular-shaped phononic crystal.

3.4.5 Line source transducer

It will be explained later in Chapter 5 that during the experiments on the imaging of point sources with the rectangular-shaped 2D crystal the need arose to use a sound source of even smaller size than the pinducer. To this end I have built several transducers

in the shape of the narrow strips. This choice of a shape is dictated by the idea of obtaining a line source, which is essentially a 2D point source and thus particularly well suited to experiments on sound focussing by 2D phononic crystals. As a material for the transducer, polyvinylidene fluoride (PVDF) polymer was used. This material is known to exhibit the piezoelectric effect. The polymer, supplied by Pennwalt Corporation, Kynar Piezo Film Department, was cast in sheets with gold film evaporated on both surfaces. The thickness of each sheet was only 110 μm , which made it very easy to cut into pieces of any desired shape. As the resonant frequency of a single sheet was around 10 MHz, five PVDF strips were glued together with a tiny amount of low viscosity epoxy, which lowered resonant frequency of the whole piece to the required value of about 0.5 – 0.6 MHz. The best transducer built in this way and used in focussing experiments with a methanol filled 2D crystal was 35 mm long, 0.58 mm thick and 0.55 mm wide, which is about 20 % of the sound wavelength in water (2.7 mm at 0.55 MHz). Once all pieces were glued together, both surfaces of the strip were covered with a thin layer of epoxy to waterproof the conducting surfaces, leaving two clean spots at the ends of each surface of the strip for electrical contacts to be attached. Because the irradiating area was so small, one of the greatest challenges was to obtain an appreciable magnitude signal from the transducer. The problem was aggravated by the impedance mismatch between the transducer and the amplifier, which prevented all the power to be delivered to the transducer. The impedance mismatch problem was solved by building an impedance matching transformer, which basically consisted of two coils wound on the same commercially available circular-shaped core made of ferrite. One coil was connected to the strip transducer while the other one was connected to the amplifier. The amount of

turns in transducer coil was 100 while the coil connected to the amplifier had 15 turns. The particular numbers of turns in each coil were found by the method of trial and error and produced the largest amplitude signals. Figure 3.4.6 shows schematic design of the strip transducer and the impedance matching transformer. Figure 3.4.7 is a picture of the strip transducer sitting in a specially designed holder.

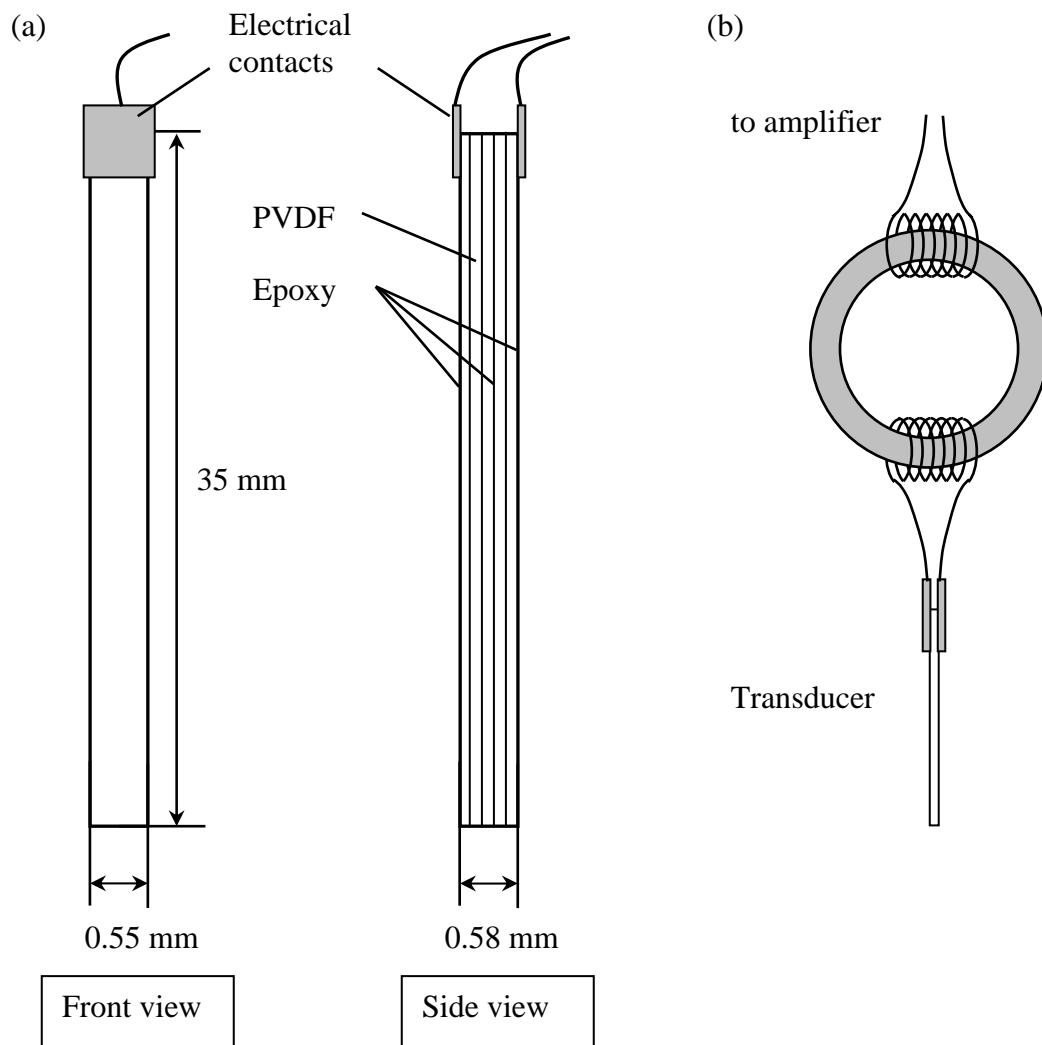
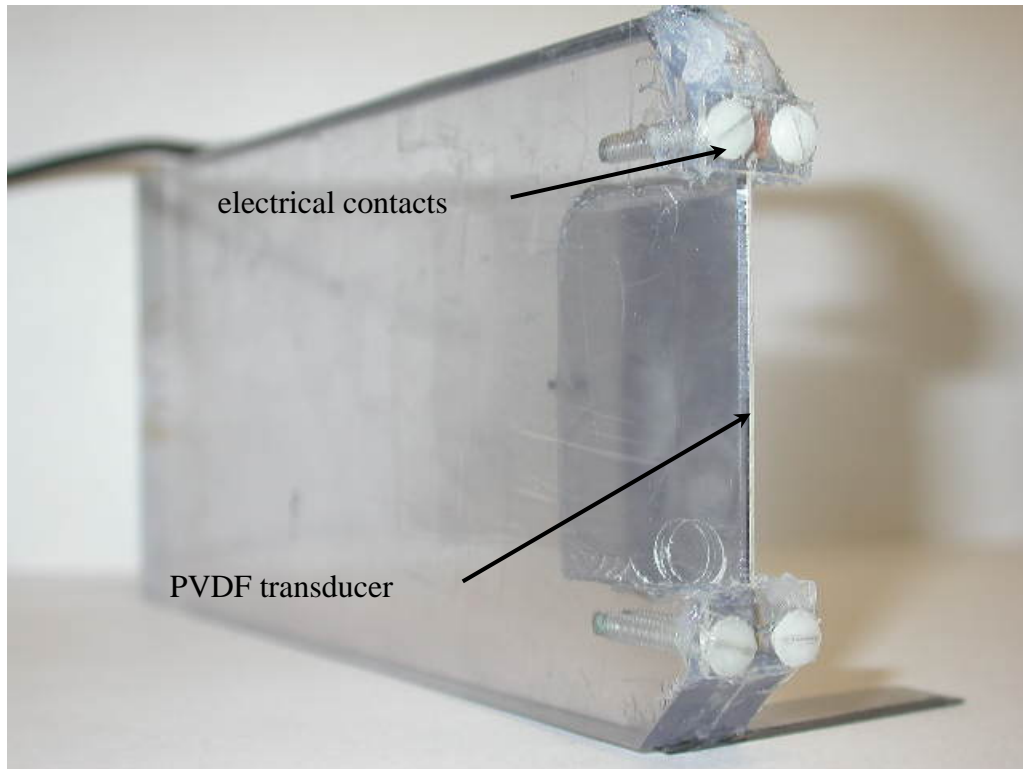


Figure 3.4.6: PVDF transducer: (a) Basic design and actual dimensions. (b) Schematic diagram of an impedance matching transformer.

(a)



(b)



Figure 3.4.7: PVDF transducer holder with the transducer in place.
(a) General view. (b) Close-up.

3.5 Measurements

All the experiments described in this thesis, independent of the samples probed, are similar to each other as they all consisted of three basic steps, namely: the generation of an ultrasound pulse, its propagation through the sample and the investigation of an outgoing pulse or, more generally, of the sound field after the input pulse has emerged on the output side of the sample. The differences between experiments came from the way the first and last steps were realized. Generally speaking, all experiments could be divided into two major types: transmission experiments and experiments on the mapping of the entire sound field emerging from the sample. This section describes both types of experiments. It also explains how the acquired data were analyzed and what information could be extracted from each measurement technique.

3.5.1 Transmission experiments

In all transmission experiments I have measured ballistic pulses emerging from the output side of the sample after a short Gaussian pulse was normally incident on the other side of the sample. I have used flat circular immersion Panametrics transducers for generation as well as detection of ultrasound pulses. To ensure the best possible approximation of the incident pulse by a plane wave, samples were placed in the far-field of both generating and receiving transducers. One of the most important parts of any ultrasonic experiment is a proper alignment of the transducers and the sample with respect to one another. Extra care was taken before beginning measurements to establish parallelism between surfaces of each transducer and the sample, which guaranteed normal incidence of the input pulse on the sample surface. In addition to the parallelism, the alignment of the transducers with respect to each other was also checked. The geometries

of the actual experiments with 3D and 2D crystals were already discussed in Sections 3.2.1 and 3.2.2. In the course of the experiments, several waveforms were recorded as the sample was moved slightly with respect to fixed transducers, allowing for pulses propagating through different parts of the sample to be recorded. The acquired pulses were then averaged to reduce the influence of the imperfections unavoidably present in any of my phononic crystals.

To analyze recorded sample pulses properly one also needs a reference pulse. In my case the reference pulse was obtained by recording a pulse with the sample removed from the experimental set-up. For 2D crystals the reference pulse propagated through just plain water, while for 3D crystals the sample was substituted by an acrylic or polyethylene block of thickness identical to the thickness of the base of the template supporting the crystal beads (see Section 3.1.2). The recorded pulse was not exactly the same as the input pulse, but as all my samples were very thin (1.5 cm at most), the attenuation of the pulse in water could be neglected, and the input pulse was obtained by time shifting the reference pulse by an amount $\Delta t = L/v_{wat}$, where L is the sample thickness and v_{wat} is the speed of sound in water. Figure 3.5.1 shows typical input and transmitted pulses for a double 3D crystal, each crystal having 4 layers of beads. Because the central frequency of the input pulse was chosen to lie in the range of frequencies corresponding to the complete band gap of the single crystals, the amplitude of the transmitted pulse is reduced by as much as three orders of magnitude compared to the input pulse. For representation purposes the input pulse was normalized to unity and the transmitted pulse was normalized by the same scale factor. The sample pulse also extends much longer in time due to multiple reflections inside the cavity (aluminum spacer) between the two crystals.

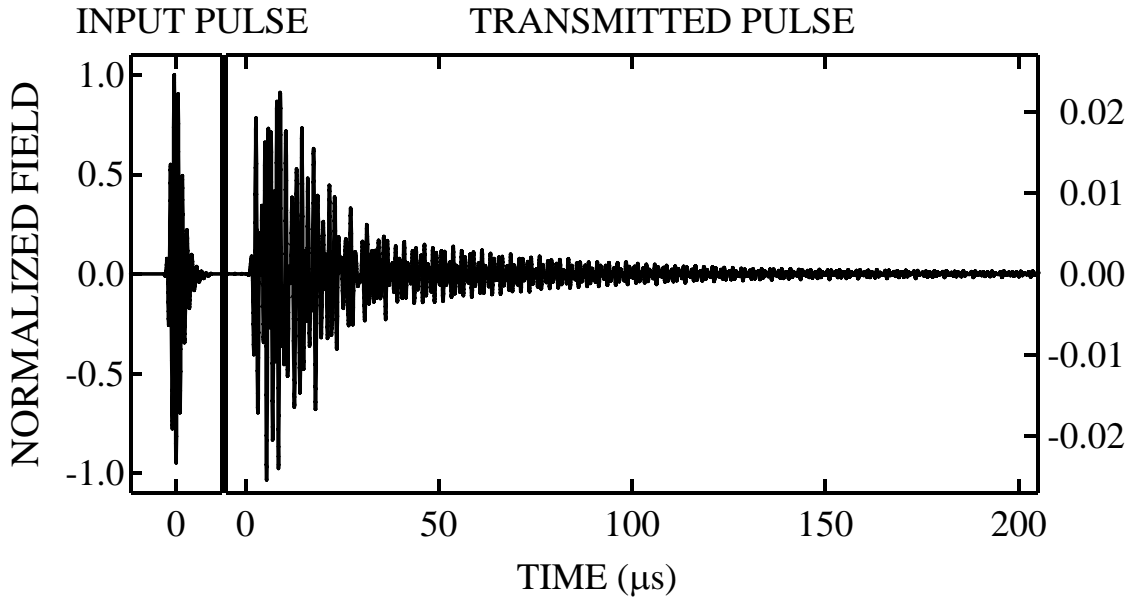


Figure 3.5.1: Input and transmitted pulses through a 3D double phononic crystal, each crystal having 3 layers. The vertical scales for the input and transmitted pulses are on the left and on the right respectively.

There are several physical quantities that I was able to measure by analyzing the transmission experiments. As suggested by the very name of the experiment, a transmission experiment provides information on the transmission coefficient through the sample. Since any pulse is actually a collection of single frequency plane waves with properly chosen magnitudes and phase shifts, one can obtain the transmission coefficient as a function of frequency. To this end, the Discrete Fourier transforms (DFTs) of the input and sample pulses were first calculated in IGOR data analyzing software. To calculate DFT, IGOR uses a Fast Fourier Transform (FFT) technique based on a prime factor decomposition algorithm. In order to increase frequency resolution of the resulting DFTs and to speed up the calculations, the original waveforms were padded with extra zeros to bring the total number of points to the integral power of 2 (2^n). The typical total

number of points in the waveform after zero padding was 2^{12} , but in some cases as many as 2^{14} points were used. The amplitude transmission coefficient for each frequency is given by the ratio of the magnitudes of DFTs of the sample and input pulses:

$$T(f) = \frac{A_{trans}(f)}{A_{ref}(f)} \quad (3.6)$$

Of course, meaningful results are obtained only in the frequency range corresponding to the bandwidth of the input pulse. FT amplitudes of the input and transmitted pulses from Figure 3.5.1 are shown in Figure 3.5.2, while the corresponding amplitude transmission coefficient, which was calculated according to expression (3.6), is presented in Figure 3.5.3.

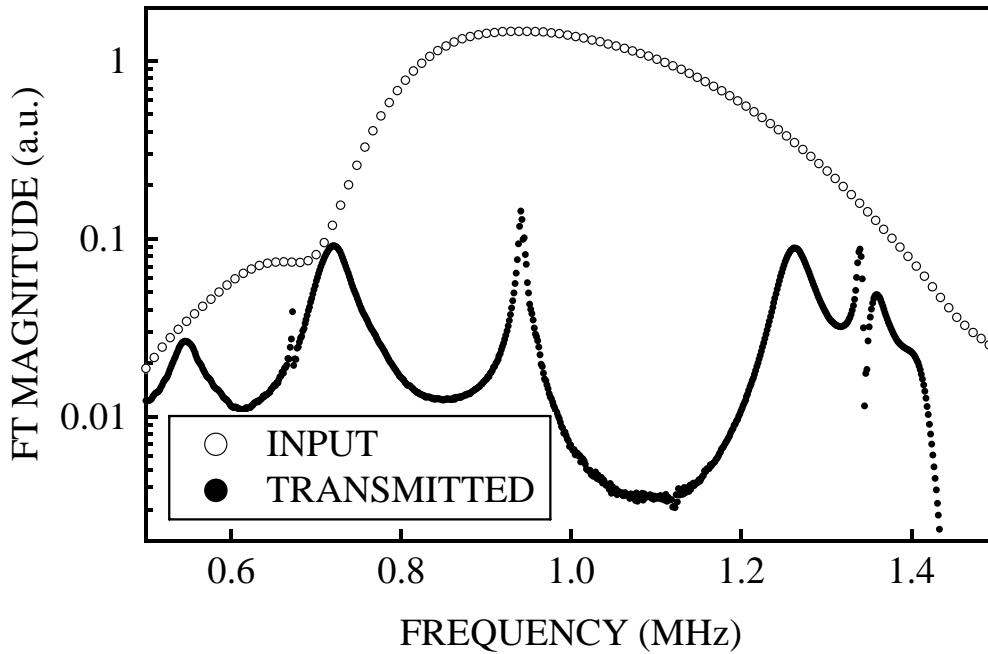


Figure 3.5.2: Fourier Transform magnitudes of the input and transmitted pulses shown in Figure 3.5.1.

The drop in transmission from about 0.70 MHz to 1.3 MHz is brought about by the single crystal's band gap. Transmission coefficient also exhibits a peak in the middle of the band gap at about 0.94 MHz, which is due to the resonant tunnelling of the incident pulse through the double crystal. Position of the peak is basically determined by the thickness of the aluminum spacer, as the resonant tunnelling occurs when cavity thickness equals an integer number of half the wavelength of the sound wave inside the cavity. This effect will be described in detail in Chapter 4. It is also worthwhile noting the excellent signal-to-noise ratio that is evident in Figure 3.5.3. Noise reduction was achieved by signal averaging many consecutive pulses using the "Average Mode" of the Tektronix oscilloscope. For example, the signal displayed in Figure 3.5.3 was obtained by averaging a maximum number of 10,000 consecutive waveforms. The minimum signal recorded in this figure is significantly larger than the minimum sensitivity of the equipment, which has enabled amplitude transmission coefficients as small as 10^{-7} to be measured [69].

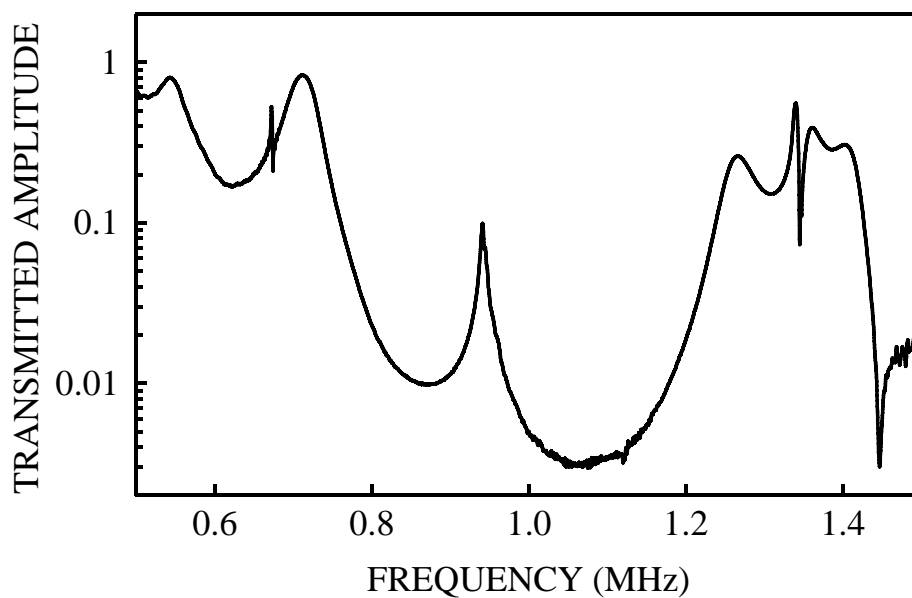


Figure 3.5.3: Transmission coefficient through the 3D double phononic crystal obtained by analyzing the input and transmitted pulses shown in Figure 3.5.1.

In addition to the transmission coefficient, ballistic pulse measurements can also provide information on the phase velocity v_{phase} of sound in the sample and eventually allow the dispersion curve to be obtained. This is achieved by analyzing the cumulative phase difference $\Delta\phi$ between sample and input pulses. This phase difference is given by:

$$\Delta\phi = kL = \frac{2\pi L}{v_{phase}} f \quad (3.7)$$

where L is the sample thickness. From (3.7) it is possible to obtain phase velocity as function of frequency. The ambiguity of 2π can be eliminated by making measurements at sufficiently low frequencies, since the phase difference must approach zero as frequency goes to zero. Expression (3.7) also allows the dependence of the circular frequency ω on the wavevector k , conventionally known as the dispersion curve, to be determined.

The last quantity to be obtained from transmission measurements is the group velocity. By its definition the group velocity is a velocity with which a wave packet travels as a whole. Since the transmitted pulse may get distorted from its original Gaussian shape as it passes through the sample, especially if the pulse bandwidth is wide, the group velocity may lose its meaning in this case [66]. Since I performed my experiments with the pulses of very wide bandwidths, the group velocity could not be generally determined from the sample pulse directly. However, it is still possible to recover two essentially Gaussian pulses by digitally filtering input and output pulses with a narrow Gaussian bandwidth centred at the frequency of interest. The group velocity at that frequency is then found by the ratio of the sample thickness L to the time delay Δt_g between two filtered pulses:

$$v_g = L/\Delta t_g \quad (3.8)$$

This procedure is illustrated by Figure 3.5.4, which shows pulses from Figure 3.5.1 filtered at the central frequency of 0.60 MHz with the bandwidth of 0.01 MHz. The delay time is also indicated. Obviously, by repeating the procedure for different frequencies, the frequency dependence of the group velocity can be found.

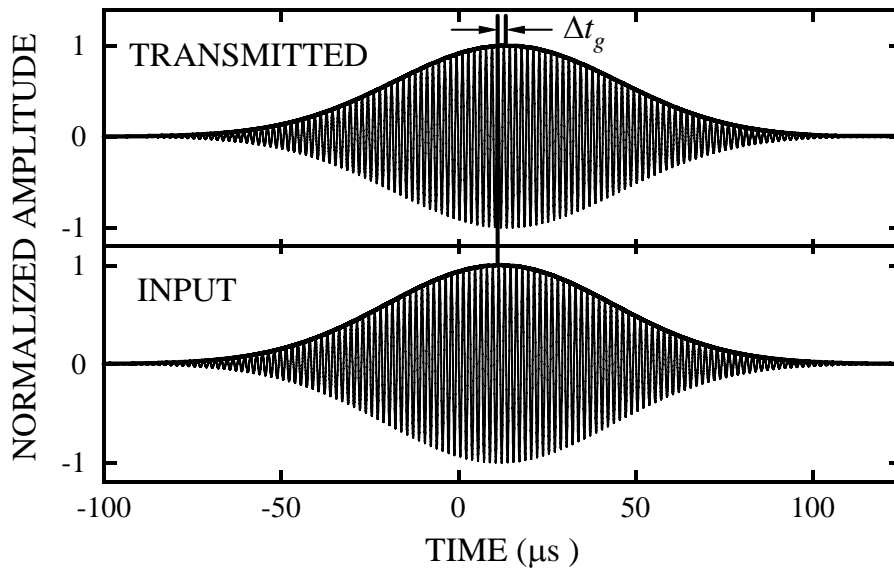


Figure 3.5.4: Group velocity calculation from the time delay measured between filtered input and transmitted pulses.

3.5.2 Field mapping experiments

As was already mentioned, in all of the transmission experiments a flat circular Panametrics transducer was used as a receiver. The diameter of the transducer (usually 1 inch) was much larger than the ultrasound wavelength in water, so that recorded field was, in fact, the average field across the face of the transducer's PZT element. In this way one

loses some details of the field, when it is not uniform spatially. It is not a problem in the transmission experiments in which one is interested in the coherent field, i.e. the field that is spatially uniform in a plane parallel to the sample faces. Another benefit of such averaging is a reduction of the noise in the signal. However, in the negative refraction and sound focusing experiments, the exact spatial distribution of the emerging field is what was of interest. For this reason, large diameter transducers could not be used in those experiments. To resolve subwavelength details and map the field accurately one needs to resort to a sound detector with physical dimensions less than a wavelength. A hydrophone with an active element diameter of 0.4 mm clearly satisfied this condition (since in all experiments involving mapping of the outgoing field sound wavelength in water ranged from 1.5 to 3.0 mm) and was exclusively used as a detector. Depending on the experiment, a flat Panametrics transducer, the pinducer, or the line source transducer were used as generators of input pulses.

In actual mapping experiments, the sound field was measured at every point of a rectangular grid, which involved mounting the hydrophone in a 3D motorized translation stage (see Section 3.2.2). The plane of the grid was perpendicular to the rods, intersecting them in their mid-points. To resolve all the essential features of the field, the distance between grid points was set at either 0.5 mm or 1.0 mm.

The net result of the experiment is a large number of data files, one file for each grid point. These files were later used to create image plots of the fields. The analysis of the acquired waveforms was done in either the time or frequency domain.

In the time domain type of analysis, the value of the field at each grid point was read at some particular time and then used to create an image plot, which was essentially a snapshot of the field. By creating several image plots for different times, one can also

investigate a time evolution of the transmitted pulses. In other words, it is possible to visualize the pulse from the moment it emerges from the sample's output surface till the time it leaves an area covered by the grid. This visualization is very helpful, as image plots can immediately tell if the outgoing pulse was refracted negatively or positively. Image plots also allow the direct measurement of the refraction angle since, by reconstructing the spatial distribution of the wave field, the wave fronts are clearly displayed. Since the refraction angle was expected to be strongly frequency dependent, its frequency dependence was investigated by initial digital filtering of each waveform with a narrow (usually 0.05 MHz) Gaussian bandwidth centred at the frequency of interest (see Section 3.5.1), which gives long (in the time domain) Gaussian pulses. These filtered pulses were then used to create image plots.

In the frequency domain picture, the analysis procedure was similar to the previous one except that first the Fast Fourier transforms of the acquired waveforms were calculated. After that, magnitudes of each FT were read at a single frequency and their values were used to make the image plot. The image plot in this case represented an amplitude map (proportional to the square root of intensity), which would be obtained from the field plot if continuous monochromatic wave were used as an input signal instead of a pulse.

To finish the discussion of the analysis part, two sample image plots are presented. The image plot in Figure 3.5.6 is obtained while analyzing one of the experiments on negative refraction with the prism-shaped 2D crystal. A typical picture produced in the focusing experiment with rectangular-shaped 2D crystal is shown in Figure 3.5.7. Since the hydrophone sensitivity is uncalibrated, the colour scales of both image plots are in arbitrary units, which correspond to the voltage measured on the oscilloscope.

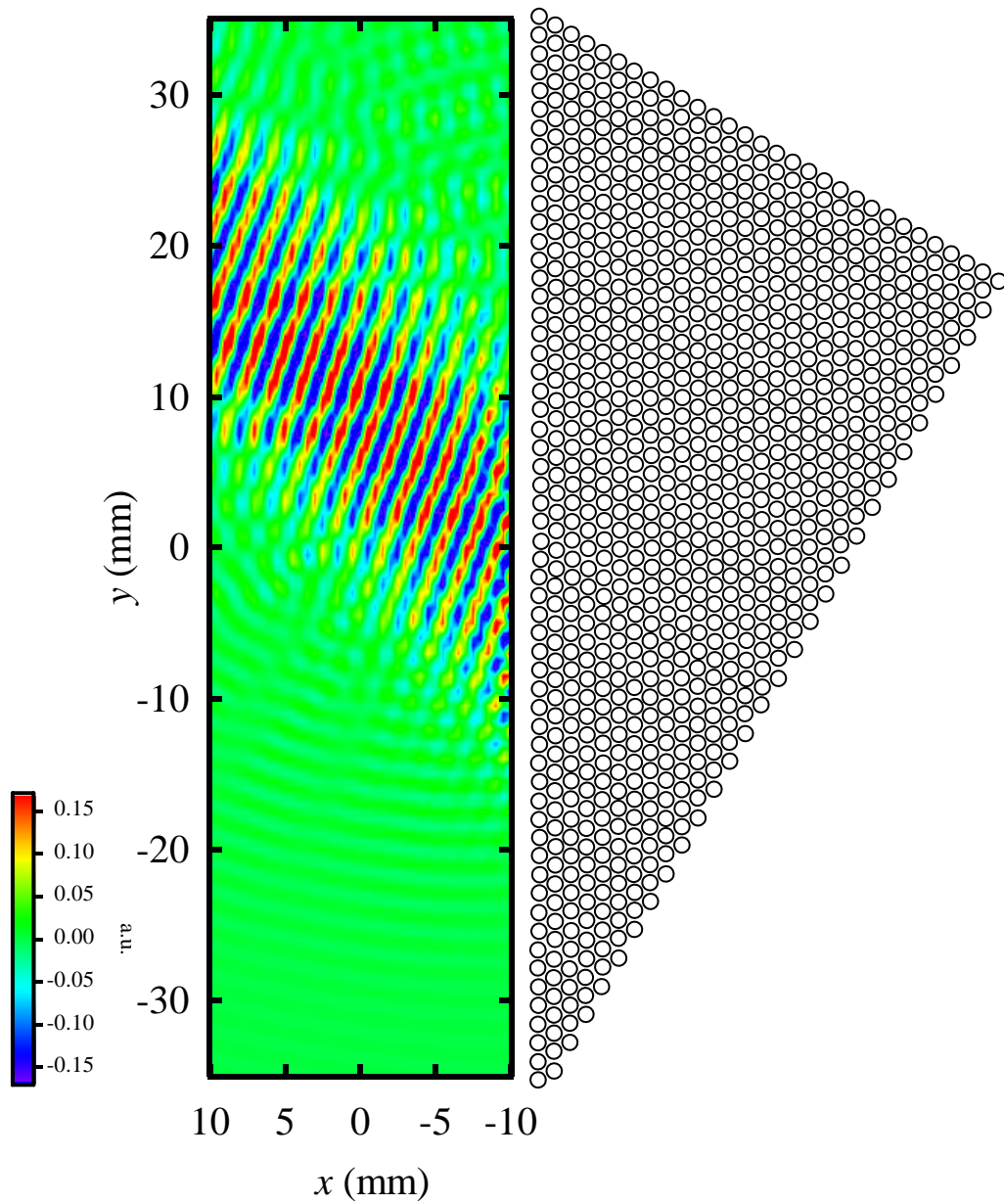


Figure 3.5.5: Sample image plot of the outgoing pulse in the negative refraction experiment with the prism-shaped 2D crystal. Original waveforms were filtered with the Gaussian bandwidth of 0.05 MHz centered at 0.85 MHz. The crystal is also shown.

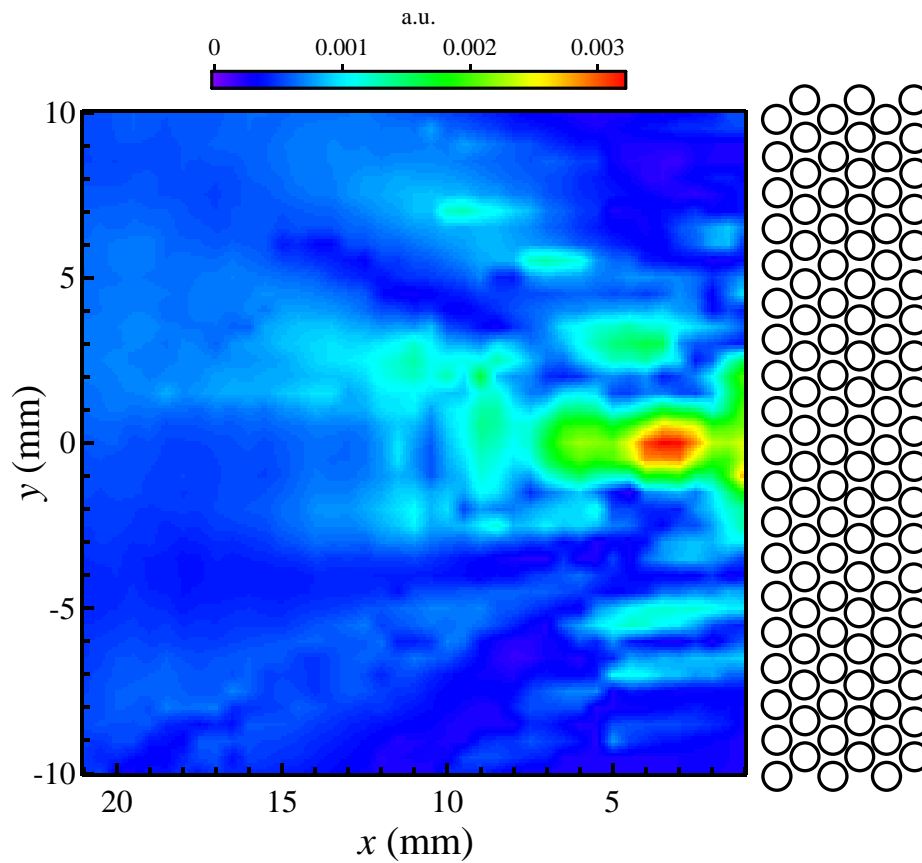


Figure 3.5.6: Sample image plot showing field amplitude distribution at the frequency of 0.54 MHz produced in the focusing experiment with the rectangular-shaped 2D crystal. The crystal is also indicated.

4. Experiments with 3D phononic crystals

This chapter is devoted to the experiments with 3D phononic crystals. (Section 3.1.2 provides a detailed description of the samples used in the experiments). The main purpose of this chapter is to present the results of the resonant tunnelling experiments through a double barrier consisting of two 3D phononic crystals separated by a cavity, which for brevity will be referred to as a *double* phononic crystal later on (as opposed to a regular *single* phononic crystal). The chapter starts by describing experiments to investigate the properties of single 3D phononic crystals and continues with the subsequent description of the resonant tunnelling experiments.

4.1 Properties of single 3D phononic crystals

This section provides a brief description of the transmission experiments through the single 3D phononic crystals. These experiments let me verify some of their major properties such as the existence of the spectral band gaps and the linear increase of the group velocity with the sample thickness for the pulses transmitted through the crystal at the band gap frequencies.

4.1.1 Transmission spectra of single 3D phononic crystals

To better understand results of the resonant tunnelling experiments with double phononic crystals, it is worthwhile to review briefly the properties of single crystals, which were already extensively studied by Suxia Yang *et al.* [29]. The main purpose for the experiments described below was to ensure that single crystals, which comprise a double crystal, exhibit behaviour consistent with that reported by Yang *et al.* and were of good quality.

As was already explained in Section 3.1.2, my 3D phononic crystals were made of very monodisperse tungsten carbide spheres (0.800 mm in diameter) immersed in water. Spheres were assembled in an FCC crystal lattice so that the normal to the crystal surface was along the [111] direction. According to the band structure calculated with the help of the Multiple Scattering Theory (MST), which was described in Section 2.1.3, a *complete* band gap exists for the range of frequencies between 0.98 and 1.20 MHz, which is indicated on the plot by a shaded area [Figure 4.1.1]. The *widest* part of the band gap is along the [111] (or the ΓL) direction and extends from 0.80 MHz to 1.20 MHz.

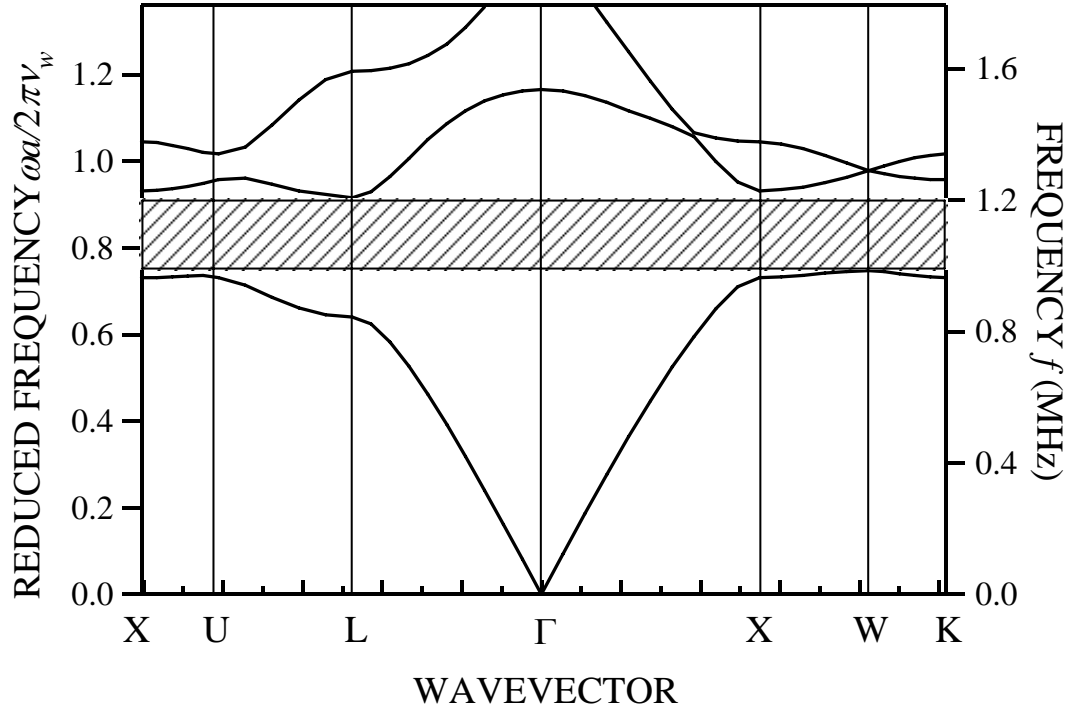


Figure 4.1.1: Band structure of the 3D phononic crystal made of tungsten carbide spheres immersed in water and assembled in an fcc crystal lattice. Reduced frequency is given in units of $2\pi\nu_w/a$, where ν_w is the speed of sound in water and a is the lattice constant; note that $a = d\sqrt{2}$, where d is the diameter of a single sphere. (Calculations courtesy of Dr. Zhengyou Liu).

The predictions of the MST have previously been shown [29] to give an excellent description of the band structure and transmission coefficient for this phononic crystal. Figure 4.1.2 presents the transmission coefficient as a function of frequency for 2-, 3- and 4-layer 3D phononic crystals. The frequency at the minimum in the transmission coefficient agrees well with the central frequency of the stop band along the ΓL direction, as displayed in Figure 4.1.1. However, the edges of the stop band seen in the transmission coefficient (Figure 4.1.2) do not agree exactly with those predicted by the MST band structure (Figure 4.1.1), a result that is not surprising since the band structure is calculated

for an infinite crystal, while the samples have a finite number of layers. As expected, the drop in the transmission caused by the band gap becomes deeper with increasing thickness of the crystal.

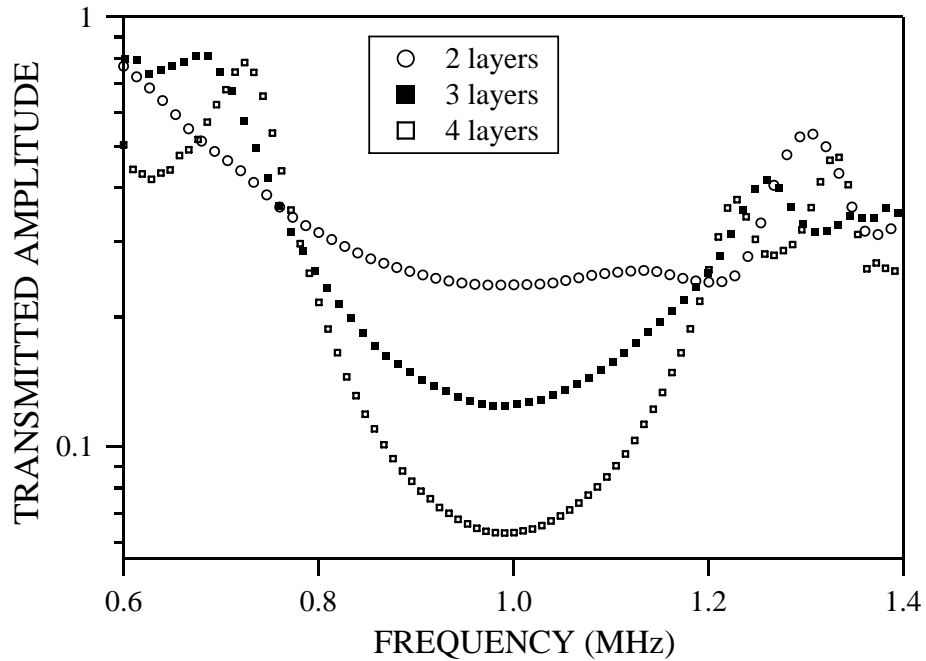


Figure 4.1.2: Transmission coefficient through 2-, 3- and 4-layer single 3D phononic crystals as a function of frequency.

4.1.2 Tunnelling of ultrasound pulses through single 3D phononic crystals

Yang *et al.* [29] also demonstrated that for frequencies corresponding to the complete band gap ultrasound pulses propagate through phononic crystals via tunnelling, an effect analogous to the tunnelling of a quantum mechanical particle through a potential barrier. This conclusion was based on the fact that in their experiments the group velocity was found to increase linearly with the thickness of the crystal, which also means that the pulse transit time (or group time) remained essentially constant for all samples. This behaviour is in analogy to the prediction by Hartman [28], who showed that the group time of the electron through a potential barrier is independent of the barrier thickness.

The group velocity dependence on the sample thickness observed in my experiments is very similar to the previous findings of Yang *et al.* (see Section 3.5.1 for the details on how the group velocity was determined). Figure 4.1.3 displays group velocity as a function of frequency for 2-, 3- and 4-layer samples.

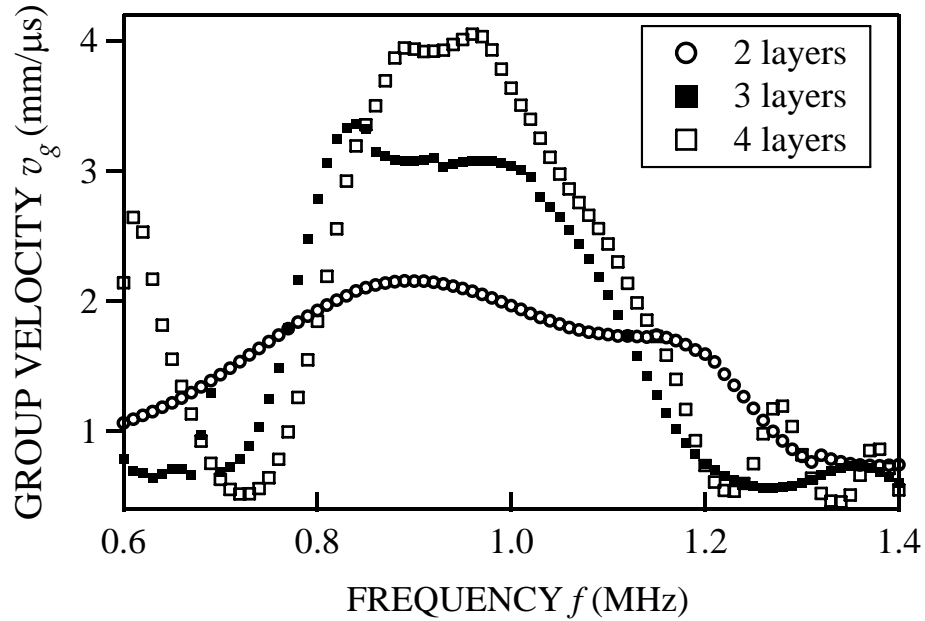


Figure 4.1.3: Group velocity of an ultrasonic pulse propagating through 2-, 3- and 4-layer single 3D phononic crystals as a function of frequency.

The group velocity dependence on the sample thickness at 0.95 MHz is presented in Figure 4.1.4. Group velocity increases linearly with crystal thickness and the inverse slope of the linear fit provides the value of the group time, which was found to be 0.68 μ s. Independence of the pulse transit time on the crystal thickness is a clear indication that tunnelling is involved at the frequency region corresponding to the band gap. It is also interesting to compare the values of group velocities observed in my experiments with those measured by Yang *et al.* [29]. This comparison is done in Figure 4.1.4, which

displays their data points for 3- and 4-layer single crystals (since Yang *et al.* did not investigate 2-layer single crystals).

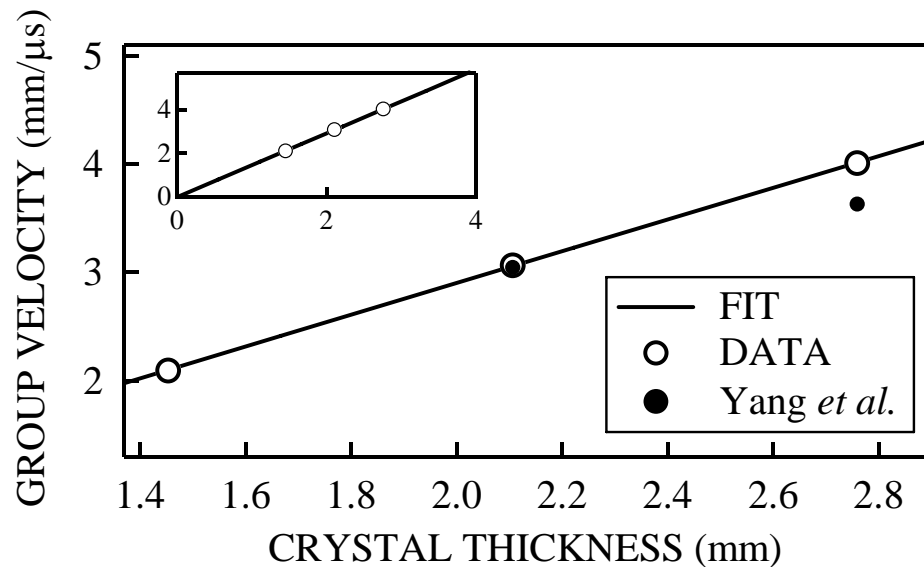


Figure 4.1.4: Group velocity as a function of crystal thickness at 0.95 MHz. The inset, which shows the extrapolation of group velocity to zero thickness, has the same axis labels as the main figure.

While the values of the group velocity for 3-layer sample are virtually identical, the group velocity for the 4-layer sample measured by Yang *et al.* falls below of the one observed by me. This might indicate that my 4-layer crystal was of better quality (e.g. better regularity, fewer crystal defects) as compared to the one employed by Yang *et al.* in their experiments. Another interesting fact is that the straight line obtained by fitting my data points passes through the origin of the coordinate system within the uncertainty associated with the fit (see inset in Figure 4.1.4), which certainly makes sense as the group time through a zero thickness sample should also be zero. In the case of the data obtained by Yang *et al.*, however, a straight line fit (for sample thicknesses up to 12 layers) did not extrapolate to zero but to some finite value of the group velocity, suggesting that their values were reduced by imperfections of the sample. Therefore, the comparison between

my results and those of Yang *et al.* signifies the high degree of regularity of my 3D phononic crystals and provides a good starting point for subsequent experiments with the double phononic crystals.

It is also of interest to investigate the dependence of the transmission coefficient through the phononic crystal as a function of the crystal thickness for the range of frequencies corresponding to the band gap. This is done in Figure 4.1.5, which presents the values of the transmission coefficient through 2-, 3- and 4-layer single crystals measured at two different frequencies of 0.880 MHz and 0.949 MHz.

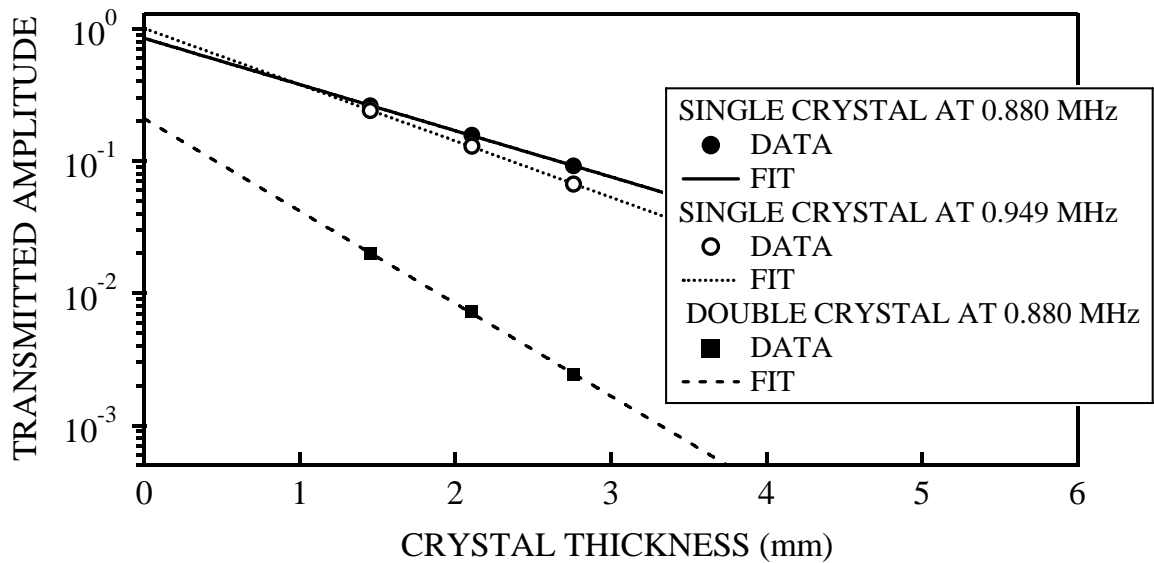


Figure 4.1.5: Transmitted amplitude as a function of the crystal thickness compared with the exponentially decaying function $\exp(-\kappa L)$.

At these frequencies the modes inside the crystal are purely evanescent and therefore the transmitted amplitude must decrease exponentially with the crystal thickness, i.e. $T \propto \exp(-\kappa L)$, where L is the crystal thickness and κ is the frequency-dependent wavevector of the evanescent mode. One can find the evanescent wavevector κ by

plotting the transmission coefficient versus crystal thickness and comparing the data with a function of the form $A\exp(-\kappa L)$, which can be seen from Figure 4.1.5 to give an excellent description of the data over the limited range of available thicknesses. The value of κ at 0.880 MHz frequency was found to be $(0.8\pm 0.1) \text{ mm}^{-1}$ and $(0.98\pm 0.02) \text{ mm}^{-1}$ at 0.949 MHz frequency. The uncertainty in κ at 0.88 MHz is larger, because this frequency is close to the band gap edge, which itself depends somewhat on the number of layers for thin crystals. At this frequency the exponential decay with thickness could be measured for the double crystals [Figure 4.1.5], giving an effective κ approximately twice as large when an amplitude is plotted versus individual crystal thickness.

The above experiments with single 3D crystals convincingly demonstrate that for sound waves at frequencies corresponding to the spectral gap a phononic crystal acts as an acoustic analogue of a potential barrier for a quantum mechanical particle of energy less than the barrier height. Quantum Mechanics also predicts that the transmission coefficient of a particle incident on a *double* potential barrier will exhibit narrow peaks of unit magnitude, an effect known as resonant tunnelling (which will be dealt with in more detail in the next section). Therefore, for frequencies in the band gap one would expect that the structure consisting of *two* phononic crystals separated by a cavity, which supports free propagation of sound waves, will act as an acoustic analogue of the quantum mechanical double potential barrier. With the goal of observing resonant tunnelling of acoustic pulses, I have performed a series of experiments on double phononic crystals, which are described in Section 4.2.2. The results of these experiments are summarized in a joint paper [67], in which resonant tunnelling of ultrasound through both 2D and 3D phononic crystals is investigated.

4.2 Resonant tunnelling of ultrasound pulses

This section presents the experimental evidence of the resonant tunnelling of ultrasound pulses, which was observed in the transmission experiments through 3D double phononic crystals. The resonant tunnelling of a quantum mechanical particle through a double potential barrier is described first, and the experimental results follow.

4.2.1 Resonant tunnelling through a double potential barrier

Before considering the experimental results on the resonant tunnelling of acoustic waves through double phononic crystals, it is worth reviewing the major predictions of Quantum Mechanics for the resonant tunnelling of a particle incident on a double potential barrier. Consider two identical rectangular potential barriers of height V_0 and width L , which are separated by the distance d [Figure 4.2.1].

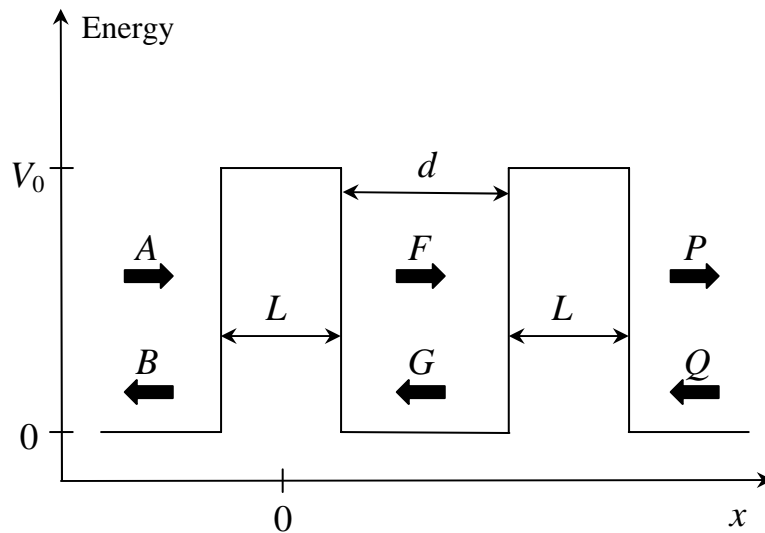


Figure 4.2.1: Double potential barrier of Quantum Mechanics.

Suppose a particle of energy E ($E < V_0$) is incident on the double barrier from either left or right. The wave function of the particle can be written as follows:

$$\begin{aligned}\psi(x) &= A \exp(ikx) + B \exp(-ikx) && \text{for } x < -L/2 \\ \psi(x) &= F \exp(ikx) + G \exp(-ikx) && \text{for } L/2 < x < d + L/2 \\ \psi(x) &= P \exp(ikx) + Q \exp(-ikx) && \text{for } x > d + 3L/2\end{aligned}$$

where k is the particle wavevector given by the usual expression $k = \sqrt{2mE}/\hbar$.

It was shown in Appendix B that coefficients A and B are related to coefficients F and G by the transfer matrix M , which describes the transmission of the particle through a single potential barrier:

$$\begin{pmatrix} A \\ B \end{pmatrix} = M \begin{pmatrix} F \\ G \end{pmatrix} \quad (4.1)$$

With the help of a translation operator T , represented by the following matrix:

$$T = \begin{pmatrix} \exp(ik(d+L)) & 0 \\ 0 & \exp(-ik(d+L)) \end{pmatrix}$$

the same matrix M also connects coefficients F and G to coefficients P and Q provided we first translate them by the distance $L + d$:

$$T \begin{pmatrix} F \\ G \end{pmatrix} = MT \begin{pmatrix} P \\ Q \end{pmatrix} \quad (4.2)$$

Combining equations (4.1) and (4.2) and setting $A = 1$ and $Q = 0$ (the particle is incident from the left), we obtain the following matrix equation describing transmission of the particle through the double barrier:

$$\begin{pmatrix} 1 \\ r \end{pmatrix} = MT^{-1}MT \begin{pmatrix} t \\ 0 \end{pmatrix} \quad (4.3)$$

from which the transmission coefficient t can be expressed as follows:

$$t = \frac{\exp(-2ikL)}{1 + S^2(1 - \varepsilon^2/4) + i\varepsilon SC + S^2(1 + \varepsilon^2/4)\exp[2ikd]} \quad (4.4)$$

where $S = \sinh(\kappa L)$, $C = \cosh(\kappa L)$, $\varepsilon = \kappa/k - k/\kappa$ and $\kappa = \sqrt{2m(V_0 - E)}/\hbar$ is the imaginary wavevector of the evanescent waves inside the potential barriers. When the incident energy E matches one of the energy levels of the potential well formed between the barriers, resonant tunnelling occurs and $|t| = 1$. A typical transmission curve is presented in Figure 4.2.2, where the absolute value of the transmission coefficient t given by (4.4) is plotted as a function of energy of the incident particle.

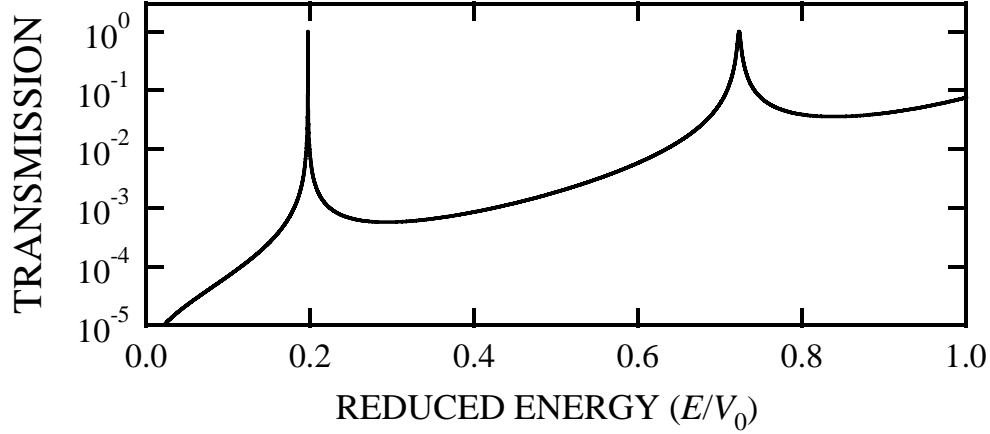


Figure 4.2.2: Transmission coefficient of a particle through double potential barrier calculated with $L = 5$ and $d = 10$ (measured in units of $\hbar/(2mV_0)^{1/2}$).

For opaque barriers ($\kappa L \gg 1$), the transmission coefficient (4.4) exhibits maxima when:

$$\exp[2ikd] = -\frac{(1 - \varepsilon^2/4) + i\varepsilon}{1 + \varepsilon^2/4} \quad (4.5)$$

From (4.5) one obtains the following resonance condition:

$$kd = \frac{1}{2} \tan^{-1}\left(\frac{\varepsilon}{1 - \varepsilon^2/4}\right) + \pi\left(n + \frac{\delta(\varepsilon)}{2}\right) \quad (4.6)$$

where $\delta(\varepsilon) = 1$ when $|\varepsilon| < 2$, and zero otherwise. When the incident energy is half the barrier height, $\varepsilon = 0$ and condition (4.6) reduces to:

$$d = \frac{\lambda}{2}\left(n + \frac{1}{2}\right)$$

which resembles the classical Fabry-Pérot resonance condition except that n is replaced by $(n + \frac{1}{2})$ due to the non-negligible barrier penetration depth.

In case of $E = V_0/2$ and $\kappa L \gg 1$, we can obtain the following simplified expression for t from (4.4):

$$t = \frac{\exp(-2ikL)}{1 + S^2(1 + \exp[2ikd])} \approx \frac{\exp(-2ikL)}{1 + \frac{1}{4}\exp(2\kappa L)(1 + \exp[2ikd])} \quad (4.7)$$

Let us find the expansion of (4.7) around the resonance in powers of $\Delta k = k - k^*$, where k^* is the wavevector at resonance. The expression for t becomes:

$$t = \frac{\exp(-2ikL)}{1 + \frac{1}{4}\exp(2\kappa L)[1 + \exp(2ik^*d)(1 + 2i\Delta kd)]} \quad (4.8)$$

It follows from (4.7) that at resonance $\exp(2ik^*d) = -1$, and from (4.8) the absolute value of the transmission coefficient $T = |t|^2$ can be found as follows:

$$T = \frac{1}{1 + \frac{1}{4}[\Delta k \exp(2\kappa L)d]^2} \quad (4.9)$$

By setting $T = \frac{1}{2}$ in the above expression, we can find the expression for the width of the resonant peak Δk :

$$\Delta k \approx \frac{2}{d} \exp(-2\kappa L) \quad (4.10)$$

from which it is clear that the resonance peak becomes exponentially narrow as the width of the barriers L increases. With the help of (4.10) we can also find the expression for the delay time t_g associated with the resonance:

$$t_g = \frac{d\phi}{d\omega} = \frac{1}{v_g} \frac{d\phi}{dk} \approx \frac{d}{2v_g} \exp(2\kappa L) \quad (4.11)$$

where ϕ is the transmitted phase¹. It follows from (4.11), that in Quantum Mechanics the transit time through a double potential barrier at resonance is inversely proportional to the tunnelling probability through a single barrier and becomes exponentially long compared with the travel time d/v_g between the barriers. I will return to this prediction of Quantum Mechanics later, when the experimental results of the resonant tunnelling of classical sound waves will be presented and discussed.

4.2.2 Resonant tunnelling of ultrasonic waves: Transmission

As was already mentioned in Section 4.1.2, in the range of frequencies corresponding to the band gap, a sample made of *two* phononic crystals separated by a cavity, which supports free propagation of sound waves, might act as an acoustic analogue of the quantum mechanical double potential barrier, thus enabling the observation of the resonant tunnelling of *classical* acoustic waves. To observe and investigate this effect, I have conducted a series of experiments on the transmission of ultrasonic pulses through

¹ When $E \neq V_0/2$, the prefactors are more complicated, but the exponential dependence on κL still dominates the behaviour of both Δk and t_g .

double phononic crystals. For these experiments I have constructed 3 double phononic crystals, each being composed of a pair of identical single crystals separated by an aluminum spacer. The choice of aluminum as a material for the spacer was dictated by its very low attenuation characteristics. The double crystals differed from one another by the number of layers in the corresponding constituent single crystals (2, 3 and 4 layers) and will be referred from now on simply as 2-, 3- and 4-layer double crystals. The input pulse, generated by a flat circular Panametrics immersion transducer, was incident normally on the crystal surface along the $[111]$ direction and the transmitted pulse was recorded on the other side of the crystal with another Panametrics transducer. The geometry of these experiments is schematically depicted in Figure 4.2.3.

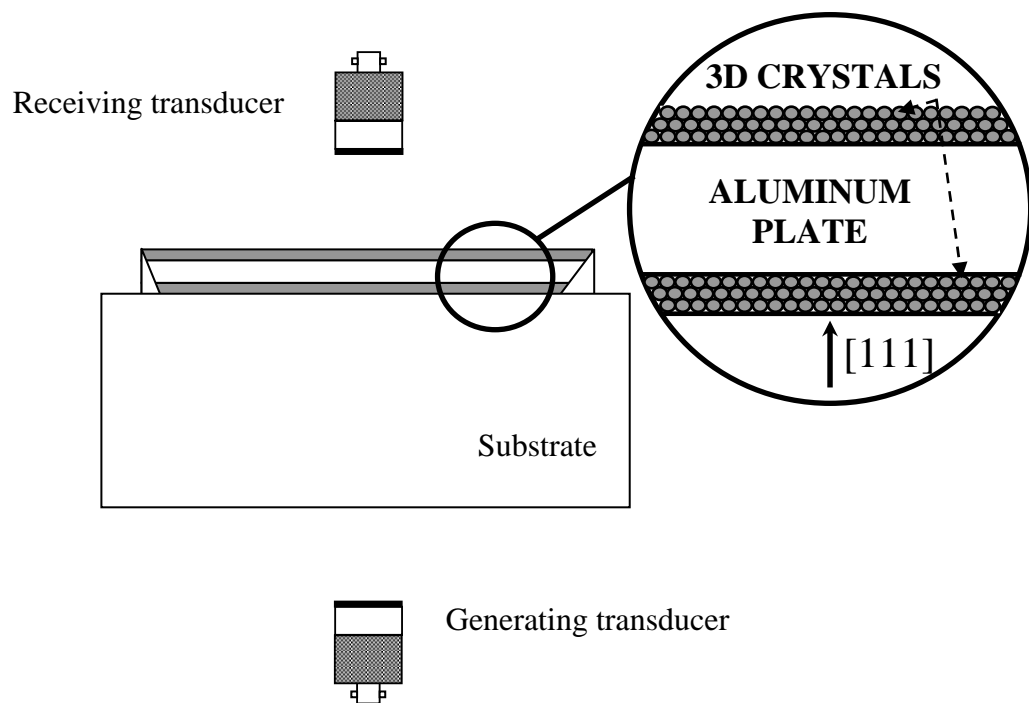


Figure 4.2.3: Schematic representation of the transmission experiments with 3D double phononic crystals.

Figure 4.2.4 shows representative input and transmitted pulses. The short input pulse undergoes many multiple reflections inside the cavity (which can be easily seen from the inset on the right panel) as it travels through the double crystal, which is the reason why the transmitted pulse extends over such a long time range.

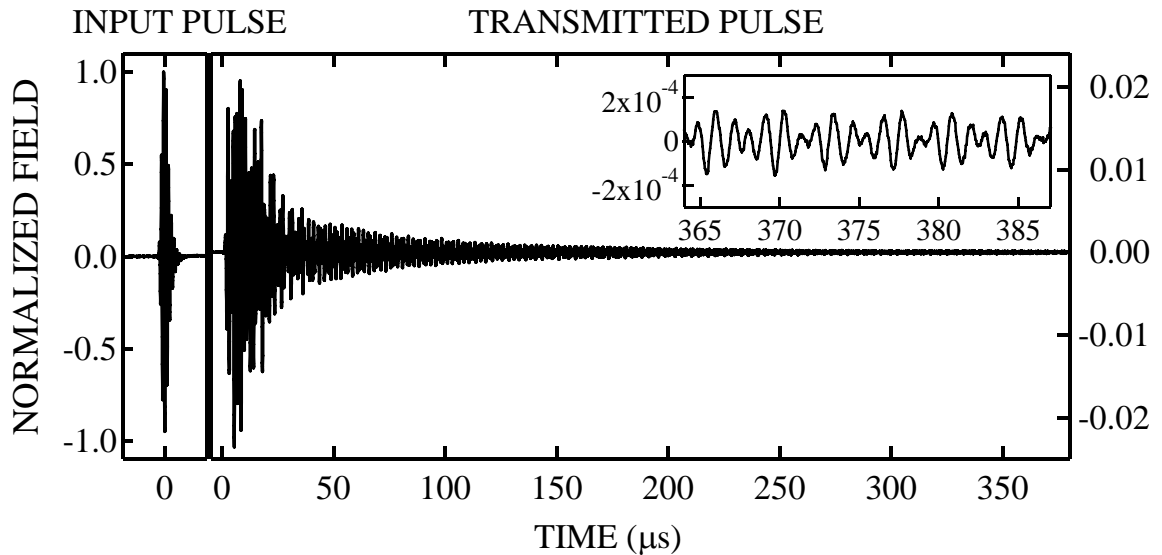


Figure 4.2.4: Input and transmitted pulses through a 3D double phononic crystal, with each crystal having 3 layers. The inset, which has the same axis labels as the main figure, magnifies a small part of the transmitted pulse at long times to demonstrate multiple reverberations of the transmitted pulse inside the cavity (spacer).

Figure 4.2.5 summarizes results of the transmission experiments with all three different double crystals. The transmission coefficient through each double crystal is compared with the transmission coefficient through the corresponding single crystal of the same number of layers. It can be seen that the doubling of the number of layers by moving from the single to the double crystal makes the drop in transmission (due to the band gap) more and more pronounced. Also, according to our expectations, the resonant tunnelling peak in transmission is indeed observed in the middle of the frequency range corresponding to the band gap.

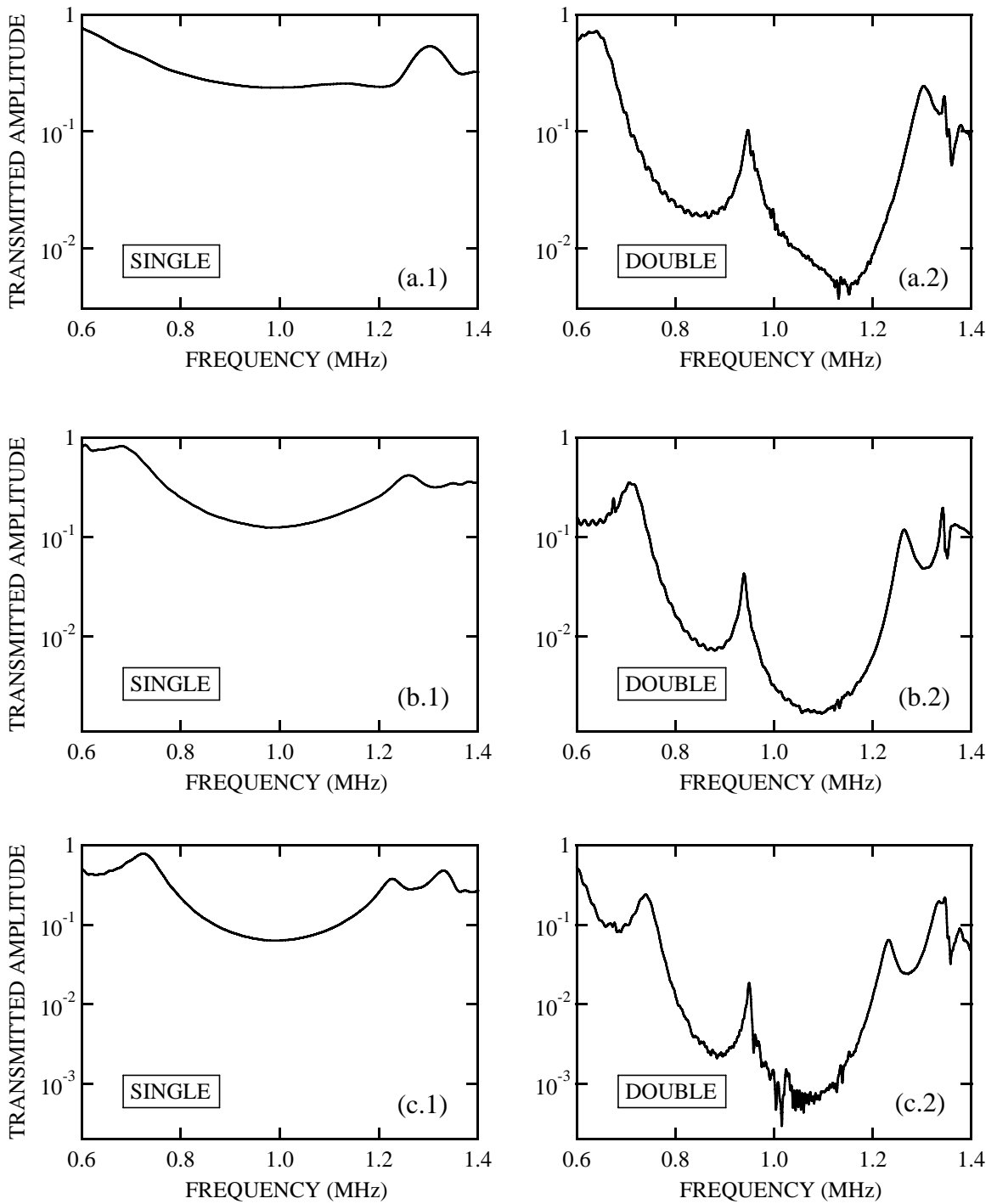


Figure 4.2.5: Transmission spectra through the double crystals with each individual crystal having: (a) 2 layers, (b) 3 layers, (c) 4 layers. Transmission through the corresponding single crystals is also shown.

The frequency at which the peak occurs is very close to (within less than 5% of) the frequency at which the spacer width is equal to the wavelength of a longitudinal sound wave in aluminum. At this frequency, all multiple reflections inside the cavity interfere constructively, giving a rise to a resonant peak in the transmission in analogy with the resonant tunnelling of a quantum particle through the double potential barrier. The main difference between quantum mechanical and classical resonant tunnelling is in the magnitude of the transmission peak, which in the case of these classical waves is far from being unity (compare Figures 4.2.2 and 4.2.5). The non-unit magnitude of the resonant peak can be explained by absorption, which is inevitably present in any classical system and has no counterpart in Quantum Mechanics. However, the situation with my double crystals is additionally complicated by the fact that there are several mechanisms contributing to the overall absorption of the system. Probably the major source of energy dissipation in the phononic crystals occurs due to the viscous losses at the interfaces between water and beads. As explained in [68], the viscosity of the fluid leads to the dissipation of the energy of the sound wave reflected/scattered by a rigid body without actually penetrating it, meaning that the velocity of the body's surface and the nearest liquid layer attached to it is zero (note that treating the beads as rigid bodies is an excellent approximation for my samples as the ultrasonic energy density inside the spheres is less than 1% of the energy density in water at frequencies inside the band gap [29]). Since the velocity of the fluid particles away from the interface is non-zero, this creates a large tangential velocity gradient, which in turn results in a *viscous* dissipation of the wave energy [68]. Another possible mechanism of absorption, as pointed out by Page *et al.* [69], arises from the relative motion of the spheres as the sound wave propagates through the crystal. This leads to *frictional* losses, since spheres rub against one another. Another

contributing factor is corrosion of the aluminum spacer surface, which gradually increased over time due to aluminum's reactivity with water and any impurities that might be present in the reverse osmosis water used [84]. The corrosive layer, which formed on the spacer surface, decreased the amplitude of the pulse as it was undergoing multiple reflections inside the spacer. This corrosion of the spacer however had an insignificant contribution to the overall absorption at the beginning of the experiments on each newly assembled sample due to the slow speed of the corrosive process, which took more than one week to have an appreciable effect on the ultrasonic experiments². As will be discussed later, these three energy dissipation mechanisms dominate the bulk absorptions of any of the crystal constituent materials (water, tungsten carbide and aluminum). Also, since the previous experiments with single crystals demonstrated the high quality of my samples, crystal imperfections are not expected to appreciably contribute to the overall losses in the double crystals.

The qualitative discussion of the role played by the absorption in reducing the magnitude of the resonant peak can be verified quantitatively using the MST by calculating the transmission through the double phononic crystal with and without absorption present in the system. However, the diversity of the absorption mechanisms makes it impossible to incorporate all of them into the MST on a *microscopic* level. Thus, the net energy dissipation in the system was taken into account by introducing an *effective* dissipation parameter κ_{abs} and assigning *complex* longitudinal moduli $\tilde{\beta}$ to both water

² This slow reaction rate was checked by independent experiments in which aluminum spacer and some beads were immersed in reverse osmosis water and the state of the aluminum surface was monitored visually.

(filling the space between the spheres) and aluminum. This results in the following expression for the longitudinal modulus $\tilde{\beta}$ of each material:

$$\tilde{\beta} = \rho v_l^2 (1 - 2i v_l \kappa_{abs} / \omega) \quad (4.12)$$

where ρ is the density and v_l is the longitudinal velocity of the sound in the corresponding material (water or aluminum). Note that $\tilde{\beta}$ was taken to be independent of frequency, which means that κ_{abs} had a linear dependence on the frequency:

$$\kappa_{abs} = \alpha \omega \quad (4.13)$$

Figure 4.2.6 presents the results of the MST calculations compared with the measured transmission through the 4-layer double crystal.

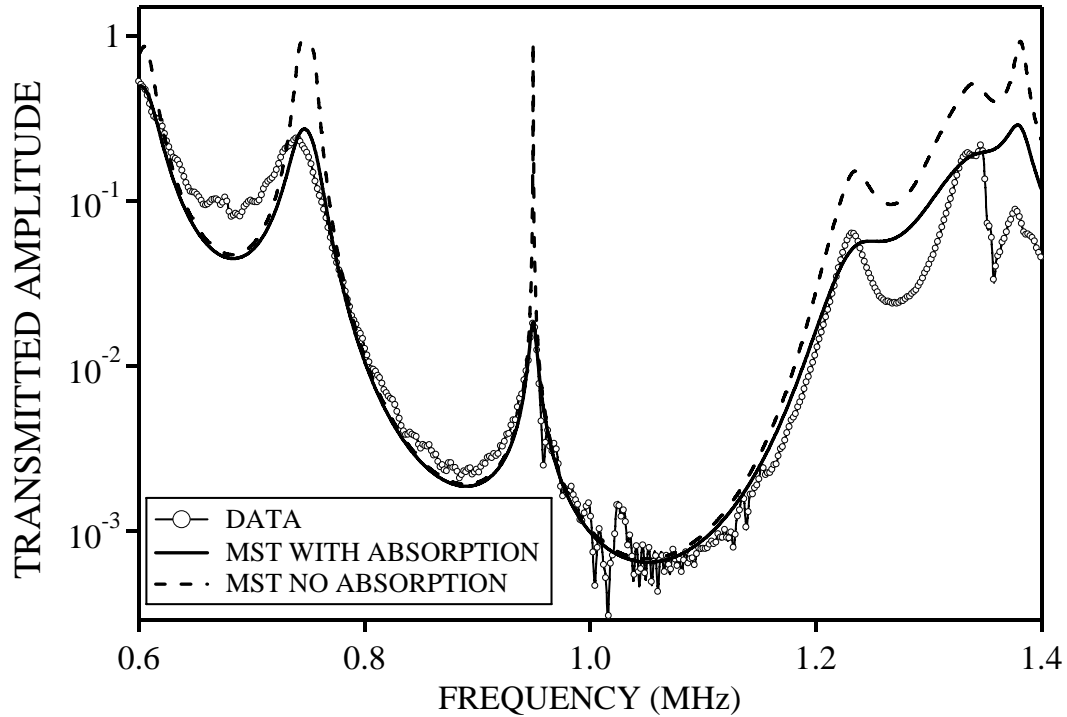


Figure 4.2.6: Comparison between transmission experiment through the double crystal (with each crystal having 4 layers) and the MST calculations.

One can see that in case of no absorption present in the system, the calculated transmission coefficient indeed reaches unit magnitude at the resonant frequency³. However, with absorption included in the model, the transmission peak magnitude is reduced and can be made to match the magnitude of the experimentally observed peak (by adjusting the amount of absorption introduced). It is also important to note that the losses arising from the previously discussed mechanisms occur at the interfaces (between beads and water, beads and beads or spacer surface and water), and therefore the overall absorption inside the system is *spatially* non-uniform. The field distribution inside the double crystal is of course also spatially non-uniform (Bloch states) and depends on the frequency of the propagating wave. The spatial non-uniformity of the absorption, combined with the spatial non-uniformity of the field and its frequency dependence, can explain why the effects of absorption are different at different frequencies. (If, for example, at some particular frequency the field is zero at the bead/water interfaces, then there will be no losses due to the first mechanism at this frequency). This can be seen from Figure 4.2.6, where MST fitted with absorption taken into account (which is assumed to be distributed *uniformly* throughout the system) agrees quite well with the experiment in the frequency region corresponding to the resonant tunnelling peak and the band gap, but does not agree with the data as well in the other frequency regions.

Table 4.2.1 contains values of the absorption coefficients κ_{abs} found from the best fits at the resonant frequency of the MST predictions for both the transmission and group time (see next section) to the experimental data.

³ The magnitude of the resonant peak (0.92) in Figure 4.2.6 is slightly smaller than unity due to the plastic substrate being taken into account during MST calculations. When no substrate is present, MST predicts unit magnitude of the resonant tunnelling peak.

3D double crystal	κ_{abs} (1/mm)	
	Spacer	Crystal (water)
2-layer	5×10^{-3}	7×10^{-2}
3-layer	2×10^{-3}	9×10^{-2}
4-layer	2×10^{-3}	4×10^{-2}

Table 4.2.1: The values of the absorption coefficients found from the best MST fits to the measured transmission and group times over the entire frequency range from 0.6 to 1.4 MHz. The values of κ_{abs} are given to only one significant figure because of correlations in the fitted values of κ_{spacer} and κ_{cryst} . Despite the relatively large uncertainties in these parameters, it is clear that κ_{spacer} is more than an order of magnitude smaller than κ_{cryst} .

The examination of the table reveals that good agreement between theory and experiment is obtained when the value of the absorption coefficient in the aluminum spacer is significantly smaller than the absorption inside the crystals. Thus, the dissipation mechanism introduced by the corrosion of the spacer surface was relatively unimportant at the time these measurements were performed. The variation of the spacer's κ_{abs} for different crystals can be explained by the fact that the state of the spacer on the day of measurements varied from crystal to crystal, since the amount of time, which elapsed between the moment the double crystal was assembled and the time the transmission experiments were performed, varied from sample to sample. Naturally, the amount of the deposit due to corrosion on the spacer surface depended on how long the spacer was in contact with water, and this fact is reflected in Table 4.2.1 by the different values of the absorption coefficients ascribed to the spacer. From Table 4.2.1, it is also clear that viscous and frictional losses in the phononic crystals are the major factors responsible for

the non-unit magnitude of the resonant peak. It is interesting to note that the crystal κ_{abs} for the 4-layer double crystal is smaller than that of the 2-layer one. This difference might be explained by a reduction of the frictional losses in the thicker crystal due to the overall decrease in the mobility of the beads relative to each other, which were pressed more tightly together by the increased combined weight of the upper beads. It also should be noticed that values of κ_{abs} inside my phononic crystals are consistent with the value found in the experiments with similar single crystals [69].

The way in which absorption in the phononic crystals reduces the magnitude of the resonant tunnelling peak can be understood in terms of the two modes model, which was introduced by Yang *et al.* [29]. In their transmission experiments with *single* phononic crystals they found that although the group velocity with which pulses tunneled through the crystals increased with the crystal thickness, it increased less rapidly than predicted by the MST with no absorption. They explained this behaviour by the presence of absorption. Absorption cuts off the long scattering paths of multiply scattered Bragg waves and makes their destructive interference, which is responsible for the appearance of the spectral gaps, incomplete. The net effect is that, in addition to the dominant tunnelling *evanescent* mode (characterized by the constant tunnelling time through the crystal's band gap), absorption introduces a small *propagating* mode travelling through the crystal with roughly constant speed, which is slower than the group velocity of the tunnelling mode. It is because of this weak propagating mode that the average group time of the transmitted pulses becomes longer, and the rate of increase of the group velocity with sample thickness is reduced.

In the case of the double phononic crystal the transmitted pulse also travels through each individual crystal by tunnelling. However, at the resonant frequency the pulse reverberates many times inside the cavity, creating a substantial build-up of the field because of the constructive interference of all multiple echoes, and this field build-up manifests itself as a transmission peak. In the case when no absorption is present, the pulse is trapped inside the cavity for a very long time, which according to the MST increases exponentially with the thickness of an individual crystal (more details will be presented in the next section), in analogy with the predictions of Quantum Mechanics in equation (4.11). On the other hand, the absorption creates a leakage of the pulse from the cavity (via the propagating mode) and reduces the time that the pulse spends inside the cavity. As a result, the field inside the cavity does not reach as large a magnitude as it would do in the case of zero absorption, leading to a decrease in the magnitude of the resonant tunnelling peak.

4.2.3 Resonant tunnelling of ultrasonic waves: Group time

The ultrasonic pulsed technique also allowed the investigation of the *dynamics* of the resonant tunnelling by measuring the frequency dependence of the group time of the pulses transmitted through the double crystals. The details on how the group time can be derived from the transmission experiments were already given in Section 3.5.1. Figure 4.2.7 presents a summary of the experimental results for the group time along with the group velocity as a function of frequency for all three double crystals. One can see that at resonance the group time has a sharp peak, which is clear evidence of the pulse being trapped inside the cavity at the resonant frequency. At the same time, the group velocity

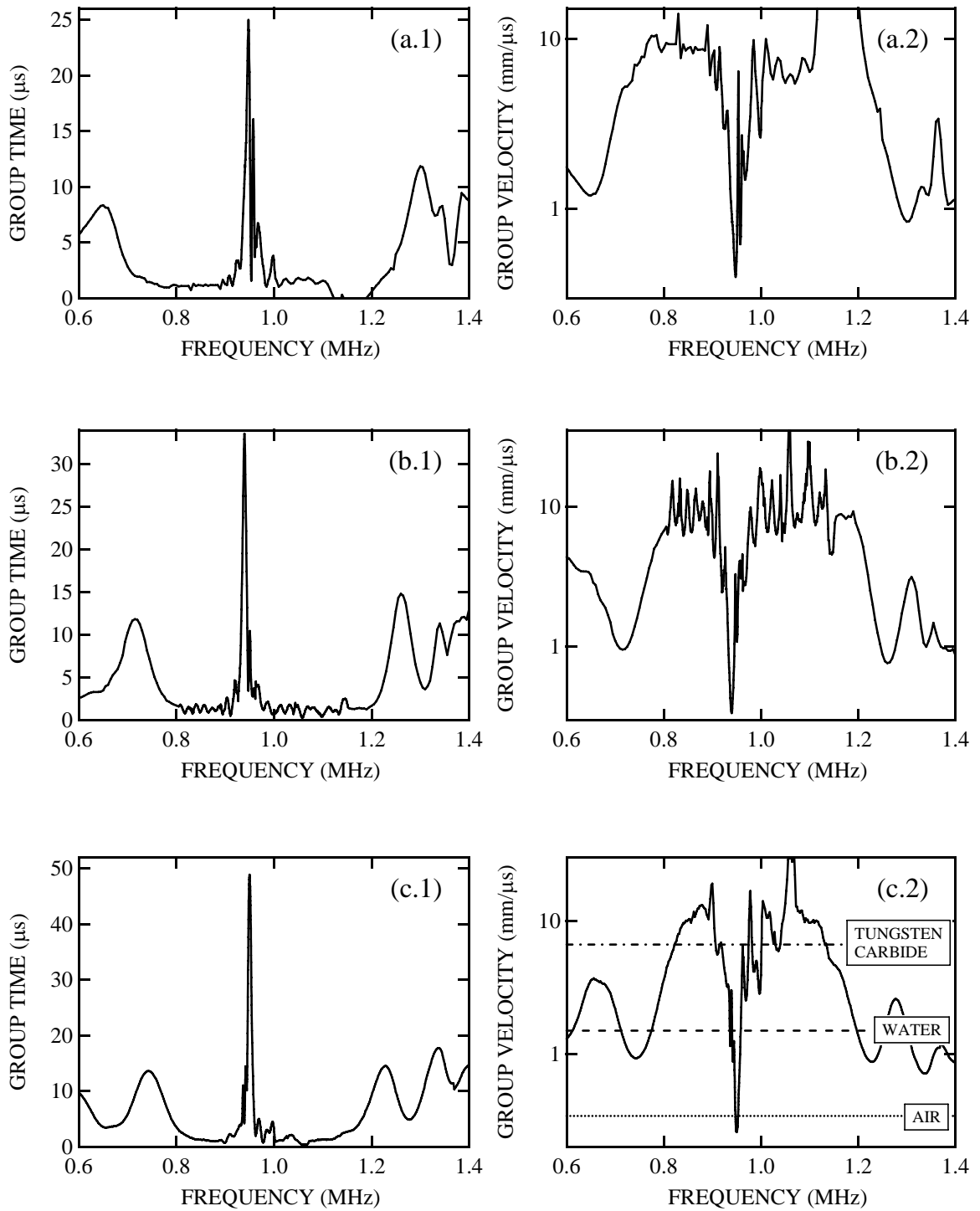


Figure 4.2.7: Frequency dependence of the group time and group velocity of the pulses transmitted through the (a) 2-, (b) 3- and (c) 4-layer double crystals.

exhibits a significant drop in its value (which is no surprise, since $v_g = (2L + d)/t_g$, where L and d are the thicknesses of the individual crystals and spacer, respectively). As the number of layers in an individual crystal increases, waves travel progressively faster at off-resonance frequencies and slower at the resonant frequency. The very large range of observed group velocities is emphasized in Figure 4.2.7(c.2).

Off-resonance and inside the band gap, the group velocity becomes larger than the speeds of sound in any of the constituent materials (1.49 mm/ μ s in water and 6.6 mm/ μ s in tungsten carbide). At the same time, on resonance, the ultrasound pulse is dramatically slowed down and propagates with a group velocity lower than the speed of sound in air!

In addition to the transmission coefficient, the MST also enables one to calculate the group time (which can be obtained by differentiating the cumulative phase of the transmission coefficient with respect to frequency, since $t_g = (1/2\pi)d\phi/df$). Thus, variation of the group time with the thickness of the double crystal can be investigated theoretically, also allowing the effect of the absorption on the group time at resonance to be identified. It was found that the group time decreases as the magnitude of the absorption coefficient is increased. Figures 4.2.8(a)-(b) present the experimental group velocity and group time for the 4-layer double crystal along with the predictions of the MST, in which absorption is included in the calculations (see Table 4.2.1). Although the best fit of the MST to both the transmission coefficient and group time overestimates the magnitude of the group time at resonance by about 6%, the physics is still very well captured by the theory. The effect of the absorption on the group time can again be understood in terms of the two modes model. In the presence of absorption, the dwell time of the pulse, which is trapped inside the cavity at the resonant frequency, is decreased

because of the leakage of the signal, which is introduced by the small propagating mode. It was already emphasized in the previous section that, because of many multiple reflections inside the cavity, the transmitted pulse extends over a very long range of times as compared to the input pulse [see Figure 4.2.4].

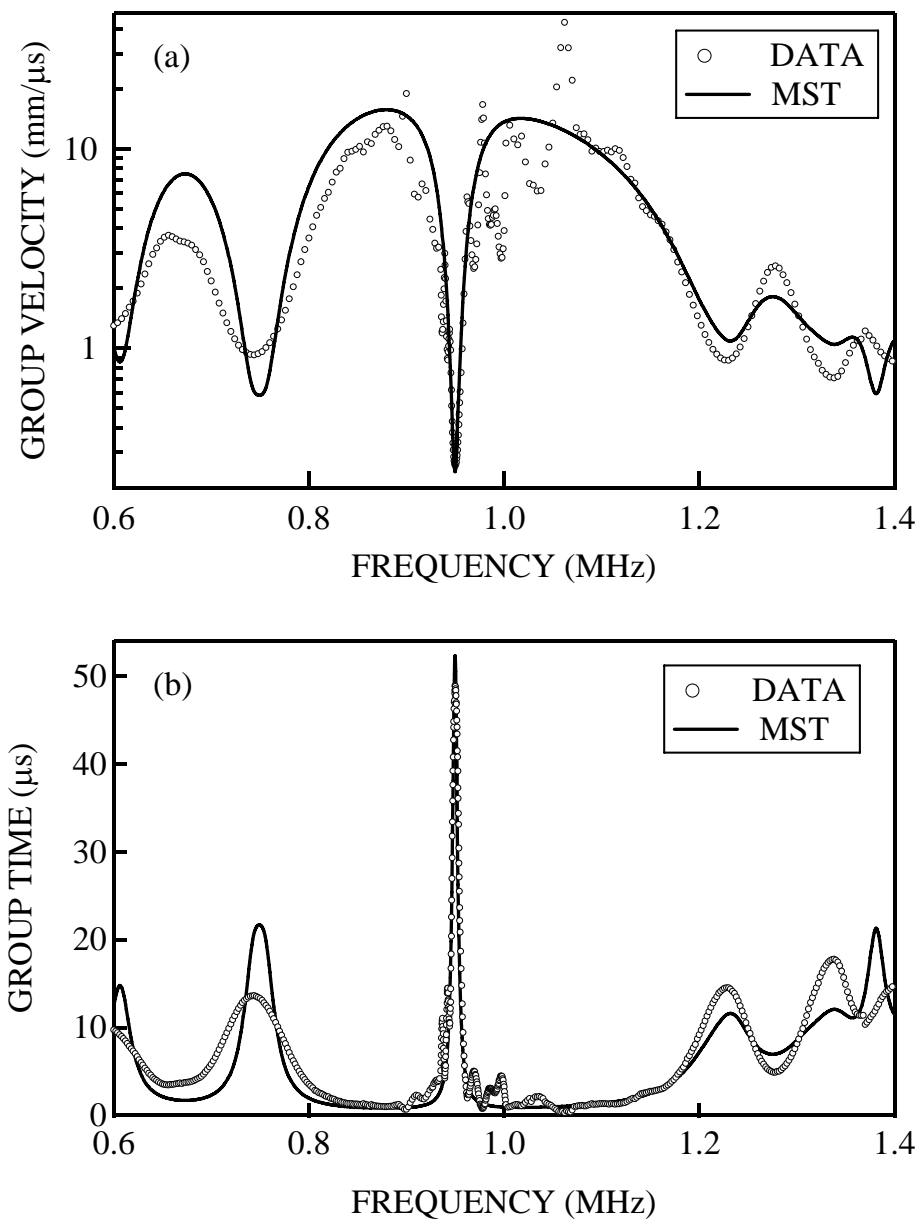


Figure 4.2.8: Comparison of the measured (a) group velocity and (b) group time for 4-layer double crystal with the predictions of the MST (absorption included).

The transmission coefficient (and correspondingly the group time) can be accurately measured from the transmitted pulse once all of the multiple reflections are recorded. However, in case of the two thickest samples (3- and 4-layer double crystals) the transmitted pulse was so long that it overlapped with its own echoes [see Figure 4.2.9] before all the multiple reflections inside the cavity were reduced to a magnitude comparable to the noise level.

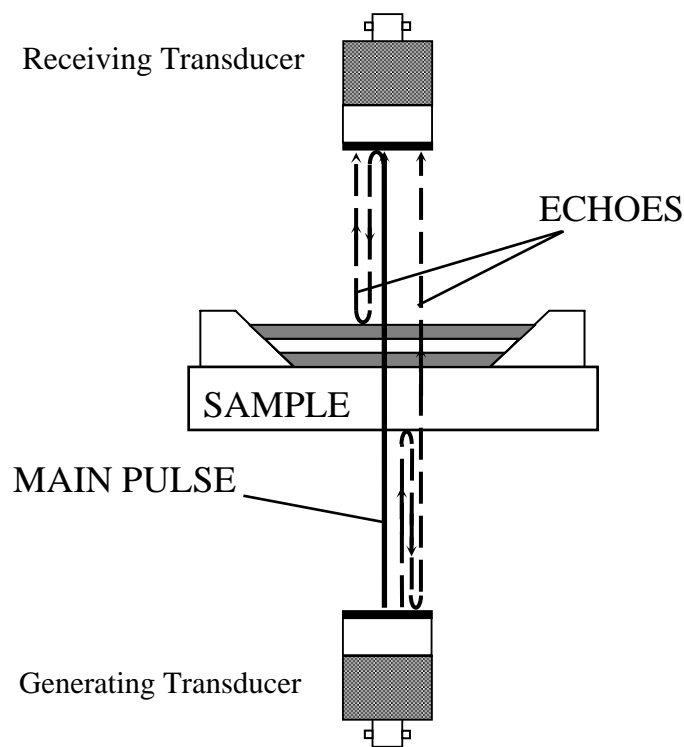


Figure 4.2.9: Schematic diagram of the transmission experiment with 3D double phononic crystals, which shows the origin of the echoes created by the partial reflections of the transmitted pulse at water/substrate, crystal/water and water/transducer interfaces.

Because of this overlap, for the purpose of the analysis the main pulse had to be truncated at some point before the beginning of the overlapping echo. This procedure is

illustrated in Figure 4.2.10 for the pulses transmitted through 3- and 4-layer double crystals.

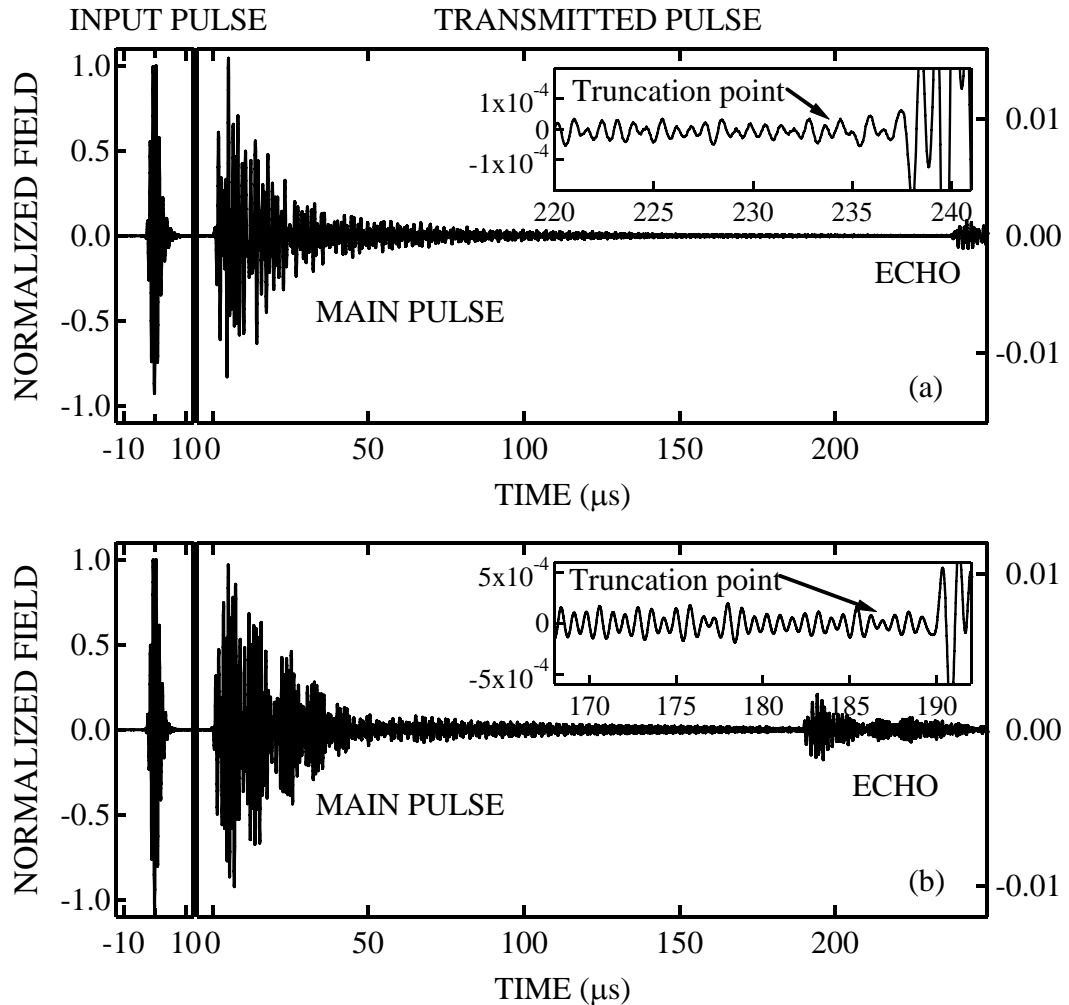


Figure 4.2.10: The main pulses transmitted through (a) 3-layer and (b) 4-layer double crystals along with the overlapping echoes. The insets magnify small parts of the main pulses at long times to illustrate the overlap between echoes and multiple reverberations of the transmitted pulses inside the cavity. The axis labels of both insets are the same as those in the corresponding main figures.

The effect of this early pulse truncation introduces an artificial reduction of both the magnitude of the resonant tunnelling peak in the transmission spectra and the value of the measured group time. One way to overcome this difficulty is to increase the distance between the sample and the transducers. It turned out, however, that there was a certain

limit beyond which the distance between the generating transducer and the sample could not be increased without running into the difficulty of the *subsidiary* transmission peaks, which appeared to accompany the main resonant tunnelling peak (this issue will be discussed later in this section). The other way was to *correct* for the artificial reduction, which was done by analyzing dependence of the magnitude of the group time at the resonant frequency as a function of the transmitted pulse truncation time. The group time was found to approach a maximum value as the truncation time increased (i.e. with more and more of the transmitted pulse being taken into account when calculating the group time). The obtained values of the group times were subsequently fit by the empirical, exponentially saturating, function of the form:

$$t_g = t_g^{sat} - A \exp(-t / \tau) \quad (4.14)$$

Here t_g^{sat} is the extrapolated value of the group time, which corresponds to the transmission of the entire pulse (without truncation due to overlapping echoes). The parameters A and τ are positive constants, which describe the rate at which pulse truncation reduces the measured group time. (The parameter τ is related to the dwell time of the pulse inside the cavity.) Table 4.2.2 compares the measured and saturated group times.

3D double crystal	Parameters (μs)		Group time (μs)	
	A	τ	Measured	Saturated
2-layer	–	–	25.0	–
3-layer	70 ± 10	43 ± 3	33.6	33.8 ± 0.2
4-layer	90 ± 10	53 ± 6	48.7	50.5 ± 0.8

Table 4.2.2: Comparison of group times measured at the largest truncation time and determined from the extrapolation procedure given by equation (4.14). For the 2-layer double crystal, the transmitted pulse was shorter and became smaller than the noise level before the overlap could occur.

From the correlation matrix, the parameters A and τ were found to be strongly correlated, a consequence of the exponential function fit to the data. Despite these correlations, these fits enable us to extract accurate values of “true” group time. Figure 4.2.11 displays the evolution of the group times as a function of the truncation time for the pulses shown in Figure 4.2.10.

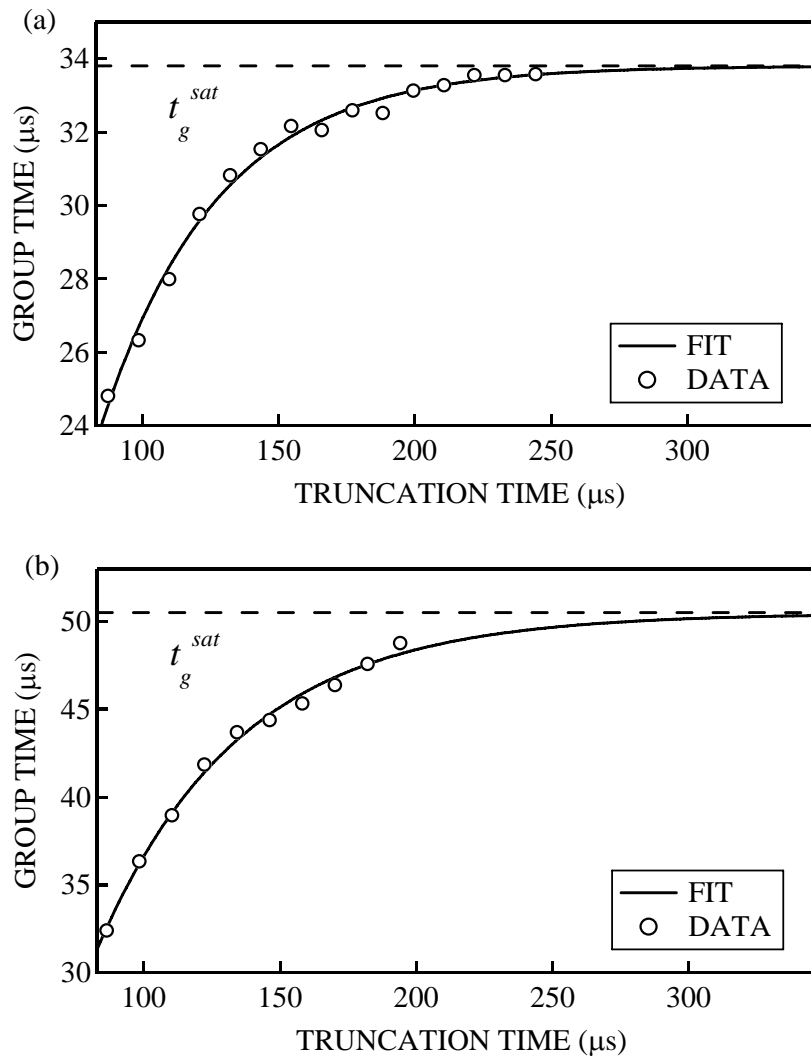


Figure 4.2.11: The evolution of the group time at resonance as a function of the pulse truncation time for (a) 3-layer and (b) 4-layer double crystals. The saturation group times are also indicated by the dashed lines.

In case of the resonant tunnelling of a quantum mechanical particle through a double potential barrier, the transit (or group) time is predicted to increase exponentially with the thickness of the individual barrier (see equation (4.11)). It is also interesting to explore whether a similar dependence exists in case of the resonant tunnelling of the ultrasound pulses and how it is modified by the presence of absorption. The case of no absorption present in the system was investigated theoretically using the MST by calculating group times through several double crystals, ranging from 2 to 5 layers, with the absorption coefficients inside both the cavity and the crystals set to zero. As can be seen from Figure 4.2.12, the group time at resonance (which occurs at 0.949 MHz) indeed increases exponentially as the thickness of the individual crystal increases.

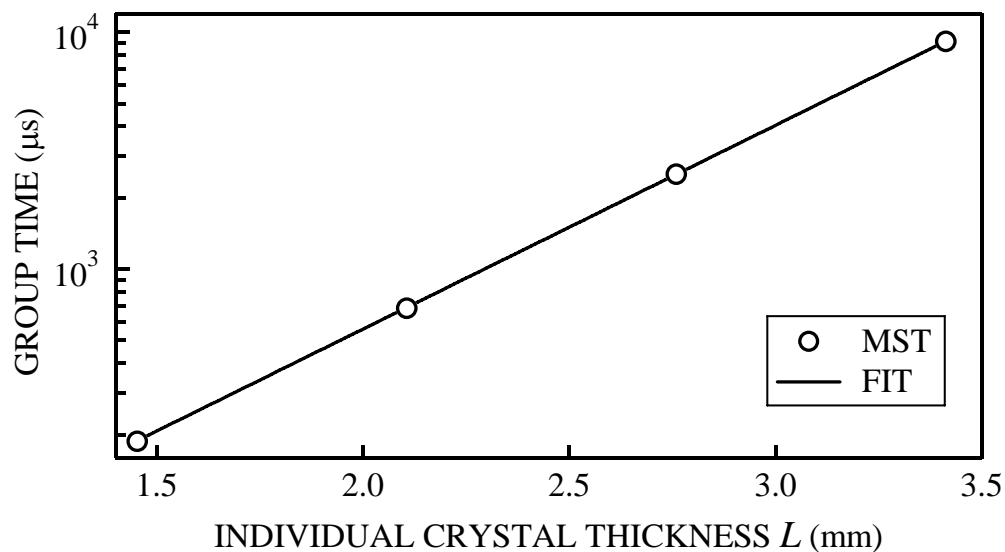


Figure 4.2.12: The evolution of the group time at the resonant frequency of 0.949 MHz as a function of the individual crystal thickness as predicted by the MST with no absorption. These calculations are compared with an exponential function (solid line) as described in the text.

By comparing the MST calculations with an exponential function of the form of $A \exp(2\kappa L)$, with A and κ as adjustable parameters, the wavevector κ of evanescent waves inside each crystal was found to be 0.99 mm^{-1} , which is in an excellent agreement with the value of κ (0.98 mm^{-1}) derived from the transmission experiments through the single crystals (see Section 4.1.2). However, when the absorption is taken into account, the group time dependence on the individual crystal thickness is significantly modified. The group time slowly increases with the thickness of the crystal and quickly reaches a saturation value for thickest samples as seen from Figure 4.2.13, which presents resonant group times calculated by the MST for *constant* values of absorption κ_{abs} inside the crystal ($6.55 \times 10^{-2} \text{ mm}^{-1}$) and the spacer ($0.18 \times 10^{-2} \text{ mm}^{-1}$). These values are intermediate to the ones shown in Table 4.2.1.

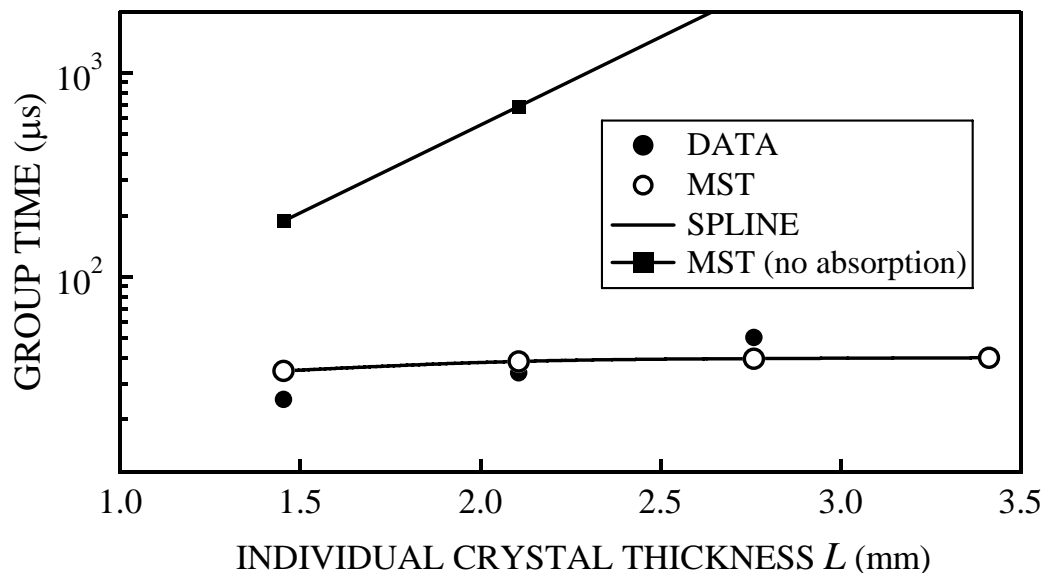


Figure 4.2.13: The comparison of the measured group times at resonance with those predicted by the MST in case of the absorption present in the system. The interpolated cubic spline is presented as a guide for the eye.

The measured group times, also shown in Figure 4.2.13, are scattered around the theoretical curve predicted by the MST. However, this scatter can be expected, as the theoretical curve was calculated with the same value of κ_{abs} for all individual crystal thicknesses, while in the actual experiments the magnitude of κ_{abs} varied from sample to sample, as is shown in Table 4.2.1. Overall, the experimental data exhibit behaviour that agrees with the one predicted by the theory, namely the saturation of the group times as a function of the individual crystal thickness. This agreement also serves as a positive indication of the validity of the MST model.

At the end of this section it is worth mentioning one of the major experimental difficulties encountered during resonant tunnelling experiments. In addition to the overlap between the echoes and the transmitted pulse, considerable complications arose from the appearance of the *subsidiary* peaks accompanying the resonant tunnelling peak in the transmission spectra of many sample pulses. The corresponding group times also exhibited the existence of the subsidiary peaks [Figure 4.2.14].

Since there was no confidence that group times measured for the pulses exhibiting subsidiary peaks were not compromised by their presence, it was important to find a way to eliminate or at least minimize the presence of the subsidiary peaks. Although the mechanisms for the appearance of the subsidiary peaks were not clearly established, it was found experimentally that their magnitude could be significantly reduced by decreasing the angular spread of the sound beam produced by the generating transducer, as well as by reducing the area of the sample illuminated by the beam. More details on this analysis can be found in the Appendix C. To minimize the presence of the subsidiary peaks, the input ultrasound pulses were generated by the largest diameter (1.5-inch) transducer

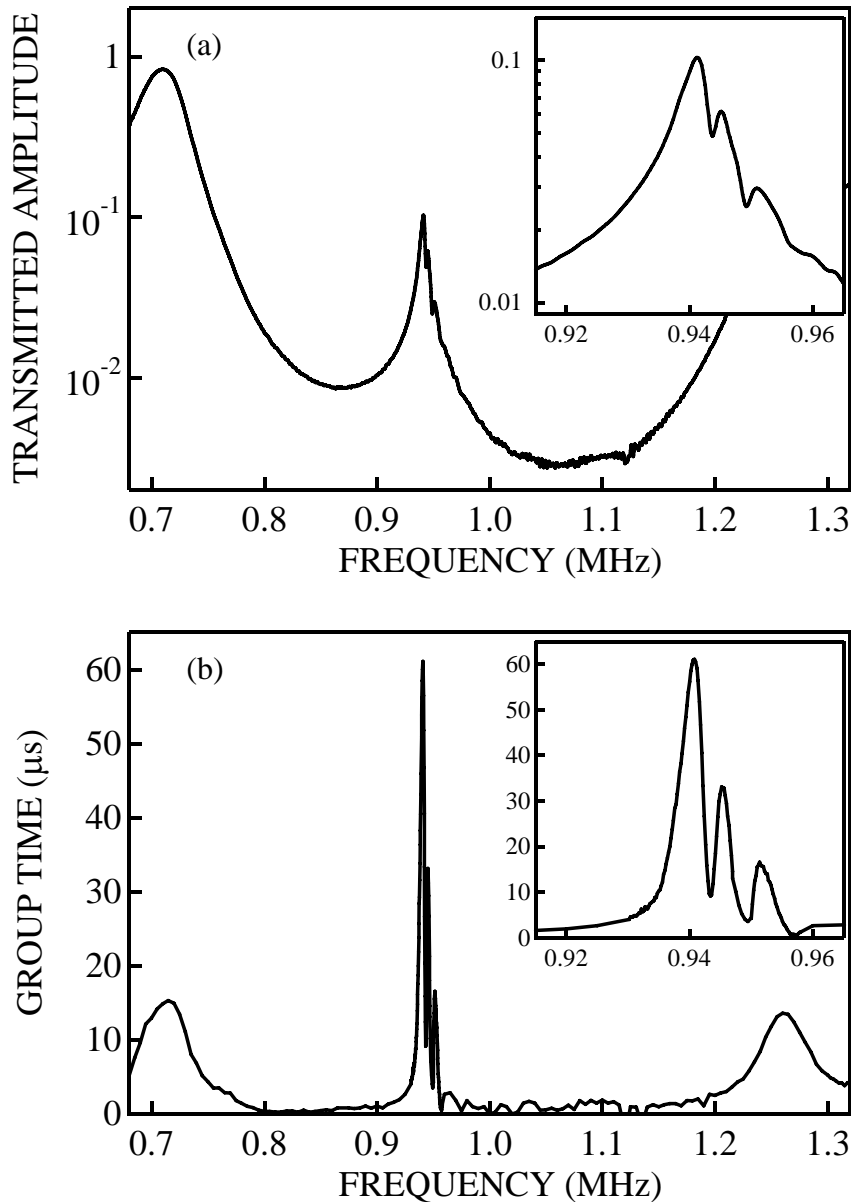


Figure 4.2.14: Representative data illustrating the problem of subsidiary peaks in (a) transmission coefficient and (b) corresponding group time measured for one of the 3-layer double crystals. The insets magnify small range of frequencies to better illustrate the problem of subsidiary peaks (the axis labels of both insets are the same as in the corresponding main figures).

because it had the smallest angular spread (see Section 3.4.1, equation (3.5)). Since the area illuminated by the generating transducer increases with the distance from the transducer, it was also important to find the optimal distance between the transducer and a

sample for which no subsidiary peaks would be observed, while at the same time the overlap between an echo and a transmitted pulse would occur at as late a time as possible. Unfortunately the importance of simultaneously taking into account all of the above considerations, as well as reducing the degree of corrosion of the spacer by minimizing the time of its exposure to the water, was not realized during the initial series of experiments from which the group times presented in Figure 4.2.13 were found. Therefore, although these experiments unambiguously provided a qualitative demonstration of the resonant tunnelling of ultrasound pulses, they were not all conducted under ideal conditions. With the goal of obtaining the data that were not tainted by any of the complications discussed above, I completed another set of measurements with a new 3-layer double crystal. While assembling the new crystal I made every possible effort to minimize the time between the moment of the spacer's exposure to the water (which happened when the spacer was placed on top of the bottom crystal) and the transmission measurements through the sample. The fast construction of the crystal was greatly facilitated by the skills that I acquired and improved in the course of assembling the previous samples. To suppress the appearance of the subsidiary peaks, the 1.5-inch diameter transducer was used as a generator during the measurements and the distance between the transducer and the crystal was carefully adjusted according to the prescriptions described above. Also, to minimize any possible complications due to the finite size of the sample (edge effects), the new 3-layer crystal had an area roughly twice as large as the area of the previous double crystals. The results of the experiments with the new 3 layer double crystal are shown in Figure 4.2.15. No subsidiary peaks (at least of magnitude comparable to the main peak) are present around the resonance in both the transmission coefficient and the group time,

which proves the importance of minimizing both the angular spread of the input beam and the area of the crystal illuminated by the transducer.

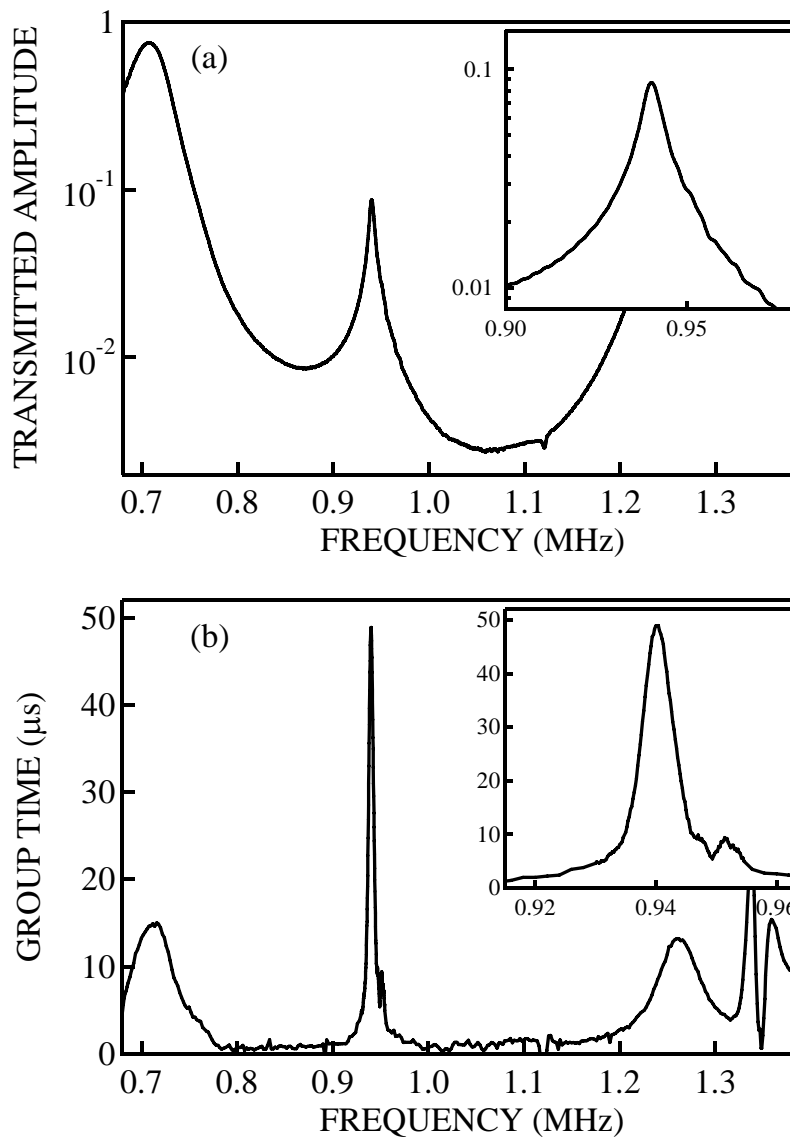


Figure 4.2.15: Measured (a) transmission coefficient and (b) group time for the new 3-layer double crystal with insets demonstrating the absence of the subsidiary peaks.

It should also be noted that the magnitude of the resonant tunnelling peak was found to be about two times larger than that shown in Figure 4.2.5(b.2). The magnitude of

the peak group time also increased significantly as compared to the value shown in Figure 4.2.7(b.1) (see also Table 4.2.2) and was measured to be 48.9 μs . This increase is the direct result of the improvements that were made in this final experiment.

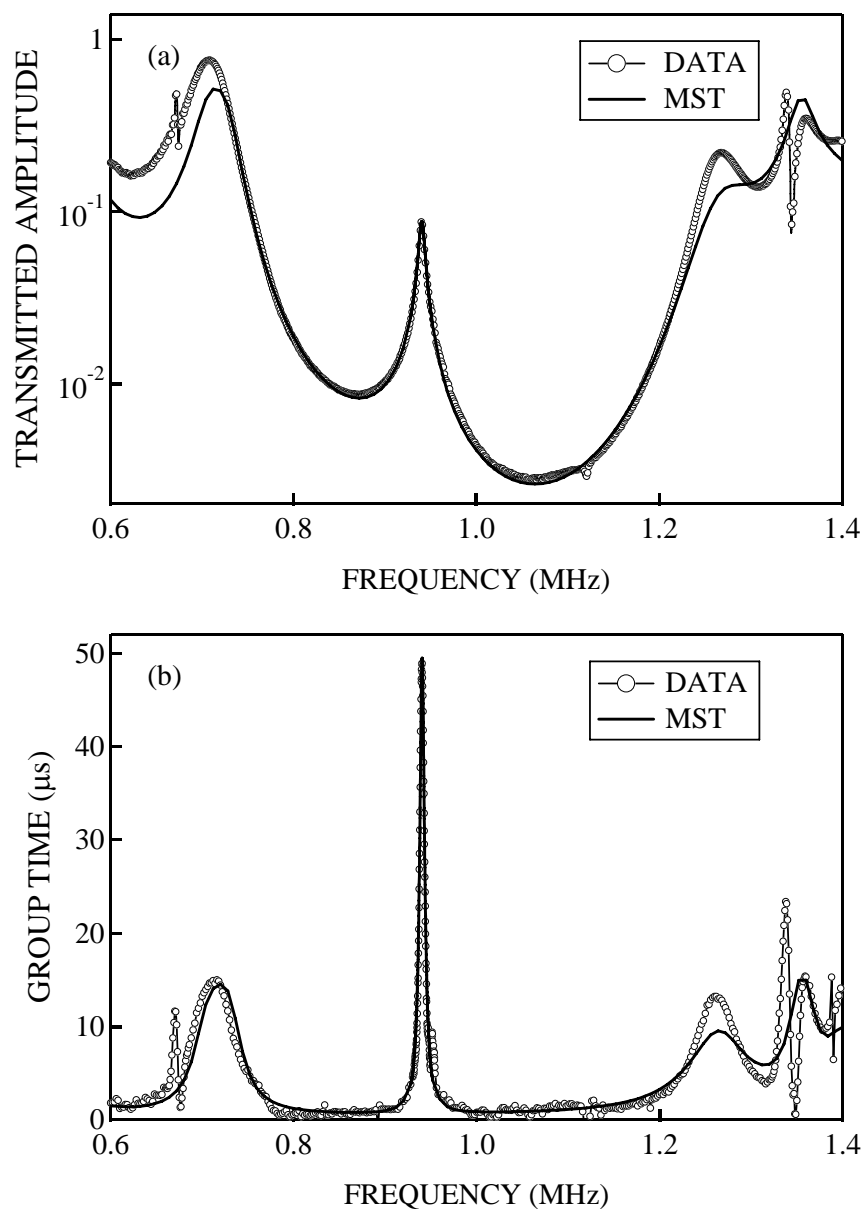


Figure 4.2.16: Comparison of the measured (a) transmission and (b) group time through the new 3-layer double crystal with the calculations by the MST.

Figure 4.2.16 presents the results of the transmission experiments (transmission coefficient and the group time) through the new 3-layer double crystal along with the fits by the MST. The best agreement between the experiment and the theory was obtained with the absorption coefficients κ_{abs} equal to $4 \times 10^{-2} \text{ mm}^{-1}$ (the crystal) and $2 \times 10^{-3} \text{ mm}^{-1}$ (the spacer). The value of κ_{abs} inside the crystal is approximately half the value found for the initial 3-layer crystal (Table 4.2.1), quantifying the improvements that were made.

I would like to conclude at this point by summarizing the experimental and theoretical findings reported in this chapter. The main result is the actual observation of resonant tunnelling of ultrasound pulses through the double phononic crystals. Also, the dynamics of the effect was investigated by analyzing the group time of the transmitted pulses. It was found that at off-resonance frequencies inside the band gap the sound pulses travel very fast (with a group velocity larger than speed of sound in any of the crystal constituent materials), while on resonance they are dramatically slowed down and travel through the crystal with a group velocity smaller than speed of sound in air. The effect of the absorption on the magnitude of the resonant tunnelling peak was investigated using the MST and explained in terms of the two-modes model. The method of correcting the measured group times for the effect of pulse truncation was also demonstrated. Finally, some experimental difficulties were discussed. It was shown that in order to observe resonant tunnelling reliably it is particularly important to ensure that the input pulses approximate plane waves as closely as possible (by minimizing the angular spread of the transducer beam) as well as to reduce the area of the crystal illuminated by the generating transducer. At the same time, it is also important to minimize the dissipation losses inside the crystal.

5. Experiments with 2D phononic crystals

This chapter states and discusses the experimental results that were obtained in the course of the experimental work done with 2D phononic crystals (for a detailed description of the samples, see Section 3.1.1). The first part of this chapter gives an account of the experiments on negative refraction of ultrasound pulses propagating through 2D phononic crystals, while the second part presents major findings of the experiments in which the focusing properties of 2D phononic crystals were investigated.

5.1 Negative refraction of ultrasound

The main goal of this part of the thesis is to present experimental evidence for the negative refraction of ultrasound waves observed in the prism-shaped 2D phononic crystal. All the experiments described in this section were performed with 2D phononic crystals immersed in and filled with water. The section starts with the description of the transmission experiments on the rectangular-shaped crystal, which allowed its band structure to be determined experimentally. The rest of the section is devoted to the results of various experiments on negative refraction along with their interpretation in the light of the theory reported previously in Chapter 2.

5.1.1 Transmission coefficient and band structure

As was already mentioned in Section 2.2.1, negative refraction of sound waves in 2D phononic crystals is a band structure effect. Therefore the main reason for the possibility of achieving it lies in the regular arrangement of the crystals' scattering units and subsequent Bragg scattering of the waves inside the crystal. It was also pointed out that the effects introduced by the crystal's regularity are conveniently described by band structure plots, which essentially represent the propagating modes inside the crystal as a function of the direction of propagation. As the degree of regularity of the crystal has an immediate impact on wave propagation inside the crystal, the quality of the sample is a crucial factor for the negative refraction experiments to succeed. A convenient check of the quality of my crystals was obtained by comparing transmission and band structure curves, determined experimentally, with those predicted by rigorous theory for a perfect crystal.

To measure both the transmission coefficient and dispersion curve along the ΓM direction, I have performed several transmission experiments with the 6-layer rectangular-shaped crystal [Figure 3.1.2(a) and Figure 3.1.3(a)], using an input ultrasound pulse incident normally on the crystal surface along the ΓM direction. However, the crystal geometry did not allow performing similar measurements along the ΓK direction. To investigate crystal properties along this direction, a new 12-layer crystal was constructed by removing the required number of rods from the prism-shaped crystal. The resulting crystal [Figure 5.1.1] made it possible to make the transmission experiment with an input pulse incident along the ΓK direction. Unfortunately, the lateral extent of this crystal was smaller than the one for the crystal used in measurement along the ΓM direction (53 mm wide and 90 mm high as opposed to 76 mm and 140 mm), which made the role of edge effects potentially more important in the final result of the ΓK experiment.

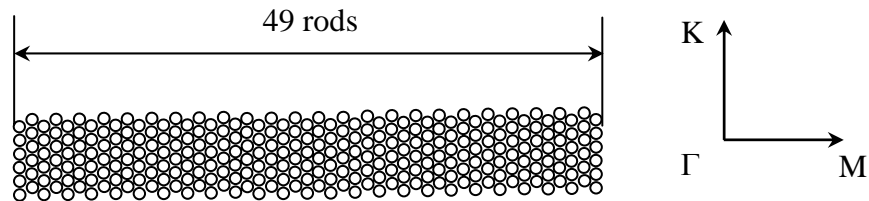


Figure 5.1.1: 12-layer rectangular-shaped 2D phononic crystal obtained from the prism-shaped one by removing the required number of rods.

To explore different frequency regions, several pairs of flat circular Panametrics transducers with central frequencies of 0.10, 0.25, 0.50 and 1.00 MHz were used as generators and receivers of ultrasound. The resulting curves were then combined to produce one net curve to cover all probed frequencies. It was already described in Section

3.5.1 how the transmission coefficient and dispersion curve can be extracted from the data acquired in the transmission experiment. In case of phononic crystals, the dispersion curve can also be viewed as part of the band structure displayed in the extended-zone scheme. The reduced-zone scheme is obtained from the dispersion curve by translating pieces lying outside the first Brillouin zone back into the first zone by the required integer number of reciprocal vectors.

Figure 5.1.2 shows the band structure for our crystals (lattice constant $a = 1.27$ mm, rod diameter $d = 1.02$ mm), calculated with the help of the MST. The theory predicts the existence of a stop band along the ΓM direction extending from 0.52 MHz to 0.68 MHz, as well as a complete band gap in the range of frequencies between 1.04 MHz and 1.18 MHz.

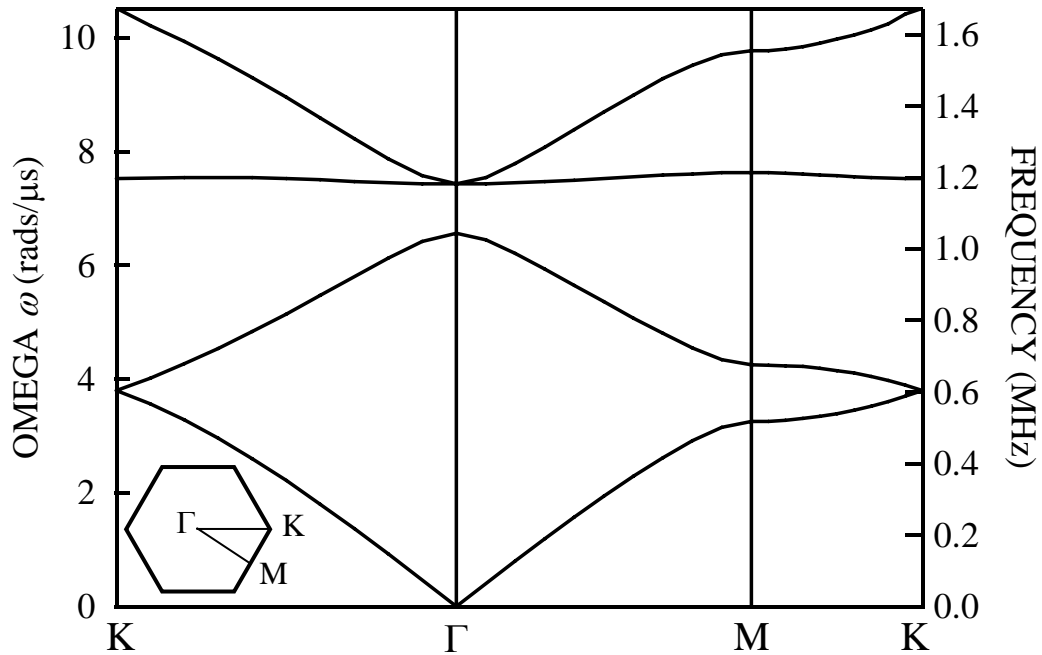


Figure 5.1.2: Band structure of the 2D phononic crystal calculated using the MST. The first Brillouin zone, with the main symmetry directions, is also indicated (Calculations courtesy of Dr. Zhengyou Liu).

The experimentally determined transmission curve along the ΓM direction is shown in Figure 5.1.3. As expected, a dip in transmission is found for frequencies ranging from about 0.49 MHz to 0.69 MHz, in good agreement with the predictions of the band structure calculations. The MST also allows calculation of the transmission coefficient through the crystal. The calculated transmission curve is also presented in Figure 5.1.3. A very good agreement between theory and experiment is observed in terms of both the position and depth of the transmission dip, indicating the reliability of the theory and the good quality of the crystal. The oscillations in transmission observed at the frequencies lying outside the band gap are due to interference of the waves multiply reflected inside the crystal from the crystal boundaries, with the peaks representing the standing-wave modes of the structure.

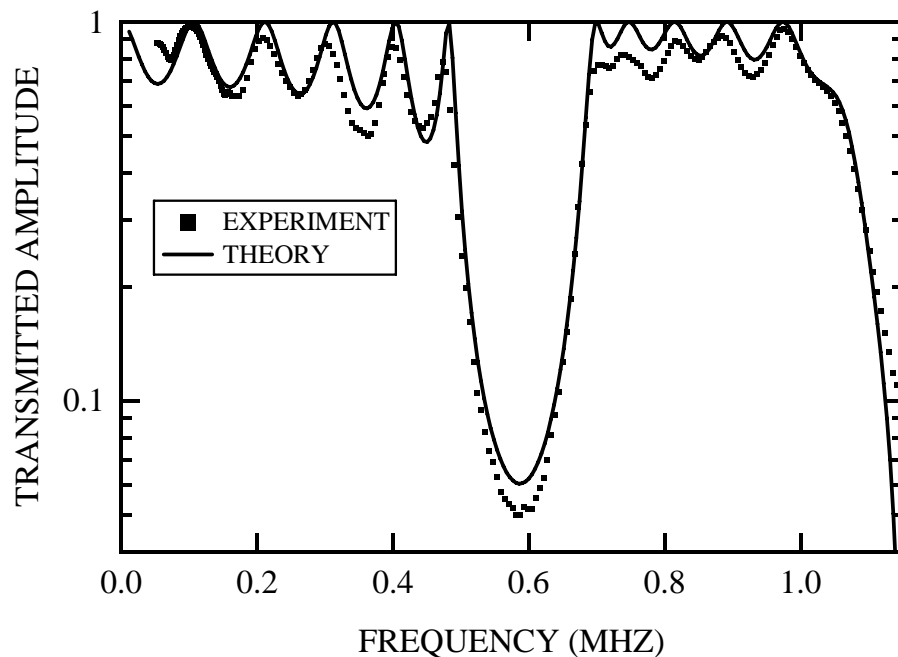


Figure 5.1.3: Experimental and theoretical transmitted amplitudes as a function of frequency for the 6-layer 2D phononic crystal along the ΓM direction.

It is also of interest to look at the agreement between the band structure using the MST and the one derived from the phase information obtained in the transmission experiment. Figure 5.1.4 displays measured dispersion curve in the *extended* zone-scheme, the experimental band-structure in the *reduced* zone-scheme (which is derived from the dispersion curve by translating its various pieces into the 1st Brillouin zone by the required number of reciprocal wavevectors b_1) and the theoretical band structure predicted by the MST (solid line).

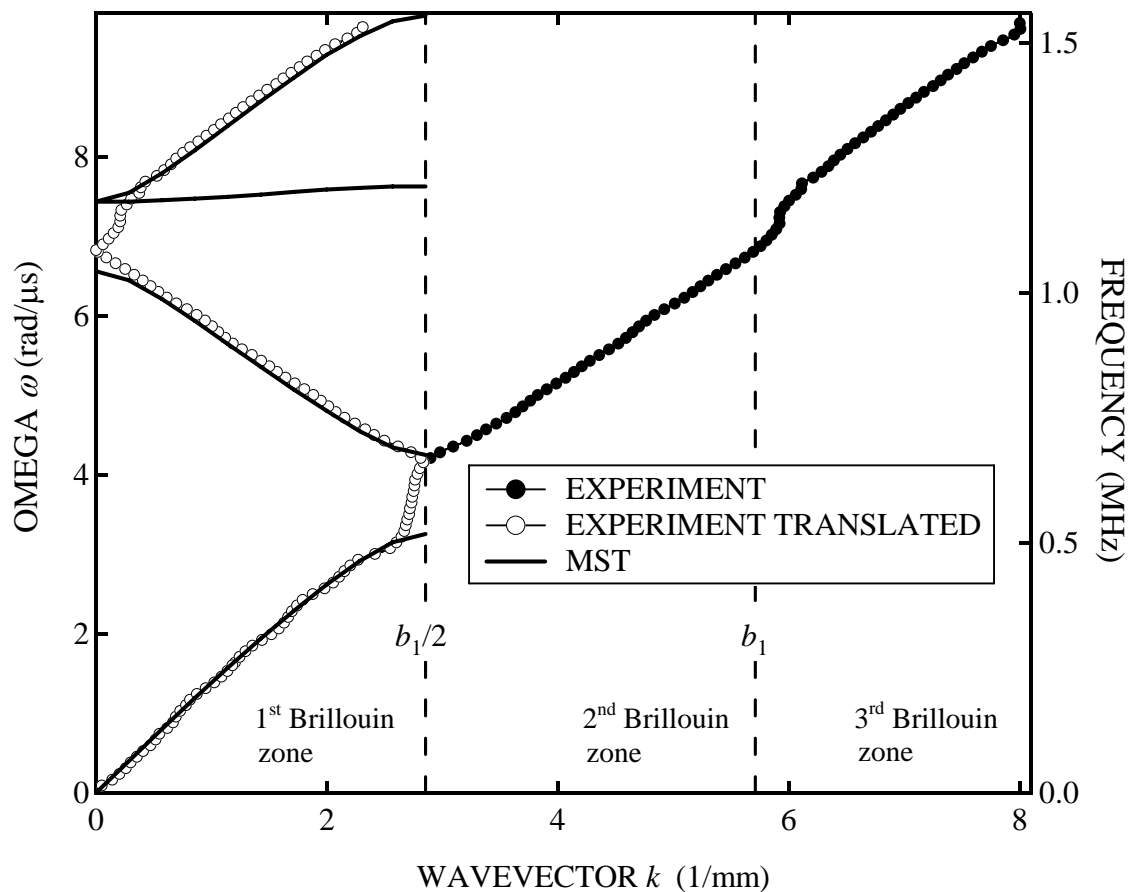


Figure 5.1.4: Comparison of the experimental and theoretical band structure curves for a 6-layer 2D phononic crystal along the ΓM direction. The reciprocal wavevector b_1 ($b_1 = 5.71 \text{ mm}^{-1}$) along the same direction is also indicated.

The agreement between theory and experiment is remarkably good suggesting a high degree of regularity of the phononic crystal.

As was already mentioned, a similar transmission experiment was performed with the phononic crystal shown in Figure 5.1.1 to investigate crystal properties along the ΓK direction. The predicted and measured transmitted amplitudes along this direction are compared in Figure 5.1.5.

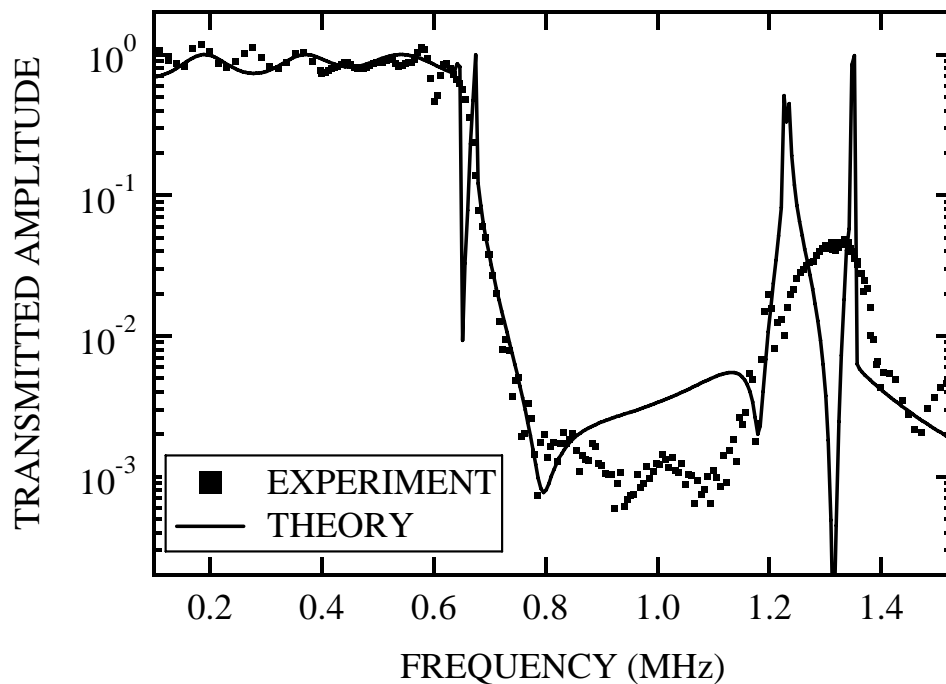


Figure 5.1.5: Experimental and theoretical transmission curves for 2D phononic crystal along the ΓK direction. The experiment was performed on a 12-layer crystal.

From Figure 5.1.5 one can observe that a significant drop in transmission exists in between 0.65 MHz and 1.20 MHz. According to the band structure [Figure 5.1.2], this frequency range covers both the second band in the ΓK direction and the complete band

gap. While the drop in the transmission at the frequency range corresponding to the complete gap (from 1.04 MHz to 1.18 MHz) is completely predictable from the band structure, the sharp plunge in the transmission at frequencies corresponding to the 2nd band (from 0.60 MHz to 1.04 MHz) was not initially expected. Additional information, which is helpful for understanding the origin of this transmission drop, is obtained by observing Figure 5.1.6, which compares the calculated band structure and the dispersion curve. The experimental dispersion curve lines up perfectly with the calculated band structure within the 1st Brillouin zone.

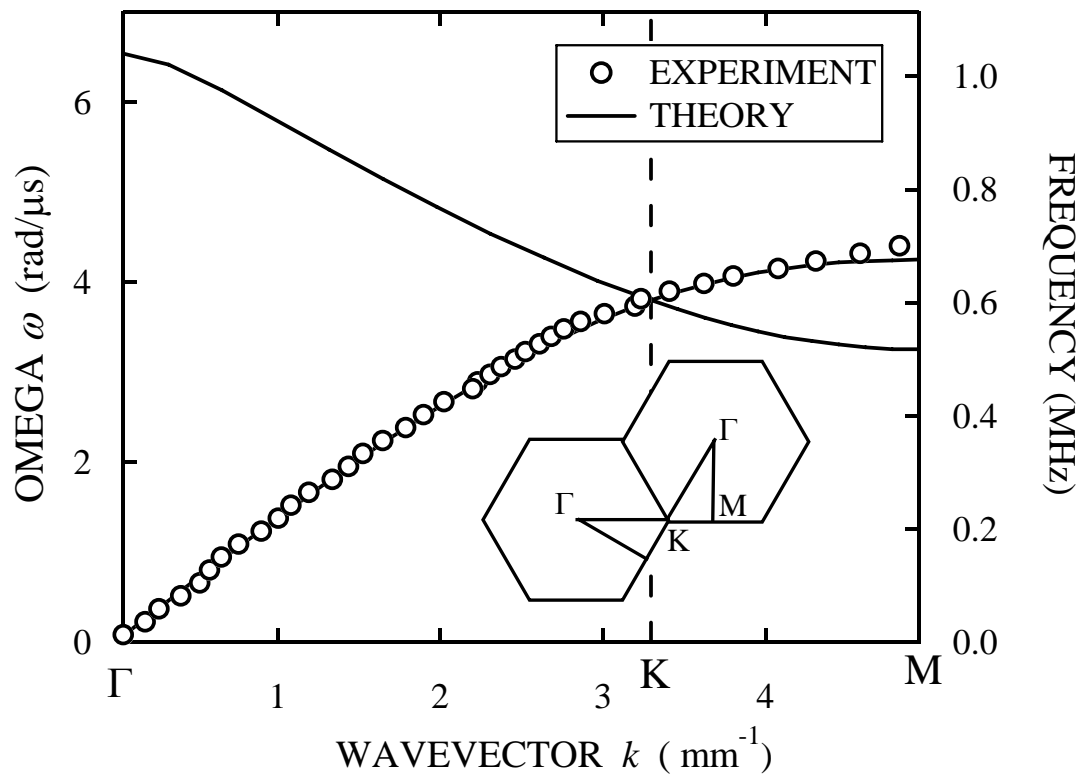


Figure 5.1.6: Experimental and theoretical band structure curves for a 12-layer 2D phononic crystal along the Γ K direction.

Beyond the 1st Brillouin zone boundary, different behaviour is observed. From Figure 5.1.6, one can see that just outside of the 1st zone the data follow the theory along the *edge* between two Brillouin zones in the KM direction (see the inset in Figure 5.1.6), implying that there is coupling to these KM modes instead of modes in the 2nd band along the Γ K direction. No coupling of the incident wave to the modes in the 2nd band along the Γ K direction is consistent with the observed drop in transmission [Figure 5.1.5]. For the experimental configuration used in these experiments (see Section 3.5.1), the comparison of the cumulative phases of the sample and reference pulses (which is how the dispersion curve is extracted) has meaning only when the output pulse is propagating in the same direction as the input pulse, i.e. normal to the crystal surface. This condition may not be met when the incident field cannot couple to the modes of the crystal along the Γ K direction. The brief explanation for this behaviour along the Γ K direction is that the 2nd band modes and incident plane wave have different symmetries, which are inconsistent with each other. This question will be addressed in more depth and detail in the next section while presenting results of different experiments on negative refraction of the ultrasound waves.

The agreement between theoretical and experimental transmission curves in the case of the Γ K direction is not as good as in the Γ M direction. Some of the sharp peaks in transmission predicted by the theory are not observed in the experiment [Figure 5.1.5], most likely due to absorption, which was not taken into account in the calculations and is always present in real samples. But in general, there is a good agreement between theory and experiment in *both* symmetry directions for my system. This overall agreement establishes the MST as a theory capable of providing an accurate description of wave

propagation in 2D phononic crystals. Another extremely important outcome of the transmission experiments reported in this section is that they enabled me to delineate the appropriate frequency range for negative refraction experiments.

5.1.2 Negative refraction experiments with the 2D prism-shaped crystal

This section reports the results of the various negative refraction experiments conducted with the 2D prism-shaped phononic crystal. Since all the experiments were conducted in water, it was important to ensure before the experiment that no air bubbles were trapped between the crystal's rods. This was achieved by slowly immersing the crystal into the water and by lightly tapping the rods (while underwater) to drive out any remaining air bubbles from the crystal. The ultrasound pulses were generated by a flat circular Panametrics transducer, 1.0 inch in diameter, with a central frequency of 1.0 MHz. The distance between the transducer and the sample was always set at 12.5 cm, which ensured that the crystal was placed in the far-field of the generator. The field emerging from the output side of the prism was mapped using the hydrophone, as was already explained in Section 3.5.2.

In the first negative refraction experiment, the input pulse was incident normally on the shortest side of the prism along the ΓM direction. The centre of the transducer face was aligned with the central point of the crystal surface. Two masks, made out of thin rectangular-shaped plastic sheets, were attached to the outer edges of the crystal input face to prevent any stray sound from reaching the hydrophone. The plastic pieces were wrapped with several layers of Teflon tape to increase absorption of incident sound. The field was scanned in a rectangular grid lying in the x - z plane. For the best resolution, grid points were separated by a distance of 0.5 mm along both the x and z -axis. The closest

line of the grid was about 1 mm away from the crystal output surface. Figure 5.1.7 shows the geometry of the experiments.

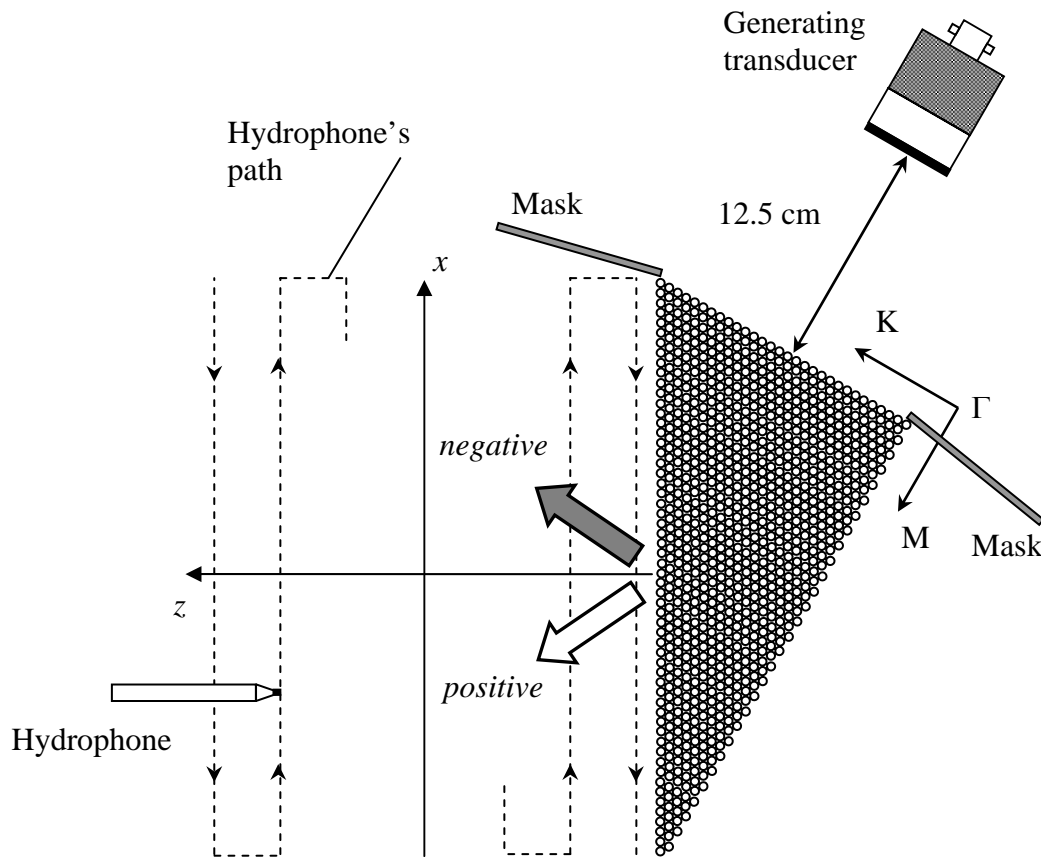


Figure 5.1.7: Negative refraction experiment geometry.

As the ultrasound pulse arrives normal to the water/crystal interface (i.e., input side of the prism), we can expect it to penetrate into and continue propagating inside the crystal without any change of its original direction (see Section 2.2.1). The question under study is the following: how will the pulse behave upon crossing the crystal/water interface as it leaves the crystal, or, more specifically, will it be refracted positively or

negatively (see Fig. 5.1.7)? According to the theory presented in Section 2.2.1, the outgoing pulse is expected to refract on the negative side of the normal to the interface.

Figure 5.1.8(a) represents a snap-shot of the outgoing pulse obtained from the scanned field after digitally filtering it with a Gaussian bandwidth centred at a frequency lying at about middle of the 2nd band (0.85 MHz), while Figure 5.1.8(b) displays the same field filtered at a lower frequency (0.75 MHz).

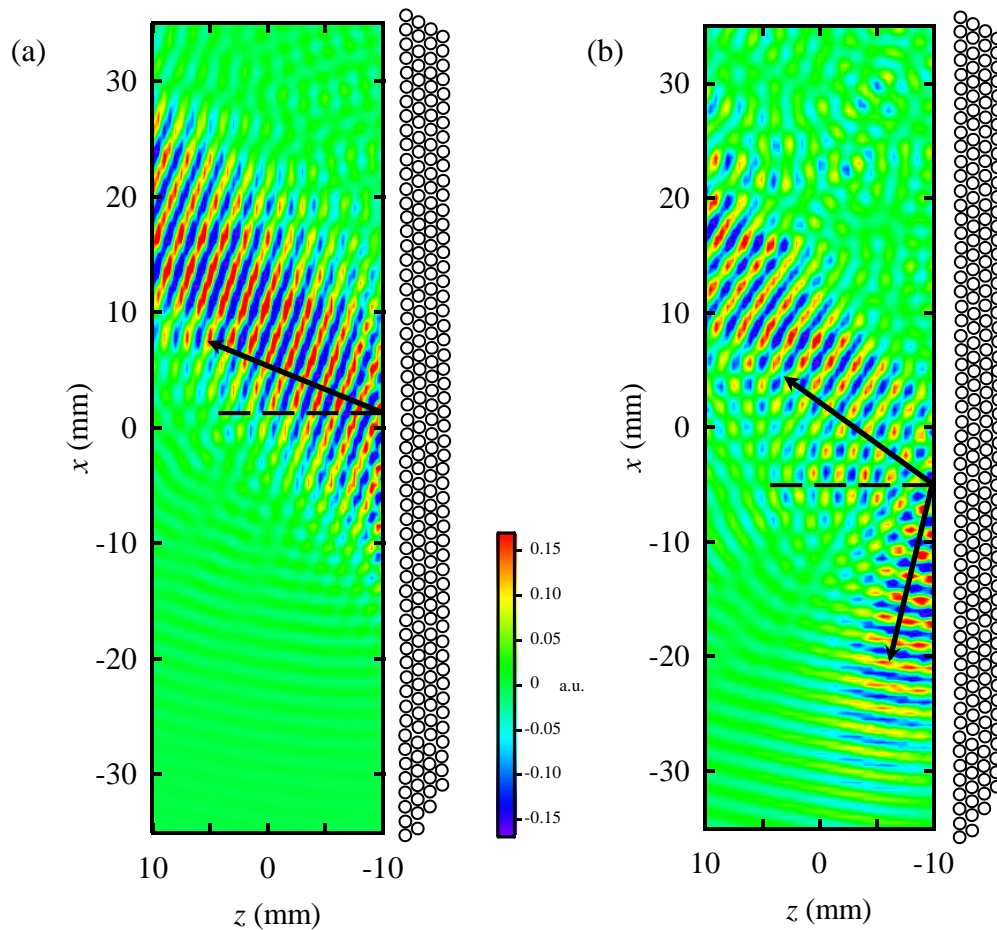


Figure 5.1.8: Outgoing pulses in the negative refraction experiment filtered at (a) 0.85 MHz and (b) 0.75 MHz. The crystal position is also indicated with the crystal surface located at the plane $z = -11$ mm.

From Figure 5.1.8(a), it can be seen that the outgoing pulse with the central frequency of 0.85 MHz is indeed refracted negatively, in complete agreement with our expectations based on the theoretical predictions. However, analysis of the field at 0.75 MHz [Figure 5.1.8(b)] reveals a somewhat unexpected result: the existence of *both* negatively and positively refracted outgoing pulses!

To understand the latter result qualitatively, we have to take into account that once the input pulse has entered the crystal, it no longer can be represented by a simple plane wave. Instead, it is transformed into a Bloch wave, which is a very complicated field pattern inside the crystal, and can be viewed as a superposition of many plane waves. In the particular case of the input pulse incident along the ΓM direction, the Bloch wave consists of many plane waves, with each plane wave characterized by its own wave vector and with all these wave vectors differing from one another by an integer number of the reciprocal wavevectors \vec{b}_1 and \vec{b}_2 . We can also think of these plane waves as all modes in the repeated-zone scheme corresponding to one frequency. All such modes can be obtained from one another by adding the required number of reciprocal wavevectors. Let us consider just two dominant modes characterized by wave vectors \vec{k}_{red} and $\vec{k}_{ext} = \vec{k}_{red} + \vec{b}_1$, where \vec{k}_{red} corresponds to the mode in the reduced-zone scheme and is *antiparallel* to the group velocity \vec{v}_g , while \vec{k}_{ext} corresponds to the mode lying in the extended-zone scheme and points in the *same* direction as \vec{v}_g [Figure 5.1.9]. Note that the disturbances created by both modes inside the crystal still propagate in the same direction, as the direction of \vec{v}_g is the same in both cases (recall that the direction of \vec{v}_g ,

or equivalently the direction of energy propagation inside the crystal, is given by the direction of the gradient of frequency ω as a function of a wave vector k).

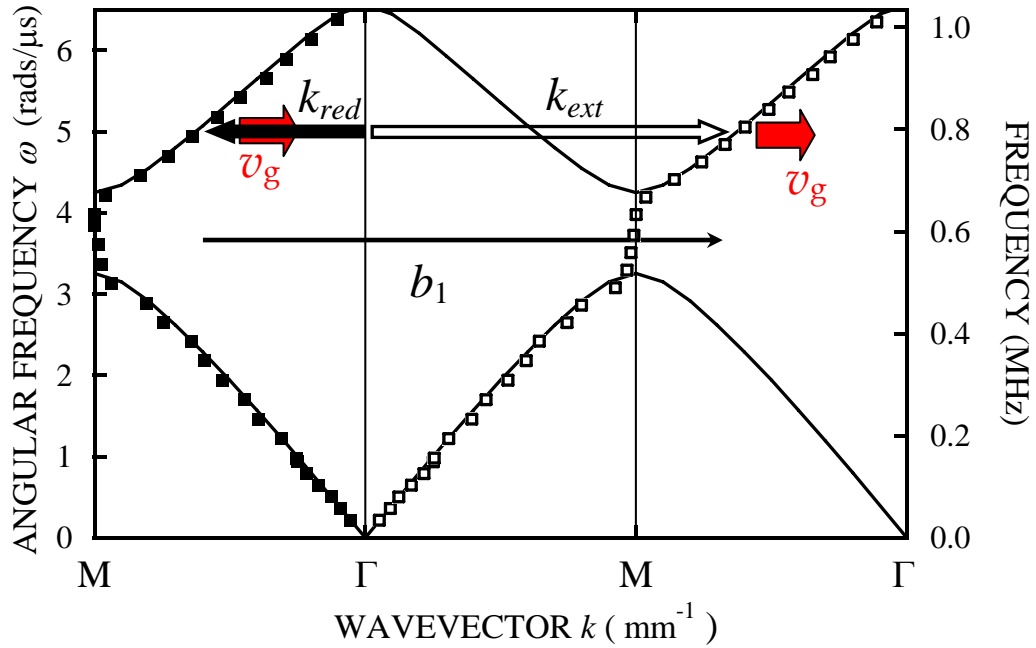


Figure 5.1.9: Experimentally measured band structure displayed in the reduced-zone (solid symbols) and extended-zone (open symbols) schemes. The wide short arrows indicate the direction of the group velocity, while the narrower arrows represent the wavevectors.

After the Bloch wave reaches the crystal/water interface, the two dominant modes \vec{k}_{red} and \vec{k}_{ext} are refracted according to Snell's law, which requires the parallel component of the wave vector to be conserved when a plane wave propagates through a boundary separating two different media. It is obvious from Figure 5.1.10 that we have to observe two types of refraction simultaneously: the mode with \vec{k}_{red} will be refracted negatively, while the mode characterized by \vec{k}_{ext} will be refracted positively.

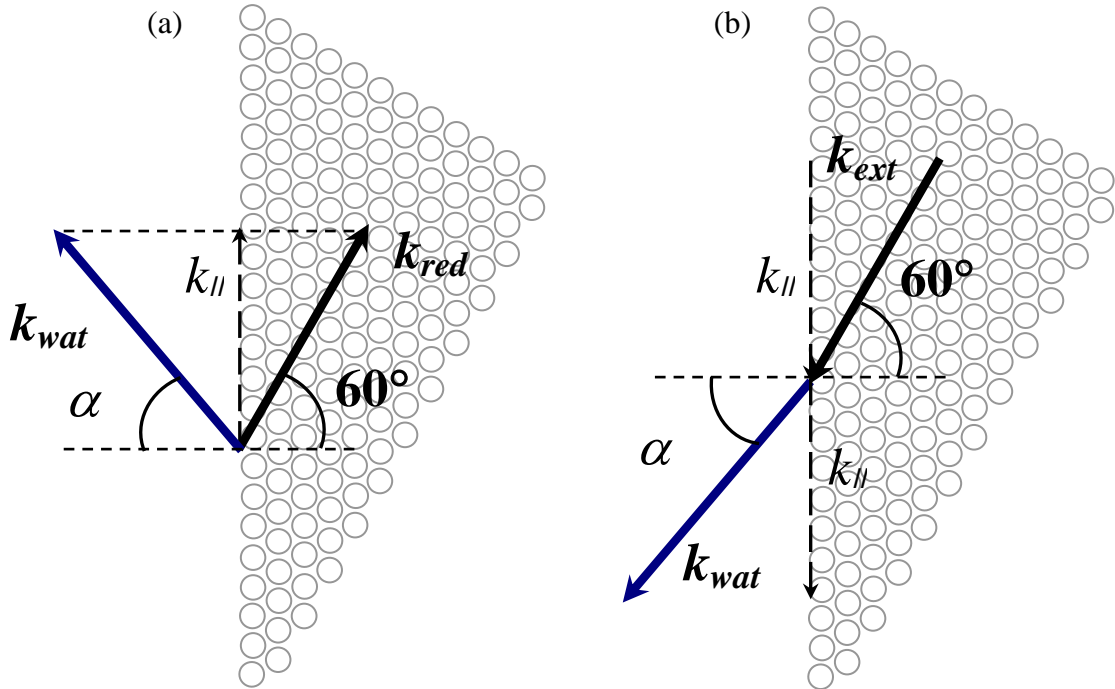


Figure 5.1.10: Negative (a) and positive (b) refraction at the crystal/water interface. Note that the parallel component of the wavevector $k_{||}$ is conserved in both cases.

This qualitative explanation can also be confirmed by a quantitative analysis. From the 2nd band equifrequency contours calculated by the MST, we can obtain the values of both \vec{k}_{red} and \vec{k}_{ext} . As the angle of incidence is the same (60°) for both modes, we can calculate the refraction angle α for positively and negatively refracted waves with Snell's law:

$$k_{wat} \sin(\alpha) = k_{cryst} \sin(60^\circ) \quad (5.1)$$

where k_{cryst} denotes the magnitude of either \vec{k}_{red} or \vec{k}_{ext} and k_{wat} is the magnitude of the wave vector in water. The calculated refraction angle is then compared with the one observed in the experiment (as measured from Figure 5.1.8). At 0.75 MHz, expression

(5.1) predicts the angle α to be 34° and 82° for negatively and positively refracted waves, respectively (here $k_{red} = 2.1 \text{ mm}^{-1}$ and $k_{ext} = 3.6 \text{ mm}^{-1}$). The refraction angles measured from Figure 5.1.8(b) give $34^\circ \pm 1^\circ$ for the negatively refracted wave and $81^\circ \pm 1^\circ$ for the positively refracted one, which is in excellent agreement with the angles predicted by the theory.

An immediate question to be asked is: why is there no positively refracted wave at the frequency 0.85 MHz? When the corresponding values are substituted into (5.1), one finds that $\frac{k_{ext} \sin(60^\circ)}{k_{wat}} > 1$ (with $k_{ext} = 4.1 \text{ mm}^{-1}$ and $k_{wat} = 3.5 \text{ mm}^{-1}$). The formal explanation then is that the wave corresponding to the mode with the extended-zone wave vector \vec{k}_{ext} undergoes the effect known as total internal reflection. At this frequency (and at all other higher frequencies in the 2nd band) the mode with \vec{k}_{ext} cannot couple to the outside medium. Table 5.1.1 provides the predicted magnitudes of \vec{k}_{red} and \vec{k}_{ext} for different frequencies, while Table 5.1.2 summarizes the results obtained in the experiment with the 2D prism-shaped phononic crystal. The experimental results are in perfect agreement with the predictions of the MST.

FREQUENCY (MHz)	$k_{red} \text{ (mm}^{-1}\text{)}$	$k_{ext} \text{ (mm}^{-1}\text{)}$
0.75	2.1	3.6
0.85	1.4	4.3
0.90	1.1	4.6
0.95	0.82	4.9
1.00	0.49	5.2

Table 5.1.1: The predicted magnitudes of \vec{k}_{red} and \vec{k}_{ext} for some frequencies.

FREQUENCY (MHz)	Negative refraction angle		Positive refraction angle	
	Predicted	Measured	Predicted	Measured
0.75	34.0°	34°±1°	81.0°	82°±1°
0.85	20.4°	21°±1°	-	-
0.90	15.0°	16°±1°	-	-
0.95	10.2°	10.5°±1°	-	-
1.00	6.0°	6°±1°	-	-

Table 5.1.2: Comparison between experimentally measured and theoretically calculated angles of refraction.

As was just mentioned, the absence of the positively refracted pulses at frequencies higher 0.75 MHz can be formally explained by total internal reflection, which the component of the Bloch wave with wavevector \vec{k}_{ext} undergoes at the crystal/water interface. In order to see if this explanation is correct, I performed another mapping experiment analogous to the one shown in Figure 5.1.7, but this time the opposite side of the prism crystal was scanned, as shown in Figure 5.1.11. If the \vec{k}_{ext} component of the Bloch wave is indeed reflected inside the crystal at the crystal/water interface, it should travel to the opposite side of the prism and refract *positively* into the outside medium (water). As can be seen from the simple ray diagram depicted in Figure 5.1.12, the \vec{k}_{ext} component should be incident at the angle of 30° at the normal to the interface. Therefore, the angle of refraction β into the water can be easily calculated with Snell's law using values from Table 5.1.1 and then compared with the experimentally observed angle.

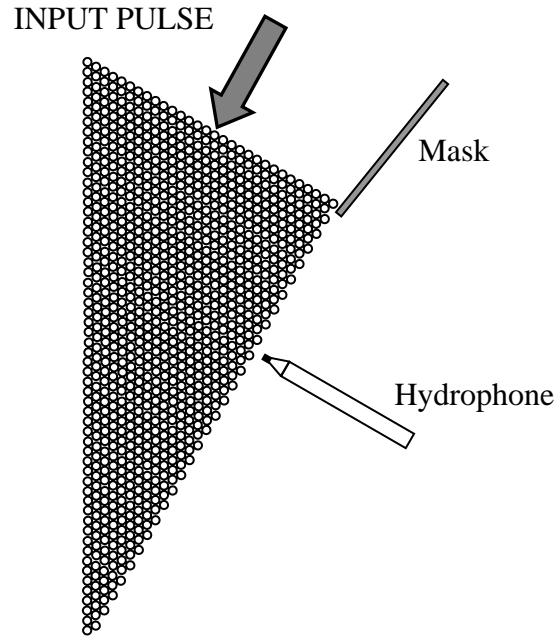


Figure 5.1.11: The scan of the opposite side of the prism-shaped crystal.

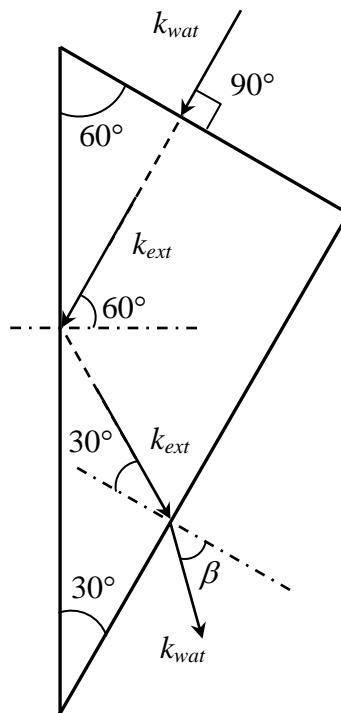


Figure 5.1.12: Ray diagram of the experiment considered in Figure 5.1.11.

The images of the field emerging on the opposite side of the prism crystal are shown in Figures 5.1.13(a)-(b) for frequencies 0.85 and 0.95 MHz. A positively refracted beam can be seen leaving the crystal surface for both frequencies. Excellent agreement is observed between measured and calculated refraction angles β . At 0.85 MHz one measures from Figure 5.1.13(a) the refraction angle of $36.5^\circ \pm 1^\circ$, while Snell's law predicts the value of 36.6° . At 0.95 MHz the measured and predicted angles are $37.5^\circ \pm 1^\circ$ and 37.6° , respectively.

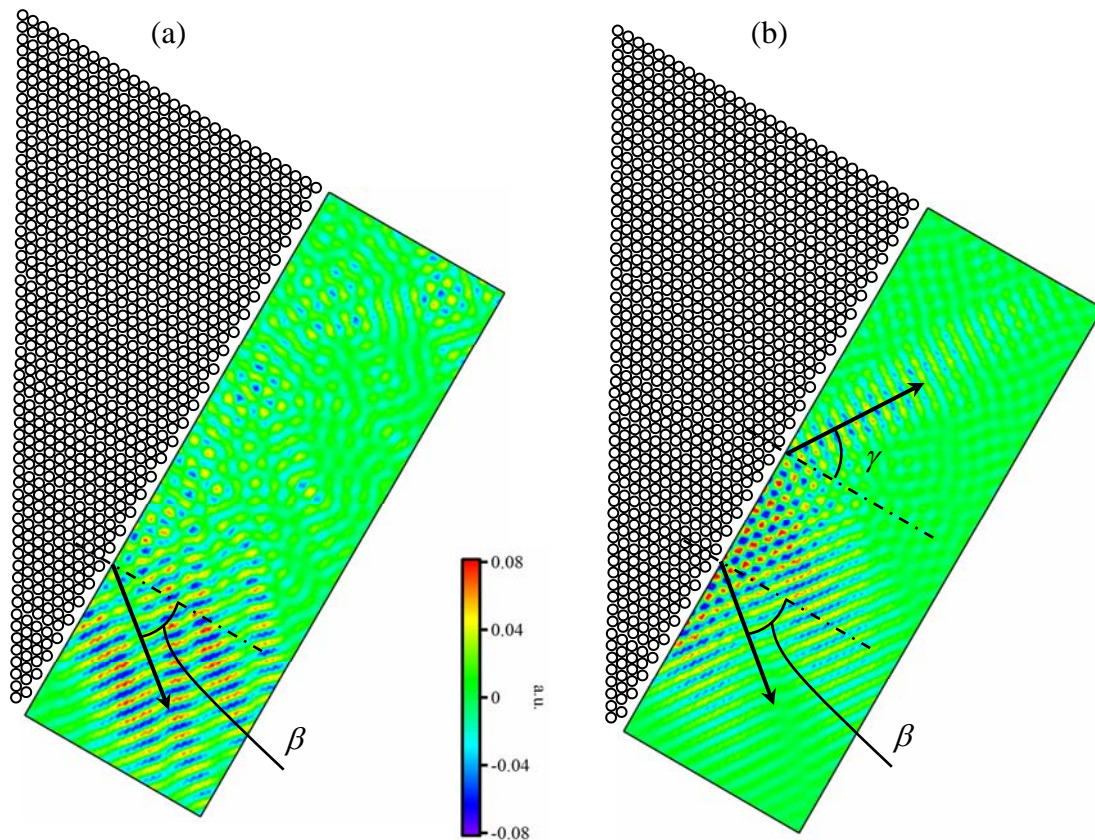


Figure 5.1.13: Images of the emerging field at (a) 0.85 MHz and (b) 0.95 MHz frequency.

Yet another intriguing result can be derived from Figure 5.1.13(b): a presence of the second weaker beam, which is refracted negatively! The average angle of refraction γ of the second beam was measured to be $53.5^\circ \pm 1^\circ$. To understand the origin of the negatively refracted beam in this case, one should take into account the periodicity of the crystal's surface. Due to this periodicity, the component of the wavevector parallel to the crystal surface \vec{k}_\parallel can assume any values differing from each other by an integer number of *surface* reciprocal vectors \vec{g}_s , i.e.

$$\vec{k}_\parallel + n\vec{g}_s \quad (5.3)$$

where n is an integer number and $|\vec{g}_s| = 2\pi/a_s$ with a_s equal to the surface period (see, for example, Every *et al.* [70]). Different parallel components \vec{k}_\parallel (given by (5.3)) will then produce beams in water refracted at different angles provided that the condition $|\vec{k}_\parallel| \leq |\vec{k}_{wat}|$ holds, since otherwise no coupling to water occurs. Let us first illustrate this idea to explain the presence of the positively refracted beam observed at 0.75 MHz [Figure 5.1.8(b)]. As follows from (5.1) and Figure 5.1.9

$$k_{wat} \sin(\alpha) = k_{cryst} \sin(60^\circ) = \left(|\vec{b}_1| - k_{red} \right) \sin(60^\circ)$$

Taking into account that $|\vec{b}_1| = 4\pi/\sqrt{3}a$ (see Section 2.1.2), the above expression assumes the following form:

$$k_{wat} \sin(\alpha) = 2\pi/a - k_{red} \sin(60^\circ) = g_{LM} - k_\parallel \quad (5.4)$$

where $g_{\Gamma M}$ denotes a reciprocal vector along the crystal surface perpendicular to the ΓM direction. One can see that the description of the refraction through the crystal/water interface with the help of reciprocal vectors along the surface is equivalent to the one in which k_{ext} is used instead. Note also that the combination of $\vec{g}_{\Gamma M}$ and \vec{k}_{\parallel} given by (5.4) is the only one that allows coupling to the water, as all other combinations produce wavevectors exceeding the magnitude of the wavevector in water at 0.75 MHz frequency. The idea leading to equation (5.4) is illustrated in Figure 5.1.14.

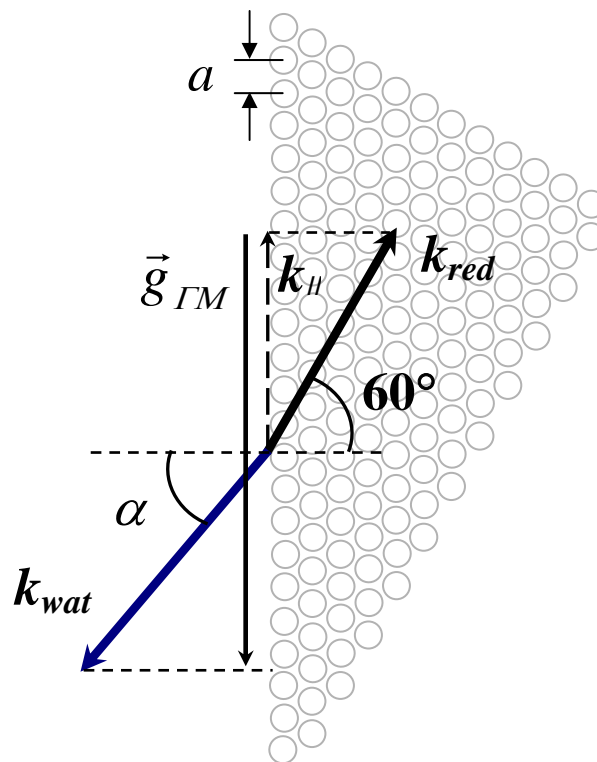


Figure 5.1.14: The positively refracted beam at the crystal/water interface originates from the parallel component of the wavevector k_{\parallel} modified by the reciprocal surface vector $g_{\Gamma M}$.

In much the same way, the results of the experiment involving the scan of the other side of the prism-shaped crystal can be explained. For example, the appearance of the positively refracted beams at both 0.85 MHz and 0.95 MHz frequencies is due to *subtraction* of k_{\parallel} from the reciprocal vector $g_{\Gamma K}$ along the surface perpendicular to the ΓK direction, as can be easily verified:

$$k_{wat} \sin(\beta) = k_{red} \sin(30^\circ) = 2\pi/\sqrt{3}a - k_{red} \sin(30^\circ) = g_{\Gamma K} - k_{\parallel} \quad (5.5)$$

since the surface period in the direction perpendicular to the ΓK direction is $\sqrt{3}a$. Similarly, one finds that the refraction angle γ observed for the negatively refracted beam at 0.95 MHz is in excellent agreement with the one predicted by the following expression:

$$k_{wat} \sin(\gamma) = 2\pi/\sqrt{3}a + k_{red} \sin(30^\circ) = g_{\Gamma K} + k_{\parallel} \quad (5.6)$$

From (5.6), one finds for the angle γ the value of 54.5° , whereas the measured value is $53.5^\circ \pm 1^\circ$. In case of 0.85 MHz, equation (5.6) predicts the value of 88° meaning that $g_{\Gamma K} + k_{\parallel}$ is very close to not being able to couple to the water because of total internal reflection, and this is probably the reason why it is not observed in the experiment. A schematic diagram visualizing expressions (5.5) and (5.6) is given in Figure 5.1.15. For the sake of clarity, the picture zooms in on a small part of the crystal surface.

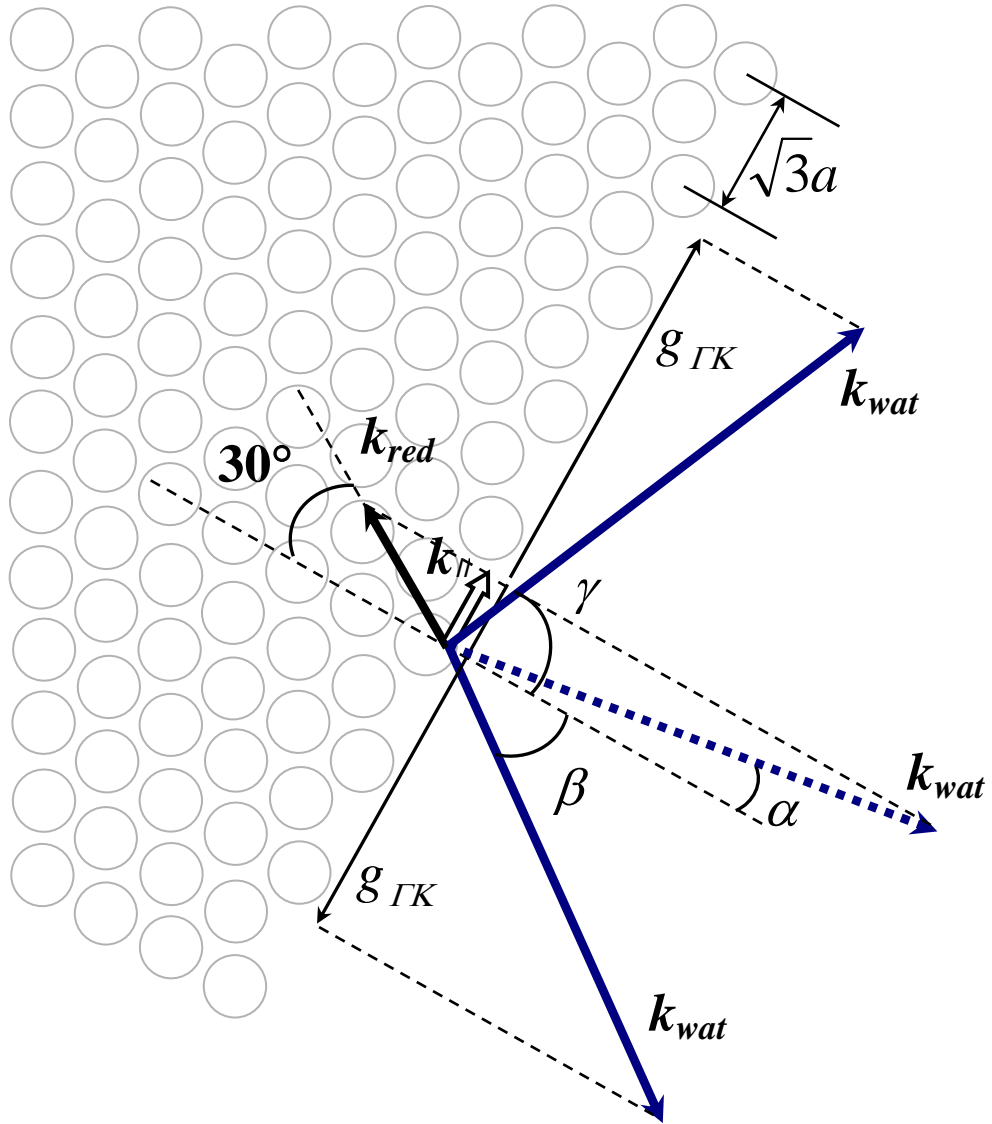


Figure 5.1.15: Negatively and positively refracted beams at the crystal/water interface perpendicular to the ΓK direction. Note that the negatively refracted beam, which originates from the unmodified component k_{\parallel} (indicated by a dashed arrow), is not observed in the experiment.

Positively and negatively refracted beams, observed while scanning the opposite side of the prism-shaped crystal, originate from the parallel component of the wavevector *modified* by addition or subtraction of the reciprocal surface vector $g_{\Gamma K}$. However, in the

same experiment one would expect to observe another negatively refracted beam originating from the *unmodified* parallel component k_{\parallel} . This beam is indicated by a dashed arrow in Figure 5.1.15. From Snell's law one finds the corresponding angle of refraction α to be 11.6° at 0.85 MHz and 5.9° at 0.95 MHz, i.e. the third beam is expected to emerge almost normally from the crystal surface. The reason for the absence of the second negatively refracted beam will be discussed later in this section.

It is always desirable to check our understanding of any physical phenomenon in as many different experiments as possible. One of the possible checks in our case would be performing a variation of the previous experiment in which input pulse is centred at lower frequency and couples to the mode lying in the 1st band of the crystal. The principal difference of this experiment from the first one is that, for any mode in the 1st band, the corresponding wave vector k will be *parallel* to the gradient of $\omega(k)$ [Figure 5.1.16].

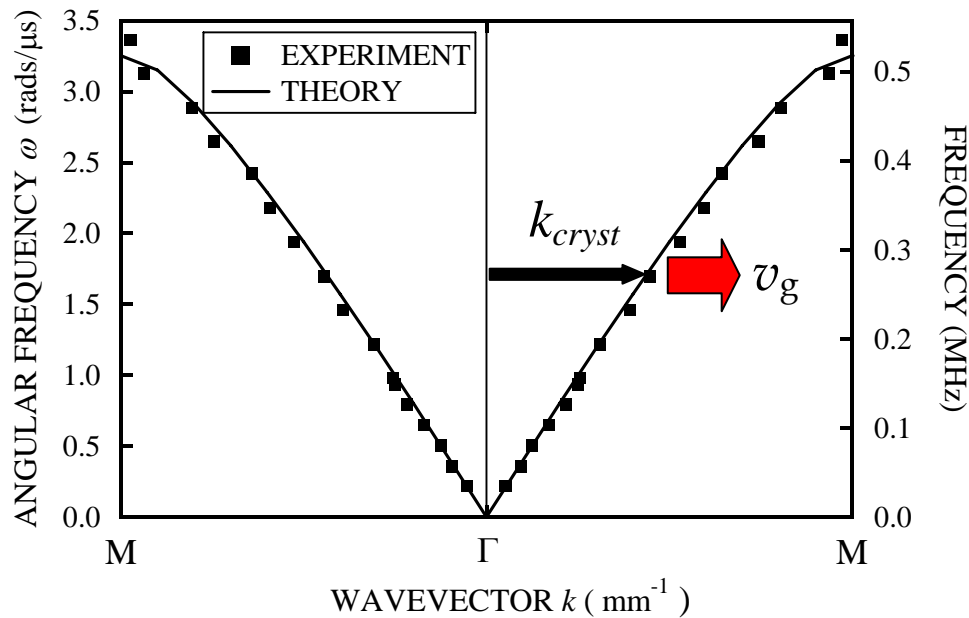


Figure 5.1.16: 1st band of the 2D phononic crystal. For *any* mode in the 1st band, the corresponding wave vector k_{cryst} coincides with the direction of v_g .

If our understanding and explanation of the first experiment are correct, upon crossing the crystal/water interface the Bloch wave must transform into a *positively* refracted outgoing pulse, as shown in Figure 5.1.10(b). The geometry of the experiment at lower frequencies was identical to the first experiment (see Figure 5.1.7). As a generating transducer I used a flat circular Panametrics transducer, 1.5-inch in diameter, with a central frequency of 0.25 MHz, which lies approximately in the middle of the 1st band. Figure 5.1.17 presents a snapshot of the field observed at some particular moment of time. The outgoing pulse is indeed refracted positively, in complete agreement with our expectations.

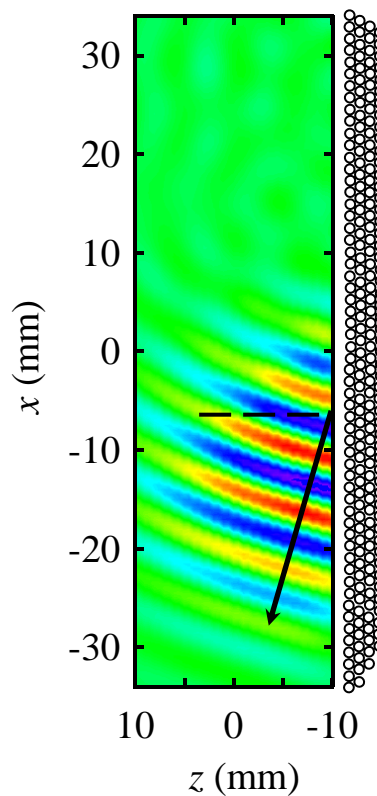


Figure 5.1.17: Snapshot of the outgoing pulse in the experiment probing the behaviour at frequencies lying in the 1st band. The picture was obtained by filtering the original field with a Gaussian bandpass filter centered at 0.25 MHz and 0.05 MHz wide. As in Figure 5.1.8, the colour scale is in arbitrary units, with wave crests and troughs indicated with red and blue correspondingly and green corresponding to zero amplitude.

The quantitative agreement between theory and experiment is also good. According to the calculated band structure [Figure 5.1.2], the magnitude of the wave vector k_{cryst} corresponding to the 0.25 MHz mode is 1.14 mm^{-1} . With the wave vector in water at this frequency being 1.05 mm^{-1} , expression (5.1) predicts the refraction angle to be 69.5° . There is some ambiguity associated with measuring the angle of refraction from Figure 5.1.17, as the edges of the outgoing pulse are slightly curved, but the measured angle falls in the range of $72^\circ \pm 2^\circ$, which is in good agreement with the calculated value.

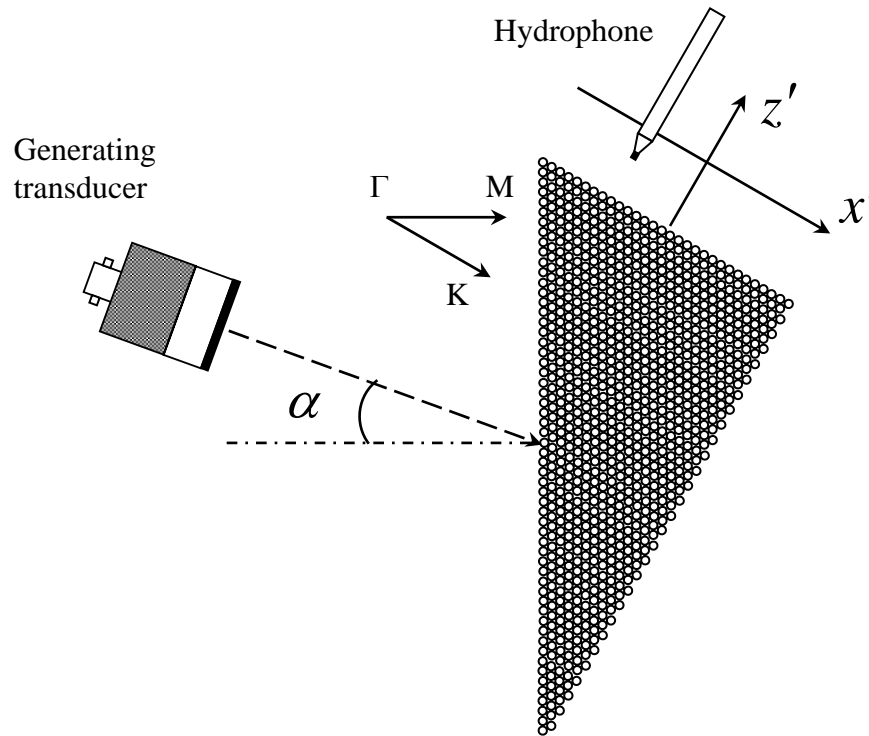


Figure 5.1.18: Geometry of the inverse experiment.

The experiments with the input pulse incident on the smallest side of the prism-shaped crystal along the ΓM direction convincingly demonstrated the negative refraction

effect at frequencies of 0.75 MHz and 0.85 MHz, and the lower frequency experiment at 0.25 MHz further confirmed the validity of the interpretation of the observed phenomena. However, in the above experiments the input pulse was incident *normal* to the crystal surface. For the sake of completeness, it would also be desirable to demonstrate the negative refraction of ultrasound waves with the input pulse incident at an angle other than 90° to the crystal surface. To achieve this, I have conducted an experiment *inverse* to the previous one, with the ultrasound generator and receiver switched and the input pulse incident at an angle on the longest side of the crystal. The geometry of the new experiment is shown in Figure 5.1.18.

As was already mentioned in Section 2.2.1, calculations using the MST predict a circular shape for the equifrequency contours in the 2nd band, implying that, in this frequency range, the wavevector and the direction of energy propagation (or v_g) are antiparallel *irrespective* of the direction inside the crystal. This fact plays a crucial role in understanding what happens in the experiment pictured in Figure 5.1.18 after the input pulse couples to the modes in the 2nd band. Because of the circular shape of the equifrequency contours, the incident pulse will refract *negatively* as it crosses water/crystal interface. The ensuing disturbance will then propagate through the crystal with the associated wavevector k_{cryst} being *antiparallel* to the direction of its propagation (given by v_g) and refract *negatively* one more time as it emerges on the side scanned by the hydrophone. The process of the negative refraction of the input pulse through the crystal/water interface is also explained in Figure 5.1.19, while Figure 5.1.20 provides a ray diagram of the inverse experiment showing that a propagating pulse is expected to undergo the negative refraction *twice*.

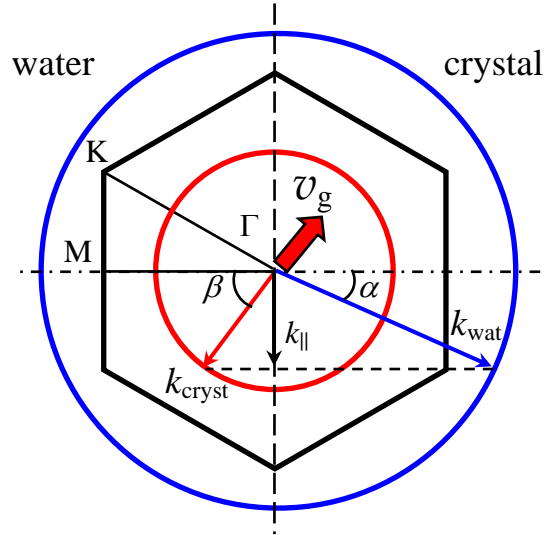


Figure 5.1.19: 1st Brillouin zone, water and crystal equifrequency contours. Note that negative refraction of the incident wave, as well as opposite directions of the wavevector k_{cryst} and v_g , is ensured by the circular shape of the crystal equifrequency contour.

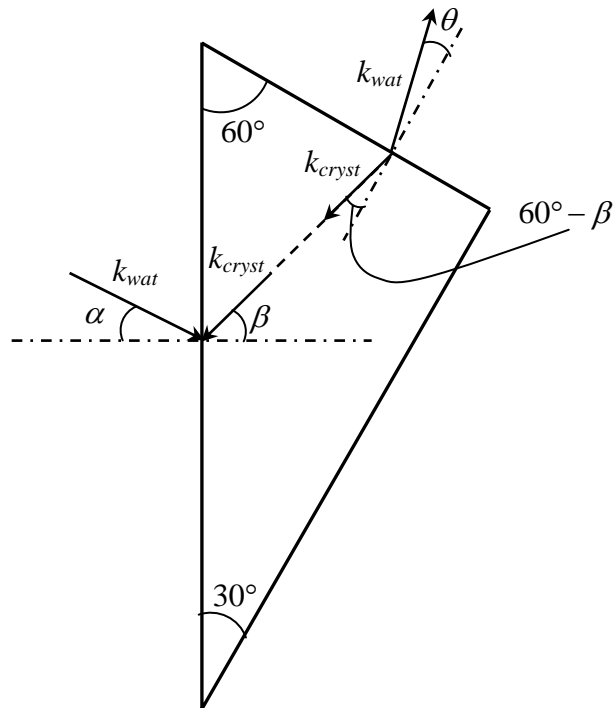


Figure 5.1.20: Ray diagram of the inverse experiment.

In the actual experiment, the magnitude of the angle of incidence α was chosen to be 20° , which was very close to the refraction angle measured in the first negative refraction experiment for the outgoing pulse at a frequency of 0.85 MHz. With this particular angle of incidence, the input pulse with a central frequency of 0.85 MHz should refract negatively into the crystal at angle $\beta = 60^\circ$, propagate through the crystal and emerge *normally* from the output side. At 0.85 MHz, the new experiment is the *inverse* of the first one in the sense that the input pulse follows an *inverse path* as compared to the path of the input pulse in the first experiment. Angles of refraction β and θ at some other frequencies can be found with the help of Snell's law and the values of the corresponding wavevectors inside the crystal k_{cryst} calculated by the MST.

Figures 5.1.21 and 5.1.22 present two snapshots of the outgoing pulses in the inverse experiment obtained by filtering the recorded field at frequencies of 0.85 MHz and 0.75 MHz, respectively. It is clear that at 0.85 MHz [Figure 5.1.21] the outgoing pulse emerges perpendicular to the crystal surface in complete agreement with our expectations. From Figure 5.1.22 one measures the angle of refraction of $19.5^\circ \pm 1^\circ$, while simple calculations based on Snell's law (see Figure 5.1.20) predict the value of 18.5° for the magnitude of the refraction angle θ at 0.75 MHz. Once again, the agreement between theory and experiment is quite good.

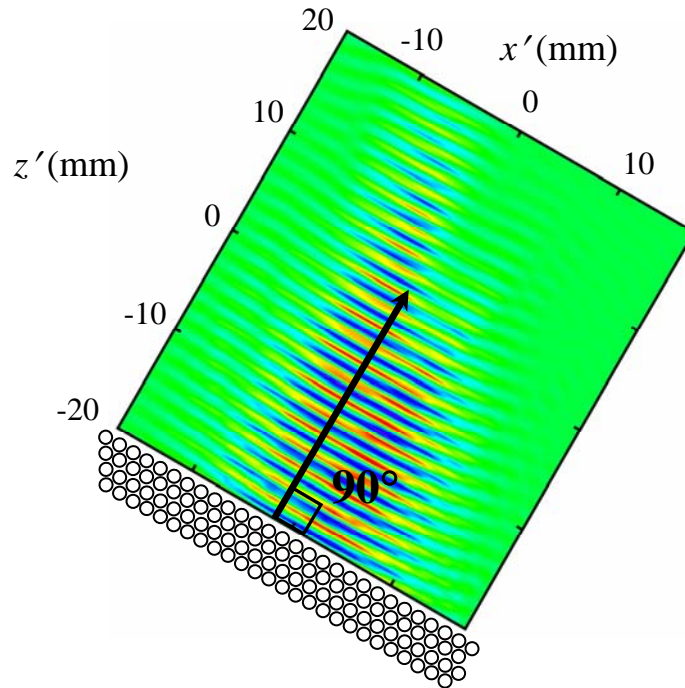


Figure 5.1.21: Snapshot of the outgoing pulse in the inverse experiment obtained by filtering the original field with the Gaussian bandwidth of 0.05 MHz centered at 0.85 MHz. The colour scale is in arbitrary units.

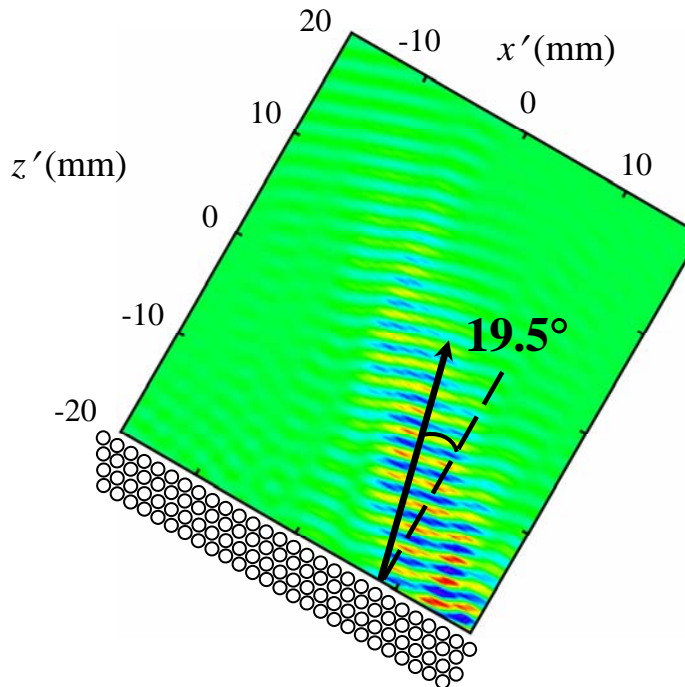


Figure 5.1.22: Snapshot of the outgoing pulse in the inverse experiment obtained by filtering the original field with the Gaussian bandwidth of 0.05 MHz centered at 0.75 MHz. The colour scale is in arbitrary units.

In the two experiments presented so far, negative refraction of ultrasound was demonstrated with the input pulses incident both along, and at some angle to, the ΓM direction. The picture would be incomplete without investigating another direction of high symmetry, namely the ΓK direction. This investigation was done in another experiment, with the input pulse incident normally on the prism's second longest side, which runs perpendicular to the ΓK direction. Figure 5.1.23 explains geometry of this experiment.

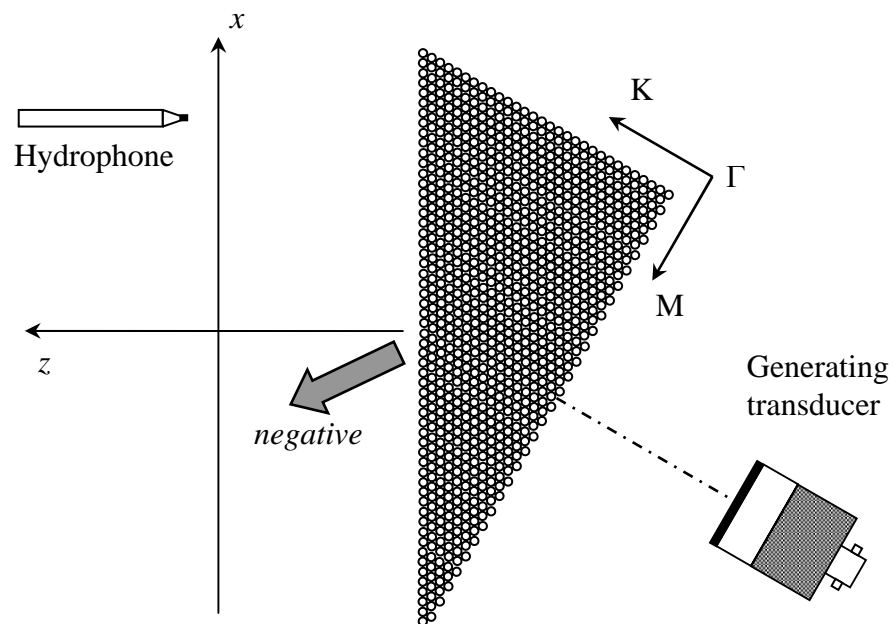


Figure 5.1.23: Geometry of the experiment with the input pulse incident along the ΓK direction.

If the behaviour were similar to the results for the experiment along the ΓM direction, one would expect the input pulse to enter the crystal without a change in its original direction. At the same time, circular equipfrequency contours must ensure that the

dominant wavevector k_{red} associated with the disturbance propagating through the crystal is antiparallel to the direction of propagation. As a result, the outgoing pulse would be expected to emerge on the negative side of the normal to the output surface of the crystal as the disturbance crosses crystal/water interface. One would anticipate the entire experiment along the ΓK direction to be quite similar to the one along the ΓM direction. However, the field measured in the experiment along the ΓK direction turned out to be quite different from the picture observed along the ΓM direction (compare Figures 5.1.24 and 5.1.8).

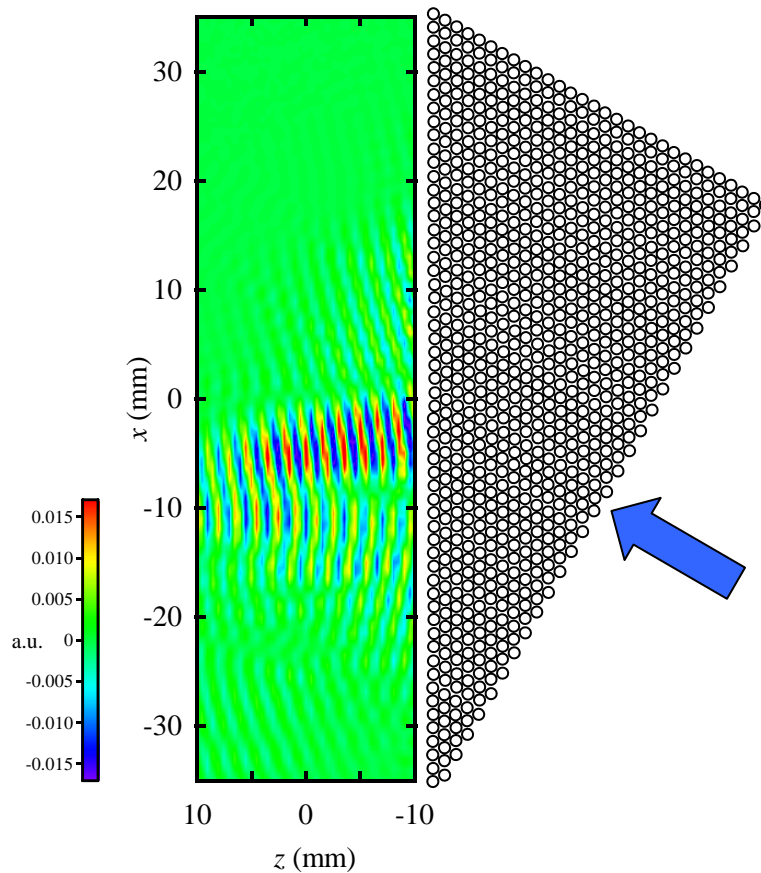


Figure 5.1.24: Snapshot of the field emerging from the output side of the prism-shaped crystal when the input pulse is incident along the ΓK direction. The original field is filtered with a Gaussian bandpass filter centered at 0.85 MHz and 0.05 MHz wide.

The most drastic difference between the two experiments is that the magnitude of the outgoing pulse in the second experiment is more than 10 times smaller than the one measured in the first experiment (Figure 5.1.8). Also, although the outgoing pulse still seems to be refracted negatively, the value of the refraction angle is in complete disagreement with the one obtained from calculations based on the band structure. Finally, the pulse shape is very irregular and never resembles the well-defined beam-like shape of the negatively refracted pulses in the experiments along the ΓM direction.

These results can be understood in conjunction with the results of the transmission experiment along the ΓK direction through the crystal shown in Figure 5.1.1. Recall that the transmission experiment revealed the existence of a gap in the frequency range corresponding to the modes in the 2nd band [Figure 5.1.5]. The dispersion curve derived from the same experiment showed that the incident pulse was not able to use, or “couple to”, the 2nd band modes for ballistic propagation through the crystal [Figure 5.1.6]. It is worth mentioning at this point that the existence of such non-coupling bands was also demonstrated experimentally in case of *photonic* crystals. Robertson *et al.* [71, 72] found several non-coupling bands while investigating the transmission of plane electromagnetic waves through a 2D *square* array of aluminum-ceramic rods along both the [10] and the [11] directions. Krauss *et al.* analyzed the transmission of plane electromagnetic waves through a photonic crystal made of a 2D *triangular* array of columns etched in a waveguide [73]. In case of a TM input wave (with E -field parallel to the etched columns) incident along the ΓK direction, they also found the 2nd band to be a non-coupling band (i.e., a similar result to the one that I obtained along the same direction for ultrasound waves). The properties of the non-coupling bands were also studied theoretically by

Sakoda [74, 75] with the help of group theory. The major reason for these bands to be non-coupling was found to be the difference between the symmetries of the band modes and an input plane wave. Figure 5.1.25(a) displays one possible example of the field distribution inside the crystal, which would correspond to the *coupling* band. The alternating regions of high and low amplitude are *symmetric* upon mirror reflection with respect to the y - z plane, just as the incoming plane wave is. One of the possible field distributions in case of a *non-coupling* band is shown in Figure 5.1.25(b), which is *anti-symmetric* upon reflection with respect to the same plane. It is exactly this difference in symmetry between an input plane wave and modes of the particular band that prevents the incoming radiation from coupling to and propagating through the crystal.

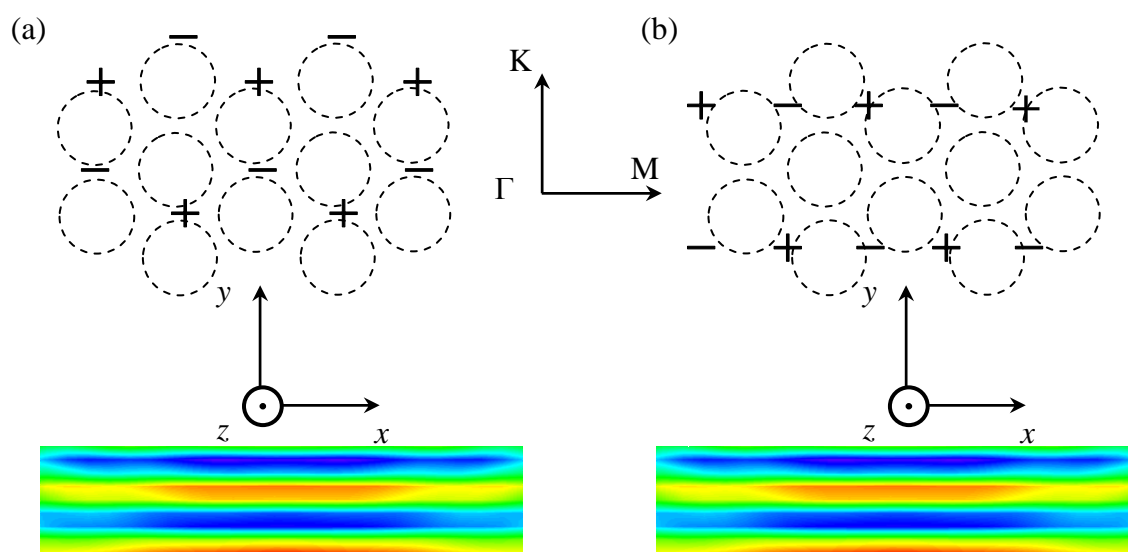


Figure 5.1.25: The possible field distributions inside the crystal corresponding to (a) coupling band and (b) non-coupling band. The incoming plane wave propagating in a positive direction of y -axis is also indicated. The colour scale is in arbitrary units, with wave crests/troughs corresponding to red/blue and zero amplitude indicated by green (For detailed calculations of the field pattern for a non-coupling band in a photonic crystal case see Krauss *et al.* [73]).

In case of *phononic* crystals, the bands, which feature symmetries inconsistent with the symmetry of a plane wave, are also known as “deaf” bands. For example, Sánchez-Pérez *et al.* observed the existence of such bands for sound waves propagating through a square array of stainless steel cylinders in air [76]. Based on the experimental evidence, it can be concluded that the second band along the ΓK direction in my 2D crystals is a “deaf” band. This statement can be verified by the MST, which allows one to simulate propagation of a plane wave through the phononic crystal. Such a simulation was performed by Dr. Zhengyou Liu for the case of a finite beam incident along the ΓK direction on a 12-layer 2D phononic crystal of infinite lateral extent [Figure 5.1.26].

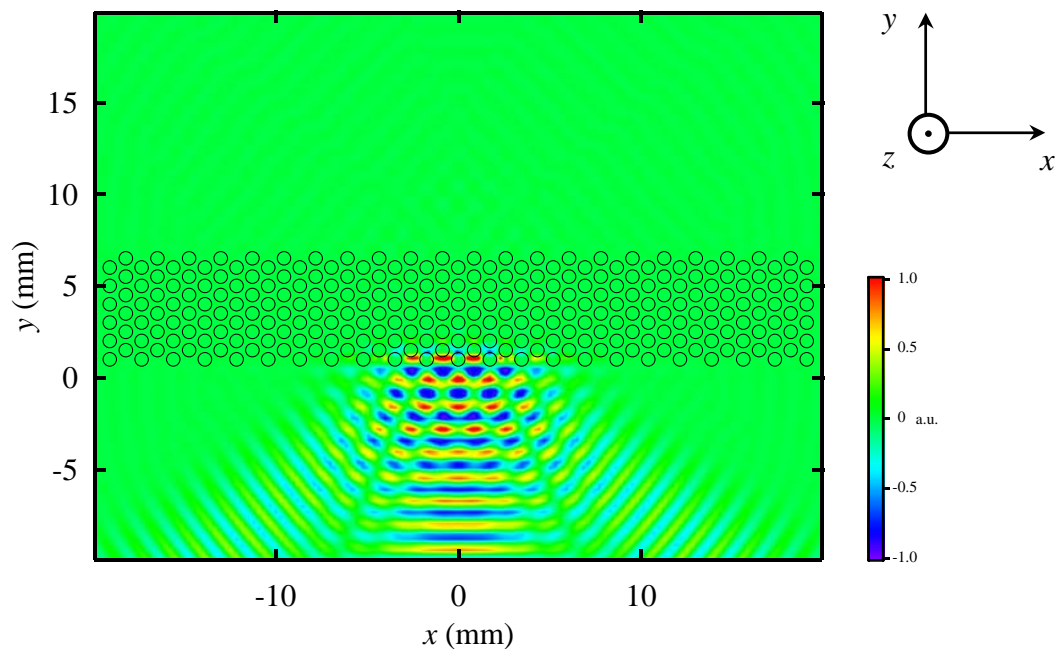


Figure 5.1.26: Field calculated with the help of MST for the case of a plane wave beam incident on a 12-layer 2D phononic crystal along the ΓK direction. The labels of both axis are given in units of the lattice constant a . The colour scale is in arbitrary units. (Calculations courtesy of Dr. Zhengyou Liu).

The frequency of the input wave was chosen to be 0.90 MHz, which lies well inside the 2nd band. As can be seen from Figure 5.1.26, the incident wave is not able to couple to the 2nd band mode, which is evidenced by the zero amplitude of the field in the central region inside the crystal. This explains the drop in transmission observed in the experiment. However, some very weak disturbances, with a magnitude of about 0.25 % of the incident wave, are observed on both sides of the central region where the field is zero. This is shown in Figure 5.1.27, which displays the image in Figure 5.1.26 plotted at smaller colour scale (the number in the upper right corner is a factor by which its colour scale should be increased to bring it to the level of Figure 5.1.26).

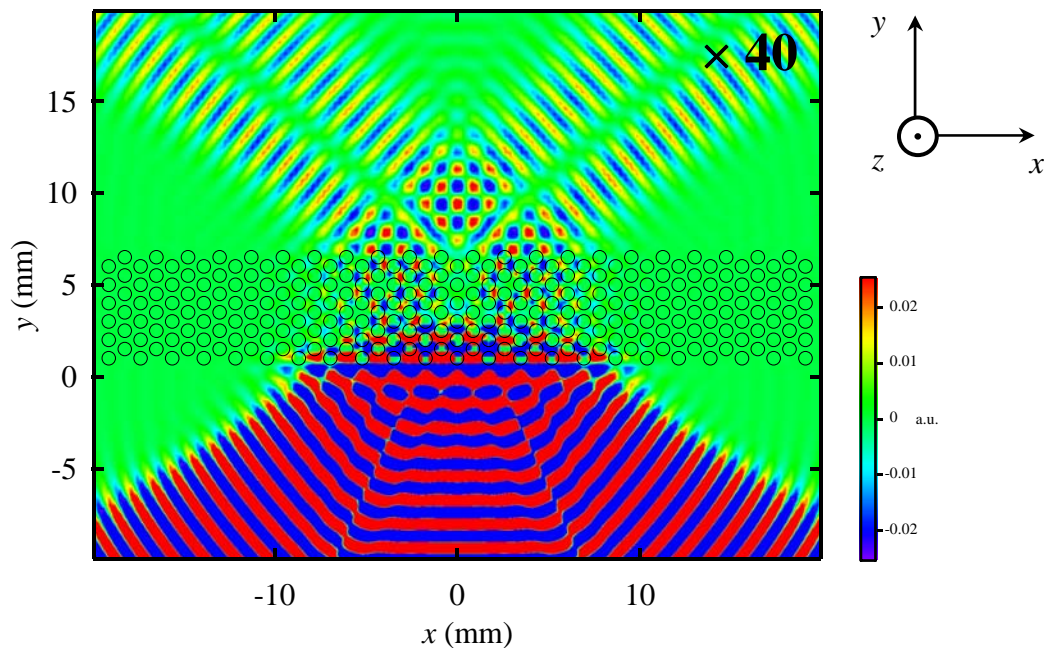


Figure 5.1.27: The image plot in Figure 5.1.26 displayed on a smaller colour scale, in order to visualize the part of the incident wave that propagated through the crystal. All the magnitudes with the values larger/smaller than the largest/smallest values of the colour scale are represented by the red/blue colour.

Presumably, these fields are excited by the *edges* of the incident beam (because the transverse confinement of the beam means that its Fourier spectrum must contain the wavevectors with non-normal angles of incidence). The portion of the field pattern inside the crystal (located to the left of the region where field amplitude is zero) is shown more closely in Fig. 5.1.28. One can see that the field distribution is anti-symmetric with respect to the y - z plane, which probably reflects the fact that this field pattern is a combination of different modes in the 2nd band (each of them being anti-symmetric itself).

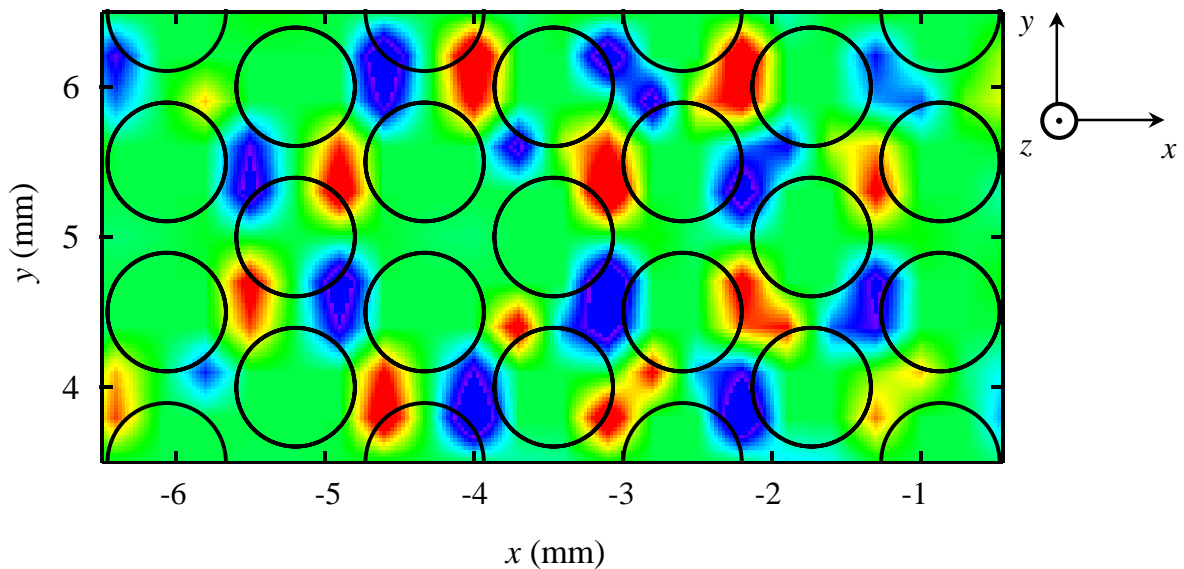


Figure 5.1.28: Left portion of the field pattern inside the crystal displayed in Figure 5.1.27. Note the sign reversal asymmetry with respect to the y - z plane. The colour scale is the same as in Figure 5.1.27.

The most interesting fact however is that transmission, calculated by the MST, still predicts that a very small part of the energy of the incident wave passes through the crystal. Each of the edge field regions excited on either side of the central region couples to the outside medium in such a way that two plane waves are produced (four in total), each propagating away from the crystal *at some angle* with respect to the normal to the

crystal surface. It is interesting to note that these angles are *not* equal. For example, the field to the left of the central area produces left propagating wave at an angle of 51° (with respect to the normal) and the right propagating wave at a 46.5° angle [Figure 5.1.29]. However, since field patterns are mirror-like images of each other with respect to the y - z plane, this relation is *reversed* for the waves produced by the field on the right of the central area, so that the total transverse wavevector (parallel to x -axis) on the input and output sides of the crystal is conserved.

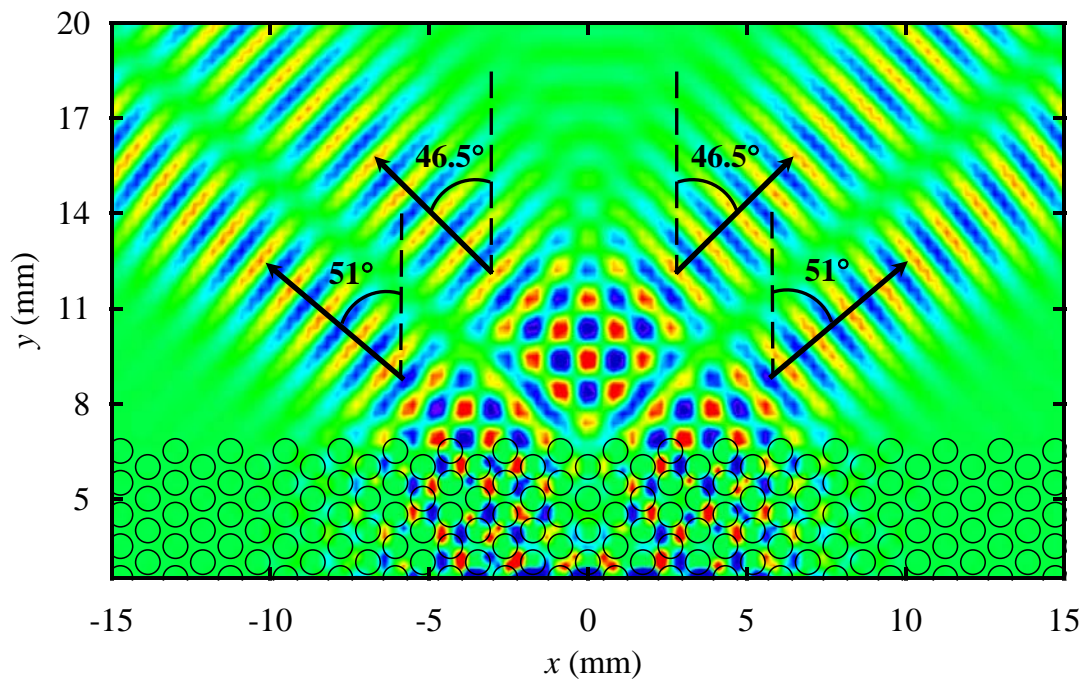


Figure 5.1.29: The outgoing part of the field displayed in Figure 5.1.26. The total transverse wavevector of the field transmitted through the crystal adds up to zero and obviously equals the total wavevector of the input (truncated plane wave). The colour scale is the same as in figure 5.1.27.

To experimentally investigate the nature of the transmitted patterns, I have conducted a field mapping experiment with the flat 12-layer 2D crystal [Figure 5.1.1], in

which the incoming pulse was incident normally on the crystal surface and the field on the output side of the crystal was scanned with the help of the hydrophone. The input pulse was centred at 1.0 MHz but had a bandwidth wide enough to cover an appreciable frequency range, including the frequency of 0.90 MHz. Figure 5.1.30 presents a time snapshot of the sound field after filtering the original recorded field by a Gaussian bandpass filter centred at 0.90 MHz and 0.005 MHz wide. The experimentally measured field certainly bears similarity with the calculated pattern in Figure 5.1.29. One can easily identify two major beams propagating to the left and to the right from the crystal surface. The angles at which beams leave crystal surface are measured from the figure and found to be almost the same: $46^\circ \pm 1^\circ$ for the left propagating beam and $45^\circ \pm 1^\circ$ for the right propagating one. The whole field pattern is shifted towards the left side of the picture, most likely due to the centre of the transducer not being coincident with the middle point of the crystal.

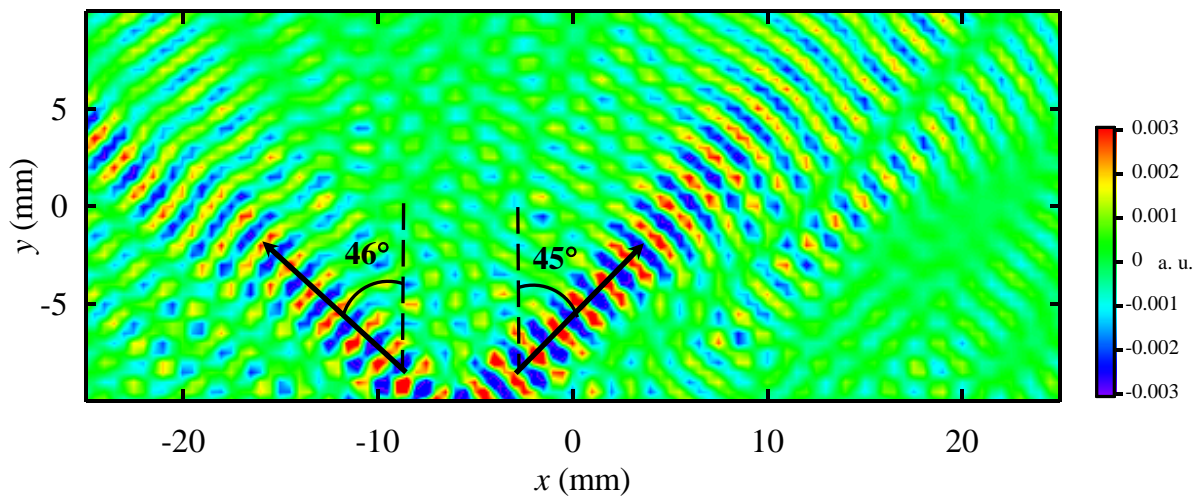


Figure 5.1.30: Snapshot of the experimentally measured field emerging from the output side of the 12-layer 2D crystal with the input pulse incident along the ΓK direction. The geometry of the experiment is identical to the one shown in Figure 5.1.26. Colour scale is in arbitrary units.

The other two beams, which are predicted by the theory and seen in Figure 5.1.29, are not observed conclusively in the experiment, possibly due to the difference between the profiles of the input beam used in the calculations and the input beam produced by the transducer in the actual experiment shown in Figure 5.1.30. These two profiles are compared in Figure 5.1.31.

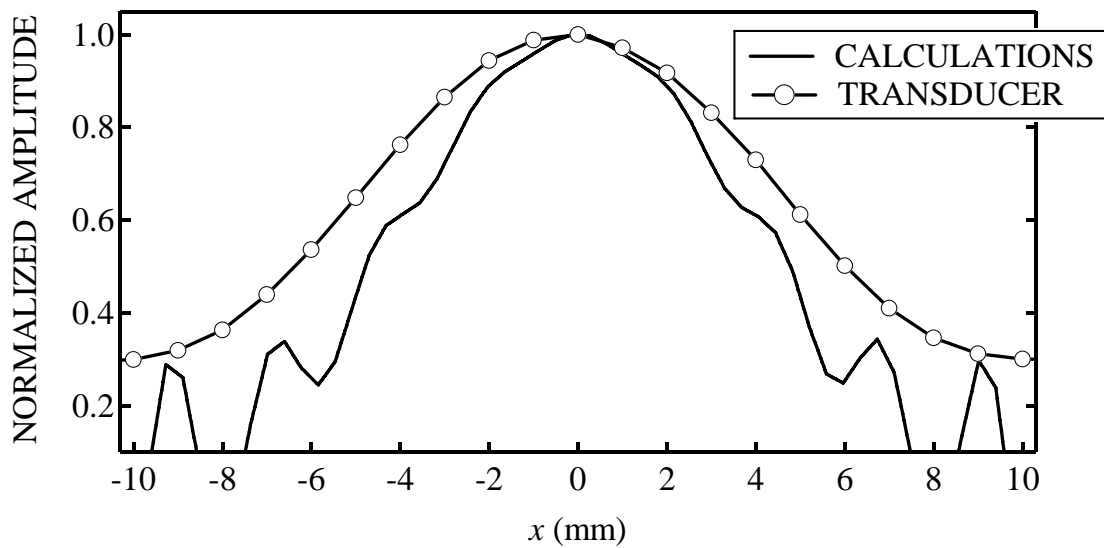


Figure 5.1.31: Comparison of the input beam profile used in the calculations of the field pattern [Figure 5.1.26] with the one produced by the transducer in the field mapping experiment with the input pulse incident along the ΓK direction.

The experimental input beam profile was obtained by measuring the field of the transducer in the mapping experiment (using the motorized stage and the hydrophone) and plotting the field amplitude along a line that is perpendicular to its axis and is located at the same distance from the transducer as the position of the crystal during the experiment shown in Figure 5.1.30. The beam profile used in the calculations was obtained by

reading the field amplitudes from Figure 5.1.26 along the line $y = -9.4$ cm. It can be seen from Figure 5.1.31 that the experimental input beam is broader than the one used in calculations, and has a different shape, which might be responsible for some disagreement between the experiment and theory. However, in general there is a good qualitative agreement between the experiment and the calculations by the MST for the case of input pulse incident along the ΓK direction.

The question of why the observed output pattern looks the way it does cannot be addressed using the band structure alone. Instead, a more sophisticated model is needed that would be able to explain how the field inside the crystal couples to the input and output beams, which likely involves a higher order mechanisms. The main message, which follows from the calculations and experiments with the flat crystal along the ΓK direction, is the prediction and experimental proof that the 2nd band along this direction is a “deaf” band, and a plane wave incident normally to the crystal surface along the ΓK direction cannot couple to the 2nd band modes.

This conclusion helps us understand why results of the experiment with the prism-shaped crystal in the case of input pulse incident along the ΓK direction [Figure 5.1.23] are in a disagreement with the simple band structure predictions. The significantly smaller magnitude of the transmitted pulse is explained again by the fact that the 2nd band along the direction of incidence is a “deaf” band and the incident pulse does not couple to any mode inside the prism-shaped crystal. However, since the width of the input beam is finite, some crystal modes are still excited by the edges of the input pulse, and those modes are responsible for the field on the output side of the crystal that is observed experimentally.

The same argument of a “deaf” band along the ΓK direction can explain why, in the experiment depicted in Figure 5.1.11, no negatively refracted beam was observed corresponding to the parallel component of the reduced wavevector that was not modified by a reciprocal surface vector (see the dashed line in Figure 5.1.15). Recall that Snell’s law predicted this negatively refracted beam to emerge nearly *normal* to the crystal surface or, equivalently, to the ΓK direction. This situation is the reverse of the experiment with the input pulse incident normally on the crystal from water along the ΓK direction [Figure 5.1.23]. It is reasonable to assume that, similar to the experiment along the ΓK direction, the field inside the crystal could not couple to the outside medium, due to the difference in symmetries between the corresponding modes inside the crystal and a plane wave outside.

This brings to an end the section on negative refraction of ultrasound observed with the help of the prism-shaped 2D phononic crystal. The main conclusion is that the negative refraction of ultrasound pulses incident along the ΓM direction was successfully demonstrated experimentally. In my case, negative refraction is a band structure effect and is observed in the frequency range where the group velocity and wavevector are antiparallel. A very good agreement is found between the refraction angles measured in the experiment and those calculated by the MST. The experiments also revealed that 2nd band along the ΓK direction is a “deaf” band and coupling between plane waves and modes of the 2nd band is prohibited due to the difference in their symmetries. Part of this work on negative refraction has already been published in a peer-reviewed publication [77].

5.2 Near-field imaging with flat 2D phononic crystals

As was explained in Section 2.2.2, the effect of negative refraction must enable a flat phononic crystal to focus sound fields of point sources, since each emitted ray should refract negatively twice while traveling through the crystal. Section 5.2 presents experimental evidence that supports this prediction. This section contains the results of the experiments, which led to the observation of focusing of ultrasound waves and allowed me to investigate the question: what is the best achievable resolution when imaging with the phononic crystal? The section starts by describing focussing experiments with the flat 2D phononic crystal filled with the same liquid as the surrounding medium, which is water in our case, and continues by discussing similar experiments performed with crystals immersed in water but filled with methanol.

5.2.1 Imaging experiments with 2D flat crystal filled with water

The first near-field imaging experiment was conducted with the rectangular-shaped 6-layer crystal [Fig. 3.1.2(a)] in the small water tank [Figure 3.2.2]. As a point source, I have utilized a pinducer, the detailed description of which is given in Section 3.4.3. In most of the experiments, the pinducer was positioned about 2.5 mm away from the crystal surface. A narrow Gaussian pulse centred at 0.75 MHz was generated by an Arbitrary Waveform Generator (AWG), amplified by the Amplifier Research power amplifier (Section 3.3.1) and sent into the pinducer. The field on the opposite side of the crystal (as in the experiments on negative refraction) was scanned with the hydrophone in a rectangular grid perpendicular to the crystal rods. The separation between adjacent grid points was chosen to be 0.5 mm. The pinducer and the hydrophone were positioned in the

same plane, with the central point of the grid lying on the pinducer axis. Figure 5.2.1 shows the geometry of the experiment.

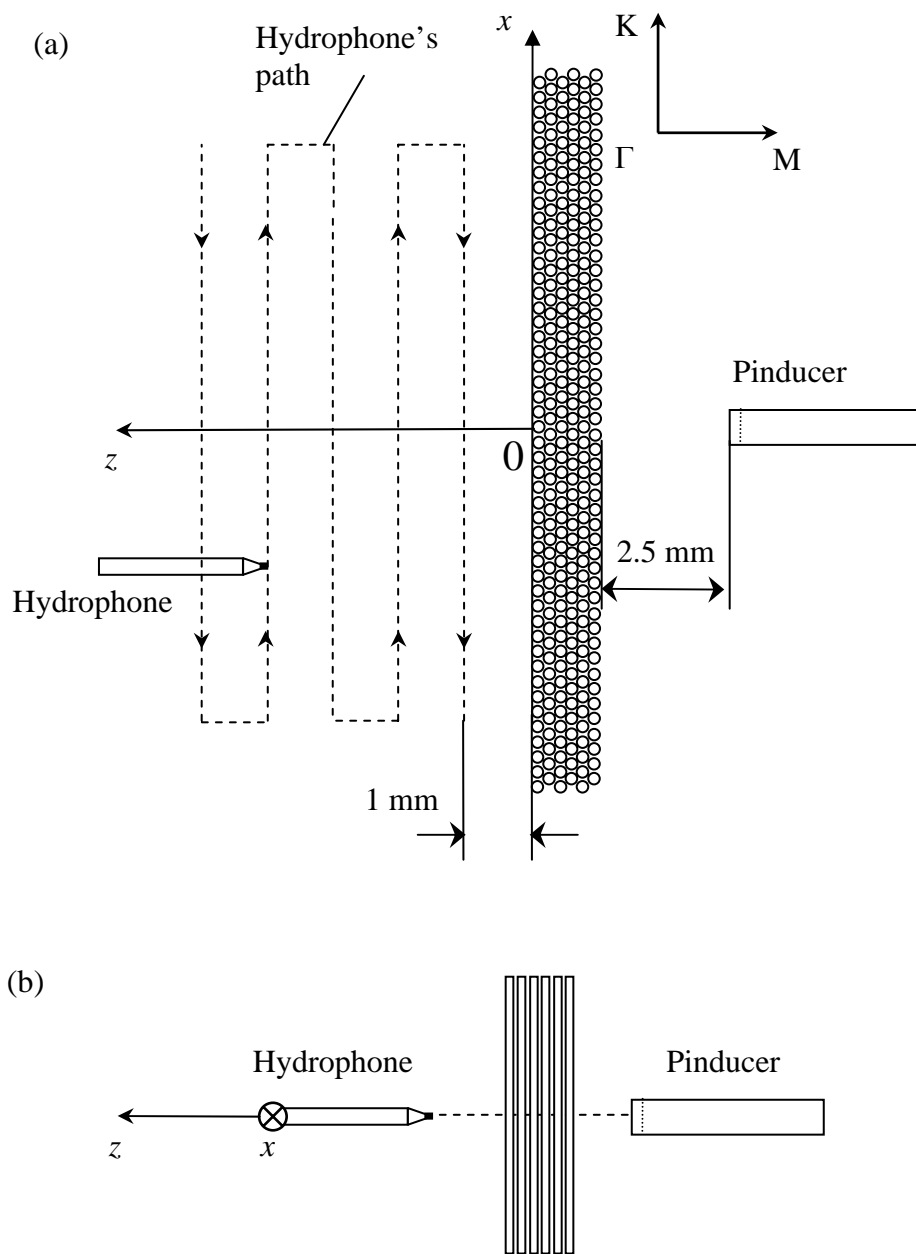


Figure 5.2.1: Geometry of the near-field imaging experiment with the rectangular-shaped phononic crystal: (a) top view and (b) side view.

By calculating Fast Fourier Transforms (FFTs) of each acquired waveform, 2D image plots were created displaying wave amplitude ($A > 0$) at a certain frequency as a function of the hydrophone position in the x - z plane (see Section 3.5.2). Equifrequency contours for selected frequencies in the 2nd band (0.75 MHz, 0.85MHz and 0.95 MHz) were calculated by the MST and have been found to have a nearly circular shape (see Figure 2.2.4). It will be shown later that there is a very wide range of the 2nd band frequencies for which equifrequency contours are almost circular. The focusing ability of the 2D flat phononic crystal is illustrated by the image plot in Figure 5.2.2, which displays the focal pattern observed at a frequency of 0.75 MHz. The pinducer field is clearly focused in both longitudinal and lateral extent, as shown by the overall focal pattern in Figure 5.2.2.

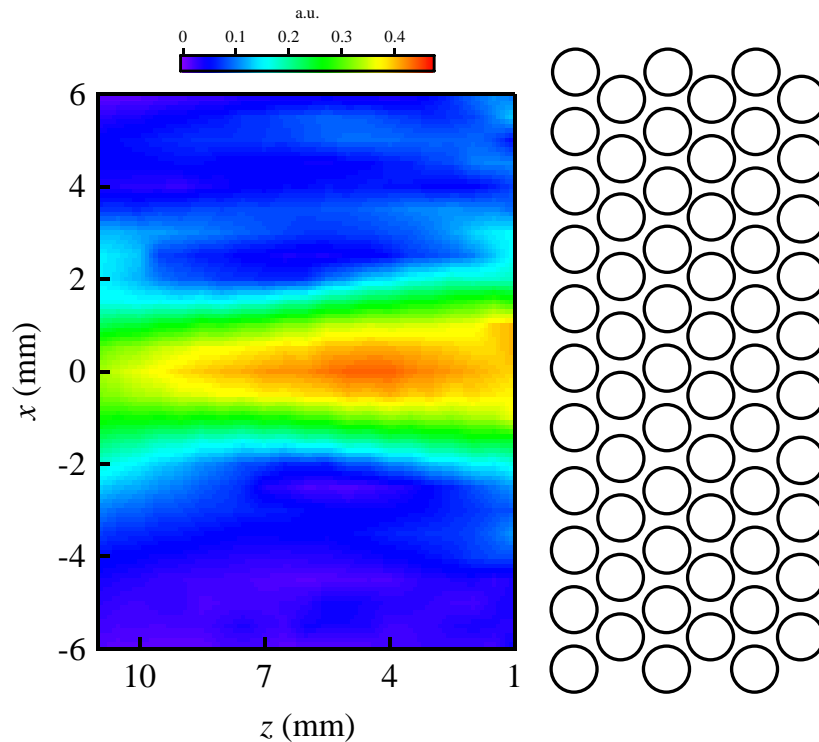


Figure 5.2.2: 2D image plot of wave amplitude at 0.75 MHz obtained in the experiment on pinducer field imaging. The colour scale is in arbitrary units.

The lateral and longitudinal confinement of the focus can be better seen from Figures 5.2.3(a)-(b), which represent measured wave amplitudes along the x -axis and z -axis (as read from image plot in Figure 5.2.2). The focal spot is much more extended along the z -axis than along the x -axis, which is expected when equifrequency contours in water and inside the crystal do not match, which is the case for my crystal at 0.75 MHz (see Section 2.2.2).

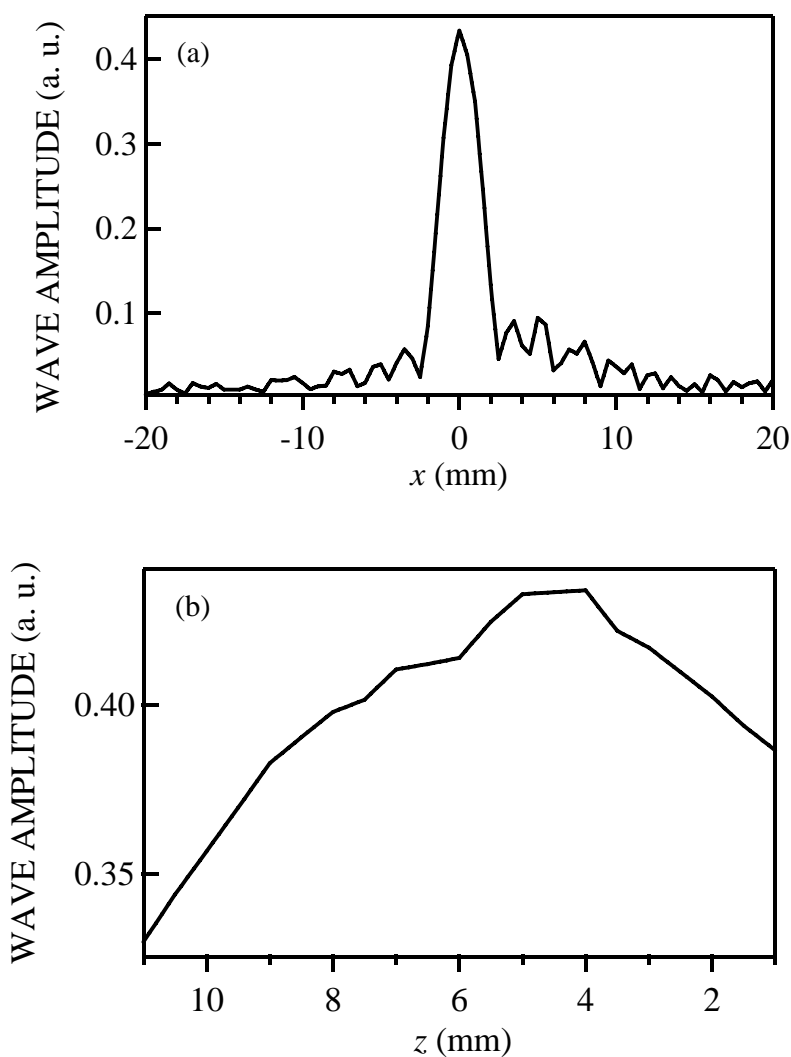


Figure 5.2.3: Wave field amplitude as a function of position obtained from Figure 5.2.2 by plotting along: (a) x -axis at $z = 4.5$ mm, (b) z -axis at $x = 0$ mm.

The central issue in any imaging application is the *best possible resolution* that can be achieved with the system used for imaging. According to Lord Rayleigh, two incoherent point sources of equal intensity are just resolved when maximum of the intensity peak produced by one of the sources falls at the first minima of the intensity peak due to the second source (Rayleigh criterion). By adopting this definition of resolution, the resolution provided by the crystal is simply half of the full width of the amplitude peak produced by imaging the pinducer [Figure 5.2.3(a)]. To determine the resolution, the width of the peak was estimated by fitting the data points by the sinc function $|\sin(ax)/ax|$, where the fitting parameter a is related to the width of the peak Δ by the expression $\Delta = 2\pi/a$. The resolution therefore is given by $\Delta/2$. The sinc function is known from diffraction theory to represent the shape of the amplitude of the peak due to diffraction of a plane wave on a single slit (which can be viewed as a line source) in the 2D case and therefore can be expected to provide a good approximation to the data peak. The experimentally observed amplitude peak [Figure 5.2.3(a)] and the fitted sinc function are shown in Figure 5.2.4. For the focal spot at 0.75 MHz, from the fit the value of the peak width Δ was found to be 5.02 ± 0.02 mm with the corresponding resolution of 2.51 mm or 1.26λ , where λ is the ultrasound wavelength in water.

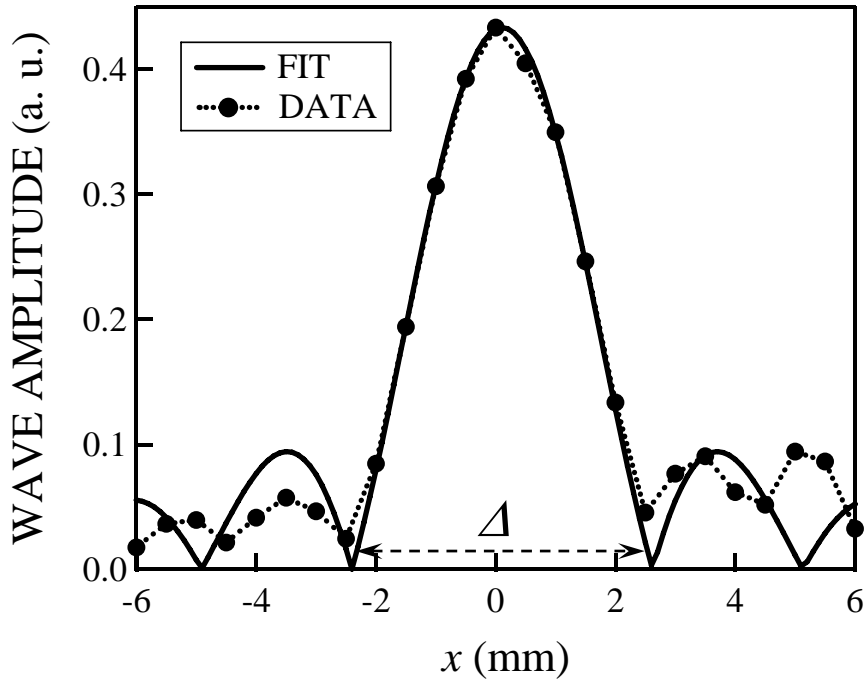


Figure 5.2.4: Focal spot amplitude at 0.75 MHz and fit of the absolute value of the sinc function. Width of the peak, Δ , is also indicated.

The imaging experiments described above demonstrated in principle the ability of the flat 2D phononic crystal to bring a point-source field to a focus in the x - z plane. The *shape* of the focal spot, however, is far from ideal. Although the focal spot is confined in lateral extent, it obviously lacks the same degree of confinement along the axis perpendicular to the crystal. The focal spot along the z -axis is very broad and has a large focal depth (the maximum field amplitude along z -direction is only about 10% higher than the field amplitude at the crystal surface) [Figure 5.2.3(b)]. As was already explained in Section 2.2.2, this shape of the focal spot is expected due to mismatch between the equifrequency contours in water and those inside the crystal. In other words, the mismatch creates an effective refractive index of the crystal that depends on the angle of incidence. This dependence can be removed by making the size of the equifrequency

contours match, which effectively would mean that the refractive index of the crystal would be -1 .

The question of the equifrequency contour mismatch should also be solved if one wants to improve the *resolution* of the image. Because of this mismatch, a certain cut-off angle θ_{cut} exists, such that, for any angle of incidence larger than the cut-off angle, incident waves cannot couple to any mode inside the crystal and therefore are not used in the image restoration on the output side of the crystal [Figure 5.2.5].

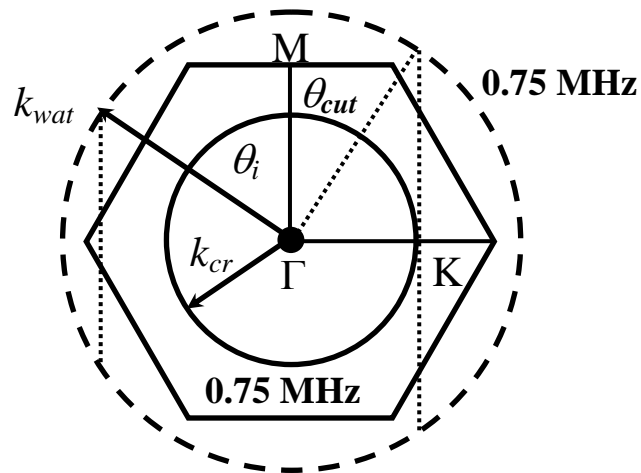


Figure 5.2.5: Diagram explaining the origin of the cut-off angle θ_{cut} in the imaging experiment at 0.75 MHz . The solid circle denotes the equifrequency contour inside crystal, and the dashed circle indicates corresponding contour in water.

The loss of some propagating part of the incident field broadens the lateral size of the focal spot and thus decreases the resolution of the image. We therefore see that both the focal depth and resolution are expected to improve if the crystal used for imaging will have its equifrequency contour matching the water contour. One also refers to the

situation of matching equipfrequency contours as the regime of All Angle Negative Refraction (AANR), which means that every incident ray is negatively refracted and transferred to the output face of the crystal.

One can easily verify that, at the frequency 0.75 MHz, the cut-off angle θ_{cut} is about 42° . It is obvious from Figure 5.2.5, that in order to increase θ_{cut} and improve the resolution of the water filled crystal, one needs to image at a frequency lower than 0.75 MHz. At the same time, this frequency cannot be too close to the stop band along the ΓM direction, since equipfrequency contours will deviate from circular shape in the proximity of the edge of the Brillouin zone. The lowest frequency with a circular equipfrequency contour can be estimated from the band structure (Figure 5.1.2) by calculating the percentage deviation between the wavevector along the ΓK direction and the wavevector along the ΓM direction. This deviation is shown in Figure 5.2.6.

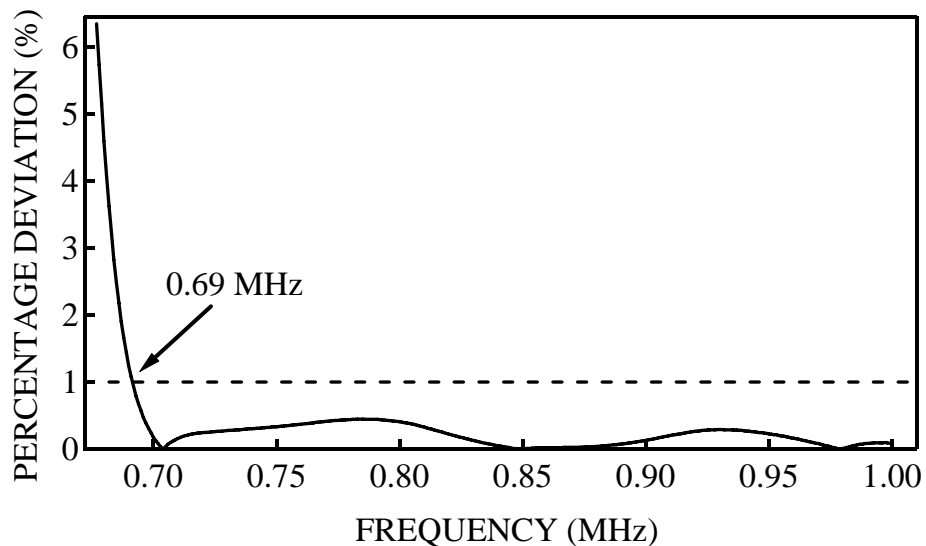


Figure 5.2.6: Percentage deviation of the wavevector along the ΓK direction with respect to the wavevector along the ΓM direction.

It can be seen from Figure 5.2.6 that the equipfrequency contours are virtually circular (difference is less or equal to 1%) for a wide frequency range in the 2nd band. The lowest frequency with a nearly circular equipfrequency contour (about 1% difference) is found to be 0.69 MHz. The corresponding image plot is shown in Figure 5.2.7, while the cross-sections of the focal spot along the x - and z -directions are presented in Figure 5.2.8(a)-(b).

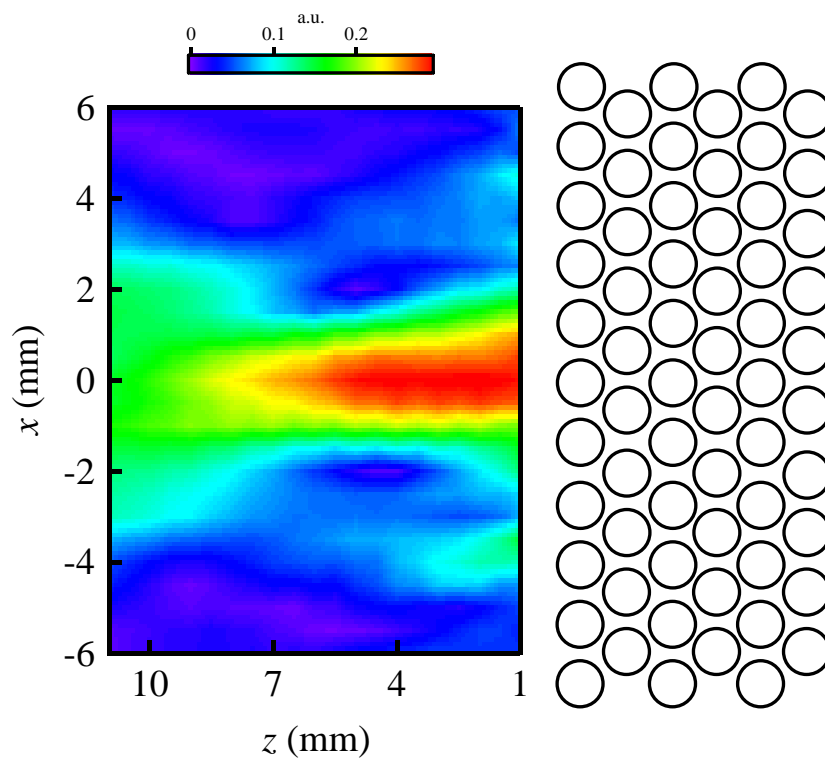


Figure 5.2.7: 2D image plot of wave amplitude at 0.69 MHz obtained in the experiment on pinducer field imaging.

From fitting the data curve in Figure 5.2.8(a) by a sinc function, the peak width Δ was estimated to be 4.6 mm with a corresponding resolution of 1.1λ , which is an improvement as compared to the resolution obtained at 0.75 MHz.

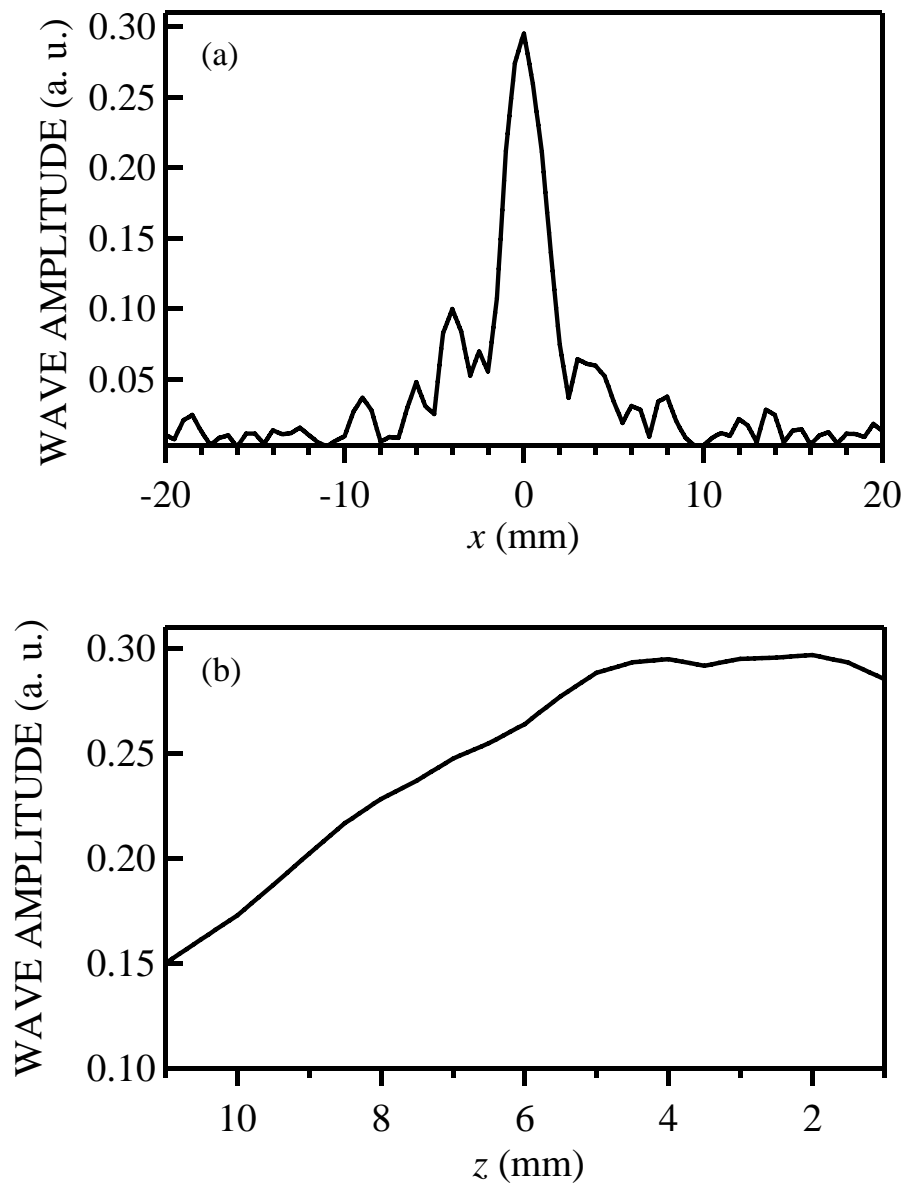


Figure 5.2.8: Wave field amplitude as a function of position obtained from Figure 5.2.7 by plotting along: (a) x -direction at $z = 2.9$ mm, (b) z -direction at $x = 0$ mm.

The importance of the *circular* shape of the equipfrequency contours used for imaging can be illustrated by the focal pattern produced at a frequency of 0.67 MHz, which corresponds to the equipfrequency contour that deviates the most from a circular

shape (see Figure 5.2.6). At this frequency, the equifrequency contours in water and in the crystal almost match each other along the ΓM direction (the exact match occurs at 0.66 MHz, which falls in the stop band along the ΓM direction and thus is not available for imaging). The deviations from the circular shape are responsible for significant distortions of the final image, as evidenced by the image plot of the wave amplitude at 0.67 MHz [Figure 5.2.9].

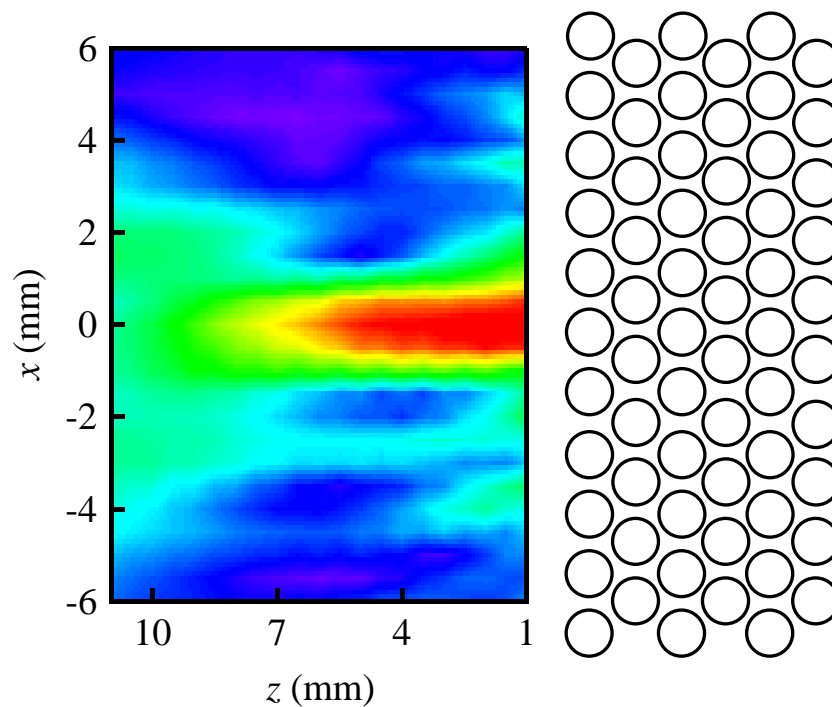


Figure 5.2.9: 2D image plot of wave amplitude at 0.67 MHz obtained in the experiment on pinducer field imaging. The colour scale is in arbitrary units and similar to Figure 5.2.7, with blue and red corresponding to zero and the largest amplitude respectively.

Image distortion can be seen even more clearly from the profiles of the focal spot along x - and z -directions, which are shown in Figure 5.2.10. As can be seen from Figure

5.2.10(a), the field profile along x -direction became distorted by two side lobes of irregular shape at the base of the amplitude peak.

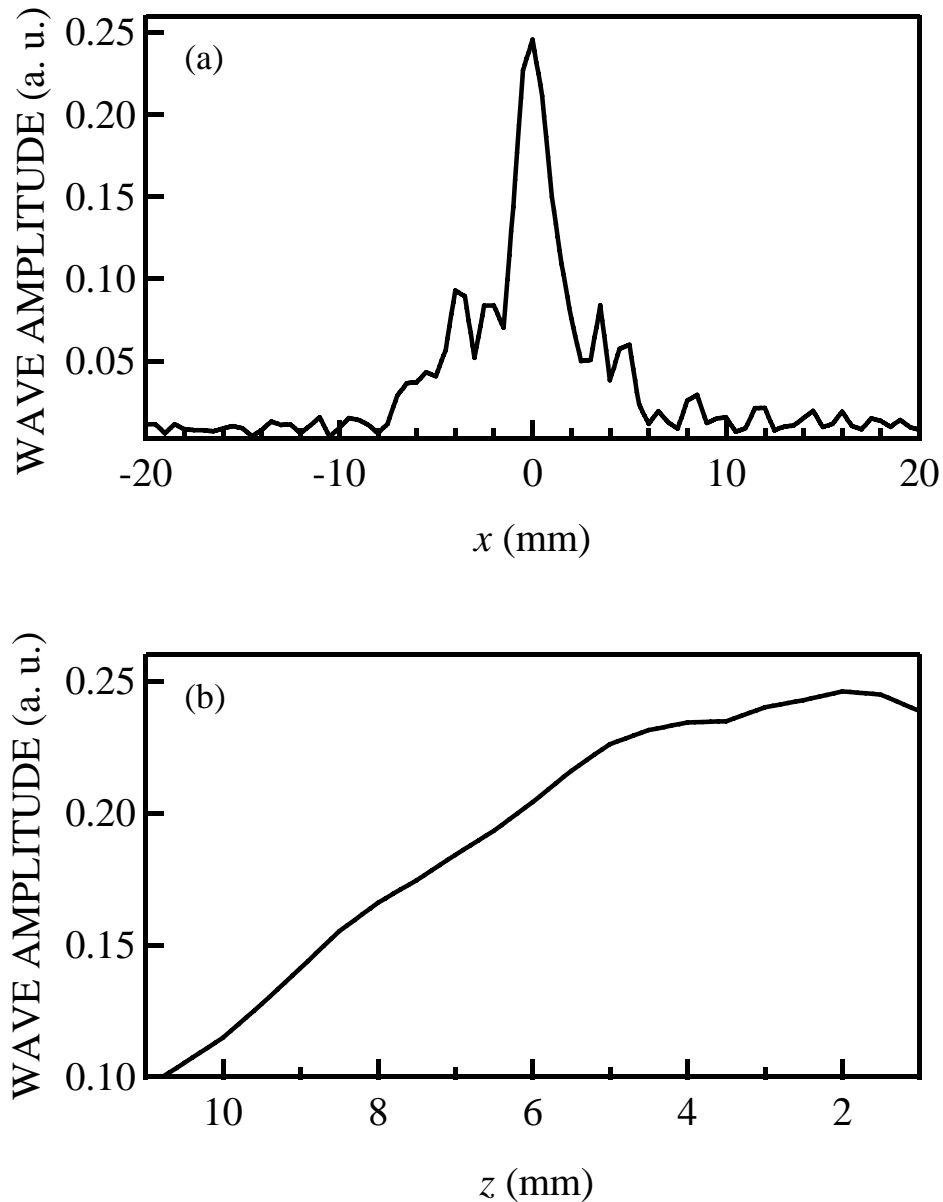


Figure 5.2.10: Wave field amplitude as a function of position obtained from Figure 5.2.9 by plotting along: (a) x -direction at $z = 1.8$ mm, (b) z -direction at $x = 0$ mm.

Thus, switching from a circular to non-circular equipfrequency contour significantly degraded the overall quality of the image and rendered it less useful from the point of

view of future imaging applications. This example illustrates the importance of the circular shape of the equifrequency contour in achieving high quality images. The next section explains how the problem of the equifrequency contour mismatch was overcome by designing a new phononic crystal. The results of the imaging experiments with such a crystal will also be presented.

It is also worthwhile investigating the applicability of the formula (2.27), which was initially introduced in Section 2.2.2 when imaging by a slab of a Left Handed (LH) material was discussed. In case of a flat phononic crystal with circular equifrequency contours, equation (2.27) assumes the following form:

$$L_1 + L_2 = d \frac{k_{wat}}{k_{cr}} \left(\frac{1 - \sin^2(\theta_{in})}{1 - (k_{wat}/k_{cr})^2 \sin^2(\theta_{in})} \right)^{\frac{1}{2}} \quad (5.7)$$

where k_{wat} and k_{cr} are the magnitudes of the wavevectors in water and in the crystal, respectively. The meaning of the remaining quantities entering (5.7) is explained in Figure 2.2.10. It is clear from (5.7) that only in the case of matching equifrequency contours ($k_{wat} = k_{cr}$) will *all* incident rays, irrespective of their angle of incidence θ_{in} , be brought to the same focal spot, which will be located a distance $L_2 = d - L_1$ away from the crystal's surface. In the following analysis, I will assume that $k_{wat} > k_{cr}$ and $d > L_1$, which is the case for my water-filled crystal. Because of the non-matching equifrequency contours, the distance L_2 , at which each pair of incident rays will intersect on the output side of the crystal, becomes dependent on the angle of incidence θ_{in} . As a result, the focal spot is elongated along the direction perpendicular to the crystal surface. The elongation of the focal spot can be estimated by plotting the distance L_2 as a function of the angle of

incidence θ_{in} for several frequencies (or effectively for different ratios k_{wat}/k_{cr}). This is done in Figure 5.2.11 for three different frequencies 0.69 MHz, 0.75 MHz and 0.80 MHz, with the values L_1 and d corresponding to their values in the actual experiment (Figure 5.2.1).

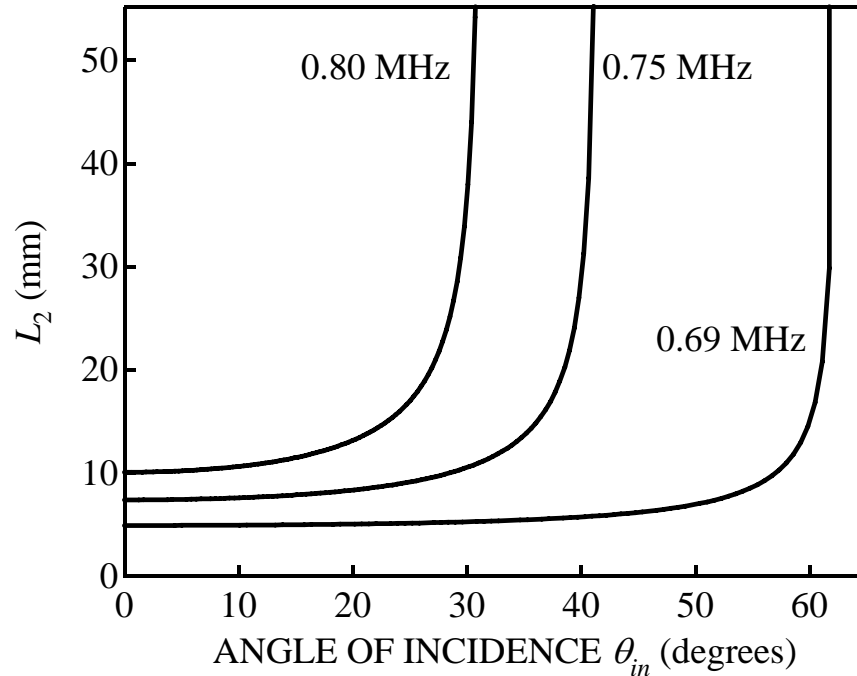


Figure 5.2.11: Distance L_2 as a function of the angle of incidence calculated according to equation (5.2) for three different frequencies with $d = 6.52$ mm and $L_1 = 2.5$ mm. Intersection with the vertical axis indicates the distance of the onset of the focal spot. As the flat parts of the curves become wider (extend to larger θ_{in}), the focal spot becomes less elongated along the z -direction, since larger range of incident angles is brought to same focal spot.

From the above graph, one can see that the elongation of the focal spot progressively *increases* with the increase of the imaging frequency, since flat parts of the curves become shorter with increasing frequency. Also, the onset of the focal spot should move *away* from the crystal surface for higher frequencies. Both results are in *qualitative*

agreement with the experimental observations, as evidenced by Figure 5.2.12. The focal profiles along the perpendicular direction become flatter (more elongated) and also tend to move away from the crystal as the frequency increases.

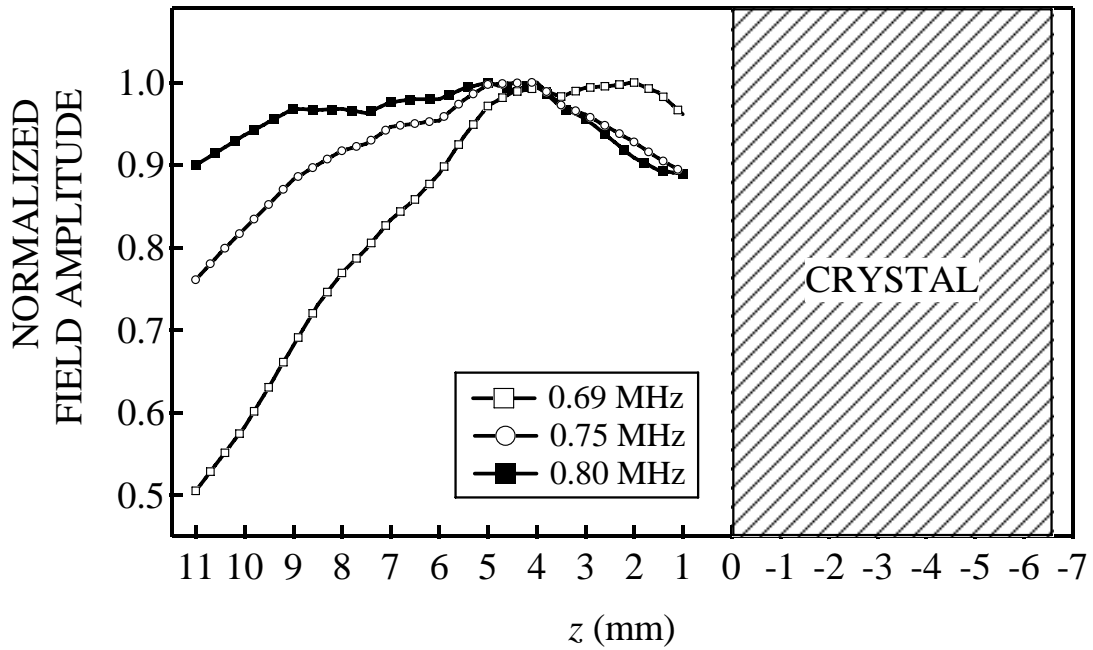


Figure 5.2.12: Measured focal profiles along the perpendicular direction for three different frequencies. As the frequency increases field profiles both become elongated and shift away from crystal’s surface.

The *quantitative* agreement, however, is poor. The main disagreement between equation (5.7) and experimental observations is that, for any frequency, the focal spot must be clearly separated from the crystal surface as can be seen from Figure 5.2.11 (the smallest separation $L_2 = d - L_1$ is achieved when equipfrequency contours are matching). For example, the focal spot at 0.69 MHz should be centred 4.85 mm away from crystal’s surface (as found from the intersection between the curve and vertical axis in Figure

5.2.11) and is expected to be elongated in the perpendicular direction away from the crystal. In Figure 5.2.12 one observes a very broad focus, which starts at the crystal's surface, in disagreement with the predictions of (5.7). Similar disagreement is observed at the frequency of 0.75 MHz, where the centre of the focal spot is located 4.5 mm away from the crystal whereas (5.7) predicts a separation of 7.3 mm. One can conclude that the position of the focal spot only qualitatively exhibits the dependence predicted by the equation (5.7), which is based on a simple ray-tracing approach of geometrical optics. My findings also disagree with the experimental results of Ke *et al.* [54], who also investigated focusing of ultrasound by a 2D flat phononic crystal similar to mine except for minor difference in some crystal parameters (lattice constant $a = 1.5$ mm, rod diameter $d = 1.0$ mm). According to Ke *et al.*, good agreement is observed between predictions of (5.7) and the measured position of the centre of the focal spot along the perpendicular direction. The reasons of this disagreement are unclear at the moment, but may reflect the fact that Ke *et al.* used a focusing transducer to create the “point” source rather than a small diameter disk-shaped transducer, such as the pinducer. Their focusing transducer likely has a rather large focal depth.

5.2.2 Imaging experiments with 2D flat crystal filled with methanol

The difficulty with the mismatch of equifrequency contours was overcome by designing a new phononic crystal, which allowed the liquid inside the crystal to be different from the outside medium (water in our case). The details of the design are discussed in Section 3.1.1. Here I would just note that it was important to make sure that the presence of the thin plastic film, which was stretched over the surface of the crystal in order to keep the liquid inside the crystal separated from water, could be ignored during the imaging experiments. The evidence of the negligible influence of the plastic film on transmission through the crystal is presented in Appendix D. This result is expected though, as the film thickness (0.01 mm) was 2 orders of magnitude smaller than the sound wavelength in water. The new crystal was then filled with methanol, which has speed of sound lower than that in water (1.1 mm/ μ s versus 1.49 mm/ μ s). Qualitatively, one expects that the change of liquid matrix inside the phononic crystal would simply either stretch or shrink the original band structure along the frequency axis by a factor equal to the ratio of the speed of sound in the liquids filling the crystal. This qualitative picture was verified by MST calculations and by transmission experiments through the methanol filled crystal, from which the dispersion curve and crystal band structure were extracted. As in the case of the water matrix crystal, a very good agreement was found between theory and experiment [Figure 5.2.13].

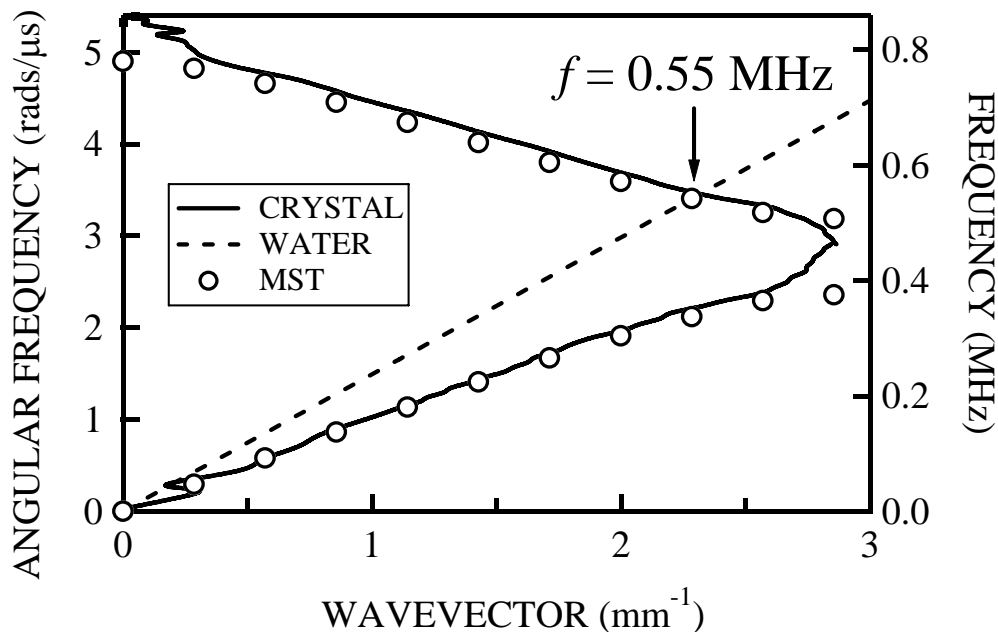


Figure 5.2.13: Comparison of the band structure calculated by the MST and measured experimentally for the 2D rectangular-shaped 6-layer crystal filled with methanol. The intersection of the dispersion curves for water and the crystal indicates the matching frequency.

Because the band structure of the methanol matrix crystal was shrunk along the frequency axis as compared to the one of the water matrix crystal, the position of the matching frequency moved away from the Brillouin zone edge and was found to be 0.55 MHz as indicated in Figure 5.2.13. Although rigorous MST calculations of the shape of this equifrequency contour were not done, it is reasonable to assume that its shape is either circular or deviates very little from a circle, since the corresponding wavevector along the ΓM direction (2.31 mm^{-1}) is only 10% larger than the wavevector along the same direction for the 0.75 MHz contour in the water-filled crystal (2.10 mm^{-1}), and this contour is known from the MST to be “perfectly” circular.

The geometry of the imaging experiment with the methanol matrix crystal was identical to the one shown in Figure 5.2.1, except that the distance between the pinducer and the crystal was reduced to 2 mm. The input pulse was centred at 0.50 MHz and had a sufficiently broad bandwidth to cover the matching frequency of 0.55 MHz. The 2D image plot of wave amplitude at 0.55 MHz is shown in Figure 5.2.14.

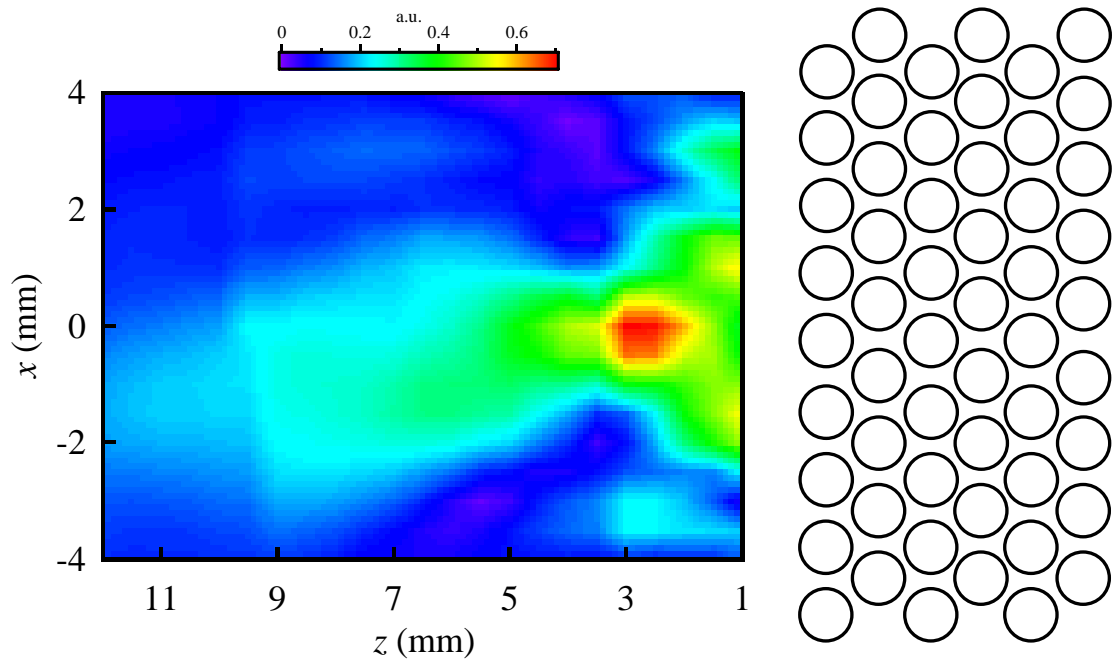


Figure 5.2.14: 2D image plot of wave amplitude at 0.55 MHz obtained in the experiment on imaging pinducer field with the methanol matrix crystal.

The dramatic improvement of the focal spot shape due to matching equifrequency contours is clear when compared to the focal pattern obtained with the water matrix crystal [Figure 5.2.2]. Figure 5.2.15(a)-(b) provides further evidence that the focal spot is now confined longitudinally (along the z -direction) as well as laterally (along the x -direction).

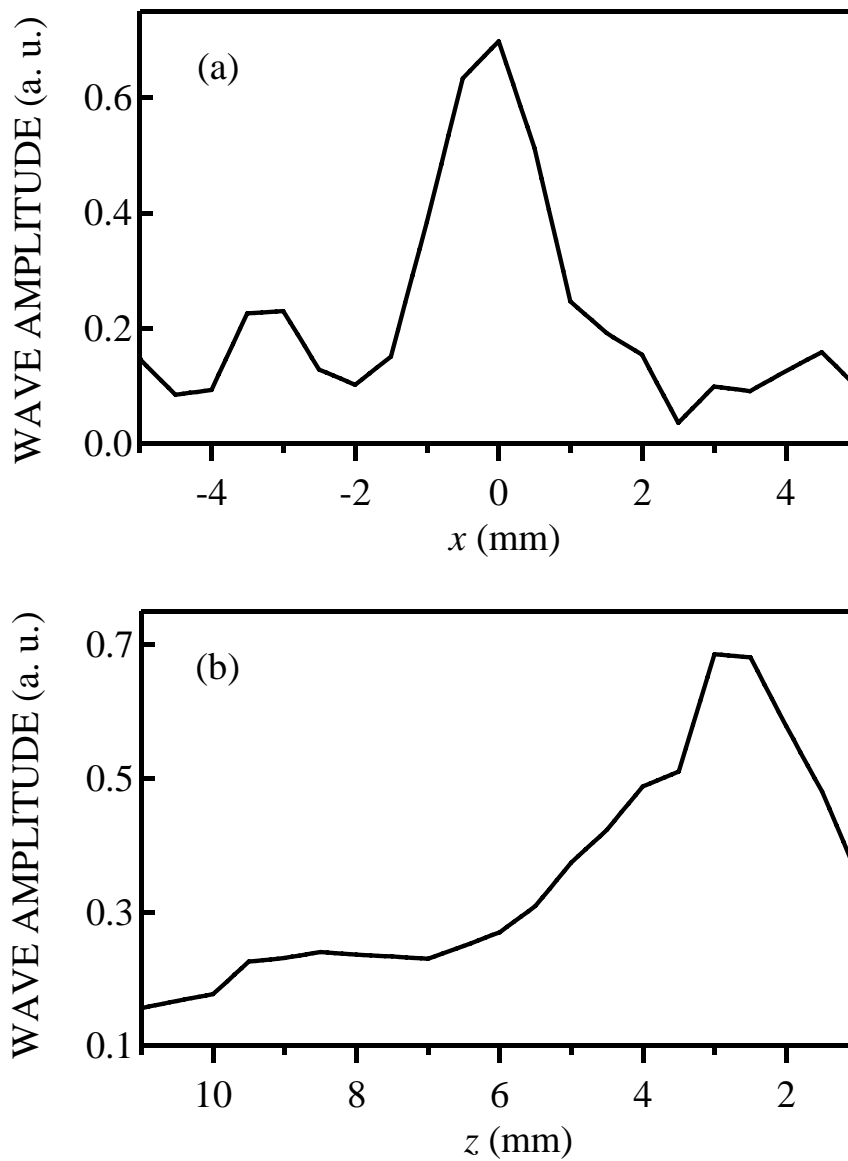


Figure 5.2.15: Wave field amplitude at 0.55 MHz read from the image plot shown in Figure 5.2.14 by plotting along: (a) the x -direction at $z = 2.9$ mm and (b) the z -direction at $x = 0$ mm.

The improvement in the shape of the focal spot along z -axis is especially impressive when compared to the broad field profile in Figure 5.2.8(b) obtained with water matrix crystal. The extent of the -6 dB region around the focal spot (i.e. the region

at whose edges field amplitude drops down by half as compared to its maximum value) along z -axis in case of the methanol-filled crystal is only 4.2 mm. Thus, by utilizing matching equipfrequency contours, the *depth* resolution was significantly improved.

Because the regime of AANR was realized, a major improvement of the *lateral* resolution of the image was also achieved. The width of the amplitude peak displayed in Figure 5.2.15(a) was estimated to be 3.16 ± 0.03 mm and the corresponding resolution was found to be 0.58λ , which is two times narrower than the resolution observed when imaging with water matrix crystal [Figure 5.2.16].

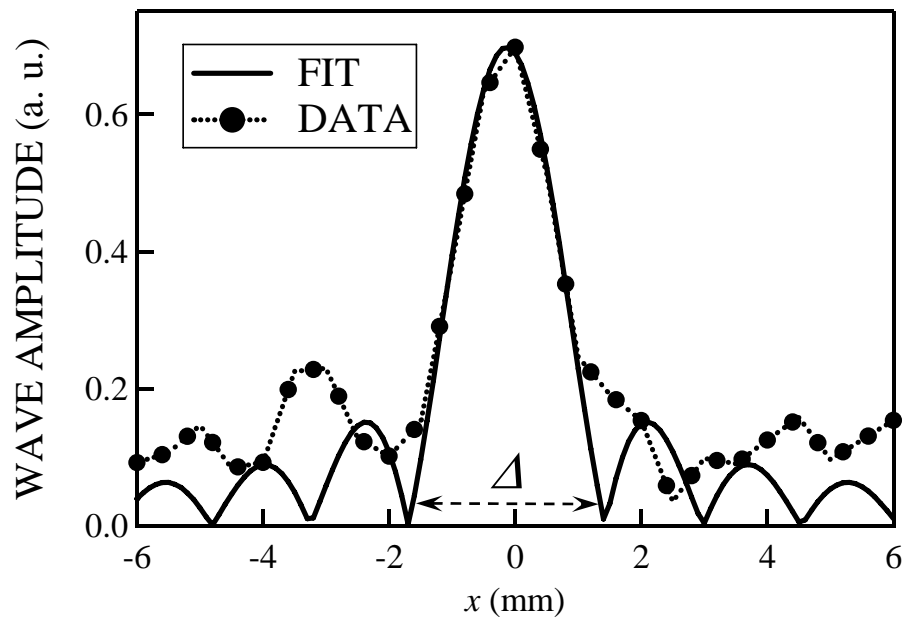


Figure 5.2.16: Amplitude peak at 0.55 MHz along with fitted sinc function. Width of the peak Δ found to be 3.16 mm.

We can see that by using a crystal with equipfrequency contours matching those in water, much better depth and lateral resolution of the focal spot was obtained. Therefore,

one can conclude that it is extremely important to work in the regime of AANR to obtain optimal results while imaging with flat 2D phononic crystals.

Although the resolution was significantly improved by moving from the water matrix to the methanol matrix crystal (and thus reaching the AANR regime), the question about the *best* possible resolution provided by the system was not resolved by these experiments. Apart from the fundamental resolution limits, which will be discussed later in this section, one obvious limitation would be the source size, or pinducer diameter in this case. Recall that by analyzing the pinducer field, its diameter was found to be 2.2 mm (see Section 3.4.3). On the other hand, the Full Width at Half Maximum (FWHM) of the amplitude peak in Figure 5.2.16 was measured to be about 2.0 mm, which is comparable to the pinducer's size. The conclusion here is that in order to investigate the true resolution limit, a smaller size source must be used in the imaging experiments.

With this goal in mind, I performed another experiment with the methanol matrix crystal in which the line source transducer was imaged. The description of this transducer was provided in Section 3.4.5. The geometry of this experiment was identical to the one depicted in Figure 5.2.1. The transducer element was aligned to be parallel with crystal rods and positioned approximately 1.6 mm from the crystal surface. A pulse, generated by the AWG and sent into the transducer, had a central frequency of 0.62 MHz, which was found to be the frequency of the best response of the transducer. That was not a problem though, as the bandwidth of the input pulse generated by the transducer was large enough so that its FT had an appreciable magnitude at the matching frequency of 0.55 MHz.

A 2D image plot of the field at the output side of the crystal is shown in Figure 5.2.17. A good quality focal pattern was obtained with the focal spot clearly seen and confined in both perpendicular and parallel directions to the crystal surface.

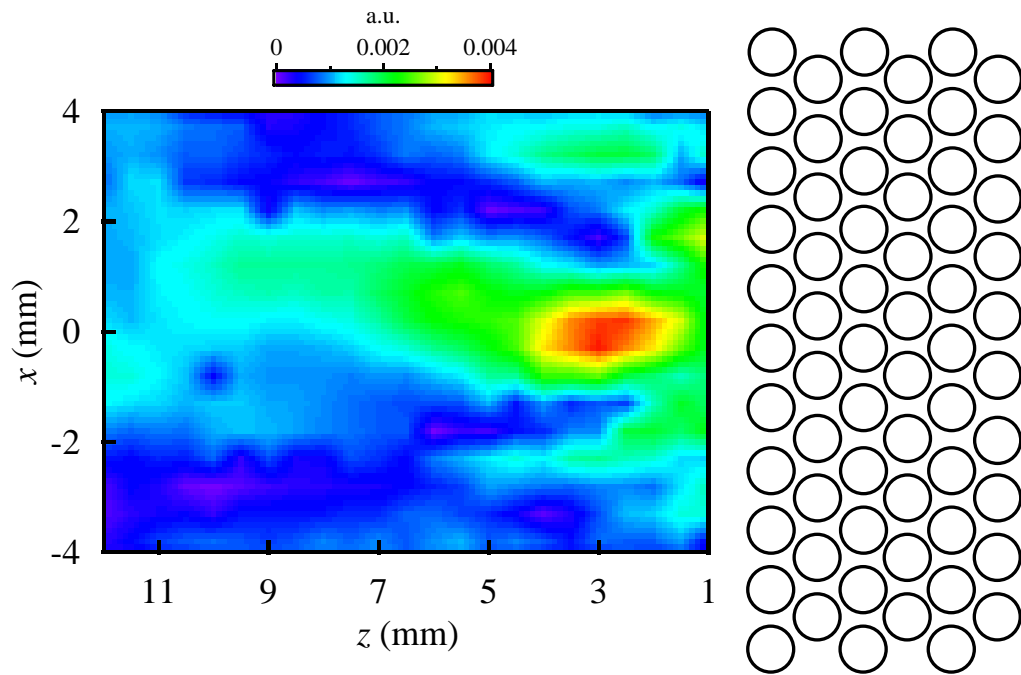


Figure 5.2.17: 2D image plot of wave amplitude at 0.55 MHz obtained in the experiment on imaging the line source transducer with the methanol matrix crystal. The colour scale is in arbitrary units.

Field profiles read along lines $z = 3.0$ mm and $x = 0$ mm in Figure 5.2.17 are also shown in Figures 5.2.18(a) and 5.2.18(b) respectively. From Figure 5.2.18(b) the extent of the -6 dB region around the focal spot along z -axis was found to be about 3.8 mm, which is slightly better than the depth resolution observed when imaging the pinducer with the same crystal [Figure 5.2.15(b)].

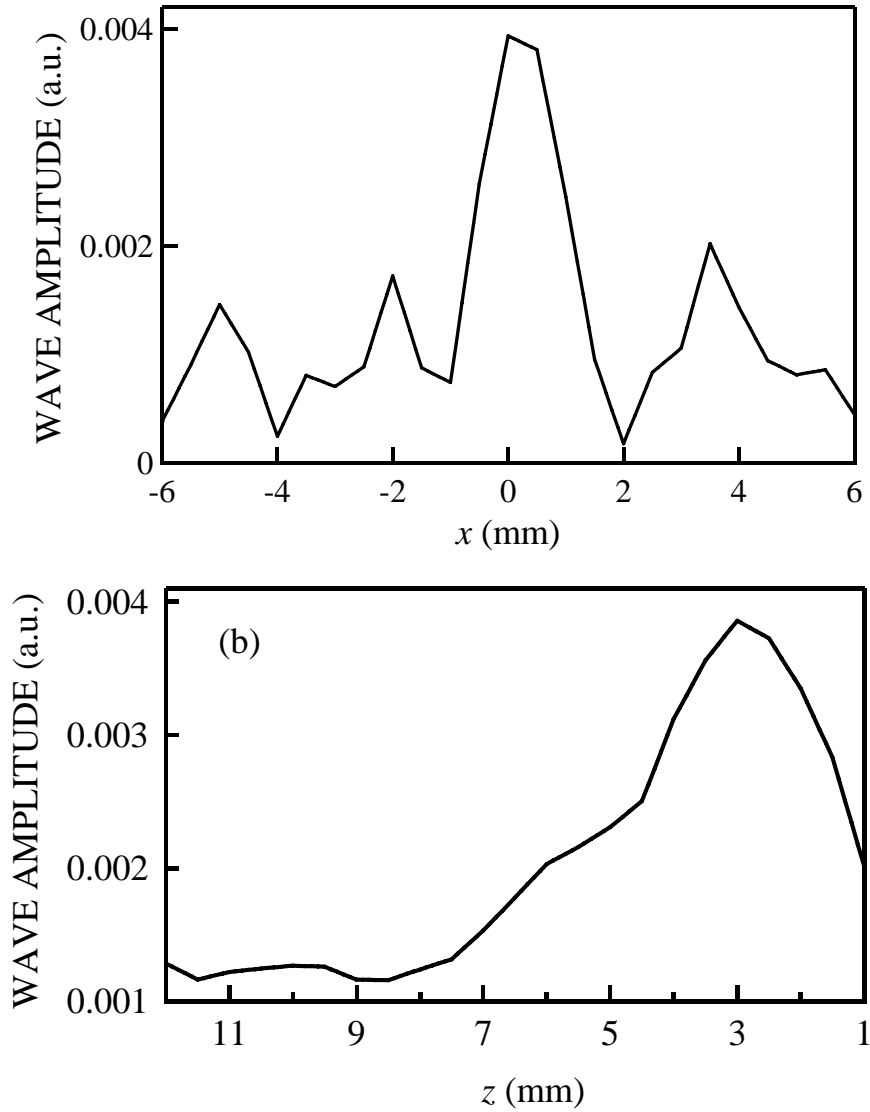


Figure 5.2.18: Wave field amplitude at 0.55 MHz read from image plot in Figure 5.2.17 by plotting along: (a) x -direction at $z = 3.0$ mm and (b) z -direction at $x = 0$ mm.

It is worthwhile noting once again that the position of the focal spot is in disagreement with the one predicted by equation (5.7), which in case of matching equifrequency contours is reduced to simple relation $L_2 = d - L_1$. This equation predicts the focal spot to occur 4.9 mm away from the crystal surface, while the measurements provide the value of 3 mm.

Just as in the previous cases, the width of the intensity peak displayed in Figure 5.2.18(a) was measured by fitting a sinc function; in this case the width was found to be 3.00 ± 0.02 mm [Figure 5.2.19], with a corresponding resolution of 0.55λ . The observed resolution differs by only 10% from the ultimate resolution limit $\lambda/2$ of any conventional imaging system as predicted by diffraction theory. This difference can be explained by losses inside the crystal, which are inevitably present in any real system. Therefore, the 2D flat phononic crystal with equifrequency contours matched to those of the outside medium is capable of producing images with an excellent resolution approaching the diffraction limit.

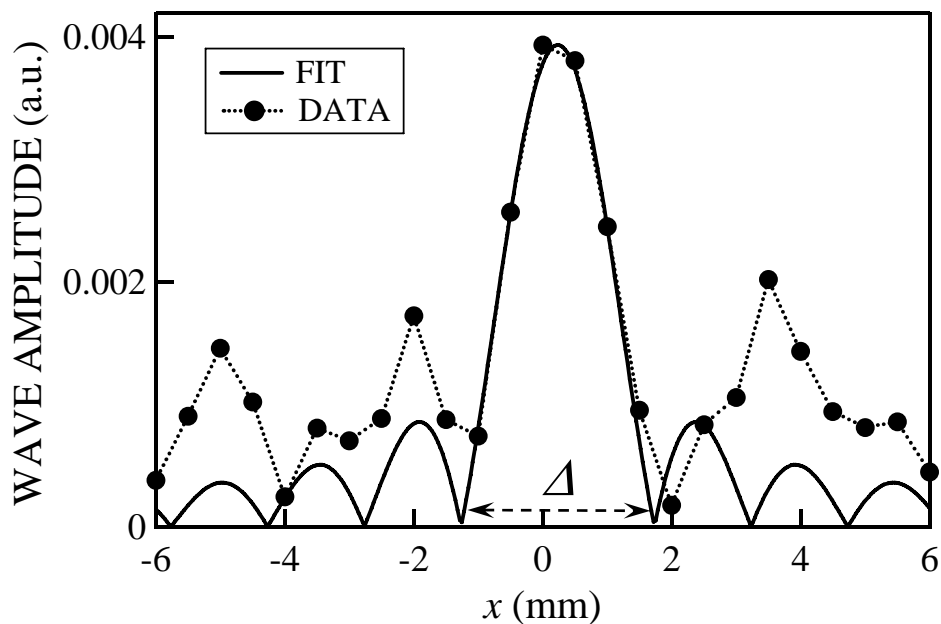


Figure 5.2.19: Amplitude peak at 0.55 MHz along with fitted sinc function. The width of the peak Δ was found to be 3.00 mm.

It is worthwhile discussing now the possibility of achieving super-resolution (better than the diffraction limit) when imaging with a flat phononic crystal. The

underlying reason for the existence of the diffraction limit is that evanescent waves, which along with the propagating waves comprise the original field emitted by the source, are not used in the image restoration, as their magnitudes decay exponentially with the distance away from the source and are usually negligibly small. Thus, to produce images with resolution better than the diffraction limit, the crystal must be able to amplify evanescent waves. In their theoretical work Luo *et al.* [48] have shown that a 2D *photonic* crystal with a certain band structure (see below) is able to amplify evanescent waves so that a resolution better than $\lambda/2$ can be achieved. Physically, the amplification of evanescent waves occurs via their resonant coupling to either *surface* or *bulk* bound (guided) photon states and the resulting growth of these states during transmission. Luo *et al.* consider predominantly the amplification of evanescent waves by surface bound photon states, which are surface modes spatially confined to the crystal's surface and decaying exponentially with the increasing distance both inside and outside the crystal [82]. For amplification to occur, the *surface* band structure must feature a sufficiently flat dispersion curve of the bound states $\omega(k)$, so that quantity $|\omega_0 - \omega(k)|$, where ω_0 is the frequency of operation, remains small for all incident evanescent waves with wavevectors $k > \omega_0/c$. Ideally, *all* evanescent waves would couple to the corresponding surface state and be amplified just to the right degree required to negate their exponential decay outside the crystal, resulting in a perfect image on the output side. This ideal situation is, of course, very difficult to realize in practice. Luo *et al.* showed, however, that one can always design a crystal, which will operate sufficiently close to the ideal situation, and good quality images still can be obtained. It remains an open question whether or not similar mechanisms for super-resolution exist in *phononic* crystals, as to the best of my

knowledge no theoretical analysis analogous to Luo *et al.*'s has been done for the case of phononic crystals. If we assume that phononic crystals with certain band structures can indeed amplify evanescent waves, another consideration should also be taken into account. In the same paper, Luo *et al.* also showed that the resolution $\Delta/2$ of a photonic crystal, which is defined as half the transverse size of an image intensity peak due to a line source, is limited by crystal's surface periodicity. By using a simplified model, which assumes perfect total transmission for all waves with transverse wavevector $|k| < k_M$ and zero transmission for $|k| > k_M$, the intensity profile in the image plane is given by the inverse Fourier transform [48]:

$$I(x) = \left| \int_{-k_M}^{k_M} \exp(ikx) dk \right|^2 = \frac{4 \sin^2(k_M x)}{x^2} \quad (5.8)$$

where the x -axis is parallel to the crystal's surface. The resolution is half the distance between the first zeros around the peak, i.e., $\Delta = 2\pi/k_M$, and is inversely related to the maximum transverse wavevector k_M transmitted by the crystal. For a conventional optical imaging system $k_M = 2\pi/\lambda$, with a corresponding resolution limited to $\lambda/2$. By contrast, the perfect lens proposed by Pendry in [37] has $k_M = \infty$ and unlimited resolution. Luo *et al.* showed that k_M in a photonic crystal can exceed the diffraction limited value $2\pi/\lambda$, but is always finite because of the periodicity of the crystal's surface. From the limits imposed on k_M they derived the upper and lower bounds of the best achievable resolution when imaging with a 2D photonic crystal, which are given by the following inequality:

$$\frac{a_s \lambda}{\lambda - a_s} < \Delta < 2a_s \quad (5.9)$$

where a_s is the surface period and λ is the operation wavelength. The upper bound in (5.9) is obtained on the assumption that *all* Fourier components of the incident field with parallel wavevectors lying *inside* the first surface Brillouin zone, i.e. $\omega_0/c < k < \pi/a_s$, couple to the surface modes ($k_M = \pi/a_s$). This is a conservative estimate since it ignores the wavevectors that originally extend past the Brillouin zone edge and are Bragg-scattered back into the first Brillouin zone *outside* the light cone. These wavevectors lie in the range between the first Brillouin zone edge and the light cone line, i.e. $\pi/a_s < k < 2\pi/a_s - \omega_0/c$ and $k_M = 2\pi/a_s - \omega_0/c$. The wavevectors, which are Bragg-scattered *inside* the light cone, i.e. $2\pi/a_s - \omega_0/c < k$, couple to the leaky photon modes, and are shown by Luo *et al.* not to produce significant amplification of evanescent waves (see [48] for more details). When the Bragg-scattered wavevectors are taken into account, the lower bound is obtained. From (5.9) it is clear that the resolution $\Delta/2$ is limited by the surface period a_s of the crystal and can overcome the diffraction limit when the surface period a_s of the crystal is less than $\lambda/2$. To estimate the possible limit on the best achievable resolution with my phononic crystal I will use only the upper bound on Δ in (5.9). In my case $a_s = 1.27$ mm, which implies the best achievable resolution of 0.47λ . Although the resolution observed in my experiments is close to the limit derived following Luo *et al.*, it is still larger than the diffraction limit. From this we can conclude that evanescent waves were not amplified by the crystal during the experiment and only propagating components of the field participated in image restoration. This conclusion is also supported by the focusing pattern displayed in Figure 5.2.18(b). If the evanescent

waves were resonantly amplified, one would expect to see a sound field of large magnitude right at the output surface of the crystal, which would decay exponentially with the distance away from the crystal. This behaviour was observed by Grbic *et al.*, who observed subwavelength resolution smaller than the diffraction limit by investigating focusing of electromagnetic waves emitted by a point source with an artificial Left-Handed material made of 2D transmission line grids loaded with capacitors and shunt inductors [42]. However, in my experiments the focal spot is confined in the direction perpendicular to the crystal surface implying that no evanescent field amplification occurs. This, however, does not rule out the possibility of achieving subwavelength resolution while imaging with phononic crystals with a different structure. A serious theoretical analysis is required to establish whether flat bound surface modes, similar to those considered by Luo *et al.* in case of electromagnetic waves, can exist in phononic crystals.

In conclusion, using the water-filled 2D flat phononic crystal, the effect of focusing of the sound field emitted by a point source was demonstrated. However, due to mismatch between equifrequency contours in water and in the crystal, the focal spot was not well confined along direction perpendicular to the crystal surface. A significant improvement in the quality of the focusing pattern was achieved by imaging with the new methanol crystal, which had an equifrequency contour matching that in water at the frequency 0.55 MHz. The observed focal spot was confined in both parallel and perpendicular directions to the crystal surface. By using a generating transducer, whose width was much smaller than the wavelength in water (about $\lambda/5$), the limit on the resolution achievable with the crystal was investigated. The resolution limit of 0.55λ was observed. No evidence of the amplification of the evanescent waves was found.

6. Conclusions

In this chapter I would like to summarize the major experimental findings and achievements reported in this thesis.

The first part of my Ph.D. work concentrated on the experiments with 3D phononic crystals made of small tungsten carbide spheres assembled in an fcc crystal structure and immersed in water. Resonant tunnelling of ultrasound pulses through the double barrier consisting of two such crystals separated by a cavity (an aluminum spacer) was successfully observed for the first time. This effect is a classical analogue of resonant tunnelling of a quantum mechanical particle through a double potential barrier. In the case of ultrasound pulses, the potential barrier was represented by a phononic crystal at the frequency range corresponding to the complete band gap. The effect manifested itself by a narrow peak in the transmission inside the band gap, which occurs due to constructive interference of all the multiple reflections of an ultrasound pulse reverberating for a long time inside the cavity. The resonant condition is satisfied when width of the cavity approximately equals an integer number of half-wavelengths of ultrasound in aluminum. The dynamics of resonant tunnelling was also investigated by measuring the group time and group velocity of the transmitted pulses. It was found that at frequencies away from resonance the transmitted pulses travelled very fast with a group velocity larger than the speed of sound in any of the crystal constituent materials. At the same time, very slow group velocities (slower than the speed of sound in air) were observed at the resonant frequency. In contrast to resonant tunnelling of Quantum Mechanics, the magnitude of the observed resonant tunnelling peak was significantly less than unity. This reduction in peak magnitude was explained by the effect of absorption, which has no counterpart in

Quantum Mechanics. The absorption introduces a small propagating component inside the crystal in addition to the dominant evanescent mode at the band gap frequencies. As a result, there exists a leakage of the pulse from the cavity, thus limiting the build-up of the field inside the cavity. The propagating component also reduces the group time by reducing the time spent by the pulse inside the cavity.

The second part of my thesis concentrated on band structure effects in 2D phononic crystals made of stainless steel rods assembled in a triangular crystal lattice and immersed in water. By employing circular equifrequency contours in the 2nd band, I was able to demonstrate negative refraction of ultrasound waves upon their propagation through the crystal/water interface. The unambiguous demonstration of this effect was secured by the use of a prism-shaped 2D crystal. The study of negative refraction was facilitated by the experimental technique, which allowed visualization of the outgoing wave field by creating image plots. Quantitative analysis of the image plots showed that the predictions of the Multiple Scattering Theory are remarkably accurate.

The same idea of bending sound negatively was used in focusing experiments. In these experiments I used flat 2D crystals to focus the sound field emitted by different point-like sources. The possibility of sound focusing by a flat phononic crystal was demonstrated in experiments with a flat phononic crystal filled with and immersed in water. In these experiments a small circular transducer (a pinducer) with diameter slightly larger than a wavelength of sound in water was used. During these experiments two important factors crucial to achieving high-quality images were established. First, it is desirable to use equifrequency contours of circular shape to avoid distortions of the image. Second, the resolution of the observed images is influenced by the degree of mismatch between sizes of the equifrequency contours in the crystal and surrounding medium (water

in my case). Since it was impossible to satisfy both conditions with the water-filled phononic crystal, a new flat crystal was designed, which allowed a liquid inside the crystal to be different from the outside medium (water). The new crystal was filled with methanol, which resulted in *matching circular* equifrequency contours at 0.55 MHz. In other words, at the matching frequency the new crystal had an effective refraction index $n = -1$ (with respect to water). A significant improvement in the quality of the image was observed while imaging the pinducer. The lateral resolution 0.58λ was found to be just above the diffraction limit.

In order to investigate the possibility of achieving the *subwavelength* resolution while imaging with phononic crystals, a new subwavelength line source was constructed. The new source was a miniature transducer in the shape of a thin strip (approximately $\lambda/5$ wide at the matching frequency). By measuring the width of the focal spot observed while imaging the line source, a resolution of 0.55λ was found, which is even closer to, but still just above, the diffraction limit $\lambda/2$. A resolution better than the diffraction limit implies the ability of the crystal to amplify an evanescent component of the incident field. The above result indicates that no amplification of the evanescent waves occurred in the imaging experiments with the 2D phononic crystals considered in my thesis.

At the end of this section it is worthwhile considering possible directions of future research in the field of phononic crystals and acoustic doubly-negative metamaterials. One obvious direction is the design of the practical devices based on phononic crystals, such as acoustic filters, mirrors and waveguides. Taking into account the large size of acoustic phononic crystals for audible sound, as dictated by the wavelength of sound in air, it is very possible that future devices will employ phononic crystals in which

individual elements will have internal structure with built-in local resonances. This would allow a significant reduction of the size of the phononic crystals for devices working with sound waves in air.

Doubly-negative acoustic metamaterials comprise another area in which a lot of activities, both theoretical and experimental, are expected. Recently the possibility of achieving the subwavelength resolution, while imaging with a slab of an acoustic metamaterial, was shown theoretically by Ambati *et al.* [81]. Just as in the case of Pendry's proposal [37], super-resolution is predicted by the amplification of the evanescent waves with the help of surface resonant states, which are excited on the surface of the slab with simultaneously negative values of both dynamic effective density and bulk modulus. In case where the thickness of the slab is much smaller than the wavelength, Ambati *et al.* also showed that negative effective density alone is sufficient to amplify evanescent waves. Future research will probably concentrate on overcoming the experimental challenges of realizing doubly-negative acoustic metamaterials and observing negative refraction and imaging with subwavelength resolution using these novel materials.

Appendices

Appendix A. Determination of the effective diameter of the pinducer

During the experiments on sound focusing with the rectangular-shaped phononic crystal, the need arose to know the size of the pinducer active element. As shown in Figure A.1, the active element, which had a circular shape, was mounted in thin metal tubing with outside diameter of 2.40 mm. This made it impossible to measure the pinducer element diameter directly.

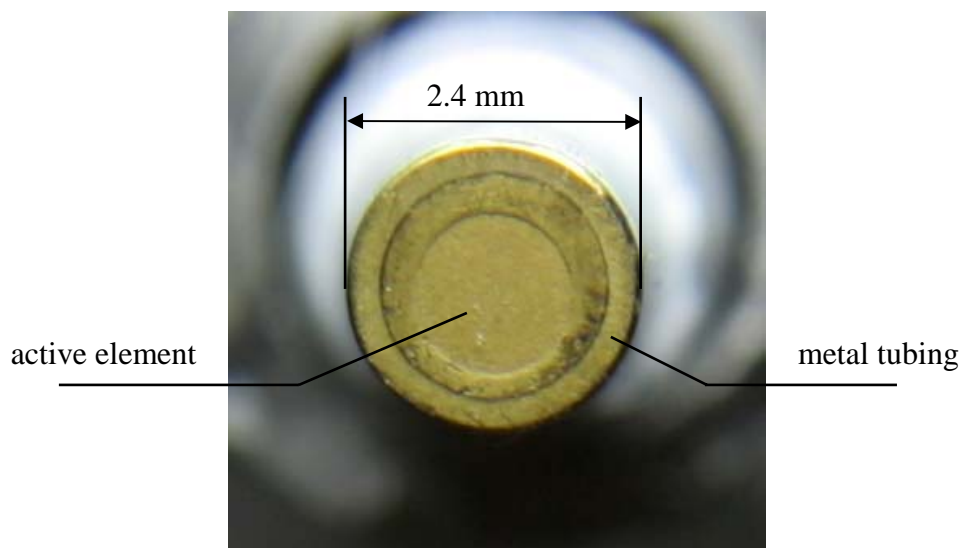


Figure A.1: The top view of the pinducer.

To estimate the size of the pinducer element, I have calculated the pinducer field at some distance away from the pinducer for different pinducer diameters, and compared theoretical curves with the pinducer field profiles measured with the hydrophone in scanning experiments. The calculations of the pinducer field were done according to the

well-known method from Fourier acoustics (as well as Fourier optics). It begins by creating the initial field distribution at the plane of the pinducer ($z = 0$). For the initial field I used the simplest model of the pinducer approximated by a disk of diameter d uniformly oscillating with frequency ω along the normal to its surface [Figure A.2]. 2D FFT of this field distribution was taken and then propagated distance z' away from the pinducer by multiplying each component of the FFT having corresponding wavevectors (k_x, k_y) by the phase factor $\exp[iz'(k^2 - k_x^2 - k_y^2)^{1/2}]$, where $k = \omega/\nu$ is the wavevector, which is defined by the frequency of the pinducer oscillation ω and the phase velocity ν in the medium (water). Finally, the field distribution in the plane at $z = z'$ was found by taking the inverse 2D FFT. More details on this approach can be found, for example, in monographs by Williams [78] or by Goodman [79].

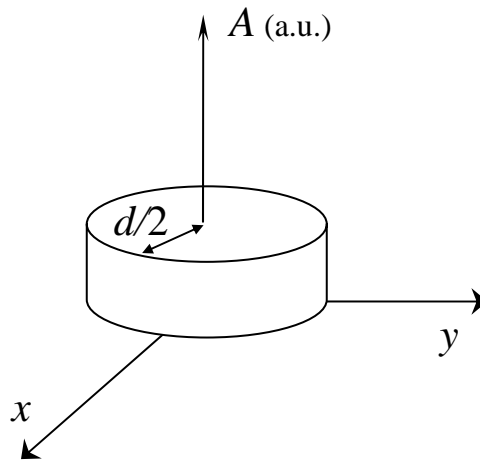


Figure A.2: Initial field distribution amplitude A (at $z = 0$) used in calculations of the pinducer field, displayed as a function of position in x - y plane.

As was already mentioned, experimental field profiles were measured by scanning the field of the pinducer with the hydrophone. The geometry of the experiment was identical to the one shown in Figure 5.3.1 but with the crystal removed. A 2D image plot of the pinducer field amplitude is presented in Figure A.3.

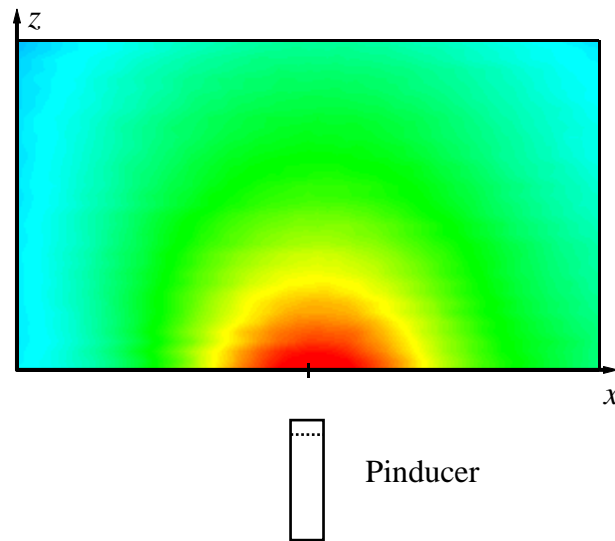


Figure A.3: 2D image plot obtained by scanning the pinducer field with the hydrophone in the x - z plane. The pinducer position is schematically indicated.

By comparing the calculated and measured field profiles, the effective diameter of the pinducer was estimated to be about 2.2 mm. Theoretical and experimental curves are compared in Figure A.4(a)-(b), in which theory and experiment are overlaid for two different distances away from the pinducer. Good agreement is observed in both cases.

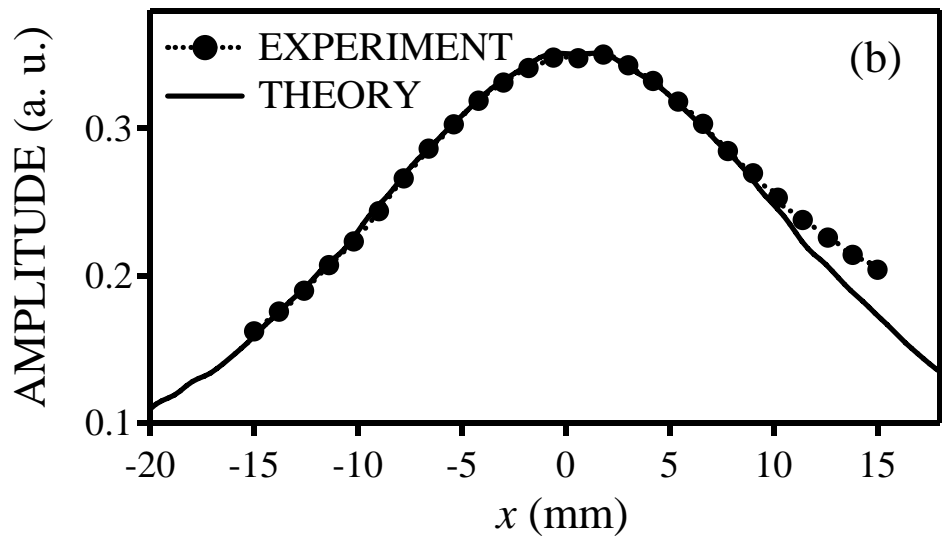
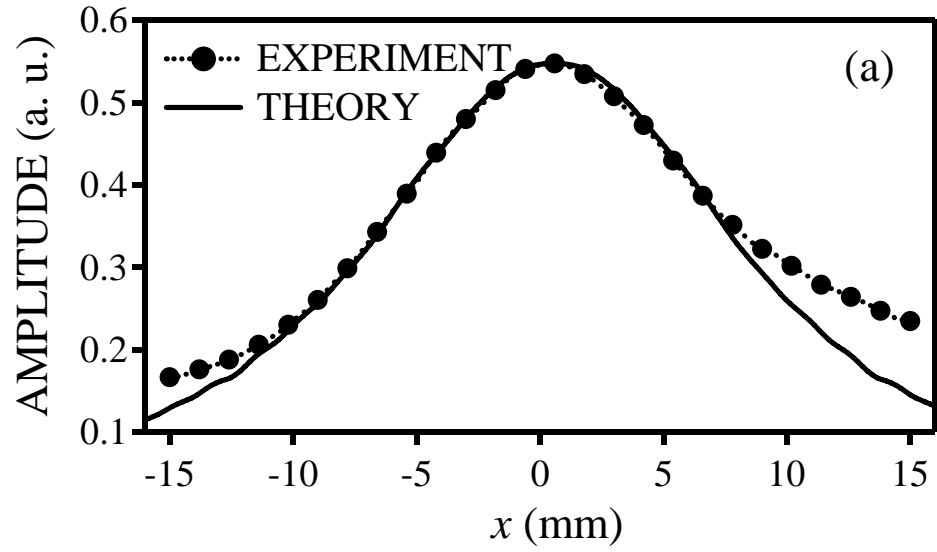


Figure A.4: Comparison of calculated and measured pinducer field profiles at (a) $z = 12.5$ mm and (b) $z = 20$ mm away from the pinducer.

Appendix B. Transfer matrix through a single potential barrier

This Appendix provides the derivation of the transfer matrix M through a single rectangular potential barrier of height V_0 and width a [Figure B.1] for an incident particle of energy $E < V_0$.

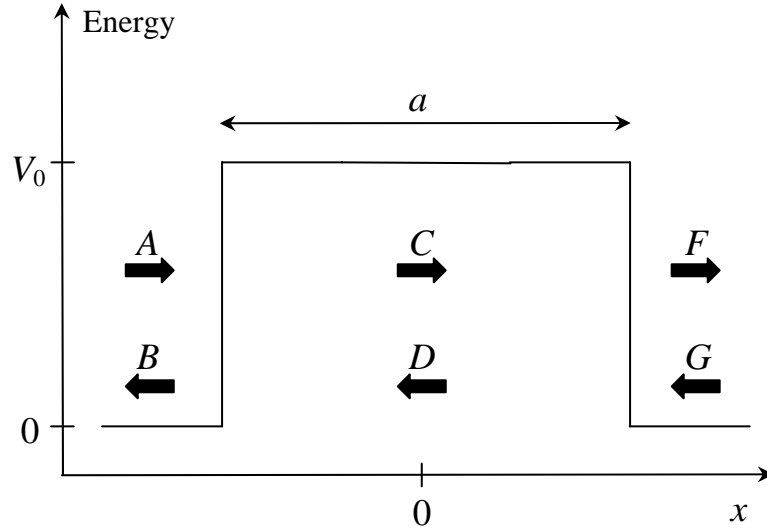


Figure B.1: A single rectangular potential barrier.

The wave function of the particle can be written in the following way:

$$\psi(x) = A \exp(ikx) + B \exp(-ikx) \quad \text{for } x < -a/2$$

$$\psi(x) = C \exp(-\kappa x) + D \exp(\kappa x) \quad \text{for } -a/2 < x < a/2$$

$$\psi(x) = F \exp(ikx) + G \exp(-ikx) \quad \text{for } x > a/2$$

where $k = \sqrt{2mE}/\hbar$ and $\kappa = \sqrt{2m(V_0 - E)}/\hbar$ are wavevectors outside and inside the potential barrier respectively, m being a mass of the particle.

Using the fact that both wave function and its first derivative must be continuous at $x = -a/2$ and $x = a/2$ one can obtain the system of four equations, which relate all six coefficients:

$$A \exp(-\frac{1}{2}ika) + B \exp(\frac{1}{2}ika) = C \exp(\frac{1}{2}\kappa a) + D \exp(-\frac{1}{2}\kappa a)$$

$$C \exp(-\frac{1}{2}\kappa a) + D \exp(\frac{1}{2}\kappa a) = F \exp(\frac{1}{2}ika) + G \exp(-\frac{1}{2}ika)$$

$$ikA \exp(-\frac{1}{2}ika) - ikB \exp(\frac{1}{2}ika) = -\kappa C \exp(\frac{1}{2}\kappa a) + \kappa D \exp(-\frac{1}{2}\kappa a)$$

$$-\kappa C \exp(-\frac{1}{2}\kappa a) + \kappa D \exp(\frac{1}{2}\kappa a) = ikF \exp(\frac{1}{2}ika) - ikG \exp(-\frac{1}{2}ika)$$

The above equations allow one to obtain expressions for coefficients A and B in terms of F and G :

$$A = \left(\cosh(\kappa a) + i \frac{\varepsilon}{2} \sinh(\kappa a) \right) \exp(ika) F + i \frac{\eta}{2} \sinh(\kappa a) G \quad (\text{B.1})$$

$$B = -i \frac{\eta}{2} \sinh(\kappa a) F + \left(\cosh(\kappa a) - i \frac{\varepsilon}{2} \sinh(\kappa a) \right) \exp(-ika) G \quad (\text{B.2})$$

where $\varepsilon = \kappa/k - k/\kappa$ and $\eta = \kappa/k + k/\kappa$. Equations (B.1) and (B.2) can be written in a matrix form:

$$\begin{pmatrix} A \\ B \end{pmatrix} = M \begin{pmatrix} F \\ G \end{pmatrix}$$

where M is the transfer matrix through a potential barrier with coefficients:

$$M_{11} = M_{22}^* = \left(\cosh(\kappa a) + i \frac{\mathcal{E}}{2} \sinh(\kappa a) \right) \exp(ika)$$

$$M_{12} = M_{21}^* = i \frac{\eta}{2} \sinh(\kappa a)$$

Appendix C. Subsidiary peaks observed in transmission spectra of the resonant tunnelling experiments

As was already mentioned at the end of Section 4.2.3, in many of the experiments on resonant tunnelling through double phononic crystals, the transmission spectra exhibited the presence of subsidiary peaks, which accompanied the main resonant tunnelling peak. Because there was no confidence that the sets of data exhibiting subsidiary peaks were not compromised by their presence, it was extremely important to find ways to eliminate this complication or at least minimize the impact of the effect. Although no explanation of how exactly the effect arises will be provided by the following discussion, the experimentally found prescriptions on how to avoid the complications of the subsidiary peaks may still serve to guide future modelling.

An example of a transmission curve affected by the presence of the subsidiary peak is presented in Figure C.1.

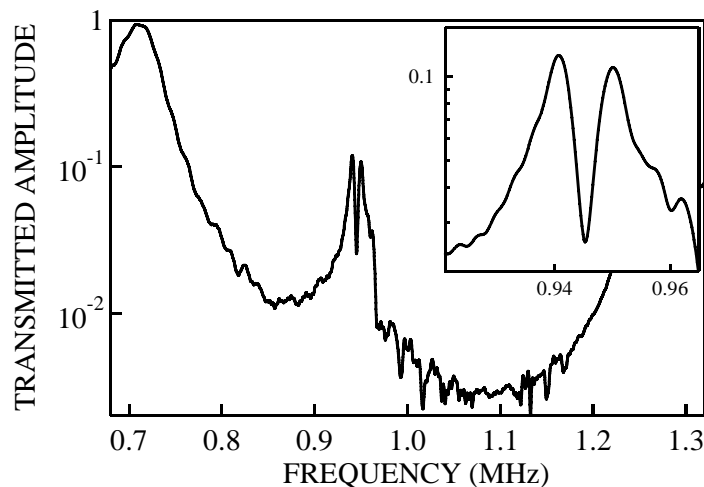


Figure C.1: Transmission spectrum through one of the 3-layer double crystals. The inset magnifies narrow range of frequencies around the resonant tunnelling peak to demonstrate how bad the subsidiary peak problem can be. The inset has the same axis labels as the main figure.

Note the huge size of the effect, as the magnitude of the subsidiary peak is only slightly smaller than that of the main peak. It is clear that these data cannot be used in any type of analysis of the resonant tunnelling effect.

Dealing with the subsidiary peak problem was somewhat facilitated by the fact that it manifested itself not only in the transmission spectra, but also in the shape of the transmitted pulse. As an example, the transmitted pulse, from which the transmission coefficient in Figure C.1 was derived, is shown in Figure C.2.

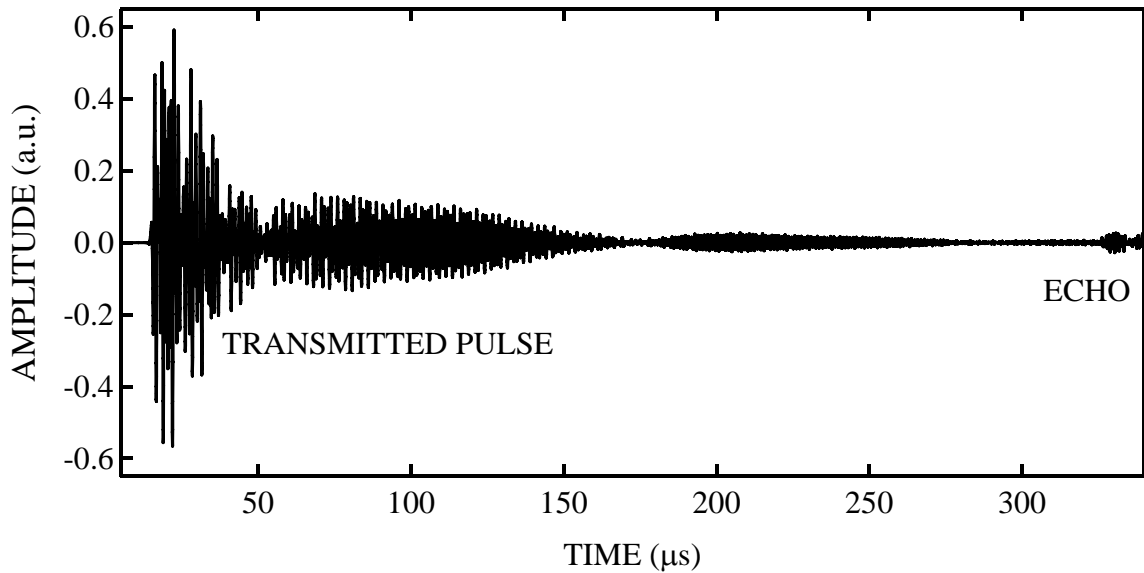


Figure C.2: The transmitted pulse through 3-layer double crystal, from which the transmission coefficient shown in Figure C.1 was found. The overall amplitude modulations are self-evident.

As the transmitted pulse extends in time, the overall shape of the pulse has a pattern similar to the one displayed by two interfering harmonic waves of slightly different frequencies ω_0 and $\omega_0 + \Delta\omega$, which also known as “beating”. This is even more

evident if one examines the shape of the envelope of the transmitted pulse, which is shown in Figure C.3 along with the smoothed curve.

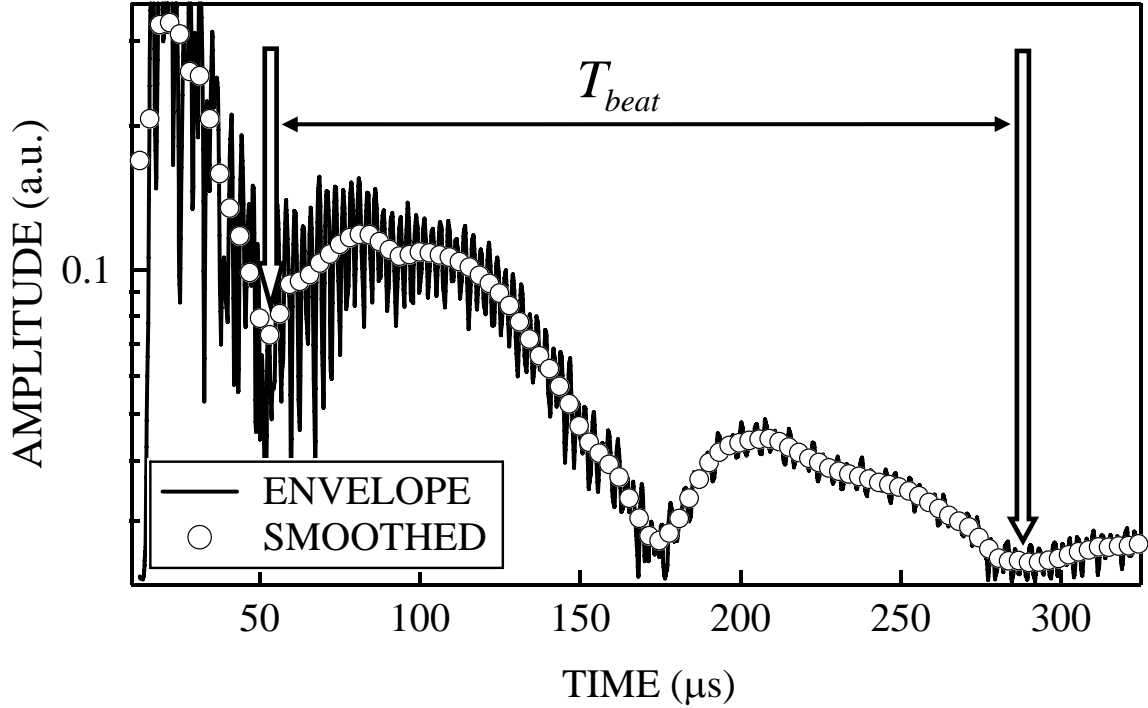


Figure C.3: The envelope of the pulse shown in Figure C.2 along with the smoothed curve.

By measuring the time between beats (e.g. between two amplitude minima), one is able to estimate the magnitude of $\Delta\omega$, which then can be compared with the frequency difference between main and subsidiary peaks. From the pulse envelope shown in Figure C.3, the period of beats T_{beat} was found to be 236 μs giving $\Delta\omega$ of 8.5 kHz, while the frequency separation Δf between main and subsidiary peaks in Figure C.1 is 9.5 kHz. The close correspondence between these two values suggests that subsidiary peaks are brought about by some interference phenomena of waves of slightly different frequencies.

Having established this, there is still a need to obtain data that are free from these complications. With this goal in mind, I have measured the transmission coefficient through the same 3-layer double crystal using three generating transducers, which differed by the diameter of their active elements (0.5, 1.0 and 1.5 inches) but had the same central frequency of 1.0 MHz. The distances between the generating transducer and a sample, and between the receiving transducer and a sample, were kept the same for all three rounds of measurements. The transmission curves are compared in Figure C.4, while Figure C.5 displays corresponding transmitted pulses.

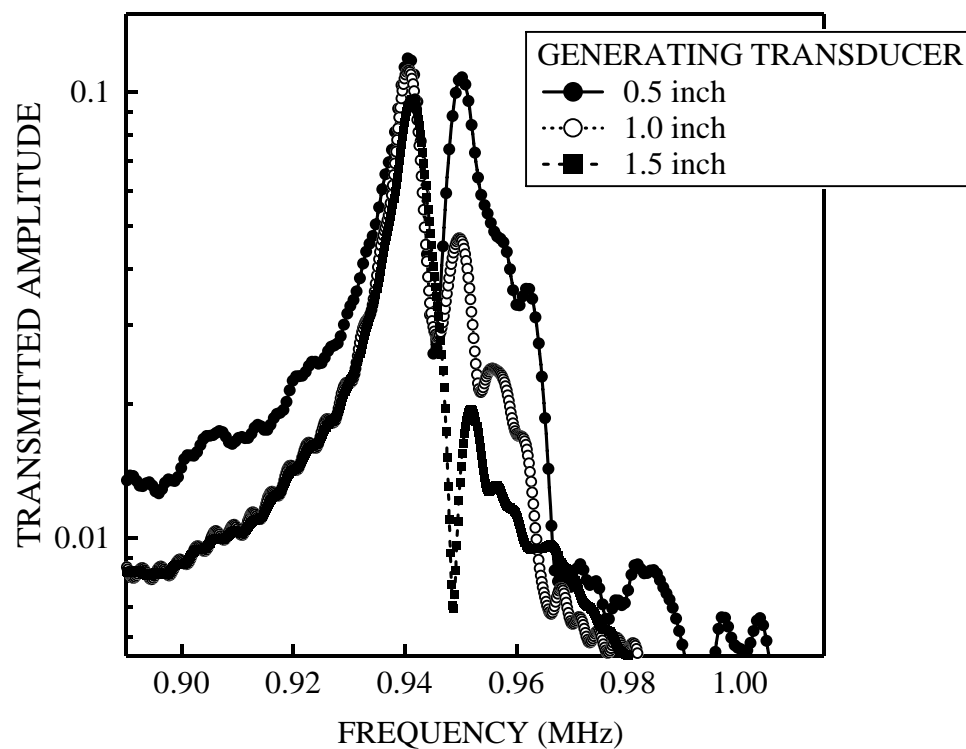


Figure C.4: Comparison of the resonant tunnelling peaks for three generating transducers of different diameters. Note the decrease in magnitude of the subsidiary peak as the diameter of the transducer increases.

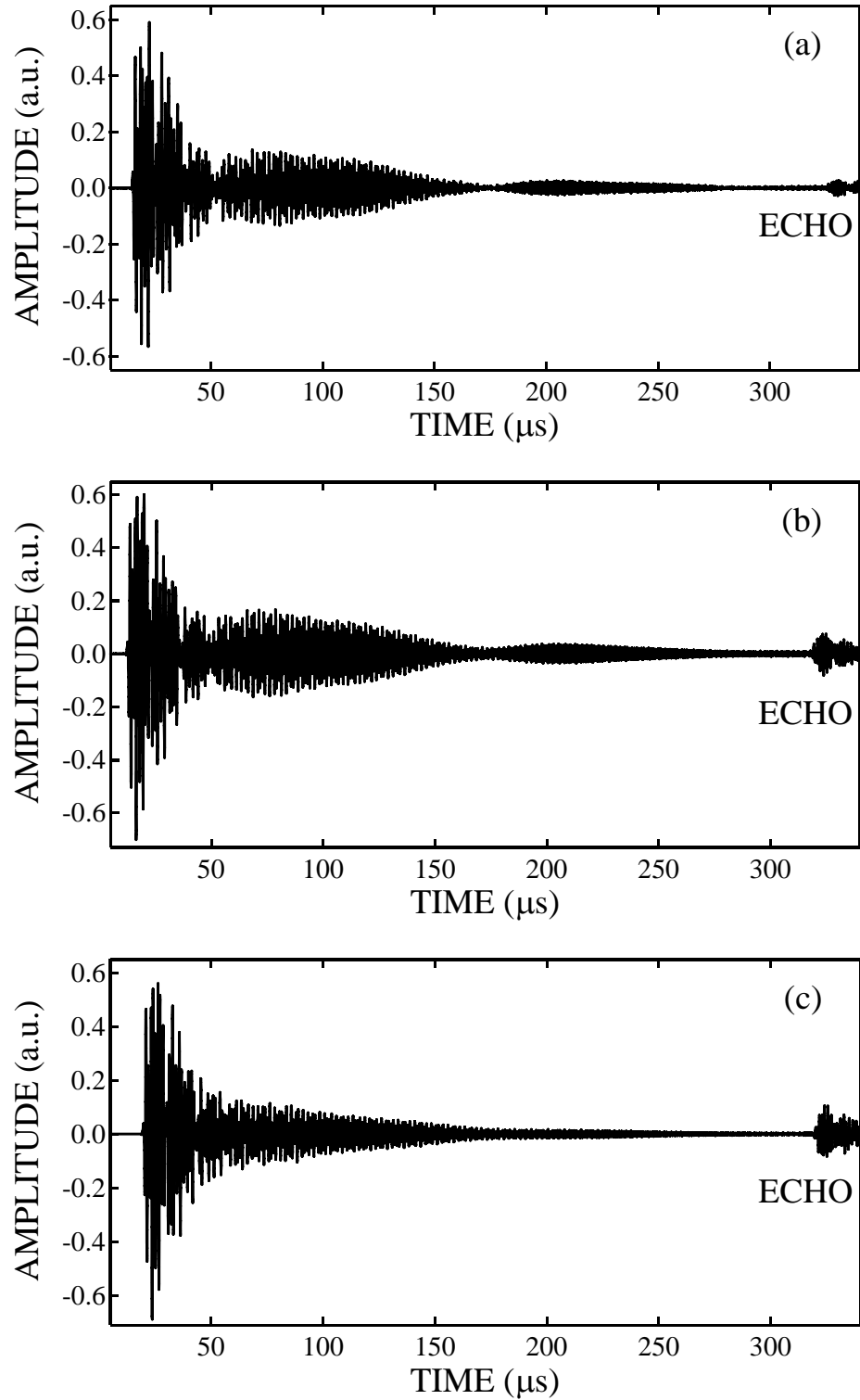


Figure C.5: The waveforms transmitted through the 3-layer double crystal in case of (a) 0.5 inch, (b) 1.0 inch and (c) 1.5 inch-diameter generating transducers.

It is obvious from Figure C.4 that the magnitude of the subsidiary transmission peak decreases as the generating transducer diameter is increased. This improvement is also reflected in the shape of the corresponding transmitted pulse, as the cancellations due to beats become almost invisible in the pulse produced by the generating transducer of the largest diameter [Figure C.5(c)].

What changes as one moves from the smaller to larger transducer diameter? Recall, that in the far-field the intensity of the field produced by a circular transducer is represented by a *spherical* wave modulated by a directivity factor, which involves ratio of a Bessel function of the first order to its argument (see Section 3.4.1):

$$I \propto \frac{1}{r^2} \left[\frac{2J_1\left(\frac{2\pi}{\lambda} a \sin \theta\right)}{\frac{2\pi}{\lambda} a \sin \theta} \right]^2 \quad (\text{C.1})$$

and whose role is to limit outgoing spherical wave to a certain angular range. The *angular* spread of the beam produced by a flat circular transducer is characterized by the angle θ_D [Figure 3.4.3], which defines the -6 dB line (i.e. the line along which magnitude of the intensity level falls half of the one on the transducer axis) and is inversely proportional to the diameter of the transducer d (see equation (3.5)):

$$\theta_D = \sin^{-1}\left(\frac{0.514\lambda}{d}\right) \quad (\text{C.2})$$

By decreasing/increasing θ_D one decreases/increases the *curvature* of the wave fronts incident on the sample surface. In other words, the experiment shows that the magnitude of the subsidiary peak seems to depend on *how well* the incident pulse approximates the plane wave. However, I found that the angular spread of the transducer field was not the only factor that influenced the magnitude of the subsidiary peaks. After

completing the experimental check, whose results are shown in Figure C.4, I repeated the transmission measurements with 1.5 inch-diameter generating transducer through the same 3-layer double crystal but with the distance between the generating transducer and the sample *reduced* by 5 cm. The two transmission curves are compared in Figure C.6. In case of the smaller separation between the generating transducer and the sample the magnitude of the subsidiary peak was reduced even more to the degree when its effect on the main resonant tunnelling peak could be neglected.

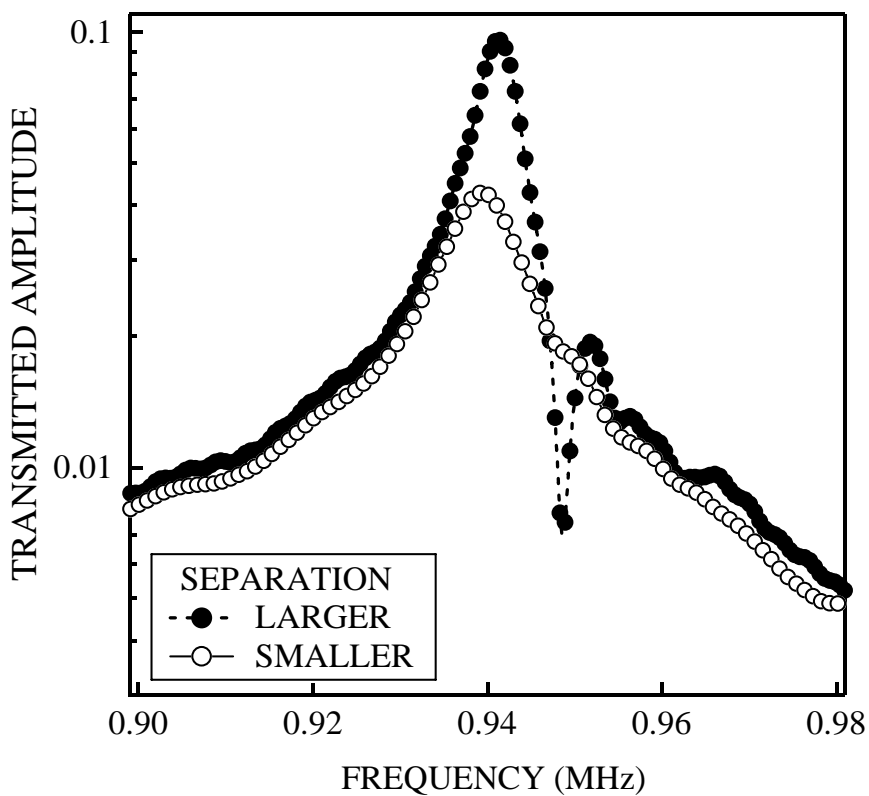


Figure C.6: Comparison of the two resonant tunnelling peaks, both measured for the same 3-layer double crystal using 1.5 inch-diameter generating transducer, but with different distances between the generating transducer and the crystal.

It is clear that this time the improvement is not due to the change in the angular spread of the transducer, which remained the same in both sets of measurements. However, by changing the distance between the generating transducer and the sample, one changes the area of the sample surface illuminated by the transducer. The decrease in the illuminated area caused a substantial decrease of the magnitude of the subsidiary peak. Therefore, based on the experimental evidence one can conclude that the area of the sample covered by an incident beam is another factor, which has a strong influence on the magnitude of the subsidiary peaks. One possible explanation of the observed dependence might be based on the assumption that the ultrasound waves, which undergo multiple reflections inside the cavity because of being trapped there at frequencies on and around the resonance, come out of phase and interfere destructively with each other. The dephasing, which leads to the destructive interference, might be caused by the non-parallelism of the spacer top and bottom surfaces. The maximum deviation of the values of the spacer thickness measured in different spots was found to be about 0.05 mm. Although this degree of the non-parallelism might seem to be extremely small, one should not forget that the pulse is trapped inside the spacer for very long times. Under these circumstances, it still might be possible that even small deviations from the ideal uniform thickness of the spacer produce the effect exhibiting itself as the subsidiary peaks in the transmission spectra. It is reasonable to assume that thickness of the spacer varies smoothly along its surface. Thus, by narrowing the incident beam, one might decrease the area of the spacer in which sound field is excited and make the spacer look “more” parallel to the multiply reflected waves.

In summary, the experimental findings presented in this Appendix show that the presence of the subsidiary peaks in the transmission seems is caused by the angular spread

of the incident beam as well the area of the sample degree illuminated by the transducer. When attempting to reduce the magnitude of the subsidiary peaks, it might be helpful to employ the generating transducers of larger diameters (to decrease the spread angle) and decrease the separation between the generating transducer and the sample (to decrease the area of the sample covered by the input beam). The latter however comes at the cost of the artificial reduction of the resonant tunnelling peak, because the larger part of the transmitted pulse has to be truncated due to its overlap with the echo, which happens at earlier times with the decrease of the separation. This is exactly the reason for the resonant tunnelling peak at smaller separation to be lower than the one measured with higher separation between the generator and the sample [Figure C.6]. Therefore, it is important to find a value of the separating distance that would present a compromise between the opposite goals of eliminating subsidiary peaks and keeping the high magnitude of the resonant tunnelling peak (and correspondingly the group time).

Appendix D. The investigation of the effect of a plastic film used to separate methanol and water in 2D phononic crystal

The design of the methanol-filled 2D crystal was presented in Section 3.1.1, in which it was explained that the inner liquid (methanol) was separated from the outside liquid (water) by a 0.01 mm thick plastic film (a commercially produced food wrap). Although it is quite reasonable to assume that the effect of the film on sound waves propagating through the crystal should be next to negligible due to its extremely small thickness (as compared to the sound wavelength in water at the frequency of experiment), it was still desirable to verify this assumption experimentally. The assumption was tested by comparing the transmission curves obtained in transmission experiments through the same 2D crystal with and without the plastic film in place. In the case when the plastic film was present, the crystal was filled with water. The input ultrasound pulses were incident normally on the crystal surface along the ΓM direction.

As can be seen from Figure D.1, the two transmission curves are practically identical. Of particular importance for the focusing experiments is the fact that above the stop band (as well as below it), the plastic wrap had essentially no effect on the observed transmission coefficient. In case of no plastic film present the stop band is slightly (by 3%) deeper than in the case of the crystal wrapped in the film and filled with water. This minor difference can be explained by the same argument used in Section 4.2.2, when explaining non-unity of the resonant tunnelling peak in the transmission experiments through the double 3D phononic crystals. The effect of the plastic film is to introduce a very small (but non-negligible) amount of absorption, which cuts the long multiple paths of the Bragg scattered waves, thus making their destructive interference incomplete. It is

this interference, which gives a rise to the existence of a band gap (or a stop band). It also affects the depth of the band gap. This is why, in the case when there is no plastic film wrapped around the crystal, the observed band gap is slightly deeper. However, even with this 3% loss in the depth of the band gap, the significant improvement in terms of the quality of the focal pattern as well as the resolution was achieved by employing the 2D crystal surrounded by the plastic film and filled with methanol (Section 5.2.2).

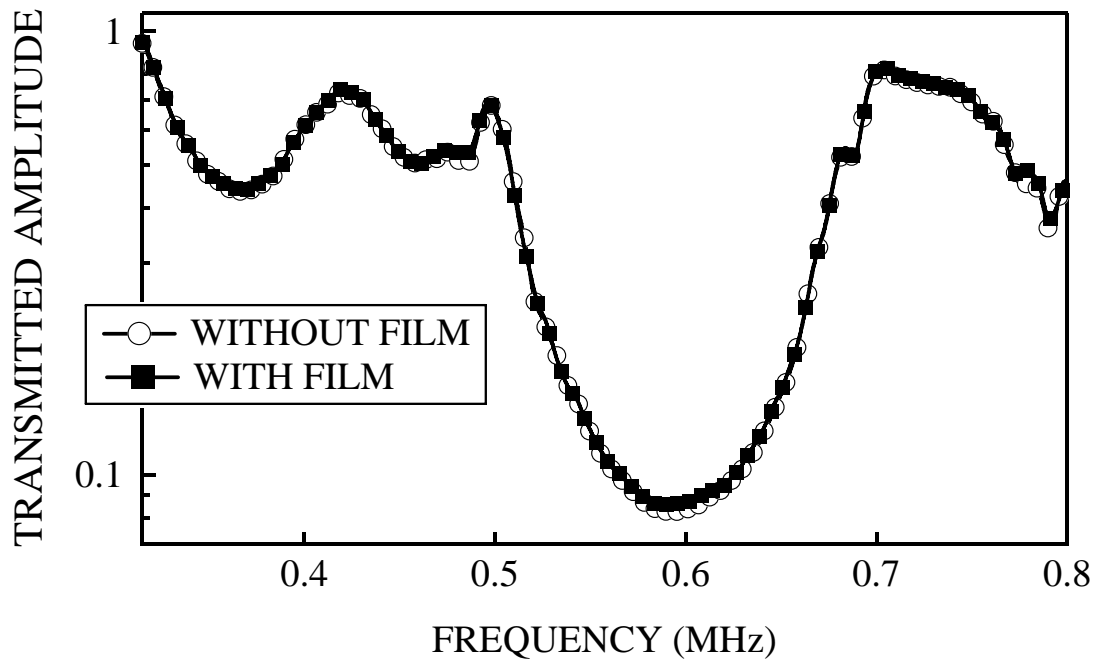


Figure D1: Comparison of the transmission spectra measured in the transmission experiments along the ΓM direction through the 2D phononic crystal immersed in and filled with water with and without plastic film wrapped around the crystal.

References

- [1] V. Narayanamurti, H.L. Störmer, M.A. Chin, A.C. Gossard, W. Wiegmann, “Selective Transmission of High-Frequency Phonons by a Superlattice: The “Dielectric” Phonon Filter”, *Phys. Rev. Lett.* **43**, 2012 (1979).
- [2] J.D. Achenbach, M. Kitahara, “Harmonic waves in a solid with a periodic distribution of spherical cavities”, *J. Acoust. Soc. Am.* **81**(3), 595 (1987).
- [3] E. Yablonovitch, “Inhibited Spontaneous Emission in Solid-State Physics and Electronics”, *Phys. Rev. Lett.* **58**, 2059 (1987).
- [4] M.S. Kushwaha, P. Halevi, L. Dobrzynski, B. Djafari-Rouhani, “Acoustic Band Structure of Periodic Elastic Composites”, *Phys. Rev. Lett.* **71**, 2022 (1993); M.S. Kushwaha, P. Halevi, “Band-gap engineering in periodic elastic composites”, *Appl. Phys. Lett.* **64**, 1085 (1994).
- [5] M.S. Kushwaha, P. Halevi, G. Martínez, L. Dobrzynski, B. Djafari-Rouhani, “Theory of acoustic band structure of periodic elastic composites”, *Phys. Rev. B.* **49**, 2313 (1993).
- [6] J.O. Vasseur, P.A. Deymier, G. Frantziskonis, G. Hong, B. Djafari-Rouhani, L. Dobrzynski, “Experimental evidence for the existence of absolute acoustic band gaps in two-dimensional periodic composite media”, *J. Phys.: Condens. Matter* **10**, 6051 (1998); J.O. Vasseur, P.A. Deymier, B. Chenni, B. Djafari-Rouhani, L. Dobrzynski, D. Prevost “Experimental and Theoretical Evidence for the Existence of Absolute Acoustic Band Gaps in Two-Dimensional Solid Phononic Crystal”, *Phys. Rev. Lett* **86**, 3012 (2001).
- [7] E.N. Economou, M.M. Sigalas, “Stop bands for elastic waves in periodic composite materials”, *J. Acoust. Soc. Am.* **95**, 1734 (1994).
- [8] M. Kafesaki, M.M. Sigalas, E.N. Economou, “Elastic wave band gaps in 3-D periodic polymer matrix composites”, *Solid State Commun.* **96**, 285 (1995).
- [9] B.K. Henderson, K.I. Maslov, V.K. Kinra, “Experimental investigation of acoustic band structures in tetragonal periodic particulate composite structure”, *J. Mech. Phys. Solids* **49**, 2369 (2001).
- [10] R. Sainidou, N. Stefanou, A. Modinos, “Formation of absolute frequency gaps in three-dimensional solid phononic crystals”, *Phys. Rev. B* **66**, 212301 (2002).
- [11] M. Sigalas, M.S. Kushwaha, E.N. Economou, M. Kafesaki, I.E. Psarobas, W. Steurer, “Classical vibrational modes in phononic lattices: theory and experiment”, *Z. Kristallogr.* **220**, 765-809 (2005).
- [12] J.H. Page, S. Yang, M.L. Cowan, Z. Liu, C.T. Chan, P. Sheng, “3D Phononic Crystals”, In *Wave Scattering in Complex Media: From Theory to Applications*, pp.283-307, Kluwer Academic Publishers: NATO Science Series, Amsterdam (2003).

- [13] D. Caballero, J. Sánchez-Deheza, C. Rubio, R. Martínez-Sala, J.V. Sánchez-Pérez, F. Meseguer, J. Llinares, “Large two-dimensional sonic band gaps”, *Phys. Rev. E* **60**, R6316 (1999).
- [14] C. Goffaux, J.P. Vigneron, “Theoretical study of a tunable phononic band gap system”, *Phys. Rev. B* **64**, 075118 (2001).
- [15] R. Martinez-Sala, J. Sancho, J.V. Sanchez, V. Gomez, J. Llinares, F. Meseguer, “Sound attenuation by sculpture”, *Nature* **378**, 241 (1995).
- [16] J.O. Vasseur, P.A. Deymier, A. Khelif, Ph. Lambin, B. Djafari-Rouhani, A. Akjouj, L. Dobrzynski, N. Fettouhi, J. Zemmouri, “Phononic crystals with low filling fraction and absolute acoustic band gap in the audible frequency range: A theoretical and experimental study”, *Phys. Rev. E* **65**, 056608 (2002).
- [17] M.S. Kushwaha, P. Halevi, “Ultrawideband Filter for Noise Control”, *Jpn. J. Appl. Phys.* **36**, L 1043 (1997).
- [18] Z. Liu, X. Zhang, Y. Mao, Y. Y. Zhu, Z. Yang, C.T. Chan, P. Sheng, “Locally resonant sonic materials”, *Science* **289**, 1734 (2000); P. Sheng, X. Zhang, Z. Liu, C.T. Chan, “Locally resonant sonic materials”, *Physica B* **338**, 201 (2003).
- [19] Z. Liu, C.T. Chan, P. Sheng, “Three-component elastic wave band gap material”, *Phys. Rev. B* **65**, 165116 (2002); Z. Liu, C.T. Chan, P. Sheng, “Analytic model of phononic crystals with local resonances”, *Phys. Rev. B* **71**, 014103 (2005).
- [20] R. James, S.M. Woodley, C.M. Dyer, V.F. Humphrey “Sonic bands, bandgaps, and defect states in layered structures – Theory and experiment”, *J. Acoust. Soc. Am.* **97**(4), 2041 (1995).
- [21] J.N. Munday, C.B. Bennet, W.M. Robertson, “Band gaps and defect modes in periodically structures waveguides”, *J. Acoust. Soc. Am.* **112**(4), 1353 (2002).
- [22] I.E. Psarobas, N. Stefanou, A. Modinos, “Phononic crystals with planar defects”, *Phys. Rev. B.* **62**, 5536 (2000).
- [23] A. Khelif, A. Choujaa, B. Djafari-Rouhani, M. Wilm, S. Ballandras, V. Loude, “Trapping and guiding of acoustic waves by defect modes in a full-band-gap ultrasonic crystal”, *Phys. Rev. B* **68**, 214301 (2003).
- [24] A. Khelif, P.A. Deymier, B. Djafari-Rouhani, J.O. Vasseur, L. Dobrzynski, “Two-dimensional phononic crystal with tunable narrow pass band: Application to a waveguide with selective frequency”, *J. Appl. Phys.* **94**, 1308 (2003).
- [25] A. Khelif, A. Choujaa, S. Benchabane, B. Djafari-Rouhani, V. Loude, “Guiding and bending of acoustic waves in highly confined phononic crystal waveguides”, *Appl. Phys. Lett.* **84**, 4400 (2004); A. Khelif, A. Choujaa, S. Benchabane, B. Djafari-Rouhani, V. Loude, “Experimental study of guiding and filtering of acoustic waves in a two dimensional ultrasonic crystal”, *Z. Kristallogr.* **220**, 836 (2005).
- [26] Y. Pennec, B. Djafari-Rouhani, J.O. Vasseur, A. Khelif, P.A. Deymier, “Tunable filtering and demultiplexing in phononic crystals with hollow cylinders”, *Phys. Rev. E* **69**, 046608 (2004).

- [27] Ch. Spielmann, R. Szipöcs, A. Stingl, F. Krausz, “Tunneling of Optical Pulses through Photonic Band Gaps”, *Phys. Rev. Lett.* **73**, 2308 (1994).
- [28] T.E. Hartman, “Tunneling of a Wave Packet”, *J. Appl. Phys.* **33**, 3427 (1962).
- [29] S. Yang, J.H. Page, Z. Liu, M.L. Cowan, C.T. Chan, P. Sheng, “Ultrasound Tunnelling through 3D Phononic Crystals”, *Phys. Rev. Lett.* **88**, 104301 (2002).
- [30] A. Sukhovich, J.H. Page, B. van Tiggelen, Z. Liu, “Resonant Tunneling of Ultrasound in Three-Dimensional Phononic Crystals”, *Physics in Canada* **60**(4), 245 (2004).
- [31] W.M. Robertson, C. Baker, C.B. Bennet, “Slow group velocity propagation of sound via defect coupling in a one-dimensional acoustic band gap array”, *Am. J. Phys.* **72**(2), 255 (2004).
- [32] V.G. Veselago, “The electrodynamics of substances with simultaneously negative values of ϵ and μ ”, *Usp. Fiz. Nauk* **92**, 517 (1964).
- [33] J.B. Pendry, A.J. Holden, W.J. Stewart, I. Youngs, “Extremely Low Frequency Plasmons in Metallic Mesostructures”, *Phys. Rev. Lett.* **76**, 4773 (1996).
- [34] J.B. Pendry, A.J. Holden, D.J. Robbins, W.J. Stewart, “Magnetism from Conductors and Enhanced Nonlinear Phenomena”, *IEEE Trans. Microwave Theory Tech.* **47**, 2075 (1999).
- [35] R.A. Shelby, D.R. Smith, S. Shultz, “Experimental Verification of a Negative Index of Refraction”, *Science* **292**, 77 (2001).
- [36] J.B. Pendry, “Negative Refraction”, *Contemporary Physics* **45**, 191 (2004)
- [37] J.B. Pendry, “Negative Refraction Makes a Perfect Lens”, *Phys. Rev. Lett.* **85**, 3966 (2000)
- [38] S. Anantha Ramakrishna, “Physics of negative refractive index materials”, *Rep. Prog. Phys.* **68**, 449 (2005).
- [39] G.W. ’t Hooft, “Comment on “Negative Refraction Makes a Perfect Lens”, *Phys. Rev. Lett.* **87**, 249701 (2001); Pendry Replies, *Phys. Rev. Lett.* **87**, 249702 (2001); J.M. Williams, “Some Problems with Negative Refraction”, *Phys. Rev. Lett.* **87**, 249703 (2001); Pendry Replies, *Phys. Rev. Lett.* **87**, 249704 (2001).
- [40] N. Garcia, M. Nieto-Vesperinas, “Left-Handed Materials Do Not Make a Perfect Lens”, *Phys. Rev. Lett.* **88**, 207403 (2002); J.B. Pendry, “Comment on “Left-Handed Materials Do Not Make a Perfect Lens”, *Phys. Rev. Lett.* **91**, 099701 (2003); Nieto-Vesperinas and Garcia Reply, *Phys. Rev. Lett.* **91**, 099702 (2003).
- [41] N. Fang, H. Lee, C. Sun, X. Zhang, “Sub-Diffraction-Limited Optical Imaging with a Silver Superlens”, *Science* **308**, 534 (2005).
- [42] A. Grbic, G.V. Eleftheriades, “Overcoming the Diffraction Limit with a Planar Left-Handed Transmission-Line Lens”, *Phys. Rev. Lett.* **92**, 117403 (2004).
- [43] G.V. Eleftheriades, A.K. Iyer, “Planar Negative Refractive Index Media Using Periodically L - C Loaded Transmission Lines”, *IEEE Trans. Microwave Theory Tech.* **50**, 2075 (2002).

- [44] M. Notomi, “Theory of light propagation in strongly modulated photonic crystals: Refractionlike behavior in the vicinity of the photonic band gap”, *Phys. Rev. B* **62**, 10 696 (2000).
- [45] C. Luo, S.G. Johnson, J.D. Joannopoulos, J.B. Pendry, “All-angle negative refraction without negative effective media”, *Phys. Rev. B* **65**, 201104(R) (2002).
- [46] E. Cubukcu, K. Aydin, E. Ozbay, S. Foteinopoulou, C.M. Soukoulis, “Negative refraction by photonic crystals”, *Nature* **423**, 604 (2003).
- [47] P.V. Parimi, W.T. Lu, P. Vodo, J. Sokoloff, J.S. Derov, S. Sridhar, “Negative Refraction and Left-Handed Electromagnetism in Microwave Photonic Crystals”, *Phys. Rev. Lett.* **92**, 127401 (2004).
- [48] C. Luo, S.G. Johnson, J.D. Joannopoulos, J.B. Pendry, “Subwavelength imaging in photonic crystals”, *Phys. Rev. B* **68**, 045115 (2003).
- [49] E. Cubukcu, K. Aydin, E. Ozbay, S. Foteinopoulou, C.M. Soukoulis, “Subwavelength Resolution in a Two-Dimensional Photonic-Crystal-Based Superlens”, *Phys. Rev. Lett.* **91**, 207401 (2003).
- [50] S. Yang, J.H. Page, Z. Liu, M.L. Cowan, C.T. Chan, P. Sheng, “Focusing of Sound in a 3D Phononic Crystal”, *Phys. Rev. Lett.* **93**, 024301 (2004).
- [51] X. Zhang, Z. Liu, “Negative refraction of acoustic waves in two-dimensional phononic crystals”, *Appl. Phys. Lett.* **85**, 341 (2004).
- [52] C. Qiu, X. Zhang, Z. Liu, “Far-field imaging of acoustic waves by a two-dimensional sonic crystal”, *Phys. Rev. B* **71**, 054302 (2005).
- [53] J. Li, Z. Liu, C. Qiu, “Negative refraction imaging of acoustic waves by a two-dimensional three-component phononic crystal”, *Phys. Rev. B* **73**, 054302 (2006).
- [54] M. Ke, Z. Liu, C. Qiu, W. Wang, J. Shi, W. Wen, and P. Sheng, “Negative refraction imaging with two-dimensional phononic crystals”, *Phys. Rev. B* **72**, 064306 (2005).
- [55] A. Hakansson, F. Cervera, J. Sánchez-Dehesa, “Sound focusing by flat acoustic lenses without negative refraction”, *Appl. Phys. Lett.* **86**, 054102 (2005).
- [56] J. Li, C.T. Chan, “Double-negative acoustic metamaterial”, *Phys. Rev. E* **70**, 055602(R) (2004).
- [57] N.W. Ashcroft, N.D. Mermin, *Solid State Physics*, (Saunders College, Philadelphia, 1976).
- [58] M. Sigalas, E.N. Economou, “Band structure of elastic waves in two dimensional systems”, *Solid State Commun.* **86**, 141 (1993); E.N. Economou, M. Sigalas, “Classical wave propagation in periodic structures: Cermet versus network topology”, *Phys. Rev. B* **48**, 13434 (1993).
- [59] M. Sigalas, N. García, “Importance of coupling between longitudinal and transverse components for the creation of acoustic band gaps: The aluminum in mercury case”, *Appl. Phys. Lett.* **76**, 2307 (2000); D. García-Pablos, M. Sigalas, F.R. Montero de Espinosa, M. Torres, M. Kafesaki, N. García, “Theory and Experiments on Elastic Band

- Gaps”, *Phys. Rev. Lett.* **84**, 4349 (2000); Y. Tanaka, Y. Tomoyasu, S. Tamura, “Band structure of acoustic waves in phononic lattices: Two-dimensional composites with large acoustic mismatch”, *Phys. Rev. B* **62**, 7387 (2000).
- [60] M. Kafesaki, E.N. Economou, “Multiple-scattering theory for three-dimensional periodic acoustic composites”, *Phys. Rev. B* **60**, 11 993 (1999).
- [61] Z. Liu, C.T. Chan, P. Sheng, A.L. Goertzen, J.H. Page, “Elastic wave scattering by periodic structures of spherical objects: Theory and experiment”, *Phys. Rev. B* **62**, 2446 (2000).
- [62] I.E. Psarobas, N. Stefanou, A. Modinos, “Scattering of elastic waves by periodic arrays of spherical bodies”, *Phys. Rev. B* **62**, 278 (2000).
- [63] J. Mei, Z. Liu, J. Shi, D. Tian “Theory for elastic wave scattering by a two-dimensional periodical array of cylinders: An ideal approach for band-structure calculations”, *Phys. Rev. B* **67**, 245107 (2003).
- [64] L. Brekhovskikh, *Waves in layered media*, (Academic Press, New York, 1960), pp. 28-30.
- [65] B.A. Auld, *Acoustic fields and waves in solids*, (John Wiley & Sons, New York, 1973)
- [66] J.H. Page, P. Sheng, H.P. Schriemer, I. Jones, X. Jing, D.A. Weitz, “Group Velocity in Strongly Scattering Media”, *Science* **271**, 634 (1996).
- [67] F. Van Der Biest, A. Sukhovich, A. Tourin, J.H. Page, B.A. van Tiggelen, Z. Liu, M. Fink, “Resonant tunneling of acoustic waves through a double barrier consisting of two phononic crystals”, *Europhys. Lett.* **71** (1), pp.63-69 (2005).
- [68] L.D. Landau, E.M. Lifshitz, *Fluid Mechanics* (Pergamon Press, Oxford, 1959), pp. 301-302.
- [69] J.H. Page, S. Yang, Z. Liu, M.L. Cowan, C.T. Chan, P. Sheng, “Tunneling and dispersion in 3D phononic crystals”, *Z. Kristallogr.* **220**, 859-870 (2005).
- [70] A.G. Every, R.E. Vines, J.P. Wolfe, “Line-focus probe excitation of Scholte acoustic waves at the liquid-loaded surfaces of periodic structures”, *Phys. Rev. B* **60**, 11755 (1999).
- [71] W.M. Robertson, G. Arjavalingam, R.D. Mead, K.D. Brommer, A.M. Rappe, J.D. Joannopoulos, “Measurement of Photonic Band Structure in a Two-Dimensional Periodic Dielectric Array”, *Phys. Rev. Lett.* **68**, 2023 (1992).
- [72] W.M. Robertson, G. Arjavalingam, R.D. Mead, K.D. Brommer, A.M. Rappe, J.D. Joannopoulos, “Measurement of the photon dispersion relation in two-dimensional ordered dielectric arrays”, *J. Opt. Soc. Am. B* **10**, 322 (1993).
- [73] T.F. Krauss, R.M. De La Rue, S. Brand, “Two-dimensional photonic-bandgap structures operating at near-infrared wavelengths”, *Nature* **383**, 699 (1996).
- [74] K. Sakoda, “Symmetry, degeneracy, and uncoupled modes in two-dimensional photonic lattices”, *Phys. Rev. B* **52**, 7982 (1995).
- [75] K. Sakoda, *Optical Properties of Photonic Crystals* (Springer, New York, 2005).

- [76] J.V. Sánchez-Pérez, D. Caballero, R. Martínez-Sala, C. Rubio, J. Sánchez-Dehesa, F. Meseguer, J. Llinares, F. Gálvez, “Sound Attenuation by a Two-Dimensional Array of Rigid Cylinders”, *Phys. Rev. Lett.* **80**, 5325 (1998).
- [77] J.H. Page, A. Sukhovich, S. Yang, M.L. Cowan, F. Van Der Biest, A. Tourin, M. Fink, Z. Liu, C.T. Chan and P. Sheng, “Phononic crystals”, *Phys. Stat. Sol. (b)*, **241**, No.15, 3454 (2004).
- [78] E.G. Williams, *Fourier Acoustics: Sound Radiation and Nearfield Acoustical Holography* (Academic Press, London, 1999).
- [79] J.W. Goodman, *Introduction to Fourier Optics* (McGraw-Hill, New York, 1968).
- [80] L.E. Kinsler, A.R. Frey, A.B. Coppers, J.V. Sanders, *Fundamentals of Acoustics* (John Wiley & Sons, New York, 1982).
- [81] M. Ambati, N. Fang, C. Sun, X. Zhang, “Surface resonant states and superlensing in acoustic metamaterials”, *Phys. Rev. B* **75**, 195447 (2007).
- [82] J.D. Joannopoulos, R.D. Meade, J. N. Winn, *Photonic Crystals: Molding the Flow of Light* (Princeton University Press, Princeton, 1995).
- [83] A.R. Selfridge, “Approximate Material Properties in Isotropic Materials”, *Transactions on Sonics and Ultrasonics* SU-32, 381 (1985) (data also available from Onda Corporation at www.ultrasonic.com).
- [84] W. Vedder and D.A. Vermilyea, “Aluminum + Water Reaction”, *Trans. Faraday Soc.*, 561, (1969).